Effect of Tissue Structure (and) Disease on Simulated Arrhythmias in the Human Heart

Sathyavani Malyala

Supervisor: Professor R.H. Clayton

Thesis submitted to The University of Sheffield Department of Computer Science for the degree of Doctor of Philosophy

October 2016

Acknowledgement

I would first like to express my sincere thanks to my supervisor Professor Richard Clayton. I would like to thank him for his guidance, support and encouragement throughout my PhD. I am grateful for EPSRC Doctoral training grant and also would like to thank ICEBERG, The High Performance Computing Cluster at Sheffield University.

A special thanks to my husband and my daughter for their support. I wouldn't have done this without you both. I dedicate this thesis to my dad who has been an inspiration whose incredible and unwavering support helped me complete my graduation.

Abstract

Ventricular Fibrillation (VF) is a severe cardiac arrhythmia. Early experiments provided evidence that the mechanism of VF is consistent with re-entry. In 3D the sources of re-entrant waves are lines of phase singularity called 'filaments'. Filament interactions and filament numbers can be used to quantify the complexity of activation patterns in simulated VF. The aim of this thesis is to study the effect of tissue structure, shape, initial conditions, and region of scar on filament dynamics using computational modelling.

Transmural heterogeneity in 3D slab tissue representing the ventricular wall did not show important difference in the number of filaments. Configuration of filaments were influenced by transmural heterogeneity. With transmural heterogeneity, clustering of filaments were observed near slow conducting border resulting in increase of filament life time.

To study the effect on the shape of the tissue on filaments, filament dynamics in 3D slab tissue was compared with filament dynamics in an idealized human left ventricle (LV) with similar apex base dimension and wall thickness. The volume of idealized LV is about twice the volume of 3D slab. Results showed idealized LV had twice the number of filaments compared to slab geometry especially with steeper restitution dynamics.

This thesis highlights non-linear behaviour of activation patterns during VF in 3D where small changes had a large influence on the number of filaments in both 3D slab and idealized LV especially with steeper restitution dynamics.

Pre-existing scar tissue in VF patients can act as a source of anatomical re-entry and pin re-entrant filaments to the scar boundary. However, the interaction of scar with complex activation during VF is not well understood. This thesis investigated how simulated scars (circumferential, transmural and sub-endo transmural) with varying size and with either regular or with irregular scar boundary, influenced re-entrant filaments in simplified computational models of 3D slab and idealized LV.

Circumferential scar did not show any influence on filament dynamics and clustering of filaments to scar boundary. Increased radius of transmural and sub-endocardial transmural scar had more clustering of filaments to the scar boundary especially with steeper restitution dynamics. Sub-endocardial transmural scar with increased radius had more clustering of filaments compared to transmural scar. Region of scar with irregular boundary had more clustering compared to scar with regular boundary.

Generally transmural scar and sub-endocardial transmural scar with regular or irregular boundary did not increase the number of filaments much but increased the length and lifetime of filaments due to clustering of filaments to the scar boundary. Since filaments pin to the boundary of the scar region, it can be hard to remove them using defibrillation techniques. It might be necessary to measure the radius and the depth of pre-existing scar tissue accurately in VF patients, as the bigger scar is likely to have more complex activation in VF. In this way it might be easier to predict the strength of defibrillation to use, in order to stop VF.

List of Abbreviations

VF	Ventricular fibrillation
AP	Action potential
APD	Action potential duration
APDR	Action potential restitution
CV	Conduction velocity
FDM	Finite difference method
FEM	Finite element method
TP06	ten Tusscher and panfilov 2006 ‘21’ variable biophysically ventricular cell model
4-variable model	Bueno- Orovio 4 variable phenomenological ventricular cell model
LV	Left ventricle
ECG	Electrocardiogram
2D	Two dimensional
3D	Three dimensional
Epi	Epicardial cells in epicardial region of cardiac (left ventricle) tissue
Endo	Endocardial cells in endocardial region of cardiac (left ventricle) tissue
M cells	Mid-myocardial cells in middle layer of cardiac (left ventricle) tissue
S1S2	S1-S2 protocol used to pace cardiac (left ventricle) tissue

Contents

Chapter 1 Introduction

The heart is a vital organ that pumps oxygenated blood to the whole body with repeated rhythmic contractions, and continued heart beats are essential for the body to survive. The heart is an electromechanical pump, the electrical activity of the heart acts to trigger and synchronise mechanical contractions. The heart's natural pacemaker initiates electrical activity that spreads in the ventricles as shown in Figure 1.1 (a), which shows activation isochrones for the human ventricles (Durrer et al. 1970). The electrical activity of the heart can be recorded using an electrocardiogram (ECG); Figure 1.1 (b) shows the ECG recording for the normal heart rhythm where each beat is registered as a single event.

When the normal electrical activity of the heart is disturbed, its capability to pump blood from the heart is affected. This in turn affects the physiological function of the whole body because of lack of oxygen. Heart disease is a very significant health problem. The electrical behaviour of cardiac cells and tissue consists of activation followed by recovery. Activation waves in tissue can only propagate into tissue that is in a recovered state. A normal beat is characterised by a wave of total activation of the heart, followed by recovery. Cardiac arrhythmia is an irregular rhythm caused by abnormal electrical activity. When there is a disturbance in the propagation of electrical activity in the heart, the electrical wave breaks forming abnormal electrical activity called re-entry. In re-entry, the activation wavefront breaks, so that the wavefront is able to continually propagate into recovered tissue. Re-entry is dangerous because the activation rate is higher than the resting heart rate, so normal pace making activity is suppressed. Ventricular fibrillation (VF) is a severe arrhythmia where the normal electrical activity is completely disturbed and experimental studies show that VF is associated with re-entry. Figure 1.1 (c) shows abnormal electrical activity during ventricular fibrillation (VF) in an idealized left ventricle, where the colour bar shows transmembrane voltage. Figure 1.1 (d) shows ECG recording of abnormal electrical activity of the left ventricle (LV).

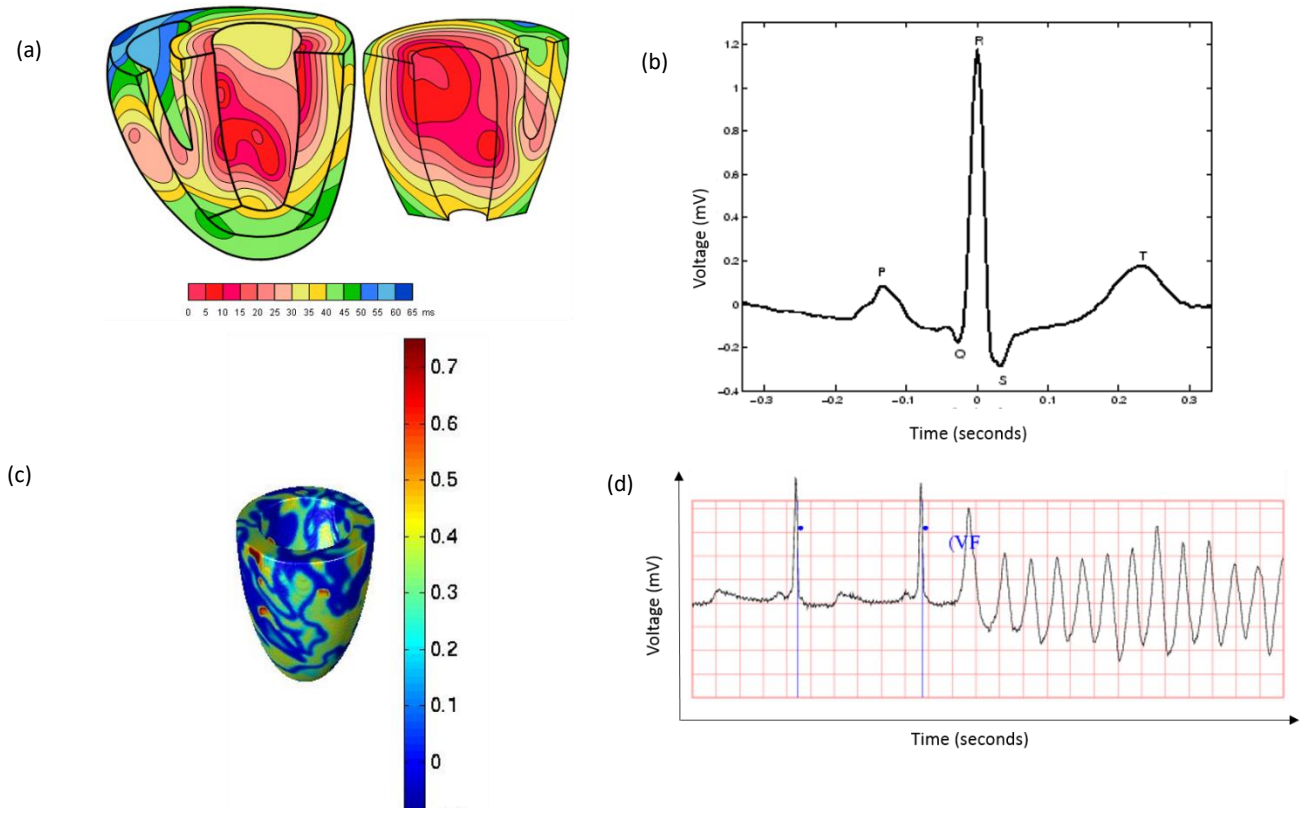

Figure 1.1 (a) Activation sequence in normal heart (Reproduced with permission from (Durrer et al. 1970)); (b) Normal ECG recording (Reproduced from physionet.org) ; (c) Activation sequence in an idealized left ventricle model during simulated VF using 4-variable model ; (d) ECG recording during VF grid interval along X axis is 0.2 seconds, along Y axis 0.5 mV (Reproduced from physionet.org).

1.1 Overview of Ventricular Fibrillation (VF)

Sudden cardiac deaths are around 300,000 annually in the United States and the majority are caused by ventricular fibrillation (Lane et al. 2005). Ventricular fibrillation (VF) is a serious cardiac arrhythmia, where the electrical activity is completely disturbed, resulting in ineffective muscle contractions (Zipes & Wellens 1998).

Cardiac arrhythmia is an irregular rhythm caused by abnormal electrical activity. Abnormal electrical activity can result from abnormal initiation or conduction of electrical activation. In re-entry, a wave of cardiac activation rotates. Experimental studies show that electrical activation during VF is consistently associated with re-entry (Choi et al. 2001, Gray et al. 1998, Samie et al. 2001, Witkowski et al. 1998). An obstructed re-entrant wave breaks, curls around and activates a particular tissue at a high speed that surpasses electrical conduction initiated by a natural pace maker and in turn affects the mechanical contractions of the heart.

Studying VF clinically is difficult because it is a medical emergency. Moreover, there can be ethical limitations to study of VF in the human heart. Experiments on animal hearts might not give precise information as there is a difference in heart size and the organisation of VF compared to human heart (ten Tusscher et al. 2009).

Most clinical and experimental studies of VF in the human heart have recorded electrical activity from the surface of the ventricles. Consequently, re-entrant waves are observed as spiral waves since the surface is 2D. However, the ventricular wall is a 3D tissue. Even though recent developments in experimental studies have recorded electrical activity from the depth of the ventricles, it often has poor resolution compared to computational studies (Li et al. 2010). Moreover, in experimental and clinical studies it might be difficult to obtain human ventricles or tissue to test for certain conditions.

In modelling studies, it is easy to control certain parameters or conditions in a systematic manner and test the hypothesis. So computational modelling can be used as a research tool alongside experimental and clinical studies.

Re-entrant waves are observed as scroll waves in 3D. During VF, several re-entrant waves can combine to generate complex patterns of spatiotemporal electrical activation. In order to understand electrical activation during VF, the core of scroll or spiral waves can be extracted and studied. The core of the spiral wave is called a ‘phase singularity’ (PS) which is observed as a point. The core of a scroll wave is called a ‘filament’ which is observed as a line. When a scroll wave filament touches the tissue surface, it is observed as PS. So filaments can be used to quantify VF (Clayton & Holden 2002).

During VF, over the course of time, filaments change in number because of the birth of new filaments, death of filaments, amalgamation or division of filaments due to underlying tissue structure and other conditions. Filaments change their shape and length over the course of time. Studying these changes in filaments can provide an insight into VF (Clayton & Holden 2002, Xie et al. 2004, F. H. Samie & Jalife 2001). This thesis studies the influence of tissue structure and/or disease on filament dynamics.

The aim of this thesis is to study the influence of tissue structure and disease on the mechanism of ventricular fibrillation (VF), using computational models of electrophysiology (EP).

The main hypothesis examined in the thesis is that:

Shape, thickness, initial conditions, heterogeneity and tissue structure and disease of human ventricular tissue have a strong influence on the behaviour of re-entrant filaments during simulated ventricular fibrillation.

The structure of this thesis is as follows:

Chapter 2: Modelling Cardiac Anatomy and Physiology

This chapter explains the basic anatomy and electrical activity in the human heart, and how electrical activity triggers the mechanical contractions of the heart. The relationship between the structure and function of ventricles is explained and cardiac arrhythmias and different types of scar formed as the result of myocardial infarction (MI) are also covered. The components for modelling electrical activity in virtual tissue geometry, technology and software used in modelling are explained. This chapter also covers computational and experimental studies in ventricular fibrillation and the effect of tissue structure and/or disease on VF and identifies gaps to formulate key research questions.

Chapter 3: Numerical Implementation

This chapter explains in detail the numerical implementation of the models used. Numerical implementation outputs electrical activation voltage readings over time (ms). Details of the post processing procedure used to interpret the voltage recordings are explained. This section also covers the modelling of the geometry and fibre orientation used in this thesis.

Chapter 4: Influence of Tissue Shape, Structure and Initial Conditions on Filament Dynamics

Transmural heterogeneity is a controversial topic. Research (Sicouri & Antzelevitch 1991a) has shown the presence of M cells while others argue there is no evidence of M cells (Taggart et al. 2001). Glukhov et al. (2010) experimentally showed the presence of M cells possibly in patches between epicardial and endocardial layers but distribution of the cells was not as sharp as in other modelling studies (Majumder et al. 2011). Consequently, the effect on filament dynamics of transmural heterogeneity in AP shape and duration needs to be systematically tested for uniform, epi-endo, epi - M - endo, epi - Mpatch -endo in both sharp and smooth distribution. The non-linear behaviour of 3D cardiac tissue model on filament dynamics is tested in this chapter.

Chapter 5: Influence of Tissue Structure and Disease on Filament Dynamics

Myocardial infarction (MI) forms a region of scar tissue. The scar region can be transmural or circumferential. Transmural scar can be either fully transmural to the ventricular wall or just sub endocardial scar. Both full and sub endocardial transmural scar regions can have either regular or irregular boundaries (Rubin & Reisner 2014). Studies have shown that scroll wave filaments pin to scar boundaries. The size and position of the scar affects the pinning of filaments (Shajahan et al. 2007). This chapter studies the effect of the scar region on filament dynamics and the pinning of filaments to the scar boundary.

Chapter 6: Discussion and conclusion

This chapter shows the overall discussion and conclusion from Chapters Four and Five. The limitations and future direction of the research are discussed in this chapter.

Chapter 2 Modelling Cardiac Anatomy and physiology

This chapter explains the basic cardiac anatomy and electrophysiology of the healthy human heart and also how electrophysiology is affected by disease. Experimental studies can give insight into electrical activity in cells and tissues, but there are many unknown factors that are difficult to measure experimentally. This chapter explains why computational modelling has become an important tool in understanding the underlying mechanisms of electrophysiology in normal and diseased heart and describes the components of cardiac electrophysiology models. It also reviews progress in the field of computational modelling and experimental studies in ventricular fibrillation, identifies gaps in this area, and formulates the key questions of this thesis.

2.1 Cardiac Anatomy and Tissue Structure

The human heart is an electro-mechanical pump that pumps oxygenated blood (rich in oxygen) to the whole body. The heart has four chambers – right atrium (RA), right ventricle (RV), left atrium (LA) and left ventricle (LV). The left side of the heart pumps blood around the body, and the right side of the heart collects blood from the body and pumps blood to the lungs. The heart is made up of electrically excitable cardiac cells and tissues, held together by connective tissue.

Coronary arteries are the blood vessels that supply oxygen to cardiac myocardium (Figure 2.1).

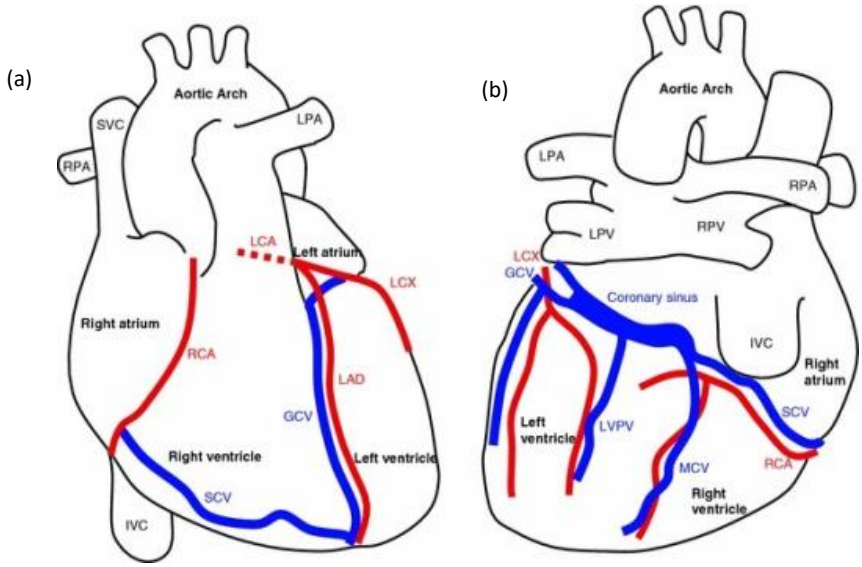

Figure 2.1 (a) Anterior view of coronary arteries; (b) Posterior view of coronary arteries. Coronary arteries shown in red: left coronary artery (LCA), left circumflex (LCX), left anterior descending (LAD), right coronary artery (RCA) with four chambers of the heart, right atrium, left atrium, right ventricle and left ventricle (Reproduced with permission from (Lee & Smith 2012)).

The human heart is 100 mm from base to apex and the wall of LV is approximately 12 mm thicker. The ventricular wall is divided into three layers: epicardium (outer layer), Midmyocardium (middle layer) and the endocardium (inner layer) as shown in Figure 2.2. Transmural heterogeneity is controversial topic and it is explained in section 2.8. Deeper to the endocardium layer is sub-endocardium layer. Underneath epicardium layer is sub-epicardium layer.

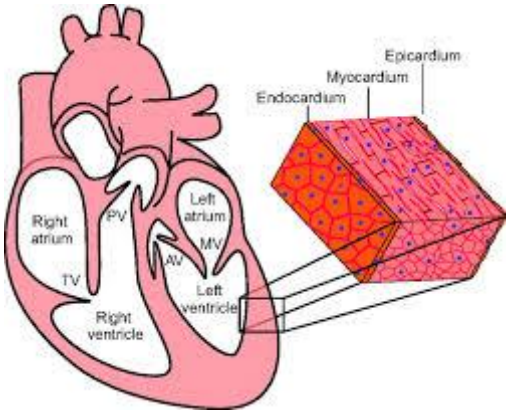

Figure 2.2 Transmural tissue heterogeneity in mammalian heart wall. Heart wall is divided in to epicardium, mid-myocardium and endocardium. (Reproduced with permission from (Lin et al. 2012)).

Ventricular tissue consists of excitable rod-shaped cells aligned in fibres. The fibre axis continuously rotates anti-clock wise between the top and the bottom sheets (from epicardium to endocardium) when observed from the epicardium. The total rotation is roughly 120^{o} anticlockwise but varies between individuals and also varies from one species to another (Streeter et al. 1969), (Fenton & Karma 1998). Fibres are organised as sheets with these sheets appearing almost parallel to one another like a laminar arrangement (Nielsen et al. 1991), (Caldwell et al. 2009). The long axis of cells (fibre axis) is identical in each sheet as shown in figure 2.3. The fibre sheet laminar arrangement has so far been observed only in animal hearts (LeGrice et al. 1995), but it is reasonable to assume that it is present in human hearts too.

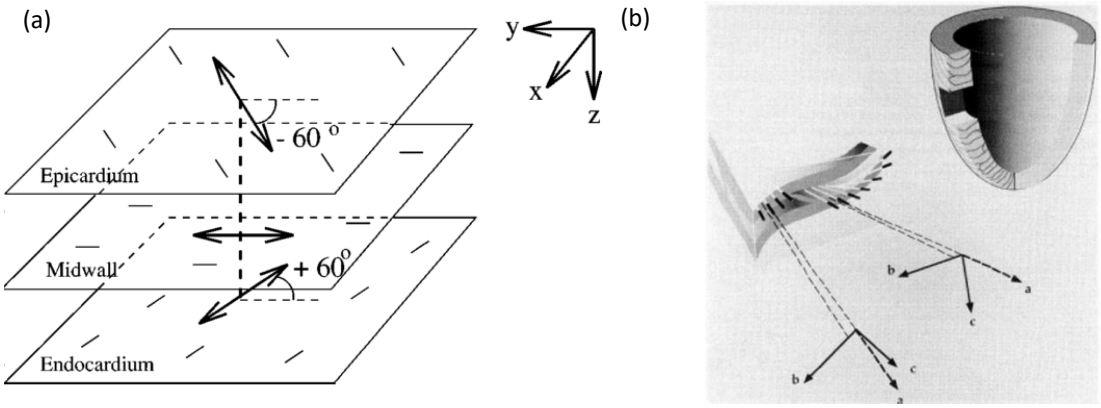

Figure 2.3 (a) Fibre axis rotation (Reproduced with permission from (Fenton & Karma 1998)); (b) Fibres organized in sheet, vectors a, b and c define local fibre axis, sheet axis and sheet normal (Reproduced with permission from (Nielsen et al. 1991)).

Fibre orientation can be measured using histology and diffusion tensor magnetic resonance imaging (DT MRI). Histology is a direct measurement of fibre and sheet orientation by dissection of cardiac tissue captured using microscope. DT MRI is a non-invasive imaging technique used to get fibre orientation. It is a time consuming imaging modality which captures the diffusion of protons along fibres. An important limitation of DT MRI is that it measures average diffusion in a tissue volume. The DT MRI signal may be not powerful to capture fibre sheet orientation at high resolution (Gilbert et al. 2007). These two techniques (DTMR and Histology) can be done on an ex- vivo tissue or organ.

2.2 Cardiac Cell and Tissue Electrophysiology

The electrophysiological function of heart cells and tissue consists of electrical activation and recovery; this results in an action potential (AP), and the restitution of AP, describing the rate dependence of AP shape and duration. These are discussed in turn below.

2.2.1 Electrical Activation and Recovery

The heart's natural pacemaker sends a regular electrical signal that initiates the cardiac cycle. During the cycle, each cell is electrically activated and then recovers. This electrical activation and recovery is called an action potential; Figure 2.4 shows an example. At rest, the voltage across the cardiac cell membrane is around -85 mV. During an action potential the voltage changes to around +20 mV before returning to the resting value after 250 milliseconds. The electrical behaviour of cells is referred to as electrophysiology.

2.2.2 Mechanism of Action Potential

Like other cells in the body, every cardiac cell is surrounded by a thin membrane. The cell membrane separates extracellular and intracellular fluid. These extracellular and intracellular fluids contain positively charged ions including sodium (Na^+), potassium (K^+) and calcium (Ca^{2+}) as well as negatively charged ions including chloride (Cl^-). The extracellular fluid contains more Na^+ and Ca^{2+} compared to intracellular fluid, and intracellular fluid contains more K^+ compared to extracellular fluid. These differences in ionic concentrations are maintained by pumps, ion channels and exchangers located in the cell membrane. The difference in ionic concentration maintains a potential difference between extracellular and intracellular regions when the cell is at rest.

At rest, the membrane potential is negative compared to when the cell is excited. This is called the resting membrane potential and is approximately -85 to -90 mV. In this state, the membrane is more permeable to K^+ than Na^+. The concentration difference of K^+ ions between intracellular and extracellular space drives K^+ ions to diffuse out of the cell. However, the membrane potential opposes the tendency to diffuse out of the cell; consequently, at equilibrium, the membrane potential is close

to the Nernst potential for K^+, -90 mV. The Nernst potential or equilibrium potential of a particular ion is the electrical gradient across the membrane that stops the net diffusion of that particular ion.

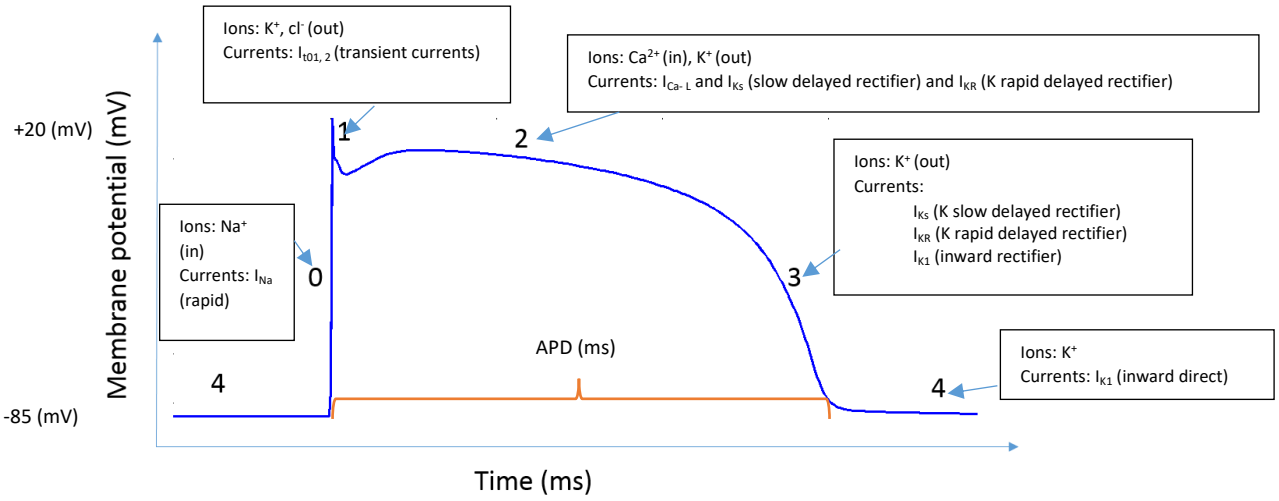

Figure 2.4 Five phases in simulated ventricular action potential (AP) (Zipes & Jalife 2004).

When an action potential occurs in an adjacent cell, the small change in membrane potential results in opening of voltage-gated Na^+ ion channels; Na^+ flows into the cell and the membrane potential quickly changes from negative potential to slightly positive. This change in membrane potential is called the action potential (AP) upstroke. This cardiac AP initiates the mechanical contraction of cells and tissues as explained below (Zipes & Jalife 2004).

The action potential consists of 0-4 phases depending upon the ions entering or leaving the cell membrane. Figure 2.4 shows the diffusion of ions and the resulting currents in each phase. Phase 4 is the resting phase. Phase 0, when stimulated Na^+ ions enter the intracellular space through voltage gated Na^+ channels, rapidly making the membrane potential slightly positive. During phase 1, K^+ ions and Cl^- ions pass out of the cell membrane resulting in the AP notch.

During phase 2 of the AP, mechanical contractions are initiated. Calcium ions (Ca^{2+}) enter through L type calcium channels resulting in $I_{Ca,L}$ current. This leads to an increase in intercellular calcium, which

in turn triggers calcium release from sarcoplasmic reticulum situated inside the cell. This is called 'Calcium Induced Calcium Release' (CICR). The cytoplasmic calcium then binds to troponin which creates active binding sites allowing myosin heads (molecular motor) to bind to the actin filament. As a result, the myosin head engages the actin filaments enabling the contraction. During phase 3 of AP, K^+ channels open and the flow of K^+ out of the cell causes the membrane voltage to fall to its resting state. Contractions are terminated at phase 4 of AP. When the intracellular calcium decreases, the troponin complex blocks the actin filament active site ending the contraction.

2.2.3 Action potential propagation in tissue

The time taken by the action potential from phase 0 – phase 4 is called the action potential duration (APD). The period between activation and recovery of a cell is called the refractory period and is roughly equal to APD. APD differs in different regions of the heart as shown in Figure 2.5 (a) (Nerbonne & Kass 2005). Action potential is very important for coordinating the contraction of the heart. At the start of the cardiac cycle (beginning of a heart beat), the right atrium and left atrium relax and are filled with blood. These upper two chambers of the heart then contract and the blood is pumped to the right and left ventricles. Finally, the blood from the lower chambers (right and left ventricles) is pumped out of the heart by a contraction. The above is repeated for every heartbeat.

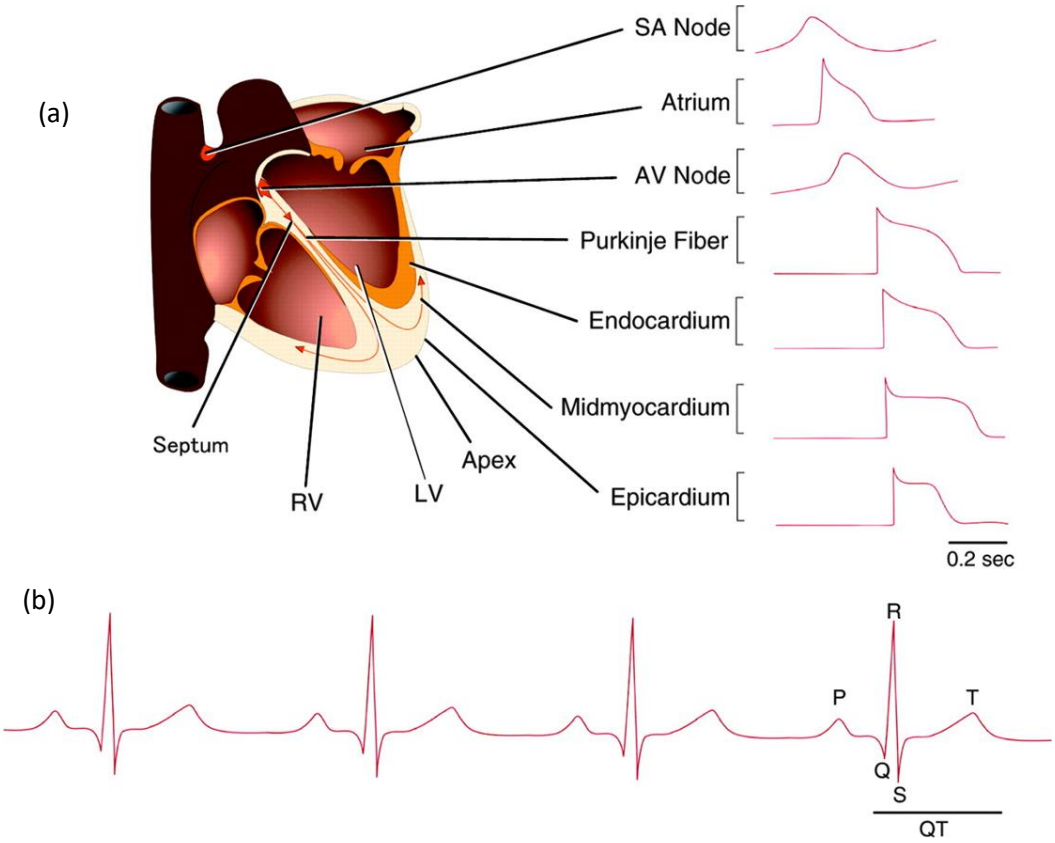

Figure 2.5 (a) Schematic representation of human heart with AP recorded at different region of heart; (b) Schematic representation of ECG for 3 sequential beats (Reproduced with permission from (Nerbonne & Kass 2005)).

The electrical activity of the heart can be monitored by electrocardiogram (ECG) from the surface of the chest. Figure 2.5 (b) shows an ECG of the normal cardiac rhythm, recorded as time (seconds) against voltage (mV). The sinoatrial node, the heart's natural pacemaker, generates electrical impulses; the P wave in the ECG shows the atrial depolarisation. PQ in the ECG shows electrical stimulus passing the AV node. QRS shows ventricular depolarisation. The ST interval shows entire ventricle depolarisation representing the plateau phase of the AP. T wave shows the ventricle repolarisation. The Q-T interval in the ECG describes ventricular depolarization and repolarization (Zipes & Jalife 2004).

Ventricular cells are aligned in fibres. Propagation of an action potential (AP) is faster along fibres compared to across fibres (Panfilov & Keener 1995). The speed at which the propagation wave (AP) conducts through tissue is called the conduction velocity. An experimental study in canine hearts (Roberts et al. 1979) showed that the conduction velocity of AP across the fibres was 21 cm/sec, and 53cm/sec along the fibre; it has also been shown (Roberts et al. 1979, Ernest Frank 1953) that the

wave front produced by a point stimulus is elliptical. The long axis of the ellipse is aligned with the fibres. This anisotropic propagation makes the fibre orientation information important in the study of electrophysiology.

2.2.4 Action Potential Restitution and Conduction Velocity Restitution

The diastolic interval (DI) is the period of time between the fourth phase (resting) of an AP and the beginning of the next AP. During this DI, the cells regain their ionic balance and the heart chambers relax and let in blood. One cardiac cycle is APD + DI. The adjustment of the heart in shortening the APD when there is a rapid heart rate is called APD restitution. When APD is plotted as a function of the previous DI, the result is called the APD restitution curve (APDR). Restitution is the rate dependent behaviour of APD (Figure 2.6 (a)). Conduction velocity plotted against diastolic interval (DI) is called conduction velocity restitution (Figure 2.6 (b)) (Zipes & Jalife 2004).

(a)

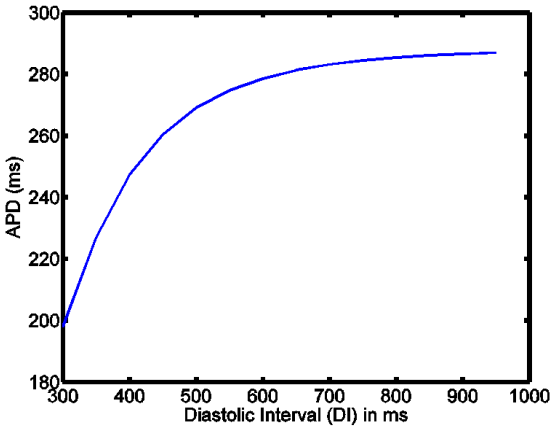

(b)

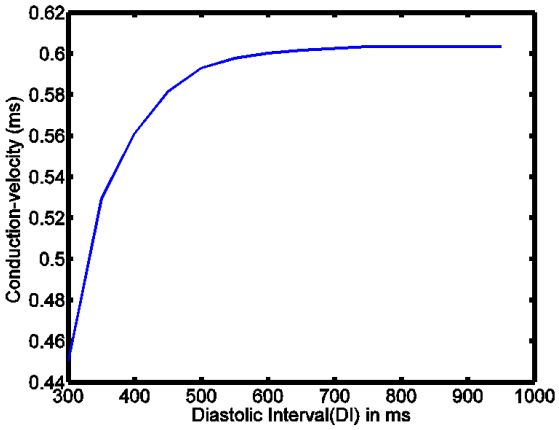

Figure 2.6 Simulated plot showing (a) Restitution curve plotted action potential duration (APD) plotted against diastolic interval (DI); (b) Restitution curve plotted conduction velocity plotted against diastolic interval (DI).

2.3 Diseased Heart

2.3.1 Cardiac Arrhythmias

A normal heart beat involves complete electrical activation of the whole heart followed by recovery. An arrhythmia is an abnormal impulse formation or abnormal impulse conduction resulting in an abnormal heart rhythm. Different types of arrhythmia can occur in either the atria or the ventricles.

- Bradycardia is a slow heart rhythm that is less than 60 beats per minute

- Tachycardia is a faster heart rhythm that is more than 100 beats per minute. Ventricular Tachycardia (VT) can be induced by different mechanisms (Wolf & Berul 2008).

    - If there is a problem with the heart's natural pacemaker, then spontaneous activity may originate in other parts of the heart; this is termed 'increased automaticity' or 'focal activity'; the myocytes are stimulated without external stimulus.
    - The second mechanism is called 'triggered activity', where arrhythmias initiate immediately after depolarization. 'Afterdepolarization' is a premature depolarization of myocytes caused by intracellular calcium oscillations (Wolf & Berul 2008).
    - The third mechanism is called re-entry. During re-entry, a propagating AP wave is blocked causing arrhythmia; this mechanism is explained in detail in section 2.4.

    Arrhythmias occurring in the ventricles are more dangerous than in the atria. Ventricular Tachycardia (VT) can deteriorate into ventricular fibrillation (VF) which is a life threatening condition as explained below. The focus of this thesis is on re-entry and ventricular fibrillation (VF).

2.3.1.1 Ventricular Fibrillation

During VF, electrical activity circulates repeatedly at higher frequency than natural heart rate leading to no effective contractions. VF is, therefore, a medical emergency and should be treated immediately using defibrillation (Zipes & Wellens 1998).

2.3.1.2 Experimental Investigation of VF

Early studies (Wiggers 1940) showed complex patterns of contractions during VF. An important controversy at this time was whether VF was sustained by re-entry or focal activity. Electrical mapping experiments done on epicardial surface to analyse VF (Frazier et al. 1989, Janse et al. 1980, Kim et al. 1997, Lee et al. 1996, Rogers et al. 1999) showed that many wave fronts are formed during VF. Optical mapping experiments (Choi et al. 2001, Gray et al. 1998, Samie et al. 2001, Witkowski et al. 1998) using voltage sensitive fluorescent dyes have provided evidence that the mechanism of VF is associated with multiple waves of re-entry.

2.3.1.3 Re-entrant Arrhythmias

When the activation wave is partly blocked, the wave can break and the loose end of the wave curls causing re- entry. The rotating wave continuously activates recovering tissue, suppressing the regular waves produced by the heart's natural pacemaker causing arrhythmias. Re-entry forms spiral waves of activity in 2D and scroll waves in 3D. Spiral waves or scroll waves are a property of excitable media where there is diffusion of activation and recovery. During arrhythmias, the blood pumped to the body from the heart is insufficient or no blood is pumped out in the serious arrhythmias called VF. Re-entry can be functional or anatomical. Functional re-entry occurs when the propagating electrical wave activates the excitable tissue which is still in the refractory period. Anatomical re-entry results when the propagating electrical wave activates an in-excitable tissue. In both cases, the electrical wave breaks and forms a re-entrant wave (Mines 1913).

2.3.1.4 Phase and Phase Singularities

VF recordings from experimental or computational simulations give membrane voltage readings from the cardiac tissue. Experimental studies confirm VF is sustained by re-entrant waves. Identifying activation membrane voltage in each re-entrant wave is difficult since it is encountered twice, once when there is a depolarisation and once when there is repolarisation (Gray et al. 1998). Since re-entry is a self-sustaining activity and a periodic dynamic system, the state of cell embedded in tissue can be represented by phase. Phase represents the unique state of each excitable cardiac cell (Gray et al.

1998, Mines 1913). Phase singularity (PS) is a point where the surrounding phase change is 2π, since the excitation wave front and repolarisation wave back meet at this point (Gray et al. 1998). PS is the point around which the re-entrant waves rotate. In 2D, it is observed as a point and in 3D, it is observed as a line of phase singularity (Bray & Wikswo 2002). Decomposing scroll waves to their cores, i.e. filaments (Figure 2.10), in 3D and PS in 2D are used to quantify the chaotic activity observed during VF (Gray & Jalife 1998).

2.3.2 Scar Region Resulting from Ischemia and Myocardial Infarction

Coronary arteries supply oxygenated blood to the heart. Coronary arteries are situated in sub-epicardium and penetrate to mid-myocardium and then onto sub-endocardium as seen in Figure 2.2. If the blood supply is interrupted in a particular area of the tissue, a condition called 'ischemia' results where there will be change in the electrophysiological function of the heart. If this ischemic condition persists longer, then the affected part of the tissue dies. Tissue death is irreversible and is called myocardial infarction (MI) or heart attack. This dead tissue eventually becomes a scar region which is in-excitable and so cannot conduct AP propagation. The size of this scar region depends upon the amount of time and depth and length of the particular coronary artery occlusion that causes oxygen deprivation (Rubin & Reisner 2014). Scar regions can be detected using contrast enhanced MRI (Bleeker et al. 2006). This contrast enhanced MRI can be obtained by clinically injecting the patient with a contrast agent called 'gadolinium'. Ten minutes after injection, normal myocardium remains black whereas the scar region is enhanced by the contrast agent. Normally, infarcts are classified into two kinds: localized and circumferential.

A localized infarct is formed if there is a block in a specific coronary artery causing regional ischemia. In the early stages of the localized block, the infarct will be limited to the sub-endocardial region of the tissue, extends outward towards the epicardial surface and becomes a transmural infarct. The outer wall adjacent to the infarct in most cases is preserved (Hackel & Wagner 1995). Localized transmural and sub- endocardial infarcts can be solid or patchy, i.e. can have a regular or irregular boundary. Scar is classified as patchy if it is 50% infarcted. Localized sub endocardial scars extend half to three quarters from endocardium to epicardium (Cook et al. 1958). Myocardial infarction (MI) is classified as small, medium and large depending upon the percentage of left ventricular myocardium that is scarred. 10% is classified as small, 10-30% is classified as moderate and more than 30% is considered as large (Thygesen et al. 2007). Regional myocardial infarction is normally found in 90% of MI patients.

Circumferential sub endocardial infarcts can occur when there is a block in all major coronary arteries causing global ischemia. Circumferential scars are seen in the mid wall of the ventricle and are less than 10mm (Choudhury et al. 2002). Circumferential sub endocardial infarction is seen in around 10% of MI patients.

2.5 Computational Modelling

Studying human heart function in health and disease is difficult because the quantities of interest are difficult to measure in-situ. This is particularly the case for studying cardiac arrhythmias. Models, therefore, provide a valuable research tool.

2.5.1 History of Modelling Cardiac Electrophysiology

To model cardiac electrophysiology, a virtual cardiac cell is necessary. In 1952, Hodgkin and Huxley developed a model of squid giant axon to understand the generation of AP. They modelled the giant squid nerve fibre as an electrical circuit with capacitance and resistance. The capacitor in the electrical circuit is to accumulate ionic charge and maintain potential difference across the circuit (cell membrane). The resistor represents across cell membrane ionic permeability which causes the uneven diffusion of ions across the circuit (cell membrane) resulting in electromotive force.

The Hodgkin and Huxley model was modified by Noble (1960) for cardiac cells. The cardiac cell model is integrated in a tissue model to create virtual tissue.

Models have been used in the study of mechanisms underlying re-entry since the 1960s, and one of the first attempts to model (Gordan 1963) atrial fibrillation has been very influential. This study used discrete modelling called a 'cellular automaton' (CA) using mathematical terms formulated by Wiener & Rosenbllueth (1946). In discrete modelling, each cell in the cardiac tissue is represented explicitly; in each time step, the state of the cell is updated using its previous state and the state of its neighbours. Even though this approach was computationally inexpensive, this earlier study reproduced AP propagation and re-entry generation but failed to produce rate dependences such as action potential restitution.

A coupled map lattice (CML) approach was developed based on CA. In the CML approach, each cell had continuous states and was updated by interactions within the lattice (Waller & Kapral 1984, Holden & Zhang 1993). This approach was used to model tissue anisotropy.

A refinement of the CML approach is coupled ordinary differential equations in 1D (Rudy 1995) and 2D sheets (Winslow et al. 1993). This approach was used to describe the dynamics of each cell using resistors to represent gap junctions. A variation of this approach used 3D tissue anisotropy. These approaches can be computationally expensive without careful optimization (Vigmond & Leon 1999).

Another approach of tissue modelling is continuous modelling where cardiac tissue is considered as functional syncytium (Neu & W 1993). Over the years, cardiac electrophysiological studies have increasingly used a continuum approach. This approach can be justified as, in larger spatial scales, the

electrical wave propagates smoothly as shown in Figure 1.1(a) (Durrer et al. 1970). This thesis is based on continuous modelling and the approach is explained in section 2.6.3.

2.5.2 Need for Modelling

Cardiac cell and tissue electrophysiology is complex and integrative. It is difficult to obtain a cell or a tissue or an organ with a particular human disease.

Studies in animal hearts use different techniques such as voltage sensitive fluorescent dyes, plunge needles, etc. to measure electrical activation in tissue (Li et al. 2010) and electrical activation measured in experimental studies often has poor spatial and temporal resolution. Experimental studies on animal hearts may be different from human hearts because of differences in heart size, heart rate, AP propagation and AP duration between animals and humans (ten Tusscher et al. 2004).

Recording electrical activation from the surface of ventricles (2D), it is not possible to capture the interactions between scroll waves as only phase singularities (PS) are observed as points (Winfree 1989) since the heart is a 3D object. It is still difficult to measure some quantities of interest such as the number of re-entrant waves that organise VF and stability of re-entrant waves in 3D and the influence of tissue structure (i.e. scar) on re-entrant filaments.

In modelling studies, it is possible to control parameters in a systematic way to find the effect on re-entrant waves; whereas this is not possible in experimental and clinical studies.

Models provide a representation of the real system and can be used to understand underlying mechanisms. Models of cardiac electrophysiology are used to understand how re-entry is sustained and to quantify VF. Models are now accepted as a valuable tool to run alongside experiments. For these reasons modelling, often combined with high performance computing and experimental data, is becoming a widely used research tool to test hypotheses that arise from experimental data (O'Hara et al. 2011). Models need to be carefully validated against observed experimental results.

2.6 Components of Modelling

A model of electrical activity in the heart has several components: excitable cells; action potential propagation in tissue; a representation of tissue shape and structure; and a numerical implementation of the model (Figure 2.7). Each of these components is described in turn in the following sections.

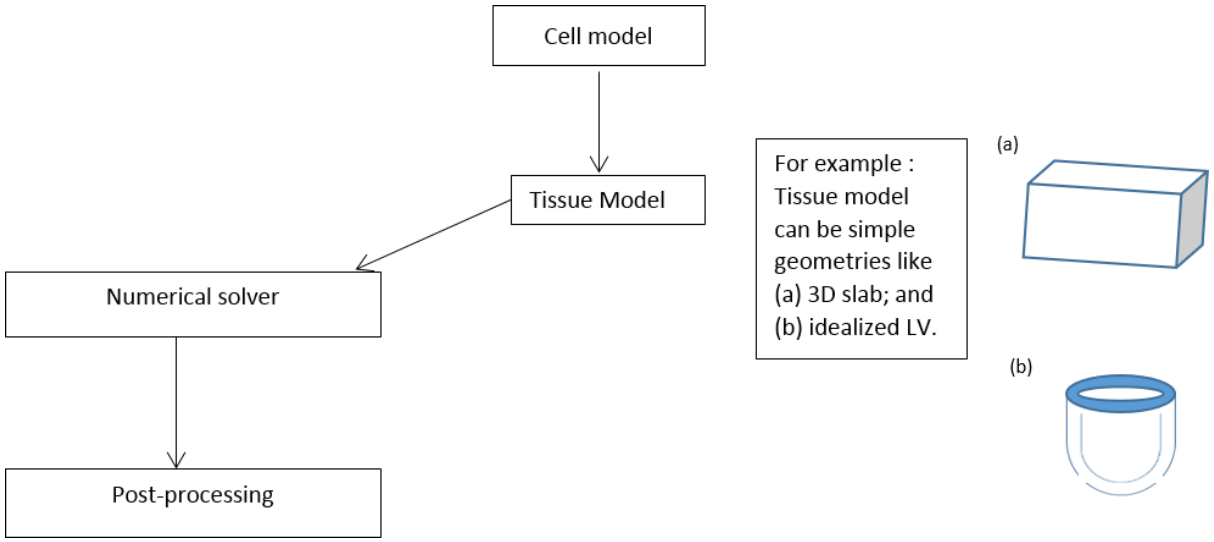

Figure 2.7 Schematic representation of components of modelling. Ventricular cell model is integrated in tissue model (a) 3D slab geometry;(b) Idealised geometry incorporating Left Ventricle (LV) and numerical solver is used to solve AP propagation in tissue.

2.6.1 Models of excitable cells

Hodgkin and Huxley (1952) assumed that current flow in the membrane of the squid giant axon could be represented by an electrical circuit as shown in Figure 2.8.

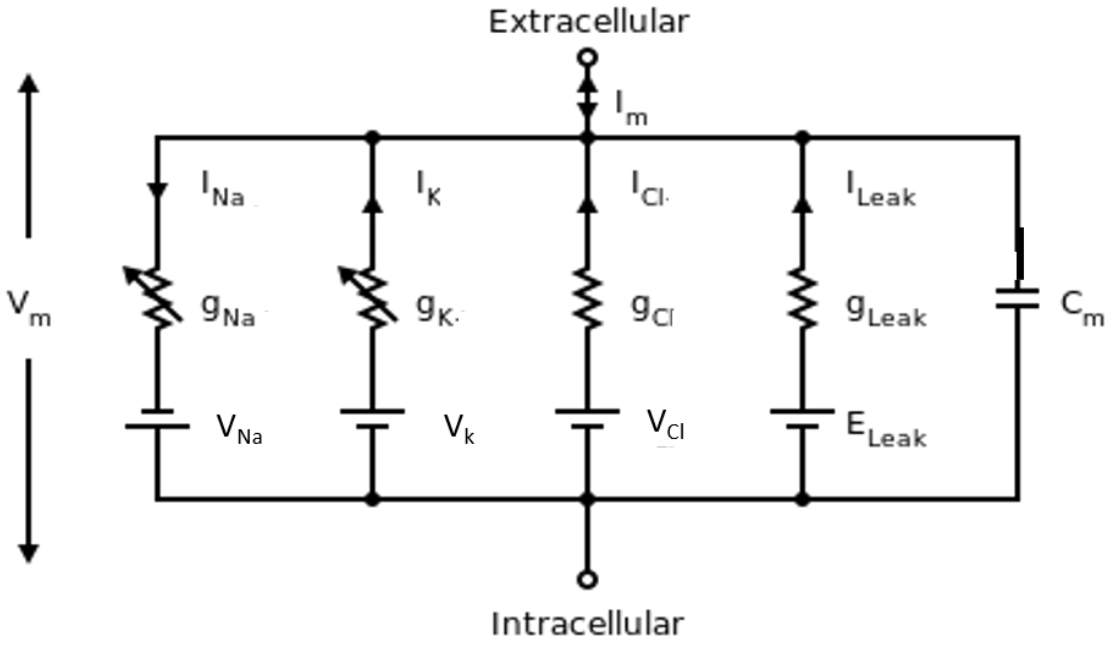

Figure 2.8 Electrical circuit representing cell membrane: g_{Na}, g_k and g_{Cl} are capacitance of sodium (Na), potassium (k) and chloride (Cl) ions respectively; g_{Leak} is conductance of leak current, V_{Na}, V_k and V_{Cl} are ionic potential for sodium (Na), potassium (k) and chloride (Cl) ions respectively; I_{Na}, I_k and I_{Cl} are current density flowing in each ion channel; V_m is membrane potential; and I_m is the sum of all the ionic current densities flowing across the membrane; C_m is membrane capacitance (Reproduced with permission and adapted from (Hodgkin & Huxley 1952)).

The membrane is represented by a capacitance, and the ion channels are represented by a battery in series with a variable conductance. Based on Ohm's law (I=V/R), the current density (current per unit membrane area) flowing in each ion channel is:

$$I_x = g_x (V_m - V_x) \tag{2.1}$$

V_m is membrane potential and g_x is the conductance of each ion channel. V_x is the equilibrium potential of each ion channel and C_m is membrane capacitance. The Nernst potential or equilibrium potential of a particular ion is the electrical gradient across the membrane that stops the net diffusion of that particular ion. For example the current density flowing for a particular ionic current I_{Na} will be:

$$I_{Na} = g_{Na} (V_m - V_{Na})$$

When no current flows through the membrane, the sum of all the ionic current densities flowing across the membrane is given by:

$$I_m = C_m \frac{dV_m}{dt} \tag{2.2}$$

At steady state, I and $\frac{dV_m}{dt}$ are zero. When there is external stimulus, the equation to calculate the sum of ionic current density is:

$$I_m = C_m \frac{dV_m}{dt} + I_x \tag{2.3}$$

In Equation 2.2 and 2.3, C is the specific membrane capacitance – i.e. capacitance per unit area, and I_{ion} is total current density flowing in each ion channel. Models of cardiac cells are based on the principles of the Hodgkin Huxley model and are discussed in section 2.6.2.

By substituting I_x from Equation 2.1, Equation 2.3 can be written as:

$$I_m = C_m \frac{dV_m}{dt} + \sum_{k=1}^{N} g_k (V_m - V_k) \tag{2.4}$$

Where k is the k_{th} ion and g_k and V_k are its corresponding conductance and equilibrium potential.

The conductance of an ion is expressed as functions of gating variables. These conductances are voltage and time dependent. An ion can enter or leave a cell through pumps, exchangers and gates located in the cell membrane. If the gating variables are taken as y, then the conductance of i_{th} ion can be written as follows:

$$g_k = \overline{g_k}\, f_k\,(y_1\ , y_2\ , \ldots\ldots,) \tag{2.5}$$

In the above equation $\overline{g_k}\ and\ f_k$ are constants determined by experiments (O'Hara et al. 2011). Gating variables y_1, y_2, etc. can be taken as y_i. Gating variables have a value between 0 and 1 that describes the activation, inactivation and recovery of ion channels. In the Hodgkin-Huxley scheme, these gating variables satisfy first order differential equation as shown below:

$$\frac{dy_i}{dt} = \alpha_{yi}(1 - y_i) - \beta_{yi} y_i \tag{2.6}$$

In the above equation α and β are rate constants and depend upon voltage. This can be expressed as:

$$\alpha_{yi} = \alpha_{yi}(V) \tag{2.7}$$

$$\beta_{yi} = \beta_{yi}\,(V) \tag{2.8}$$

Gating variables are formulated using parameters. Model parameters used to calculate specific ionic currents are based on experimental data (Clayton & Panfilov 2008). However, the experimental data vary depending upon factors such as environment, specific species, temperature and tissue preparation. The experimental data, therefore, may not be completely correct. Models should reproduce experimentally observed electrophysiological characteristics at both cell level and tissue level. So model parameters are optimized to achieve plausible AP as observed in experiments.

In-depth calcium dynamics (CICR) are modelled using Markov state chain models. A Markov state chain is a random process; transition of one state to another depends only on current state. Shannon et al. (2004) used a 4 state Markov chain model representing resting state, open state, inactivated and resting activated state to model CICR. Resting state represented the closed state of sarcoplasmic reticulum. Open state represented open sarcoplasmic reticulum, when Ca^{2+} diffuses inside the cell during the plateau phase of AP. Inactivated state represented diffused intercellular Ca^{2+} triggering sarcoplasmic Ca^{2+}. Decrease of intercellular calcium represents resting activated state.

2.6.2 Models of Human Ventricular Cells and Tissue

In the last 20 years, biophysically detailed models of cardiac cells have been developed that are specific to different species and different parts of the heart (Fink et al. 2011). This thesis focuses specifically on models of human cells and tissue and will use models of human ventricular myocytes.

A model of the human ventricle needs to combine local electrical excitation, a model of excitation propagation in tissue, a model of the tissue geometry mechanical contraction and the blood flow. Each of these components is described and reviewed in turn.

2.6.2.1 Ventricular Cell Models

Most models of cardiac ventricular cellular electrophysiology are based on the Hodgkin Huxley formalism. Detailed models have more ion channels compared to simplified models. The Noble (1960) and Beeler & Reuter (1977) models are examples of basic AP models. In contrast, the model of Grandi et al. (2010) is more detailed with a great deal of biophysical information. More recent models are specific to individual species and models of human ventricular cells include ten Tusscher et al. (2004), ten Tusscher & Panfilov (2006)(TP06) and Fink et al. (2008). Recently, the O'Hara et al. (2011)(ORd) model was developed by O'Hara and Rudy based on new experimental data from 100 healthy human hearts. All of these models can reproduce the AP observed in experiments and were based on experimental data. These biophysically detailed models (Grandi et al. 2010, O'Hara et al. 2011) include detailed intercellular Ca^{2+} dynamics which describe CICR. However, the Grandi et al. (2010) and Fink et al. (2008) models lack sufficient data to validate the $I_{Ca,L}$ current. Table 2.1 compares some representative human ventricular cell models. The TP06 model (ten Tusscher & Panfilov 2006) has 21 variables with 14 ionic currents and the ORd model (O'Hara et al. 2011) has 41 model variables with 15 ionic currents. More detailed biophysical models have more ordinary differential equations arising from the gating variable for each ionic current. Consequently, they are computationally expensive.

Model	Ten Tusscher et al. 2004	Ten Tusscher et al. 2006 (TP06)	Fink et al. 2008	Grandi et al. 2010	O'Hara et al. 2011
Model purpose	To study re-entrant arrhythmias	To study VF dynamics	Modified TP06 model which includes updated I_{kr} and I_{k1} ionic currents I_{KR} (K^+ rapid delayed rectifier) I_{K1} (inward rectifier)	To explore Excitation-contraction coupling mechanisms and repolarisation abnormalities	Understanding cardiac arrhythmia mechanisms
Number of state variables	16	20	20	38	41
Model variants	Epi, Endo and M cell	Epi, endo and M	Epi, endo and M	Endo and Epi	Epi, Endo and M cell
Advantages	Model reproduces electrophysiological behaviour of cardiac myocyte	New version of previous model with intracellular calcium dynamics	Rate of AP repolarisation is more accurate with experimental results	Includes new definitions of ionic densities and kinetics gathered from experimental data	Data from 100 non-diseased human hearts were used to build this model. In-depth calcium handling is incorporated.
Limitations	I_{ks} and I_{kr} ionic currents are based on animal data I_{Ks} (K^+ slow delayed rectifier) I_{KR} (K^+ rapid delayed rectifier)	Data giving insight into variation rate dependency of APD are not available	Slow run time speed	Did not reproduce s1-s2 properties and did not produce APD_{90} rate adaption dynamics	Experimental data to calculate I_{Nak} current are not available I_{NaK} (Na^+/K^+ ATPase Current)
Validation against experimental data	Validation has been done with experimental data for APD rate dependency	Validation has been done for rate dependency of action potential duration	Not done	Validation has been done for Ionic currents I_{kr} and I_{k1} currents and for rate dependency of action potential duration	ICaL (L-type Ca^{2+} current) Ito (transient outward K+ current) INaCa (Na^+ /Ca^{2+} exchange current) I_{k1}(inward rectifier) I_{kr} (K^+ rapid delayed rectifier) I_{ks} (K^+ slow delayed rectifier) Fast I_{Na} and late I_{Na} (Na^+ current) and Rate dependency of APD

Table 2.1 compare and contrast the human ventricle cell models

Simplified models reproduce the overall behaviour of cardiac myocyte like APDR and conduction velocity restitution, but more biophysically detailed models can give the influence of specific ion channels (Niederer et al. 2009). This can be very useful in studying and finding a cure for problems with specific ion channels. There are major challenges in developing biophysically detailed models. One of the most significant is the difficulty in obtaining healthy human cells and tissue.

Models are a simplified and virtual representation of real cells and tissue. Choosing the right model is very important for the kind of simulations made and the hypothesis being tested (Quinn & Kohl 2011). Many simplified and detailed models are available for each biological system for different species, including humans. The choice of simple and detailed model depends upon the type of results expected: a detailed model could be more expensive in terms of computer memory and speed of simulations; a simple model is better if it can provide results that match the experimental data. Both simplified and detailed models at cell level and tissue level are validated against observed experimental results.

To reduce the computational time of simulations some simplified phenomenological models have been formulated. The Bueno-Orovio et al. (2008) (4-variable model) and Fenton & Karma (1998) models are examples explained below.

The Fenton & Karma (1998) model is a phenomenological model, with three ionic currents, 3 variables and 12 parameters. This model produces APD restitution and conduction velocity restitution that agrees with experimental studies and has been used in studies of cardiac arrhythmias and VF. It is a phenomenological model that does not represent ion channels using Hodgkin Huxley (1952). The transmembrane currents are calculated by summing the fast inward, slow inward and outward currents instead of using a wide range of ionic currents.

Two models have been used in this thesis: a simplified model of 4 variables (4-variable model) (Bueno-Orovio et al. 2008) and a detailed model TP06 (ten Tusscher & Panfilov 2006). Both are explained below.

Phenomenological Minimal Model

The minimal model (4-variable model) (Bueno-Orovio et al. 2008) is a ventricle cell model that is an extension of the Fenton Karma (1998) model described above with 4 variables and 28 parameters. Even though the Fenton Karma model reproduced APD and conduction velocity restitution correctly, it did not reproduce the spike and dome morphology of AP shape. A fourth variable was then added to get the correct spike and dome morphology in AP shape as AP shape is a very important electrophysiological property. This model reproduces the AP, APD, conduction velocity (CV) and rate dependency of APD as in ionic models. Table 2.2 gives the minimal model currents and variables.

Phenomenological currents	4 variables	Differential equation for the 4 variables
J_{fi} – fast inward current that is responsible for the depolarisation of membrane current in the cell which is analogous to sodium current. The model equation for this current is: $$J_{fi} = -vH(u-\theta_v)(u_u - U)/\tau_{fi}$$	Variable u is the membrane voltage. Variable v is the gate that regulates current J_{fi} Variable w is the gate that regulates J_{si} Variable s is the surface area of human ventricular cell. This is the additional variable added to the Fenton Karma 3 variable model (Fenton & Karma 1998). It is added to adjust J_{si} current to get correct morphology of AP shape.	$\frac{\partial u}{\partial t} = \nabla(\widetilde{D}\nabla u) - (J_{fi} + J_{so} + J_{si})$ $$\frac{\partial v}{\partial t} = \frac{(1-H(u-\theta_v))(v_\infty - v)}{\tau_v^-} - \frac{H(u-\theta_v)v}{\tau_v^+}$$ $$\frac{\partial w}{\partial t} = \frac{(1-H(u-\theta_w))(w_\infty - w)}{\tau_w^-} - \frac{H(u-\theta_w)w}{\tau_w^+}$$ $$\frac{\partial s}{\partial t} = \left(\frac{(1+\tanh(k_s(u-u_s)))}{2} - s\right)/\tau_s$$ **H (x) is the standard Heaviside function** **Infinity values are defined as** $$v_\infty = 1 \; when \; u < \theta_v^-$$ $$v_\infty = 0 \; when \; u \geq \theta_v^-$$ $$w_\infty = (1-H(u-\theta_o))\left(1 - \frac{u}{\tau_{w\infty}}\right) + H(u-\theta_o)w_\infty^*$$ **Initial values :** **u=0 ; v=1; w=1 and s=0**
J_{so} – slow outward current that is responsible for repolarisation of cell membrane which is analogous to potassium current. It is time independent. The model equation for this current is: $$J_{so} = \frac{(u-u_o)(1-H(u-\theta_w))}{\tau_o} + H(u-\theta_w)/\tau_{so}$$		
J_{si} – Is the slow inward current that is responsible for the plateau phase in AP which is analogous to calcium current. The model equation for this current is: $$J_{si} = -H(u-\theta_w)ws/\tau_{si}$$		

Table 2.2 showing minimal model (4-variable model) (Bueno-Orovio et al. 2008) currents and variables

Several time constants in the above differential equations of 4 variables are functions of membrane voltage u and shown as follows. Parameters that make up the above model equations are fitted to human AP for epicardial, endocardial and M cells.

$$\tau_v^- = \left(1 - H(u - \theta_v^-)\right)\tau_{v1}^- + H(u - \theta_v^-)\tau_{v2}^- \quad (2.9)$$

$$\tau_w^- = \tau_{w1}^- + (\tau_{w2}^- - \tau_{w1}^-)(1 + \tanh\left(k_w^-(u - u_w^-)\right))/2 \quad (2.10)$$

$$\tau_{so} = \tau_{so1} + \frac{(\tau_{so2} - \tau_{so1})\left(1 + \tanh\left(k_{so}(u - u_{so})\right)\right)}{2} \quad (2.11)$$

$$\tau_s = (1 - H(u - \theta_w))\tau_{s1} + H(u - \theta_w)\tau_{s2} \quad (2.12)$$

$$\tau_o = \left(1 - H(u - \theta_o)\right)\tau_{o1} + H(u - \theta_o)\tau_{o2} \quad (2.13)$$

Membrane voltage ‘u’ in the phenomenological model is normalized to dimensions of unit of voltage mV as V_{mV} = 85.7u -84. In the 4-variable model, u ranges from 0 to 1.4 normalized membrane voltage.

TP06 model

The TP06 (ten Tusscher & Panfilov 2006) model is a biophysically detailed model based on the Hodgkin Huxley formulation with 21 variables out of which 9 are gating variables. This model has 12 currents. Transmembrane current is formulated by adding all the 12 ionic currents. This model includes a representation of calcium dynamics. Gating variables are governed by the Hodgkin Huxley formulation explained in section 2.6.1 and defined in the form of differential equations. Membrane voltage in the TP06 model ranges from -100 to +40mV. Table 2.3 gives the detailed formulation of currents.

Ionic currents	**21 Gating variables**
Sodium current: $I_{Na} = G_{Na} m^3 hj(V - E_{Na})$	m- activation gate h- fast inactivation gate j- slow inactivation gate
L-type calcium current: $I_{CaL} = G_{CaL} d f f_2 f_{cass} 4 \frac{(V-15)F^2}{RT} \frac{0.25 Ca_{ss} e^{2(V-15)F/RT} - Ca_o}{e^{2(V-15)F/RT} - 1}$	d- Voltage dependent activation gate f- slow voltage dependent inactivation gate f_2 – fast voltage inactivation gate f_{Cass} – fast subspace calcium inactivation gate C_{ass} – free dyadic subspace calcium concentration
Transient outward current: $I_{to} = G_{to} rs(V - E_k)$	r- voltage dependent activation gate s- voltage dependent inactivation gate
Slow delayed rectifier current: (For 3 different cell types) $I_{Ks} = G_{Ks} x_s^2 (V - E_{Ks})$	X_s – is activation gate
Rapid delayed rectifier current: $I_{Kr} = G_{Kr} \sqrt{\frac{K_o}{5.4}} x_{r1} x_{r2} (V - E_k)$	x_{r1} - is activation gate x_{r2} – is inactivation gate
Inward rectifier K^+ current: $I_{K1} = G_{K1} \sqrt{\frac{K_o}{5.4}} x_{K1\infty} (V - E_K)$	$X_{K1\infty}$ is time-independent inward rectification factor that is a function of voltage
Sodium/Calcium exchanger current: $I_{NaCa} = K_{NaCa} \frac{e^{\gamma VF/RT} Na_i^3 Ca_o - e^{(\gamma-1)VF/RT} Na_o^3 Ca_i \alpha}{(K_{mNai}^3 + Na_o^3)(K_{mCa} + Ca_o)(1 + K_{sat} e^{(\gamma-1)VF/RT})}$	Ca_i: free cytoplasmic calcium concentration Na_i: intracellular sodium concentrations
Sodium/potassium pump current $I_{NaK} = R_{NaK} \frac{K_o Na_i}{(K_o + K_{mK})(Na_i + K_{mNa})(1 + 0.1245 e^{-0.1VF/RT} + 0.0353 e^{-VF/RT})}$	
Plateau calcium current $I_{pCa} = G_{pca} \frac{Ca_i}{K_{pca} + Ca_i}$	C_aSR: free sarcoplasmic reticulum calcium concentration
Plateau potassium current $I_{pK} = G_{pK} \frac{V - E_K}{1 + e^{(25-V)/5.98}}$	X_{mem} : memory
Background sodium current : $I_{bNa} = G_{bNa}(V - E_{Na})$	

Background Calcium current : $I_{bCa} = G_{bCa}(V - E_{Ca})$	

Table 2.3 showing TP06 model (ten Tusscher & Panfilov 2006) currents and variable

2.6.3 Models of AP Propagation in Tissue

Applying Ohm's law to a distributed medium such as a cell or a tissue, the relationship between current density (J) and electrical field (E) can be expressed as J=GE where G is the material conductivity (S m^{-1}). Taking into account the conservation law of charge and current (Henriquez 1993), the bidomain model equations can be derived by considering the current flow from the extracellular domain to the intracellular domain.

The electrical field at any point within a bidomain is defined as the gradient of electrical potential:

$$E = -\nabla\varphi \tag{2.14}$$

Ohm's law can therefore be expressed (substituting E):

$$J = -G\nabla\varphi \tag{2.15}$$

The current density for each extracellular and intracellular domain can be written as:

$$J_e = -G_e\nabla\varphi_e \qquad J_i = -G_i\nabla\varphi_i \tag{2.16}$$

Current and charge are conserved within each domain, so any current source or sink must be accounted for by current flowing across the cell membrane, units of current flow per unit volume.

$$\nabla.J_i = -I_m \text{ (sink)} \qquad \nabla.J_e = I_m \text{ (source)} \qquad \nabla.(J_i + J_e) = 0 \tag{2.17}$$

The current (I_m) flowing across the cell membrane is a capacitive current plus current flowing through ion channels, pumps, and exchangers, and is given as:

$$I_m = \beta\,[C\frac{dV_m}{dt} + I_{ion}] \tag{2.18}$$

Where the constant β is the surface to volume ratio of cardiac cells. Substituting I_m by source and sink equations, we obtain:

$$\nabla . J_i = -\beta \left[C \frac{dV_m}{dt} + I_{ion} \right] \tag{2.19}$$

$$\nabla . G_i \nabla \varphi_i = \beta \left[C \frac{dV_m}{dt} + I_{ion} \right] \tag{2.20}$$

$$\nabla . G_e \nabla \varphi_e = \beta \left[C \frac{dV_m}{dt} + I_{ion} \right] \tag{2.21}$$

Since $V_m = \phi_I - \phi_e$, these equations can be rearranged into two equations that can be solved for V_m and then ϕ_e. The bidomain equation is:

$$\begin{gathered} \nabla . G_i (\nabla V_m + \nabla \varphi_e) = \beta_m \left(C_m \frac{\partial V_m}{\partial t} + I_{ion} \right) \\ \nabla . \left((G_i + G_e) \nabla \varphi_e \right) = -\nabla . G_i \nabla V_m \end{gathered} \tag{2.22}$$

The assumption in monodomain models is that the gradient of potential of the extracellular domain is zero and intracellular and extracellular anisotropy (directional dependent) is the same. The Monodomain model equation is a simplified, single partial differential equation (PDE) and, therefore, easier to compute. The Bidomain model allows better representation of extracellular current flow, which plays an important role during stimulation or defibrillation. However, based on Potse et al. (2006), in bulk tissue, i.e. away from boundaries, the two models give similar results. Therefore, it is reasonable to use the monodomain model. Sambelashvili & Efimov (2004) showed that the boundary conditions in a bidomain model for extracellular potential had a small effect on filament behaviour. Since this thesis addresses the effect of tissue structure and disease on filament dynamics, it is reasonable to use monodomain models.

No-flux boundary conditions (no diffusion of ions in and out of boundaries) are typically used with monodomain models. The monodomain model equation has the same form as a reaction diffusion PDE and is shown in equations 2.23 and 2.24. C_m is the membrane capacitance and I_{ion} is the flow of current through the cell membrane.

$$C_m \frac{\partial V_m}{\partial t} = \nabla^2 \mathrm{D} V_m - I_{ion} \quad \text{(For Isotropic tissue)} \tag{2.23}$$

$$C_m \frac{\partial V_m}{\partial t} = \nabla . \boldsymbol{D} \nabla V_m - I_{ion} \quad \text{(For Anisotropic tissue)} \tag{2.24}$$

∇^2 is the gradient operator for two dimensions: $\nabla^2 DV$ – Diffusion (current flow between cells in the geometry, resulting from diffusion of ions) and I_{ion} - Reaction (current resulting from AP propagation). By combining the ionic cell model with the geometrical (tissue) model, whole ventricle electrophysiological behaviour can be studied with simulations.

One important parameter for AP propagation in the tissue is the diffusion tensor or diffusion coefficient. The diffusion coefficient (D) is the amount of particular ion that diffuses across a unit measured as $m^2 s^{-1}$. In isotropic models, D is a single (scalar) number and in anisotropic models, **D** is a tensor. This is because the propagation of AP is along and across fibres for 3D anisotropic, and in orthotropic, it is along (x axis) across (y axis) and traverse (z axis). D is calculated in 2D as $D= G/ S_vC_m$. C_m is the specific capacitance, G is the corresponding component of the bulk conductivity tensor and S_v is the surface volume ratio of cells (Sambelashvili & Efimov 2004). C_m for the cell membrane experimentally measures from 1-10 μFcm^{-2}. Normally, for computational simulations C_m is determined as 1 μFcm^{-2}

The diffusion **D** is tensor in 3D anisotropy is shown below (Gilbert et al. 2007):

$$\boldsymbol{D} = \begin{pmatrix} d11 & d12 & d13 \\ d21 & d22 & d23 \\ d31 & d32 & d33 \end{pmatrix} \tag{2.25}$$

Where the components are:

$$d_{ij} = D\perp + (D\parallel - D\perp) a_i a_j \; when \; i = j \tag{2.26}$$

$$d_{ij} = (D\parallel - D\perp) a_i a_j \; when \; i \neq j \tag{2.27}$$

D⊥ and D∥ are diffusion coefficient across and along fibre direction and a_i and a_j are the components of fibre orientation in x, y directions. Sections 3.2.1.2 and 3.2.1.4 explain modelling of fibre orientation and how components of fibre orientation a_i and a_j are modelled in both slab and idealized LV.

For 3D orthotropic tissue, the laminar microstructural axis is defined by three directions (AV Panfilov & Keener 1995a):

$$d_{ij} = D_1 f f^T + D_2 s s^T + D_3 n n^T \tag{2.28}$$

$$(f f^T + s s^T + n n^T = 1)$$

Where D_1 D_2 and D_3 are diffusion coefficients longitudinal to fibres, normal to fibres in the sheet plane, and normal to both fibres and sheets, f, s and n are unit vectors in orthogonal direction describing fibre directions, sheet direction and sheet normal direction (a_i, a_j and a_z). The transpose of unit vectors f, s and n are f^T, s^T and n^T respectively.

In both 2D and 3D for a particular model, the tissue parameter diffusion coefficients are determined by adjusting them to obtain a plausible conduction velocity comparable with experimental observations (Clayton & Panfilov 2008).

2.6.4 Models of Tissue Geometry

2.6.4.1 Simplified Geometries

Simple tissue geometries such as a slab or a cube are often used to represent cardiac tissue (Fenton & Karma 1998, Clayton & Holden 2002, ten Tusscher et al. 2004). These simple geometry models can be represented in 2D or 3D (Figure 2.7 (a, b). Use of simple geometries gives valuable information on electrical propagation and mechanisms underlying ventricular fibrillation without the complication of tissue structure and shape. Section 3.2 shows a simplified model of a tissue slab and idealized geometry incorporating the left ventricle (LV).

2.6.4.2 Patient Specific Modelling

For clinical usage, however, models should ideally use anatomically detailed patient-specific geometry because this gives detailed information on fibre and sheet structure for that individual patient. Patient-specific modelling is the combination of structural geometry and functional heterogeneities as explained in Plank et al. (2009). In patient-specific modelling, the shape and the thickness of the ventricles for each patient are represented in the form of mesh geometry. Cardiac mesh geometry is developed by converting segmented MRI images into an anatomical mesh. This mesh geometry representing the tissue or ventricles or whole heart is made up of elements and nodes as explained in the finite element method in section 2.6.5. Elements are the regions of tissue and the nodes are the points at which the different elements are joined together. Image based modelling is the tool for patient-specific assessment. However, image based models are extremely hard to

construct. This is because segmentation of cardiac myocardium is difficult; because of its complex nature, boundaries are blurred and there is an overlap of image intensities between different voxel groups of myocardium in both diseased and healthy tissue (Vadakkumpadan et al. 2010).

2.6.4.3 Modelling Fibre Orientation in a Tissue Geometry

Fibre orientation is often modelled in tissue geometry since it is hard to measure directly. Some studies (Potse et al. 2006, Bishop & Plank 2010) have used rule-based logic to model fibre orientation in tissue geometry. In the rule-based algorithm, transmural distance between endocardial and epicardial surface is calculated based on minimal distance. The fibre angle is calculated as the function of transmural distance between endocardial and epicardial rotating 60° to -60°. Modelling of fibre orientation is explained in detail in Chapter Three.

2.6.5 Numerical Solution of Cardiac EP Models

2.6.5.1 Cell Models

Cell models have ordinary differential equations arising from the gating variable for each ionic current. These ODEs are problematic and solved either using either implicit or explicit method.

Explicit method: When solving ODEs when the new value of the variable (voltage) is formulated without the dependency on the updated value in the same time step, there are stability issues.

Implicit method: Implicit method calculates the new value of the variable (voltage) in the equation as a function depending on its future value. It is difficult to find the value in the next time step that satisfies the equation. This approach is unconditionally stable.

Rush Larsen (1978) used a simplified approach for solving ordinary differential equations to solve gating variables as shown in Equation 2.6 by taking α and β as constant and made the solution of Equation 2.6 exponential as shown in Equation 2.9:

$$\frac{dy_i}{dt} = y_i(\alpha_{yi} - \beta_{yi}) = \alpha_{yi} \tag{2.29}$$

From the above equation if at the steady state t approaches ∞ y_i becomes constant and the term $\frac{dy_i}{dt}$ becomes 0 and the term $y_i(\infty)$ becomes:

$$y_i(\infty) = \frac{\alpha y_i}{(\alpha y_i + \beta y_i)} \tag{2.30}$$

By assuming α and β constant the solution of $\frac{dy_i}{dt}$ can be formulated as in Equation 2.31. Calculation of gating variable y_i in new time step depends on the voltage in the current time step Δt

$$y_i = y_i(\infty) - [y_i\,(\infty) - y_i\,(0)]e^{-\Delta t/\tau_i} \tag{2.31}$$

Where and τ is $\frac{1}{(\alpha y_i + \beta y_i)}$

The above equation is used to calculate the ionic current in new time steps and the membrane voltage resulting from it. The advantage of using Rush & Larsen's (1978) method is it uses larger time discretization compared to other methods (Clayton & Panfilov 2008).

2.5.5.2 AP Propagation in Tissue

Monodomain or bidomain models of electrical activation can be solved on the geometry (with boundary conditions) using Finite Difference Method (FDM), Finite Element Method (FEM), or Finite Volume Method (Niederer et al. 2009).

In FDM the whole ventricle simulations are done by solving the monodomain equation for each grid (each region of tissue is represented as a grid point) in turn across the cardiac geometry. In FEM each region of tissue is represented as an element and variables of interest are interpolated within the element. Each region of the tissue contains several actual cardiac cells. For isotropic geometry the finite difference explicit method is widely used to calculate the membrane voltage for each time step. But in the real heart geometry which is a curved surface the boundary conditions are realistically solved using finite element. By choosing the appropriate space step (approximate to the size of cell) in the grid, FDM can solve curved structure and boundaries (ten Tusscher & Panfilov 2006). The time step and space step are set satisfying the von Neumann stability analysis as shown below:

$$\frac{D\Delta t}{\Delta x^2} \leq \frac{1}{2d} \tag{2.32}$$

Where D is diffusion coefficient, d is the dimension of the geometry, Δt is the time step and Δx is the space step. Diffusion coefficient, time step and step size must be chosen to give reasonable propagation as observed experimentally. The monodomain model is implemented in a computer program. The ionic current flowing across the membrane I_{ion} is calculated from the cell model which is calculated at each time step (from V_m of the previous step) and integrated using Euler method. The diffusion current (current formed by diffusion of ions in tissue geometry) is calculated. Then finally, the change in membrane voltage is calculated using reaction current and diffusion current.

There are currently many solvers available for the cardiac electrophysiological simulations, for example, SCAM (Sheffield Cardiac Arrhythmia Model), CARP (cardiac arrhythmias research package), Memfem and Chaste (Cancer, Heart and Soft Tissue Environment).

2.7 Computational Investigation of Re-Entry and VF

Early modelling based on cellular automata (Gordan 1963) showed that heterogeneity in refractoriness was the underlying mechanism of re-entry generating multiple wavelets causing fibrillation. Later, Krinskii (1966) showed that underlying ionic heterogeneity could initiate re-entrant spiral waves. Ionic heterogeneity leads to heterogeneity of refractoriness. The van Capelle & Durrer (1980) spiral wave model used a sheet of coupled excitable elements and showed that when the sheet was a sufficient size, re-entry could be initiated without heterogeneity of refractoriness or an obstacle. Pertsov et al. (1993) showed in an experimental and computational study that spiral waves could sustain fibrillation, anchor to an inexcitable obstacle, and rotate around it. Later models with detailed tissue description showed that the re-entrant wave can be initiated with a sufficient inexcitable obstacle (A. V Panfilov & Keener 1993). Later studies from the authors showed that rotational anisotropy and tissue thickness can produce unstable re-entrant waves which break forming fibrillation (AV Panfilov & Keener 1995b). Qu et al. (2000a) showed that the stability of re-entry in 3D can also result from steep APD restitution as in 2D (Fenton & Karma 1998). Steep restitution in both 2D and 3D leads to unstable re-entry forming a spatio-temporal fibrillation pattern. The authors showed that the fibrillation can be stopped if restitution is flattened (Garfinkel et al. 2000).

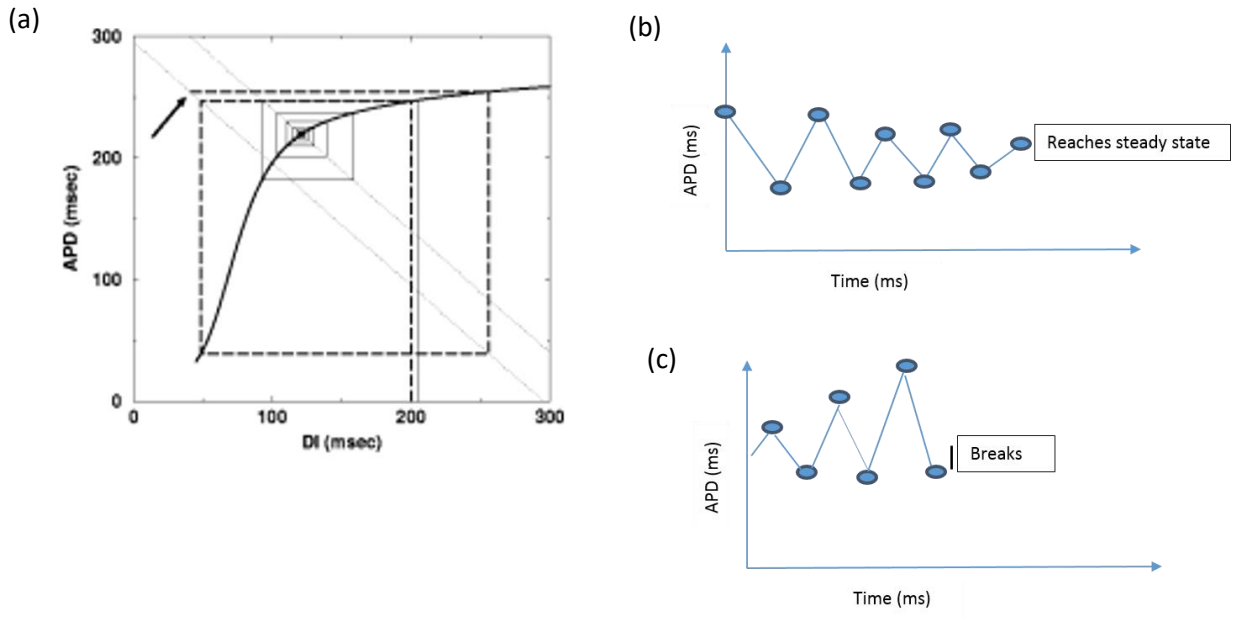

Figure 2.9 (a) Effect of APDR on stability of re-entrant wave; solid line show the effect of shallow restitution curve and dashed line represent effect of steeper restitution curve and; (b) showing oscillations in APD reaching steady state in shallow restitution ; (c) showing oscillations of APD leading to break in steeper restitution, (Reproduced with permission from (Fenton et al. 2002)).

Fenton et al. (2002) discussed multiple mechanisms of breakup of spiral waves and scroll waves. This study highlights steep restitution as one of many instability mechanisms. As explained in section 2.2.3, the adjustment of the heart in shortening the APD when there is a rapid heart rate is called APD restitution. The APD restitution curve obtained by pacing the tissue with fixed cycle length (APD +DI = cycle length) can be used to predict the next diastolic interval (DI). In Figure 2.9 (a) the solid line represents the shallow restitution curve and the dashed line represents the steeper restitution curve where there is a block in conduction of AP. When the restitution curve is steep (slope > 1), a small change in DI results in a much greater change in APD. Over a period of time, these oscillations grow until a long APD produces a short DI, smaller than the minimum DI. This produces conduction block and wave break. When the restitution curve is shallow (slope < 1), small changes in DI produce only small changes in APD, which converge to steady state without causing conduction block.

Figure 2.9 (b) shows the oscillations of APD for shallow restitution curve and Figure 2.9 (c) shows the oscillations of APD in the steeper restitution curve. For shallow restitution (slope is equal to one or less than one), the oscillations become steady as shown in figure 2.9 (b), but the oscillations of APD are unstable for the steeper restitution curve as shown in Figure 2.9 (c).

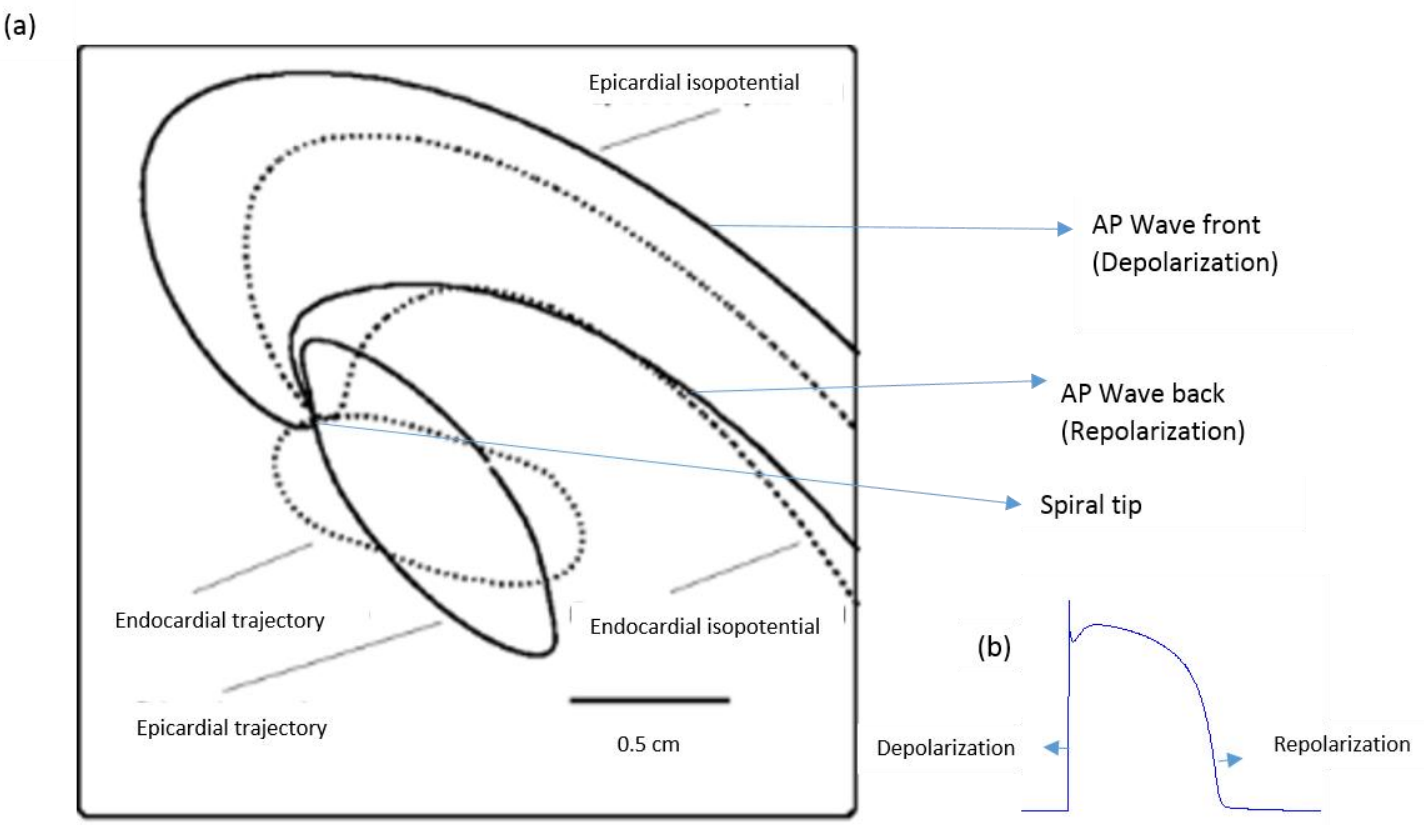

Figure 2.10 (a) Phase delay resulting from anisotropic fibre orientation making an elliptical scroll wave trajectory. Scroll wave is formed when AP progation is blocked and curls making depolarisation wave front and repolarization wave back meet as shown (Reproduced with permission from (Fenton et al. 2002)); (b) Simulated AP wave with depolarization and repolarization.

When AP propagation is blocked, the AP wave breaks and curls forming a scroll wave in 3D and spiral wave in 2D. A scroll wave is formed when depolarization wave front and repolarization wave back meet as shown in Figure 2.10. Fenton et al. (2002)] explain how scroll waves break up because of anisotropic fibre orientation since propagation of AP is faster along fibres compared to across fibres. 3D scroll waves in high excitability regime break up because of the phase delay on the wave between the layers forming the thickness of the tissue as shown in Figure 2.10. This phase delay is caused by fibre orientation because the circular trajectory of the scroll wave is transformed into an ellipse. This elliptical trajectory makes the filament twist and elongate. When the twisted and elongated filament touches the boundary, it breaks.

2.7.1 Other Factors of Scroll Wave Breakup

Re-entry forms scroll wave activity in 3D. The core of a scroll wave is the line of phase singularity called 'filament'. To understand spatio temporal electrical activation during VF, the cores of scroll waves are extracted in many studies, for example in Clayton & Holden (2002). Unstable filaments sustain VF. This section explains filament stability.

Unlike Phase singularities, filaments bend, twist and curve as shown in Figure 2.11. Other mechanisms responsible for scroll wave filament breakup are discussed below.

- Low Excitability

Some studies (Winfree 1973, Panfilov et al. 1984, Panfilov, Rudenko & Krinsky 1986, Panfilov & Rudenko 1987), have found that the filament motion can be influenced by geometrical curvature. They found that the drift velocity of the filament is inversely proportional to the filament curvature. Filament tension is the change of filament length over time. A decrease in filament length is known as 'positive tension' and an increase as 'negative tension'. It has been shown (Biktashev et al. 1994 ,Fenton et al. 2002) that the negative tension can destabilize the filaments and can sustain VF; under low excitability, the filaments expand, curve and collide with boundaries and break in to multiple filaments. In a high excitability regime, 'positive tension', filaments shrink and disappear. Normally, low excitability leads to less excitation, normally caused by ischemia.

- Filament Interactions
  Fenton et al. (2002) showed that the filaments interact with each other and cause more chaotic spatio temporal patterns.

(a)

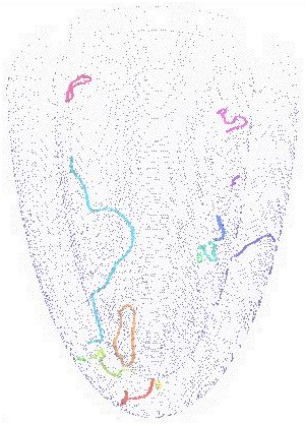

(b)

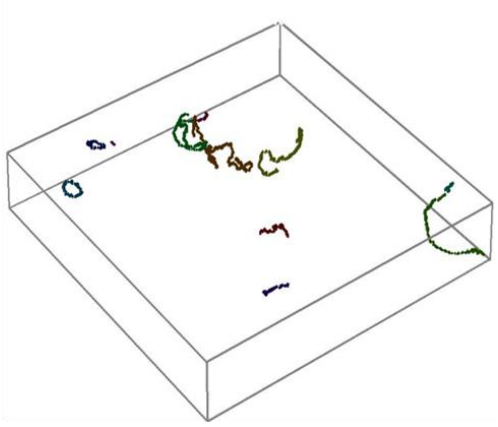

Figure 2.11 Filament interactions showing the bend, twist and curve of filaments in (a) idealized LV and (b) 3D Slab

2.7.2 Mechanism of Re-entry to Sustain VF

Activation patterns during VF are complex. Mechanisms that sustain VF have been examined in many experimental studies (Gray et al. 1998, Lewis 1925, Lee et al. 2001). This section explains the mechanisms of re-entry to sustain VF.

The multiple wavelet and mother rotor hypotheses are proposed mechanisms of VF. Both are explained below.

A single re-entrant wave can result in Ventricular Tachycardia (VT). This re-entrant wave can break further into multiple re-entrant wavelets or a single fast re-entrant mother fibrillation depending upon the underlying structural and/or electrophysiological heterogeneity present in the ventricular tissues.

Studies (Choi et al. 2001, Lewis 1925, Gordan 1963) have explained how multiple wavelets are responsible for sustained VF. While studies have proposed a fast re-entrant source (Lewis 1925, Samie & Jalife 2001, Gray 1995), a mother rotor is the organising source that maintains multiple wavelets in isolated animal hearts. However, so far a mother rotor VF has not given any consistent results. A computational study (Keldermann et al. 2009) showed when the mother rotor is removed, the fibrillation stopped. However, this is not true in multiple wavelet fibrillation because each wavelet is independent of another. This study also showed long-lived filaments can possibly be mother rotors.

Other studies (Wu et al. 2002, Baher et al. 2007, Keldermann et al. 2009) have shown that depending on the initial location of the re-entrant source, both multiple re-entrant and mother rotor fibrillation can be present in the same heart. So the mechanism underlying the dynamics of VF can be

classified as multiple wavelet and mother rotor fibrillation. There might be other mechanisms which are as yet unknown.

2.7.3 Filament Dynamics

During VF, several re-entrant waves are present; therefore, the number of re- entrant filaments can quantify VF complexity and understanding filament dynamics can give an insight into the mechanisms that act to sustain VF. A number of studies (Clayton & Holden 2002, Keldermann et al. 2009, Ten Tusscher et al. 2007) have investigated filament dynamics to understand the mechanisms of VF. Figure 2.11 shows filaments in 3D slab and idealized LV.

Filaments can drift, meander and destabilize due to fibre orientation (Ten Tusscher et al. 2007), tissue heterogeneity (Henze et al. 1990, Vinson et al. 1994) or boundary conditions (Fenton et al. 2002, Rogers 2002). Because of fibre orientation, filaments can twist and bend, and bending of a filament can result in collision with a boundary leading to filament breakup or formation of a ring filament (Qu et al. 2000a). Since there will be a continuous wave rotating around a filament, there are topological constraints on the shape of the filaments. According to the laws (rules) governing filaments, "A filament can end only at the outer boundaries of cardiac tissue, or at an ''inner'' boundary by pinning to a heterogeneity within the myocardium" (Pertsov 2000); the shape of filaments can be classified as I, O or U depending upon their shapes. When a filament touches the opposite surface of the tissue, it is known as an 'I' shaped filament (transmural filament). 'O' shaped filaments (ring filament) are in the form of closed rings and act on the single surface. 'U' shaped filaments have broken ends touching either the same or different surfaces of the tissue (Winfree & Strogatz 1984).

The number of filaments varies depending upon filament birth, death, amalgamation (filament merge) and bifurcation (filament split). Birth of filament occurs when a new re-entrant wave is formed. One possibility of birth of new filament can occur when intramural filament breaks and forms two counter rotating (Biktashev et al. 1994, Fenton & Karma 1998, Keener & Tyson 1992, (Panfilov 2000). When a filament moves out of boundary, it is considered the death of the filament (A. . Panfilov & Keener 1993); two filaments rotating in opposite directions can collide and die (Fenton & Karma 1998, Panfilov 2000, Panfilov, Rudenko & Krinskii 1986). Filament lifespan provides information on the amount of time re-entrant waves sustain. According to Pertsov et al., (2000), only ring filaments can die inside heart tissue.

The drift velocity of a filament is inversely proportional to filament curvature and the drift velocity in the normal direction determines the filament length. Filament length increases with negative tension and this can destabilize the filament forming more filaments (Panfilov & Pertsov 1984). So the mean filament length over time can give an insight into the stability of filaments over time.

2.8 Summary

Ventricular Fibrillation is a serious cardiac arrhythmia. Focal or triggered activity or re-entry can initiate cardiac arrhythmia. However, experiments have shown that VF is sustained by re-entry. Re-entry is observed as scroll wave in 3D, rotating around a core called a filament. During VF, an initial re-entrant wave breaks and forms chaotic spatio temporal activity. One approach for understanding the chaotic pattern during VF, is to decompose the activity into scroll waves and each associated core has been observed in many computational studies (Clayton & Holden 2002, Panfilov & Keener 1995a, ten Tusscher et al. 2007).

The heart is a 3D object. When filaments intersect with the epicardial surface of tissue, they are observed as PS. If a transmural filament is present, it only touches the epicardial surface of the tissue forming one PS; whereas, if a U shaped filament is present, it can touch the epicardial surface twice forming 2 PS. A ring filament does not touch any surfaces and does not form any PS. Computational studies have shown that APD restitution, fibre orientation, tissue thickness, transmural heterogeneity and filament interactions play an important role in the number, shape, volume and life time of filaments. This makes 3D simulations necessary to study VF.

The behaviour of scroll waves is model dependent (Rappel 2001). In this thesis, filament dynamics are compared in two different models: a biophysically detailed model (TP06); and a phenomenological 4 variable model (4-variable model). If the filament dynamics are similar in both models, then this justifies the usage of a simplified model in this thesis.

Most computational studies (Clayton & Holden 2002, Qu et al. 2000b) use an untwisted transmural filament as the initial condition as it is simple. Few studies (Panfilov & Winfree 1985, Bray & Wikswo 2003) have used scroll ring as the initial condition. In the real human heart, focal activity can induce ring filaments on the ventricular wall; this thesis will compare filament dynamics with transmural and ring filament as initial condition.

Transmural heterogeneity is a controversial topic. Sicouri & Antzelevitch (1991b) showed the presence of M cells while some others argue that there is no evidence for M cells (Taggart et al. 2001). Studies have shown the transmural gradient of APD in the human heart (Antzelevitch et al. 1991, Antzelevitch 2010), but the experimental study by Glukhov et al. (2010), (Lin & Scott 2012) showed the presence of M cells as shown in Figure 2.12, possibly in patches between epicardial and endocardial layers, but cell distribution was not as sharp as in other modelling studies like Majumder et al. (2011). So effect of transmural heterogeneity on filament dynamics needs to be systematically tested for uniform, epi-endo, epi - M - endo, epi - Mpatch -endo in both sharp and smooth distribution.

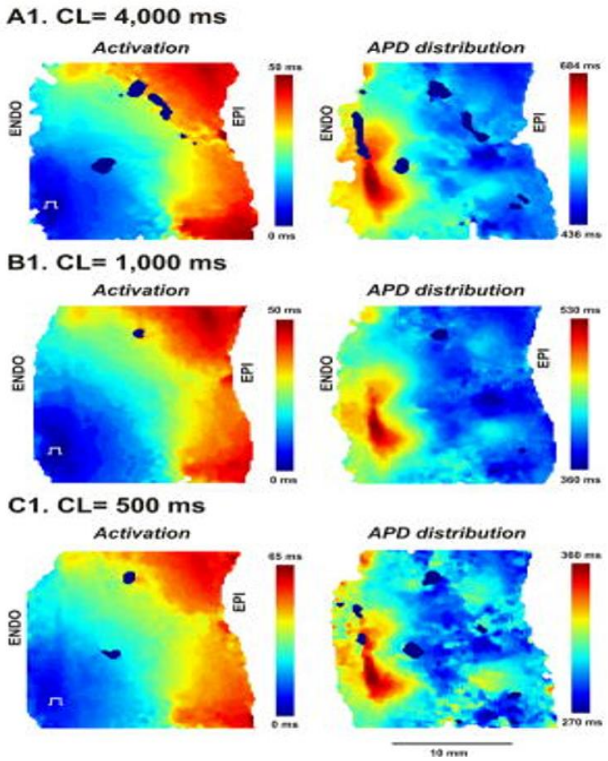

Figure 2.12 Reproduced with permission (Glukhov et al. 2010) showing transmural gradient of APD in the human heart.

In computational studies, simplified or anatomically detailed geometrical models are used. While some studies use slab geometry, others use idealised LV geometry. Rogers et al. (2002) suggest that the shape of ventricle can influence filament behaviour. Therefore, a systematic way of testing whether the sharp and the curved shape of the geometry has an effect on filament behaviour is needed. Slab geometries considered just taking the slice of tissue from ventricles where filaments can breakup colliding with side walls. Qu et al. (2000b) explained how in the real heart, having curved borders, filaments can only collide with epicardium and endocardium surfaces. Consequently, an idealised geometry incorporating left ventricle is also used in this thesis. Since the left ventricle is

considered prolate ellipsoid (Rankin et al. 1976), its long axis directed from apex to base, an idealised left ventricle is modelled as a truncated prolate ellipsoid as in Nielsen et al. (1991). Bishop & Plank (2012) showed that in an anatomically detailed model, fine scale anatomical features had no significant effect on ventricular fibrillation. This further justifies the use of a simplified geometry with no fine scale endocardial structures such as blood vessels for this thesis.

Cherry et al. (2012) demonstrated the nonlinear behaviour of the heart by showing that making a small difference in pacing a 2D tissue had a huge effect on the stability of spiral waves. The nonlinear behaviour should be tested in 3D models to study the effect on filament behaviour.

When there is an obstruction in the coronary artery, the part of the tissue supplied by the artery becomes ischemic. Prolonged ischemia results in myocardial infarction. The part of the tissue deprived of oxygen forms scar tissue after a few days. Normally, scars are formed on the left rather than right ventricle. The scar region can be localised or circumferential. Localized scars which can be solid or patchy are formed by regional ischemia and can be transmural or sub-endocardial. Localised scars formed on the front of the ventricle are called anterior scars, normally formed when there is a block in the left anterior descending coronary artery (LAD) (Figure 2.1). Scars formed on the back of the ventricle are called posterior scars and are normally formed when there is a block in the left circumferential coronary artery (LCX). However, since idealized LV is symmetrical, this thesis does not compare anterior and posterior scars. Computational studies have shown that the shape and position of the scar region has an effect on filaments as they act as a source to pin re-entrant filaments (Majumder et al. 2011, Sridhar 2010, Shajahan et al. 2007, Malyala & Clayton 2013, Malyala et al. 2014). While computational studies have modelled scar region with smooth edges, clinical studies shows that the scar region might not have regular border. Most computational studies represent scar region as only transmural and were done mostly on slab geometry. Therefore, a systematic study is needed to find filament dynamics in the presence of circumferential and localised scars (transmural & sub endocardial both of which can be solid and patchy). Pinning of filaments to the scar boundary stabilizes them and makes them hard to remove even using powerful defibrillation (Luther et al. 2011). As studies have shown that the size of the scar influences cardiac arrhythmias by anchoring the filaments, this needs to be tested with varying scar size.

Keldermann et al. (2010), in an electromechanical modelling study, showed that re-entry was destabilized by the interaction of both electrical and mechanical activity. During VF, there will be few or no mechanical contractions. As a result, to study the effect of tissue structure and disease on scroll wave filaments, cardiac mechanics are not included in this thesis.

Since there is strong evidence that steep restitution (APDR) is an important mechanism underlying unstable re-entry and hence fibrillation, each simulation is tested on both comparable steep and flat restitution dynamics of epicardial cells (Qu et al. 2000b).

Anisotropic fibre orientation is incorporated in both slab and ellipsoid geometry. This is explained in sections 3.2.1.2 and 3.2.1.4.

2.9 Novelty of this Thesis

The computational and experimental investigations done so far on the effect of tissue structure and disease (scar) on filament dynamics in the human heart have been studied, a knowledge gap has been identified and key questions of this thesis have been formulated.

2.9.1 Knowledge Gap

There is some evidence that tissue heterogeneity (Henze et al. 1990, Vinson et al. 1994) and boundary conditions (Fenton et al. 2002, Rogers 2002) influence the behaviour of filaments.

Some aspects of tissue heterogeneity, especially the functional importance of M cells, are a controversial topic. Some studies (Sicouri & Antzelevitch 1991b, Antzelevitch 2010) have shown the existence of M cells in the cardiac tissue while others (Taggart et al. 2001) showed no M cells. Experimental study (Glukhov et al. 2010) has shown transmural heterogeneity may not be sharply distributed as assumed in some computational studies (Majumder et al. 2011).

How electrical heterogeneity combined with structural heterogeneity (e.g. scar) influence filament behaviour and stability is poorly understood. Studies (Pertsov et al. 1993, Majumder et al. 2011, Malyala & Clayton 2013, Malyala et al. 2014) have shown that scroll wave filaments can pin to the edge of scar regions and sustain fibrillation. Shajahan et al. (2007) showed theoretically and computationally that the fractal-like boundary of the scar region separates the basin of attractors of fixed points to the basin of attractors of strange attractors and plays an important role in the chaotic spatiotemporal nature of the activation pattern of VF in 2D. Normally in chaotic dynamic systems, attractors are not fixed, they are distributed in space (strange attractors). Cherry et al. (2012) showed the non-linear behaviour of the activation pattern of VF in 2D, not tested on 3D scroll wave filaments. If the activation pattern in 3D showed a non-linear nature (chaotic dynamic system), then it supports strange attractors and can pin more filaments. So, the bigger the scar region, it will tend to anchor more filaments. In order to test the fractal-like boundary as mentioned in Shajahan et al. (2007), varying sizes of both irregular and regular scars with transmural and sub-endocardial transmural scars can be used in 3D tissue geometry. By testing both the non-linear nature of the activation pattern during VF and the effect of the fractal-like boundary of scar regions, it will be clear which has greater effect on pinning of filaments to the scar boundary.

An experimental study on human heart (Massé et al. 2007) showed that fictitious centrifugal force around a rotating system forces it to the border of slow conducting tissue since there will be conduction block of AP near the slow conducting border; this can be checked in 3D cardiac tissue with transmural heterogeneity as explained in Glukhov et al. (2010). This may be another reason for pinning of re-entrant filaments to the scar boundary and needs to be tested systematically.

2.9.2 Key Questions

The key questions are formulated such that the first two questions justify the model and the use of initial re-entrant filaments for simulations; the next question is formulated on the effect of transmural heterogeneity on filament dynamics; the next on the effect of tissue shape on filament dynamics; the non-linear nature of the activation pattern in 3D is tested next; and the remaining six questions are formulated on the effect of the type and size of the scar region on filament dynamics.

This thesis is a systematic study using simplified geometries of:

a) 3D slab representing a section through the wall of the left ventricle and
b) a half ellipsoid representing the left ventricle

Both geometries incorporate fibre orientation to examine the effect of filament dynamics on the following conditions.

- **Comparison of the filament dynamics in simulated VF with simplified and biophysically detailed cell models**

Studies suggest scroll waves are model dependent. This section compares filament dynamics using a phenomenological 4 variable (4-variable model) (Bueno-Orovio et al. 2008) and biophysically detailed (TP06) (ten Tusscher & Panfilov 2006) model.

- **Does initial shape of the filament affect filament dynamics?**

This section compares the effect of initial filament on filament dynamics. Single transmural filament is used as the initial condition for inducing re-entry in the simulations. Qu et al. (2000b) showed that by using no-flux boundary conditions, the initial filament can only be perpendicular to fibre direction, i.e. a transmural filament touching both epicardial and endocardial surfaces. Since transmural filament is used with the no-flux boundary conditions, ring filament as the initial condition is tested on periodic boundary conditions. Periodic boundary conditions on a 3D slab geometry can be considered as a topological cylinder as in Fenton et al. (2002). Topological cylinder

can be considered as a truncated left ventricle with apex removed. Section 4.22 explains how periodic conditions are modelled.

- **Does transmural heterogeneity have effect on filament dynamics?**

Filament dynamics are compared between uniform epicardial cells, endo-epi, endo-M-epi and endo-Mpatch-epi. The sharp transition of endo-epi cell type is compared with smooth transition of endo-epi on filament dynamics and, similarly, the sharp and smooth transitions of endo-M-epi are compared.

- **Does the shape of the tissue geometry (sharp against curved) have an effect on filament dynamics?**

Filament dynamics are compared in slab geometry, which has sharp edges, versus the idealised left ventricle, which has curved edges. In slab geometry, filaments move towards the boundaries and disappear; however, in ellipsoid geometry, they can move around the other side. This needs to be tested if the ellipsoid geometry has more filaments as well as long-lived filaments compared to slab geometry.

- **Testing the non-linear behaviour of activation pattern during VF**

Nonlinear effect behaviour of the heart is tested by perturbing the initial filament to check the effect on filament dynamics. This is tested on slab and idealised left ventricle.

- **Do the size, depth and regular and irregular boundaries influence pinning of filaments to the scar boundary?**

    - **Size of scar region**
    - **Depth of scar region**
    - **Regular and irregular scar boundary**

- **Does the scar affect the filament dynamics?**

    - **Compare the effect of scar on filament dynamics in slab geometry**
    - **Compare the effect of circumferential scar on filament dynamics in idealized LV**
    - **Does the depth of the scar-size in the scar have an effect on filament dynamics in idealized LV?**
    - **Do the regular and irregular boundaries affect filament dynamics in idealized LV?**
    - **Does the size of the scar have an effect on filament dynamics in idealized LV?**

Since the mid wall of the left ventricle is susceptible to circumferential scars, localised scars are modelled in the mid wall as well. The above open questions are systematically addressed in this thesis.

3. Numerical Implementation

A cell model represents a virtual ventricular cell. The cell model provides ODEs arising from the gating variable for each ionic current to model AP, APD and APDR in a single cell and is integrated in a tissue model to represent virtual tissue. To model the propagation of electrical waves in the tissue model, PDE is coupled with ODEs. Numerical solvers model electrophysiology in tissue to provide solutions given initial and boundary conditions. Numerical solvers use high performance computing with distributed memory to give a solution in reasonable computation time with good accuracy.

Many numerical solvers are available for cardiac electrophysiology simulations. For this thesis, the Sheffield Cardiac Arrhythmia Model (SCAM) was used. It is very well developed software model for cardiac arrhythmias and was used to test hypothesis in this thesis. SCAM is a monodomain solver that uses an explicit finite difference method to calculate new voltage values at each time step. The time step and space step were chosen satisfying von Neumann stability analysis. Neumann boundary conditions or no-flux boundary conditions are used to electrically insulate the geometry by bounding non excitable cells so that there is no net current flow normal to the surface of the boundary in the tissue geometry. For 2D modelling, the isotropic model equation was used, and for 3D modelling, the anisotropic equation was used. Simplified slab geometry representing ventricular wall and a half ellipsoid representing an idealized human left ventricle with similar apex base dimensions and wall thickness was used. The geometry was represented using Cartesian coordinates and the fibre orientation was modelled adopting the rule-based method (Potse et al. 2006). A fibre sheet is not included since detailed structural information of the fibre sheet is not available for humans. To date, a few experimental studies have been done on dogs and pigs to understand fibre sheet structure (LeGrice et al. 1995, Lunkenheimer et al. 2006). A Single straight re-entrant filament was used as the initial condition in 3D simulations.

This section shows how isotropic and anisotropic monodomain equations were solved and how boundary conditions were implemented using the 4-variable model. Section 3.3 explains implementation using the TP06 model. The solver was written in C language. 3D slab and idealised left ventricle construction and incorporation of fibre orientation are explained. Modelling geometry incorporating fibre orientation and modelling scar regions was done using Matlab. The post processing (done in Matlab) section explains how filaments were detected and how filament shape, volume and life time were calculated.

3.1 Scam Solver for Solving Isotropic Monodomain Equation in 2D

For simulations in 2D geometry, a 300 by 300 grid point (75 cm X 75 cm) sheet was used. The four variable minimal model and Isotropic monodomain model (Equation 3.1) were used. The same procedure was followed with the TP06 model explained in section 3.3.

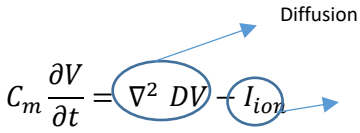

(3.1)

C_m is the membrane capacitance and the value is 1µF /cm^2. D is the diffusion coefficient set to 0.001171cm^2/ms, in isotropic equations D is a scalar number. The geometry had insulated boundaries and the Neumann boundary conditions were imposed at each edge of the geometry by setting the gradient of membrane voltage to zero.

The time step was set to 0.10 ms and the space step to 0.025cm. Von Neumann stability analysis is satisfied as follows:

$\frac{D\Delta t}{\Delta x^2} \leq \frac{1}{2d}$ (Stability analysis)

$\frac{D\Delta t}{\Delta x^2}$ = (0.001171 * 0.10)/ (0.025)^2 =0.18736

$\frac{1}{2d}$ = 1/ (2*2)=1/4= 0.25

0.18736 ≤ 0.25 (satisfies von Neumann stability)

To test stability analysis, the time step was increased to 0.2 ms and the space step kept at 0.25 cm and this did not satisfy the stability analysis as shown below:

$\frac{D\Delta t}{\Delta x^2} \leq \frac{1}{2d}$ (Stability analysis)

$\frac{D\Delta t}{\Delta x^2}$ = (0.001171 * 0.2)/ $(0.025)^2$ =0.37472

$\frac{1}{2d}$ = 1/ (2*2)=1/4= 0.25

0.37472 > 0.25 (does not satisfy von Neumann stability)

Conduction velocity (CV) was obtained in 2D tissue using the S1S2 protocol as explained in section 3.1.1. Figure 3.1 shows CV obtained under conditions of both satisfied and non-satisfied stability analysis. Since an explicit method was used to solve cell model ODEs, with increased time step, it might not be able to capture increase in voltage due to fast diffusion of sodium ions (Na^+) in phase 0 of action potential. This results in incorrect calculation of new voltage and is reflected in unstable CV in Figure 3.1, shown by the blue line.

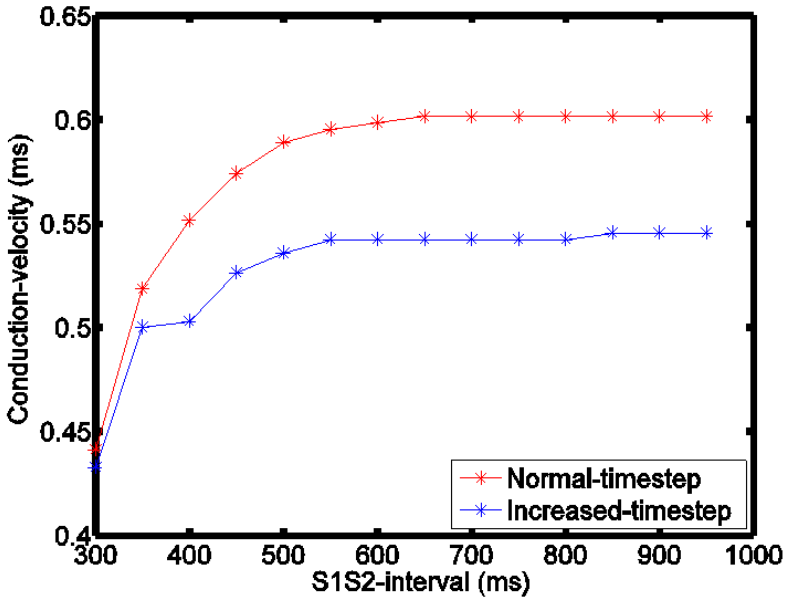

Figure 3.1 showing conduction velocity obtained with time step 0.1 ms that satisfies stability analysis (RED) and conduction velocity obtained with increased time step 0.2 that did not satisfy stability analysis (BLUE).

In the isotropic model there are 8 neighbours for every grid point inside the tissue and there are 8 neighbours for grid point X as shown in Figure 3.2.

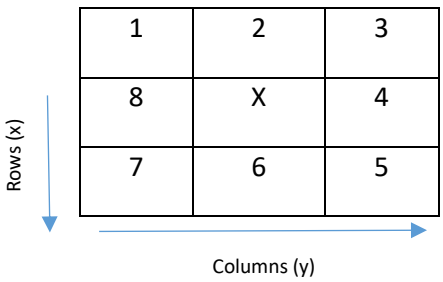

Figure 3.2 Schematic representation of 8 neighbours for grid point X in 2D.

The first part of equation 3.1 is the diffusion term and the second the reaction term as explained in Chapter Two section 2.2.3. The diffusion term can be written as:

$$D\nabla^2 V = D\frac{d^2V}{dx^2} + D\frac{d^2V}{dy^2} \tag{3.2}$$

$$\frac{d^2V}{dx^2} = \frac{V_{x+1} + V_{x-1} - 2V_x}{dx^2} \tag{3.3}$$

Using the Euler method, the change in $\frac{dV}{dt}$ can be expressed as:

$$\frac{dV}{dt} = \frac{V_{t+1} - V_t}{dt} \tag{3.4}$$

By substituting the following in equation 3.1:

$$V_{t+1} = V_t + dt\,(D\nabla^2 V - I_{ion}) \tag{3.5}$$

$$V_{t+1} = V_t + dt(\left(D(\frac{V_{x+1} + V_{x-1} - 2V_x}{dx^2}) + D(\frac{V_{y+1} + V_{y-1} - 2V_y}{dy^2})\right) - I_{ion} \tag{3.6}$$

When calculating voltage in the new time step V_{t+1}, the change in voltage $\frac{dV}{dt}$ was formulated without the dependency on the updated value of voltage, thus using the explicit method. The reaction current I_{ion} was calculated with the sum of ionic currents passing through the cell membrane resulting from action potential propagation in the cell membrane. Since the phenomenological 4 variable model (4-variable model) was used (Bueno-Orovio et al. 2008), I_{ion} is the sum of fast inward, slow inward and outward currents. Updated Voltage V_{t+1} and the remaining state variables for each grid point for every 2ms was stored in an array and saved in a file. If the nearest neighbour was a boundary grid point, the voltage was taken from the current grid point as default value.

3.1.1 2D Simulations

An S1S2 protocol can be used to pace virtual cells. In S1S2 protocol, a cardiac tissue model can be stimulated using S1 stimulus from the left end of the tissue until steady state is reached followed by S2 stimulus. In the 4-variable model, stimulus was set to a fixed cycle length of 600 ms. Six S1 stimuli with the strength of 2 μA/μF were used for a duration of 0.1 ms followed by S2 stimulus. The same procedure was repeated for a range of S2 intervals (1000ms ….. 250ms). Normalized transmembrane voltage is shown in Figure 3.3. Figure 3.4 shows the S1S2 stimulus.

Threshold potential was set in the program just above the resting potential and used to detect upstroke and downstroke for calculating DI and APD. Change in voltage was calculated using reaction and diffusion current. The upstroke and down stroke time of the AP was calculated using the threshold. Threshold was set to 0.15 for detecting APD_{90}. Upstroke was detected if the change in the membrane potential was greater than the threshold and the old membrane potential was less or equal to the threshold. Down stroke was detected if the new membrane potential was less than the threshold and old membrane potential greater or equal to the threshold. APD (milliseconds) was calculated by subtracting upstroke from down stroke time.

Conduction velocity was calculated by distance travelled in AP divided by time taken to travel. This again was plotted against S1-S2 interval (Figure 3.1). Since S1 stimulus is the same throughout, S1-S2 interval was used instead of diastolic interval (DI). The only difference between using S1-S2 interval and DI is that in S1-S2, the minimum APD in APDR curve is actual S1 time. Diastolic interval can be calculated with the difference between downstroke of previous stimulus with upstroke time of current stimulus. This will give actual minimum DI.

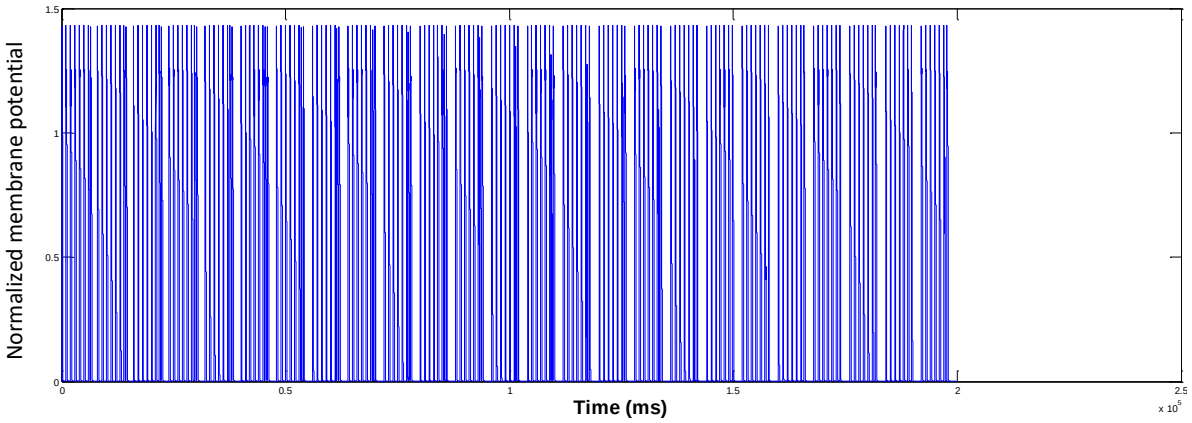

Figure 3.3 Transmembrane potentials obtained from S1S2 protocol in 2D sheet using 4-variable model.

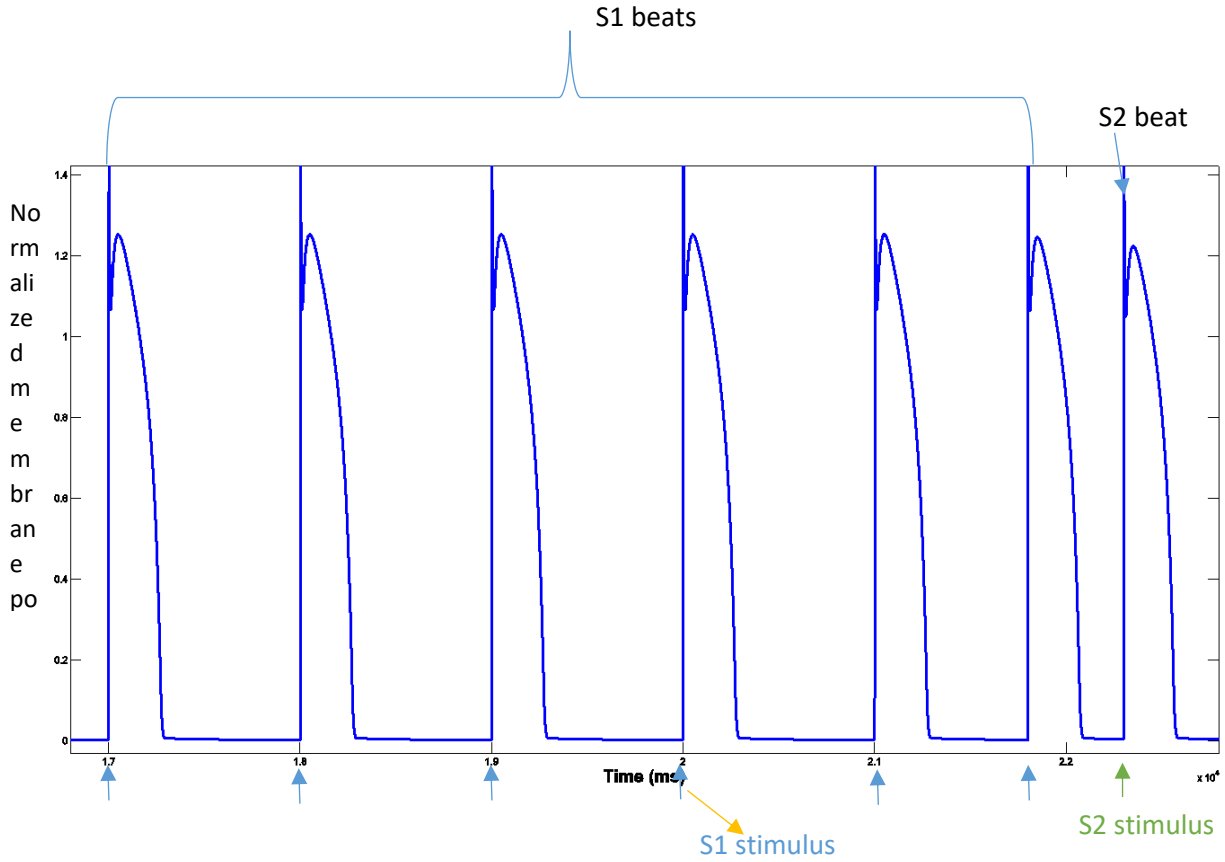

Figure 3.4 Showing S1-S2 protocol for pacing 2D tissue using 6-S1 and 1-S2 stimulus using 4-variable model.

At the steady state action potential (AP), all the state variables of the model including voltages from the centre of the geometry are extracted for the whole single APD and saved in a file as input record. This input record was used as the initial condition for transmurally stacked Archimedean spirals used to model initial re-entrant wave in 3D simulations. This is explained in section 3.2.2.

3.2 SCAM Solver for Solving Anisotropic Monodomain Equation

3.2.1 3D Geometry

Two different 3D tissue geometries were used for the simulations. The first was a rectilinear 8.0 x 8.0 x 1.2 cm slab representing a section through the wall of the left ventricle; this is about one third of the volume of typical human ventricles as shown in Figure 3.5.

3.2.1.1 3D slab

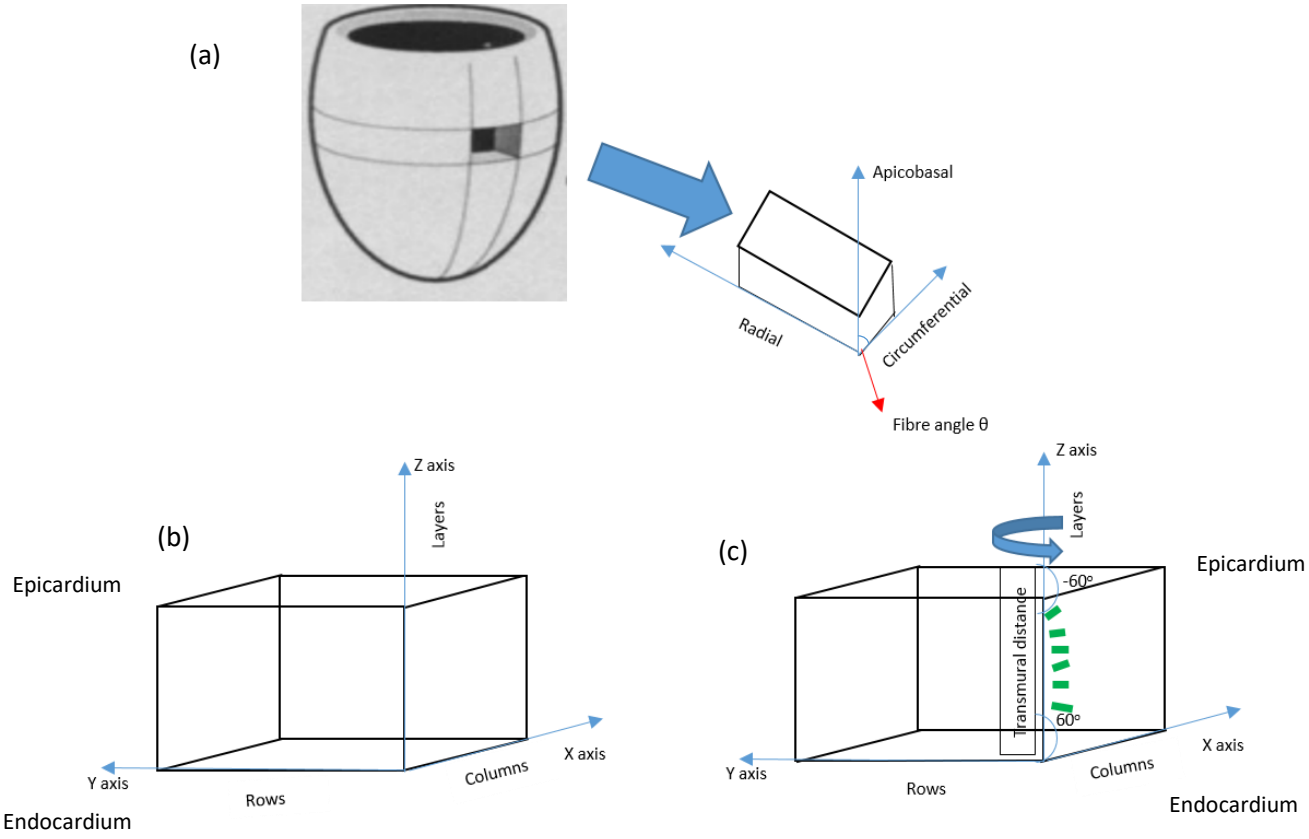

Figure 3.5 Schematic representation of (a) 3D slab taken from the left ventricular wall showing local apicobasal, circumferential and radial axis; (b) 3D slab in Cartesian coordinates; (c) fibre orientation modelled along transmural distance.

The 3D slab geometry was represented in Cartesian coordinates using a space step of 0.02cm, so the dimensions are represented by 400 x 400 x 60 Cartesian grid points. There are 400 rows, 400 columns and 60 layers in the 3D slab. In the tissue geometry, the excitable grid points are set a value of '1' and non-excitable points as zeros. The 3D tissue geometry was modelled as bounded by zeros representing non excitable cells to act as electrical insulators.

3.2.1.2 Anisotropic Fibre Orientation in 3D Slab

Ventricular cells are aligned as fibres and these fibres are aligned parallel to the surface of the ventricles and rotate through the whole wall. Propagation of AP is faster along fibres than across and plays an important role in the electrical activity of the heart. Modelling fibre orientation, therefore, is important. The fibre angle θ is the angle of fibre orientation from epicardium to endocardium making -60° to +60° when observed from the top of the epicardium. It is a function of distance in transmural direction or apicobasal or z axis as shown in Figure 3.5 making a total of 120°. Layer is in the same direction as z axis (transmural distance). So fibre angle was modelled in 3D slab as Equation 3.7 (Hyatt et al. 2003). Figure 3.6 shows the rotation of fibre angle (θ) with transmural distance (endo – epi) from 90^0 to 210^0 in clockwise direction and making the total of 120^0.

$$\theta(z) = 90° + (layer - 1) * \frac{120°}{z} \tag{3.7}$$

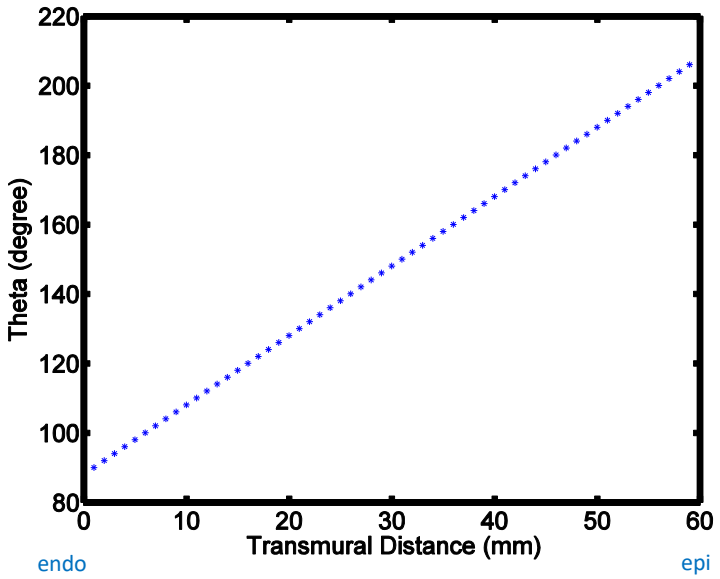

Figure 3.6 Rotation of fibre angle theta (θ) with transmural distance (endo – epi) from 90^0 to 210^0 in clockwise direction and making the total of 120^0.

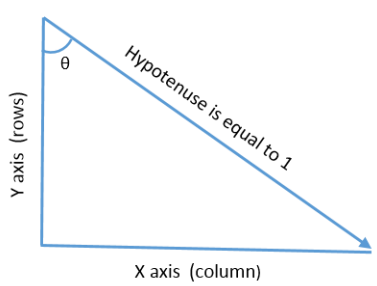

X (a1) = sin(θ)
Y (a2)= -1 * cos(θ) -1 is multiplied because of anticlockwise rotation of fibre angle θ
Hypotenuse is taken as 1 since θ increased linearly for each layer

Figure 3.7 Schematic representation of calculation of components of local fibre orientation in x, y axis as a1 and a2 respectively; a3 is set to 0 as in the same direction of z axis (transmural).

From Equation 3.7, θ was calculated for each layer and the fibre rotation components a1, a2 and a3 were calculated for Cartesian coordinates x, y and z as explained in Figure 3.7. Component a3 was set to zero because it is in the same direction as the transmural distance. Fibre orientation angle changes linearly in the ventricular wall with transmural distance (Greenbaum et al. 1981).

3.2.1.3 Idealized Left ventricle (LV)

The normal left ventricular shape is approximately a prolate ellipsoid (Rankin et al. 1976). So a half ellipsoid representing the left ventricle (base-apex 9.0 cm, wall thickness 1.1 cm) with LV radius 2.4cm was used as idealized LV geometry as shown in Figure 3.8 (a). The space step was taken as 0.02cm. So the geometry had 352 x 352 x 510 grid points bounded by zeros as explained in 3D slab geometry. The half ellipsoid was modelled using the prolate spheroid equation centred as origin as shown in Equation 3.8.

$$\frac{x^2 + y^2}{a^2} + \frac{z^2}{c^2} \qquad (3.8)$$

Where x, y and z are rows, columns and layers respectively. In Equation 3.8, ‘a’ and ‘c’ are radius and base to the apex length of the spheroid. The half ellipsoid was constructed by assigning grid points to ‘1’ if the result of Equation 3.8 was less than ‘1’, or otherwise, zeros mimicking inside geometry and outside geometry respectively. Using the wall thickness dimension, another larger dimension spheroid was formulated. This was done by adding thickness value to both radius and apex to base length. The smaller spheroid was taken out from the larger one to get an idealized left ventricle (hollow) in Cartesian coordinates as shown in Figure 3.8. The half ellipsoid geometry was embedded inside a cube as shown in Figure 3.8.

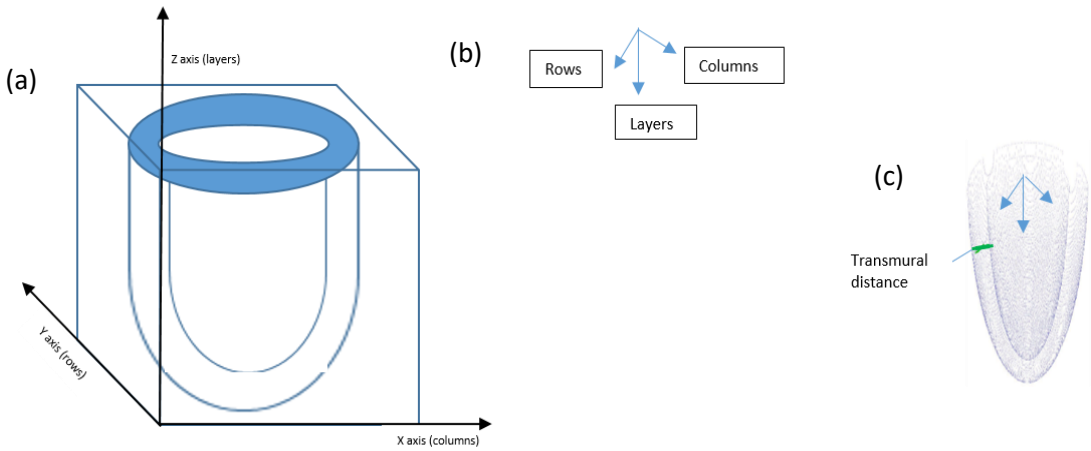

Figure 3.8 (a) and (b) Schematic representation of half ellipsoid representing idealized LV in Cartesian coordinates, (c) transmural distance in idealized LV.

3.2.1.4 Anisotropic Fibre Orientation in Idealized LV

As explained earlier in the section, fibres align and rotate around the whole heart. The angle of rotation of a fibre is called the fibre angle and it rotates from -60° to +60° anticlockwise from epicardium to endocardium.

A rule based method (Potse et al. 2006) was adopted for the finite difference tissue model of an idealised left ventricle. The transmural 2D distance map was created finding the transmural depth between epicardium and endocardium surface. The fibre angle alpha (α) was calculated as clockwise rotation from endocardium to epicardium of +60° to -60°; the fibre angle was adjusted by subtracting 5° (0.0873 radians) to match the experimental angle rotation (imbrication angle) (Potse et al. 2006, Muzikant et al. 2002, Taccardi et al. 1994). Fibre angle was calculated in radians using the normalised transmural distance which was then calculated using tissue thickness as shown below in Equation 3.9.

$$\alpha = \left(\frac{pi}{3}\right) * (1 - 2 * normalised\ transmural\ distance) - 0.0873 \quad (3.9)$$

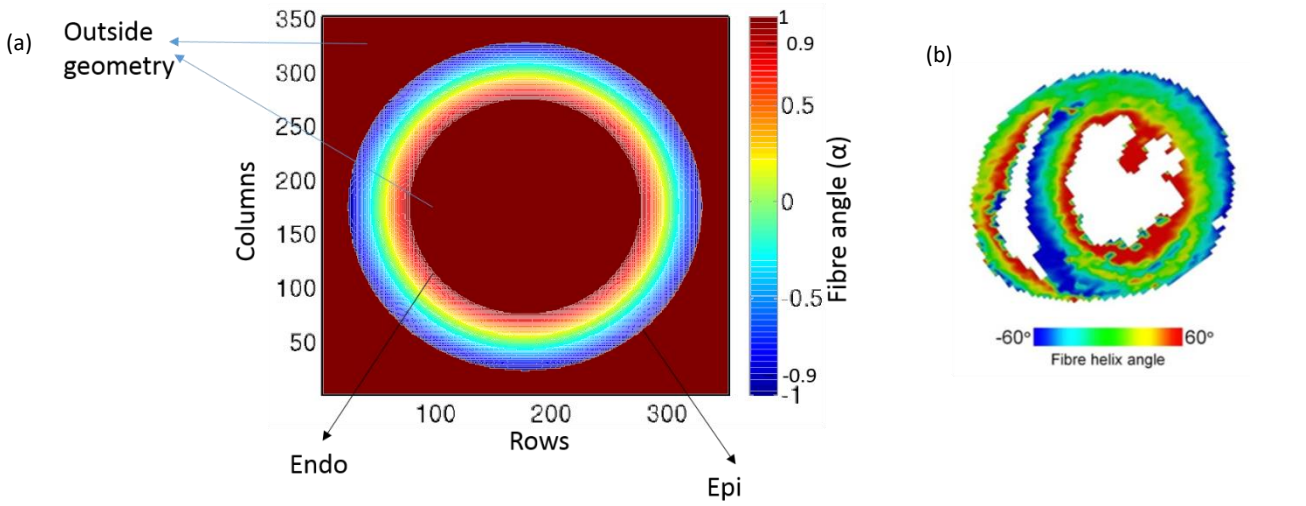

Figure 3.9 (a) Cross section view of fibre angle (α) rotation in idealized LV; Fibre angle rotates from +55^0 (+0.9599 radians) to -55^0 (-0.9599 radians)in clockwise from endo to epi ; Fibre angle obtained in experimental study (Reproduced with permission (Benoist et al. 2012)).

Figure 3.9 (a) shows the fibre rotation obtained through modelling in this thesis, matching fibre rotation acquired in experimental study (Benoist et al. 2012) (figure 3.9 (b)). The components of a vector describing transmural distance were calculated by taking the gradient of distance in endocardium as erow, ecol and elay. The components of vectors in Cartesian coordinates (x, y, z) were converted to spherical coordinate system (r, θ, ϕ) calculating the angle made by local apical-base axis with layer axis. The radial component (r) of the spherical coordinate system was unknown, so erow and ecol were used to create eRadial as shown in Figure 3.10.

$$eRadial = sqrt((erow)^2 + (ecol)^2) \quad (3.10)$$

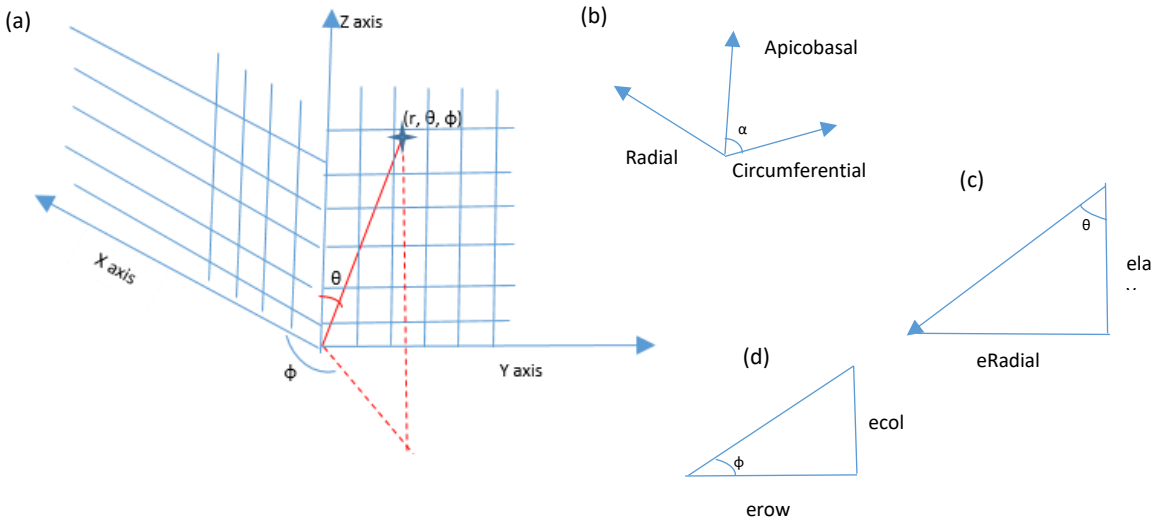

Figure 3.10 Schematic representation of construction of local fibre orientation in idealized LV (a) showing polar coordinates (r, θ, ϕ); (b) local apicobasal, radial and circumferential; (c) and (d) calculation of polar angle θ and azimuthal angle ϕ.

$$\theta = \text{atan}(\frac{elay}{eRadial}) \quad (3.11)$$

$$\emptyset = \text{atan}(\frac{ecol}{erow}) \quad (3.12)$$

From the calculated eRadial, polar angle θ and azimuthal angle ϕ of the spherical coordinate system were calculated as shown in the above equations. Fibre orientation angle α is made between circumferential and apicobasal angle as shown in Figure 3.10. Using α, θ and ϕ, the local components of fibre orientation in lay, row and column were calculated in Cartesian coordinates using trigonometric basics of angle sum of (α+θ) and product identities. For each grid point in idealised left ventricular geometry, the components of fibre orientation in x, y and z direction were extracted as a1, a2 and a3 respectively and stored in a file.

3.2.1.5 4-variable Cell Model and its Variants

Since APD restitution plays an important role in filament dynamics as explained above, two variants of the epicardial cell model were used, based on the parameters in the original paper (Bueno-Orovio et al. 2008). The first variant (epiMod1) supported unstable re-entry, but had relatively flat action potential duration (APD) restitution. The second variant (epiMod2) had steeper APD restitution resulting in more unstable re-entry. For the variant epiMod1 the parameter τ_{v1}^{-} was changed from 60.0 to 10.0, and τ_{v2}^{-} was changed from 1150.0 to 20.0. In epiMod2, τ_{v1}^{-} and τ_{v2}^{-} were changed as for epiMod1, and in addition, τ_{so1} was changed from 30.0181 to 28.0, and τs2 from 16.0 to 40.0.

3.2.2 3D Simulations

Single transmural filament was used as the initial condition by imposing an Archimedean spiral in each layer (transmurally) of the geometry. The geometry is represented as Cartesian coordinates where a point is uniquely represented by coordinate system of (x, y), and the Archimedean spiral is modelled in polar coordinates (Biktashev 1998) where each point in the system is represented as distance from reference point and angle from the reference direction (r, θ). The centre of rows and column in layer of the geometry is taken as the origin and the radial (r) coordinates are calculated to determine the maximum trajectory of the spiral (maxr). To model the Archimedean spiral polar angle, (θ) is varied from 0^o - 360^o. For each radial coordinate (r), the polar angle (θ) is incremented (θ+ dθ) and the corresponding Cartesian coordinates (x, y) are calculated using trigonometric functions as shown in Figure 3.11 (a). If the Cartesian coordinates are within the geometry and the length of the spiral arm is within the limit of the input record obtained from pacing, the voltage measure from the corresponding position from the input record (obtained in section 3.1.1 by pacing 2D tissue using S1S2 protocol - this record is used as initial condition) was mapped to the position of initial re-entrant wave (Figure 311 (b)) initializing an array 'U' used to store state variables of each grid point (x, y).

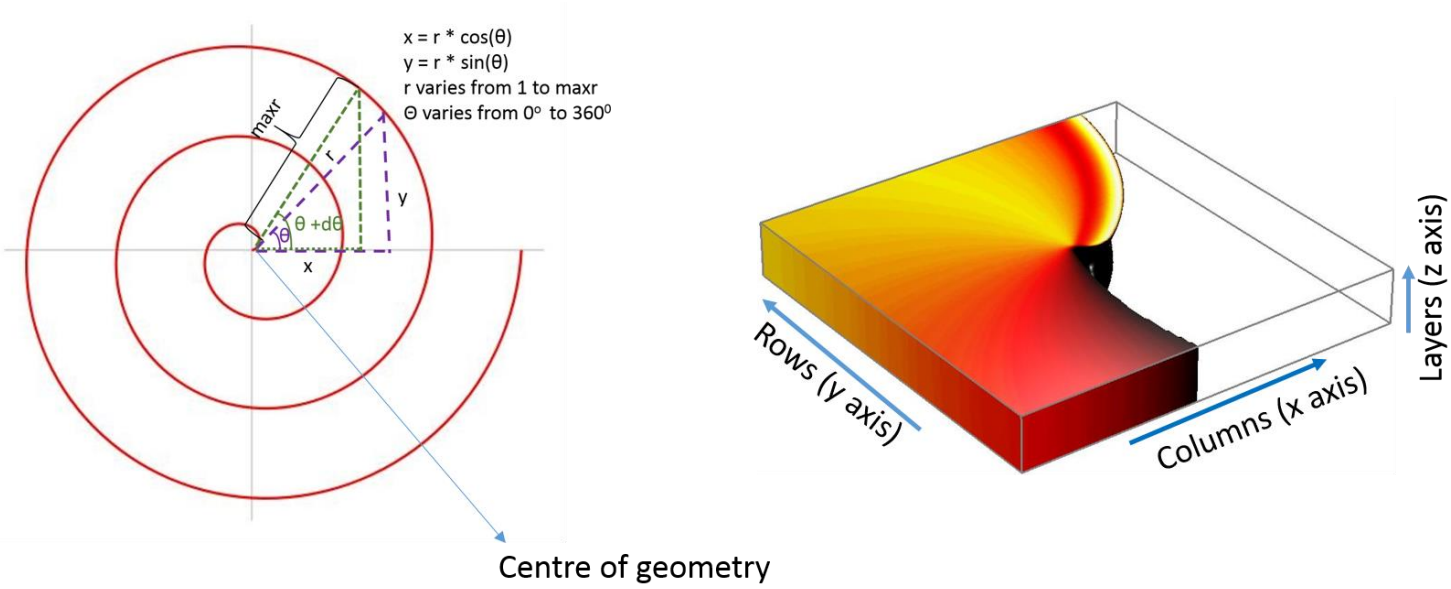

Figure 3.11 (a) Schematic representation of Archimedean spiral used to initiate re-entry in 2D; (b) Initial re-entrant scroll wave modelled stacking Archimedean spiral transmurally along z axis or layers in 3D slab geometry.

An anisotropic monodomain model equation was used as shown below. Again, an explicit method was used to solve it. Time step was set to 0.05ms and the space step was set to 0.02cm. C_m was set as 1 µFcm^{-2}.

$$C_m \frac{\partial V}{\partial t} = \nabla . D \nabla V - I_{ion} \qquad (3.13)$$

Diffusion current

$$V_{t+1} = V_t + dt(\nabla . \boldsymbol{D} \nabla V - I_{ion}) \qquad (3.14)$$

Reaction current

The 3D geometries are electrically insulated by inexcitable cells and, therefore, there is no net current flow normal to the surface boundary of the tissue (Fenton & Karma 1998). Neumann boundary conditions were imposed so that if $\hat{n}$ is the normal unit vector to the boundary then

$$\hat{n} . (\boldsymbol{D} \nabla V) = 0 \qquad (3.15)$$

The diffusion term in the anisotropic equation has a diffusion tensor as shown below:

$$\boldsymbol{D} = \begin{pmatrix} d11 & d12 & d13 \\ d21 & d22 & d23 \\ d31 & d32 & d33 \end{pmatrix} \quad (3.16)$$

The tissue geometries used in this thesis incorporated orientation of fibres with 120° rotation between endocardial and epicardial surfaces (Streeter et al. 1969). The details of how it was modelled are explained in the relevant sections 3.2.1.2 and 3.2.1.3. The components of fibre orientation in x, y and z directions were calculated and stored in a file as cosines of a1, a2, a3 as explained in sections 3.2.1.2 and 3.2.1.4.. According to Fenton & Karma 1998 and Panfilov & Keener 1995, the components of vector D are used as shown below:

$$d_{ij} = D\perp + (D\parallel - D\perp)a_i a_j \; when \; i = j \quad (3.17)$$

$$d_{ij} = (D\parallel - D\perp)a_i a_j \; when \; i \neq j \quad (3.18)$$

D⊥ and D∥ are diffusion coefficients across and along fibre direction. For the 4-variable model, the diffusion coefficient along the fibres was set to 0.001cm^2/ms and the diffusion coefficient across the fibres was set to 0.00025cm^2/ms.

The change in voltage in grid point was calculated using the above equation. The reaction current I_{ion} was the result of action potential propagation in the cell membrane and was calculated with the sum of ionic currents through the cell membrane. Since the phenomenological 4 variable model is used (Bueno-Orovio et al. 2008), I_{ion} is the sum of fast inward, slow inward and outward currents.

In the anisotropic model, there are 26 neighbours of every grid point as shown in Figure 3.12.

If the nearest neighbour was outside the medium, then the nearest neighbour was taken as zero. Boundary points in the geometry were determined as the grid point outside the geometry and the nearest neighbour grid point inside the geometry (A Panfilov & Keener 1995).

For those boundary points, the row, column and layer components of current flowing from the boundary in to the medium was calculated (A Panfilov & Keener 1995). From these current components, the grid point inside the tissue geometry that was closer to the boundary grid point was found. The boundary grid point was set to the negative value of the closer grid point. For a grid point whose nearest neighbour is negative, it shows that grid point is a boundary element.

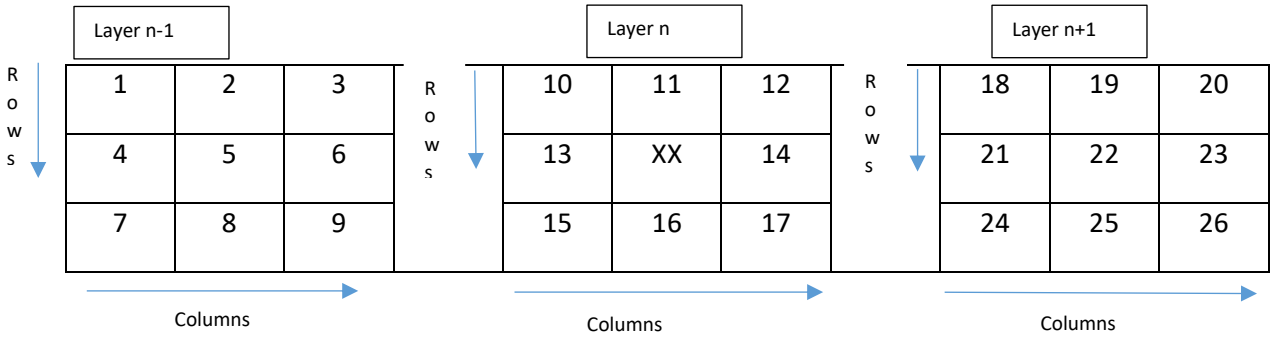

Figure 3.12 Schematic representation of 26 neighbours of grid point XX in 3D.

Calculation of diffusion current is modelled as shown below:

$$\nabla . \begin{pmatrix} d11 & d12 & d13 \\ d21 & d22 & d23 \\ d31 & d32 & d33 \end{pmatrix} \nabla Vm \tag{3.19}$$

∇ is a vector differential operator called nabla; in 3D cartesian coordinates, it is defined by:

$$\nabla = \frac{d}{dx}\hat{x} + \frac{d}{dy}\hat{y} + \frac{d}{dz}\hat{z} \tag{3.20}$$

This makes the diffusion component as shown below:

$$\begin{aligned} &\mathrm{d/dx\ d11\ dV/dx\ +\ d/dx\ d12\ dV/dy\ +\ d/dx\ d13\ dV/dz\ +\ d/dx\ d21\ dV/dx\ +\ d/dx\ d22\ dV/dy} \\ &\quad +\ \mathrm{d/dx\ d23\ dV/dz\ +\ d/dx\ d31\ dV/dx\ +\ d/dx\ d32\ dV/dy\ +\ d/dx\ d33\ dV/dz} \end{aligned} \tag{3.21}$$

The first term (d/dx d11 dV/dx) in the above equation is solved as follows:

Using product rule $\frac{d}{dx}(uv) = u\frac{dv}{dx} + v\frac{du}{dx}$ (1)

$\frac{d}{dx}\ d11\ \frac{dV}{dx}$ was solved as:

$$d11\ \frac{d}{dx}(\frac{dV}{dx}) + \frac{dV}{dx}\left(\frac{d}{dx}\right)d11 \quad (2)$$

It can be shown as:

$$d11\frac{d^2V}{dx^2} + \frac{dV}{dx}(\frac{d}{dx}\ d11) \quad (3)$$

The first part in (3) can be solved using the diffusion equation

If D1= D‖ (diffusion coefficient along fibre) and D2=D⊥ (diffusion coefficient across fibre)

$$d11(\frac{V_{x-1} + V_{x+1} - 2V_x}{2dx}) \quad (4)$$

Since in d11 i = j according to equation 3.11, it can be written as:

$$d11 = D2 + (D1\text{-}D2)fx^2 \quad (5)$$

In (5) fx is fibre component of fibre orientation in x direction, that is a1 as explained in sections 3.2.1.2 and 3.2.1.4

The part $(\frac{d}{dx}\ d11)$ in (3) was discretized as follows substituting d11

$$\frac{d}{dx}d11 = \frac{d}{dx}D2 + \frac{d}{dx}\ (D1 - D2)fx^2 \quad (6)$$

$$= 0 + (D1 - D2)\frac{d}{dx}fx * fx \quad (7)$$

(8)

$$= (D1 - D2)(\ fx\ \frac{dfx}{dx} + fx\frac{dfx}{dx}) \quad (9)$$

So the second part $\frac{dV}{dx}(\frac{d}{dx}\ d11)$ in (3) will be

$$\frac{dV}{dx}((D1-D2)(fx\ \frac{dfx}{dx}+fx\ \frac{dfx}{dx}) \quad (10)$$

$\frac{dV}{dx}$ in (10) can written as

$$\frac{dV}{dx}=\frac{V_{x-1}+V_{x+1}}{2dx} \quad (11)$$

(d/dx d11 dV/dx) is equal to :

$$d11\ \frac{d^2v}{dx^2}+\frac{dv}{dx}\ (D1-D2)(fx\ \frac{dfx}{dx}+fx\ \frac{dfx}{dx}) \quad (12)$$

$$(D2+(D1\text{-}D2)\ fx^2\ *\ (\frac{V_{x-1}+V_{x+1}-2V_x}{2dx})\ )+(\frac{V_{x-1}+V_{x+1}}{2dx}\ *((D1-D2)(fx\ \frac{dfx}{dx}+fx\ \frac{dfx}{dx})) \quad (13)$$

In a similar way

$$\frac{d}{dx}d12\ \frac{dV}{dy}=d12\ \frac{d}{dx}\frac{dV}{dy}+\frac{dV}{dy}\ (\frac{d}{dx}\ d12) \quad (14)$$

$$d12=(D1-D2)fxfy \quad \text{according to Equation 3.18}$$

In (14), fx is fibre component of fibre orientation in x direction, that is a1, and fy is fibre component of fibre orientation in y direction, that is a2 as explained in sections 3.2.1.2 and 3.2.1.4

$$d12\ \frac{d^2V}{dxdy}+\frac{dV}{dy}(\frac{d}{dx}(D1-D2)fxfy) \quad (15)$$

$$d12\ \frac{d^2V}{dxdy}+\frac{dV}{dy}\ ((D1-D2)\left(fx\ \frac{dfy}{dx}+fy\ \frac{dfx}{dx}\right)) \quad (16)$$

And this continues…

The voltage value of the corresponding neighbour in x, y direction was substituted in the above equations. If the nearest neighbour was negative, that denotes that it was a boundary element and the value was made positive. If the nearest neighbour was zero, then the voltage of the current grid point was taken.

In the above calculation (12) and (16), fx is the component of fibre rotation in x direction a1 and $\frac{dfx}{dx}$ was solved using Euler equation. The neighbours of fibre rotation in x y and z direction were taken as nearest eight. In the above equations, dx is the space step. The components of diffusion vector were solved as shown earlier in sections 3.2.1.2 and 3.2.1.4.

$\frac{d^2V}{dxdy}, \frac{dV}{dy}, \frac{dfy}{dx}, \frac{dfx}{dx}$ were discretized accordingly (AV Panfilov & Keener 1995b) and the nearest 26 neighbours' voltage was used accordingly to get the whole of the equation. The implementation is shown in 1 – 16. The updated Voltage V_{t+1} and the remaining state variables for each grid point for every 2ms were stored in an array called U and stored in a file. Normalized voltage in the 4-variable model ranges from 1 to 1.4. Voltage readings for slab geometry were decimated 200 by 200 by 30 to save storage; that spatial resolution is enough to capture the voltage reading and this will increase the speed of the simulations. For idealized LV voltage, readings were decimated 175 by 175 by 255. Open multi-processing (OpenMP) was used for parallelizing the serial implementation of reaction and diffusion current to minimize computational time.

3.3 TP06 Model Implementation

A 2D simulation was done to provide the initial conditions for initial re-entrant wave as explained in 3.1.1. Diffusion coefficient was set at 0.001171cm^2/ms (as in the TP06 (ten Tusscher & Panfilov 2006) model to get correct conduction velocity; time step was set to 0.2ms; and space step was set to 0.025 cm. An S1S2 protocol was used to pace. In the TP06 model, stimulus was set to a fixed cycle length of 1000 ms. Ten S1 stimuli with the strength of -52 µA/µF were used for the duration of 1 ms followed by S2 stimulus. The same procedure was repeated for range of S2 intervals (1000ms ….. 250ms). Threshold potential was set to -65mV.

For 3D simulation, diffusion coefficient along was set at 0.000928 cm^2ms^{-1}, and diffusion coefficient across was set at 0.000121 cm^2ms^{-1}. Maximum time step was set at 0.2 ms and space step was set at 0.025 cm. C was set as 1 μFcm^{-2}.

The TP06 (ten Tusscher & Panfilov 2006) model is a detailed model with 14 currents and 21 variables. To reduce the computation time, the equations that contain quantities that are functions of voltage were pre-computed and stored in a look up table (Victorri et al. 1985). Voltage in the TP06 model ranges from -100 to 40 mV.

Adaptive time step (Cherry et al. 2003) and operator split (Garfinkel 1999) were also used to minimize the computational time. Operator split is the concept of splitting the calculation of reaction current and diffusion current. Adaptive time step was used in the calculation of reaction current. The concept is to use a shorter time step at the grid point when there is an upstroke of AP. Sodium

dynamics are responsible for the upstroke and the gating variables responsible for conduction of sodium ions open and shut quickly compared to other gating variables. So a shorter time step will be able to capture the change in voltage during upstroke of AP. So at every grid point in the geometry, if the change in voltage was above the threshold value, a shorter time step was used, otherwise a longer time step was used. For the TP06 model, the threshold voltage of -65 mV was used. Open MP was used to parallelize the serial implementation.

3.4 Post-Processing

Simulations were run for 2000 milliseconds. The source code produced output files of U array for every 2 milliseconds. Each file provided the voltage measurement for every grid point in the geometry for that particular millisecond. For example, file fk3d0010.stf provided the voltage recording in each grid point at 10 ms of the simulation. All post-processing was done in Matlab.

3.4.1 Make Movie

The Matlab file was used to show a snapshot of re-entry for every 2ms on the surface of the geometry as shown in figure 3.13 and jpegs were created for each snapshot. This Matlab code used isonormals that compute the normal of the isosurface vertices from the vertices created using patch function. Patch function creates a filled polygon of the desired tissue geometry. Using the gradients of voltage recorded for each 2ms, it plots the activation and recovery in the geometry as shown in Figure 3.13 and the colour bar in the snap shot represents voltage recorded.

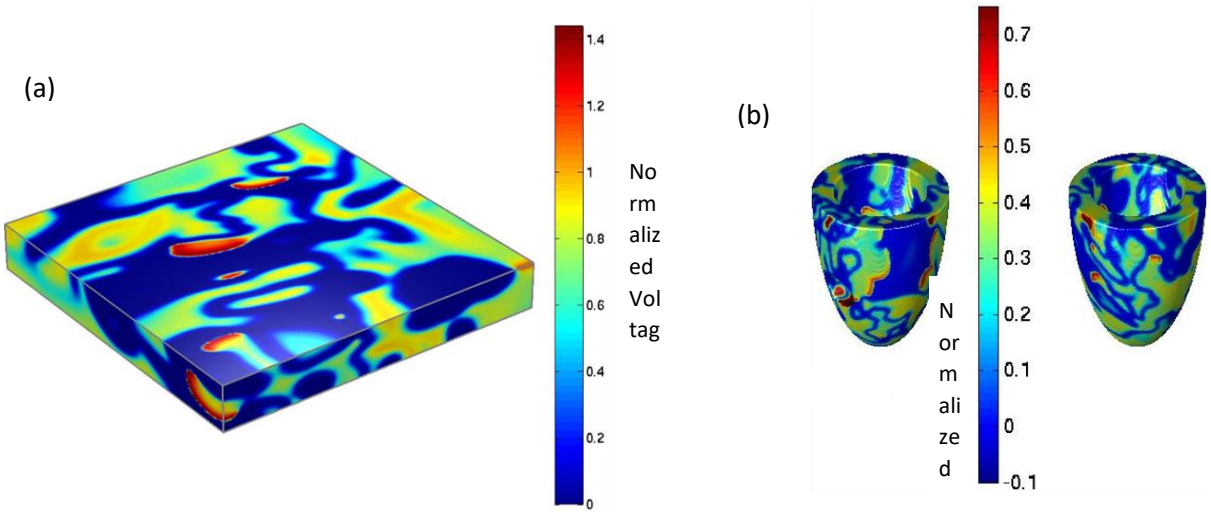

Figure 3.13 Snapshot of re-entry using 4-variable cell model in (a) in slab; (b) in idealized LV front and back view.

3.4.2 Phase Detection

As explained above for 2D, PS is a point where the excitation wavefront and repolarisation waveback meet. PS can be identified at the point where all the phase values ($-\pi$ to π i.e., one cycle from rest -> excited -> refractory -> rest) (Gray et al. 1998) meet, so the phase of the wave is arbitrary. In 3D, it is observed as line of phase singularity, called filament. During VF, several re-entrant scroll waves present forming complex activation patterns. Filament interactions and filament numbers can be used to quantify the complexity of activation patterns in simulated VF (Clayton & Holden 2002).

To detect the source of each re-entrant wave in chaotic activation pattern, membrane voltage was converted to phase time delay embedding method. According to Taken's embedding theorem, when there are N evenly sampled values of V(t), the state space in 2D can be constructed by:

$$V(t)=[V(i),V(i+\tau)] \qquad (3.22)$$

Where τ is the embedded time delay and i=1…N-1.

Phase gives the trajectory of activation-recovery of the re-entrant wave as an angle in each point in 3D (Figure 3.14). In Figure 3.14, V(t) is the membrane voltage value at time t, and R(t) is the membrane voltage at time-time delay (τ), expressed in Cartesian coordinates. Since the re-entrant wave was initiated as an Archimedean spiral in a geometry model (modelled in Cartesian coordinates), it can be expressed in mathematical format in polar coordinates and the phase angle (ϕ) in the interval of (-π, π) can be calculated by converting Cartesian coordinates into the polar coordinates equation below (Gray et al. 1998).

$$\phi(t)=atan2(V(t)-V^{*},R(t)-R^{*}) \tag{3.23}$$

In Equation 3.23, time delay (τ) can range from 2-32 ms (Bray et al. 2001, Bray & Wikswo 2002). V(t) is activation and R(t) is the recovery voltage. V* and R* are the origin. So the phase of each point can be calculated with respect to the origin V* and R*. This is the point encircled by all trajectories. Since the amplitude of AP is less close to the core of the re-entrant wave and trajectories of the points near the source have smaller orbits, the origin should encircle all trajectories. Choosing the origin V* and R* is model dependent. Tau (τ) should be chosen so that the mutual dependence of activation voltage and recovery voltage are minimum (Fraser & Swiney 1986). For the 4-variable model, tau (τ) was chosen as 2ms and for the TP06 model tau (τ) was chosen as 20ms. For each excitable cell model, 2D simulations were performed by introducing spiral wave re-entrant wave as an initial condition, the trajectories of each point are plotted in state space and the point that encircles the smallest trajectory is chosen as origin (Figure 3.15). The activation and recovery plots with chosen V^{*} and R^{*} for both 4-variable model and TP06 are shown in Figures 3.15 and 3.16 respectively.

For the 4-variable model, V^{*} was taken as the mean of voltages at a particular time t in x, y and z directions. R^{*} was taken as half the value of the mean of V at (t-τ) taken in x, y and z directions as shown in Figure 3.15. For the TP06 model, the origin was taken as the mean of activation and recovery as shown in Figure 3.16. Since the half ellipsoid geometry was first inside a cube, the points surrounding the ellipsoid were removed before finding V^{*} and R^{*}.

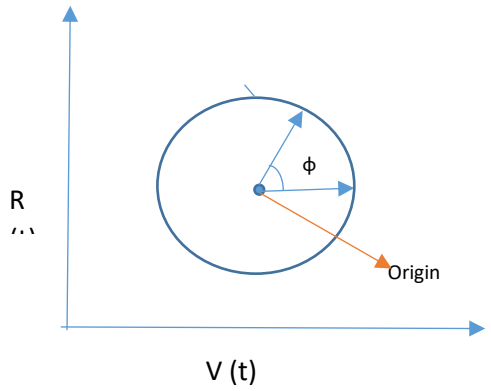

Figure 3.14 Schematic representation of phase diagram based on (Garfinkel 1999).

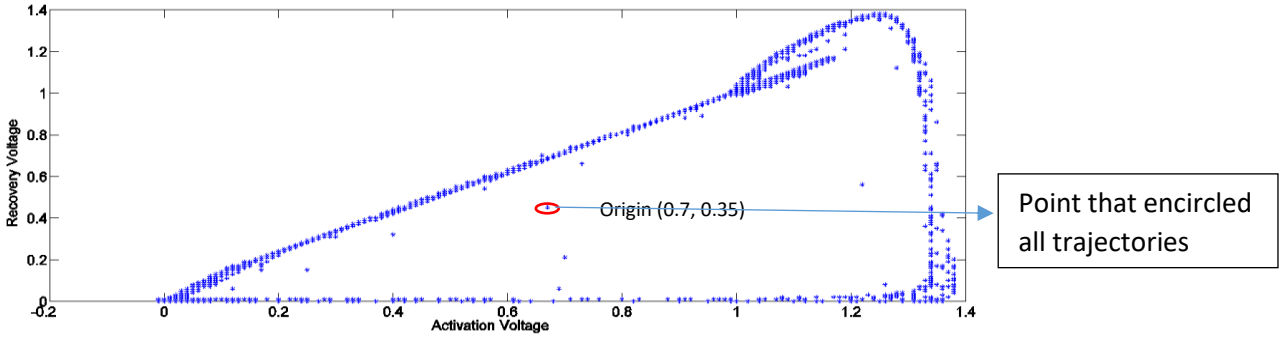

Figure 3.15 4-variable model - Activation-Recovery.

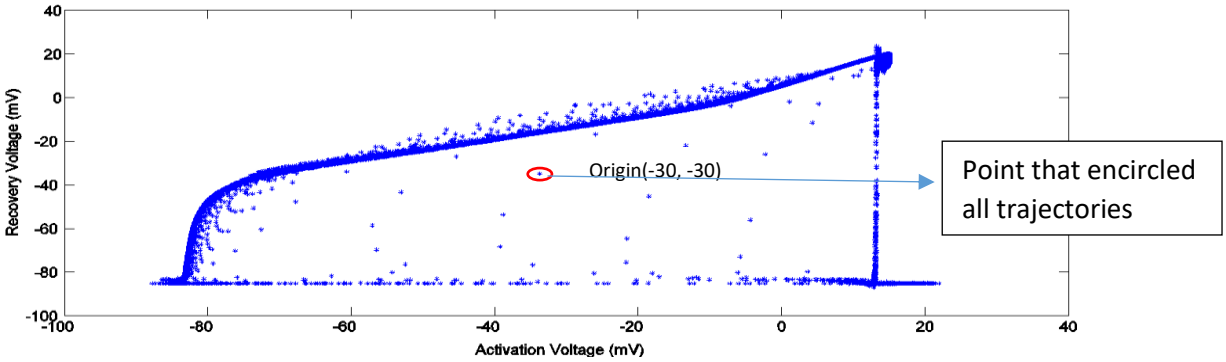

Figure 3.16 TP06 model- Activation recovery.

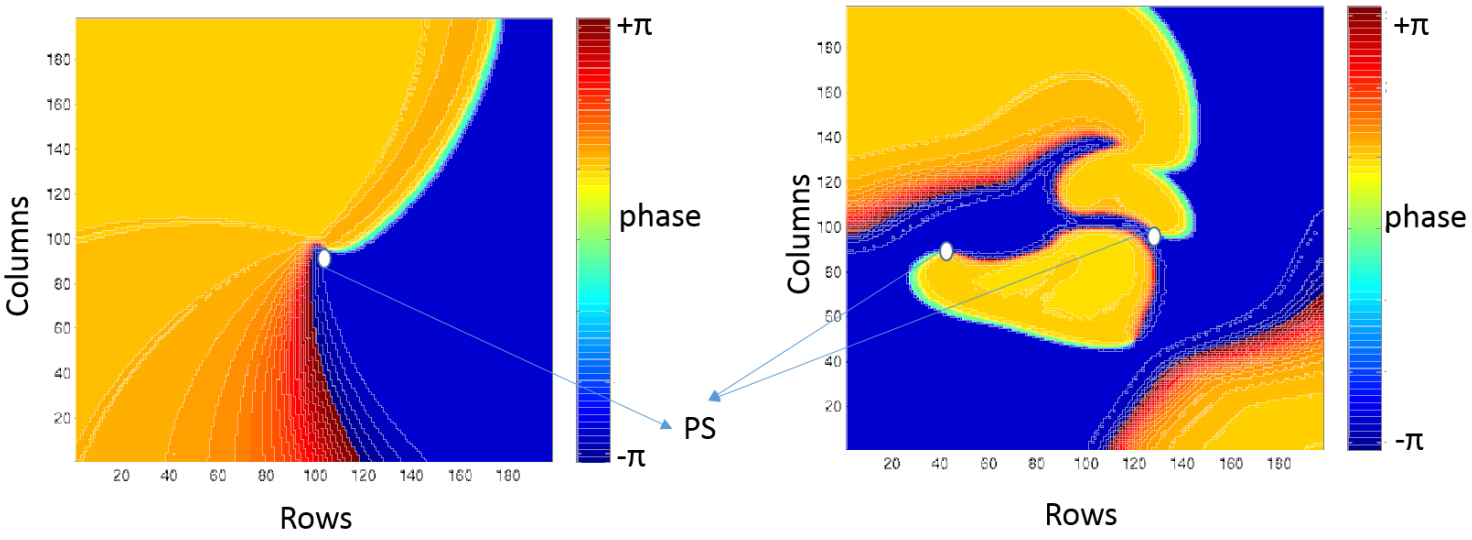

Figure 3.17 Detecting phase singularity (PS) from the surface of the 3D slab (a) with single wave; (b) with multiple wave.

3.4.3 Detecting Filaments

When the propagating AP is blocked, it breaks and curls forming re-entrant scroll waves in 3D. Since there are several re-entrant scroll waves present during VF, it is easier to decompose scroll waves to their core, called filaments in 3D and PS in 2D. These filaments or PS can be used to quantify VF. Bray & Wikswo (2002) established a method to detect filaments using phase. They calculated topological charge using phase to detect filaments as shown in Equation 3.35. The change in phase around every PS must be 2π times the topological charge. Topological charge or winding number is the number of times the curve travels counter-clockwise around a point in a closed curve. It is an integer number with negative sign if the curve travels in clockwise direction or positive otherwise. The negative sign is usually ignored.

$$n_t \equiv \frac{1}{2\pi} \oint_c \nabla\emptyset \,.\, \overline{d}\, l \tag{3.24}$$

Winding number is calculated using the above equation and is usually $2\pi n_t$. This winding number detects 2π phase change around the point. Line integral ($\oint c$) is calculated around the path $\bar{l}$ on the closed curve c (re-entrant wave) surrounding the phase singularity (PS). Line integral is calculated by dividing the path $\bar{l}$ into very small multiple paths and finding the directional derivative of phase for each little path and summing them all to find $2\pi n_t$.

By assuming the gradient of phase ϕ as the wave vector, the winding number becomes proportional to the curl of the wave vector. The curl of the wave vector provides the rotation of wave vector at every point. The change in function ϕ in a given direction (specified as a unit vector a) is determined from the scalar product (grad ϕ) · a. This scalar quantity is called the directional derivative. So, the directional derivative of phase gives the wave vector components in each direction. Since the wave vector is calculated from the differential of ϕ which is scalar, the curl of wave vector is zero apart from when PS is present. While calculating the directional derivative of phase, to avoid discontinuity in phase between two adjacent points in state phase, the phase angle greater than π is corrected to its 2π compliment. This is done by finding the magnitude of each wave vector component greater than π and finding its 2π compliment.

Convolution kernel masks were used to identify the voxels containing filaments and the individual filaments were labelled using grassfire algorithm. A convolution kernel is a filter matrix used to identify filament voxels in an original matrix that contains filaments. Each voxel in the original matrix is multiplied by 26 surrounding voxels in the convolution kernel filter matrix and the results are summed. This summed result is replaced with the initial voxel and continues with each voxel in the original matrix. In this case, the convolution kernel filter matrix was set used to sharpen the original matrix in order to identify filament voxels. Individual filaments present in the chaotic system were counted and the voxels that make a single filament used to mimic the length of each filament. Smaller filaments that are made up of less than 5 voxels are ignored. In 3D simulations, Phase Singularities (PS) are normally counted as the intersection of the filament with the surface of the tissue ignoring very closely spaced ones. While plotting the filament in a jpeg file, the surface of the tissue is created or extracted and the filaments are masked on the surface. Figure 3.17 shows PS detection from the surface of a 3D slab. Figure 3.18 shows an initial filament detected in both slab and idealized geometry.

3.4.3.1 Logic of Grass Fire Algorithm

A grid point in the geometry is selected, given a certain value and tagged with a number. The value of the initial point is used as a threshold. Twenty-six neighbours of this voxel are tested to see if they satisfy the threshold and are inside the boundary. If the neighbouring voxel satisfies this criteria it is tagged with the same tag number as the initial point. This is repeated until the criteria are satisfied.

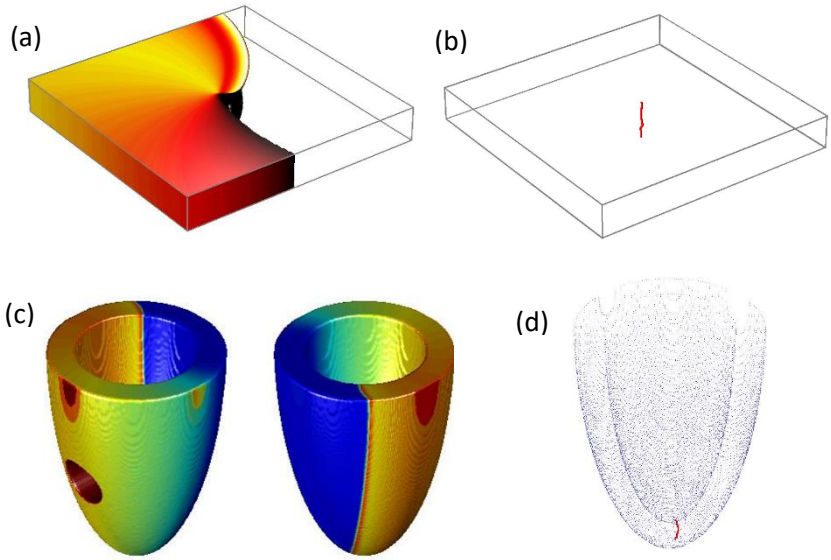

Figure 3.18 (a) and (b) show initial re-entrant scroll wave and corresponding filament detected in slab; (c) and (d) initial re-entrant scroll wave and corresponding filament in idealized LV.

3.4.4 Number of Filaments and Volume of filaments

The above logic counts the number of filaments present in the chaotic system and individual voxels that makes a single filament are used to mimic the length of each filament present in the tissue geometry at each particular time (Figure 3.19 (a)). To obtain a clearer picture of the number of filaments, a moving average was calculated using a rectangular window extending ±50ms from each time sample and plotted (Figure 3.19 (b)). The length of each filament gives information about the positive and negative tension and Fenton et al. (2002) showed that the negative tension affects the stability of filaments. Mean volume of filaments was plotted using the moving average window extending ±50ms from each time sample to obtain a smoothed number of filaments (Figure 3.19 (c)).

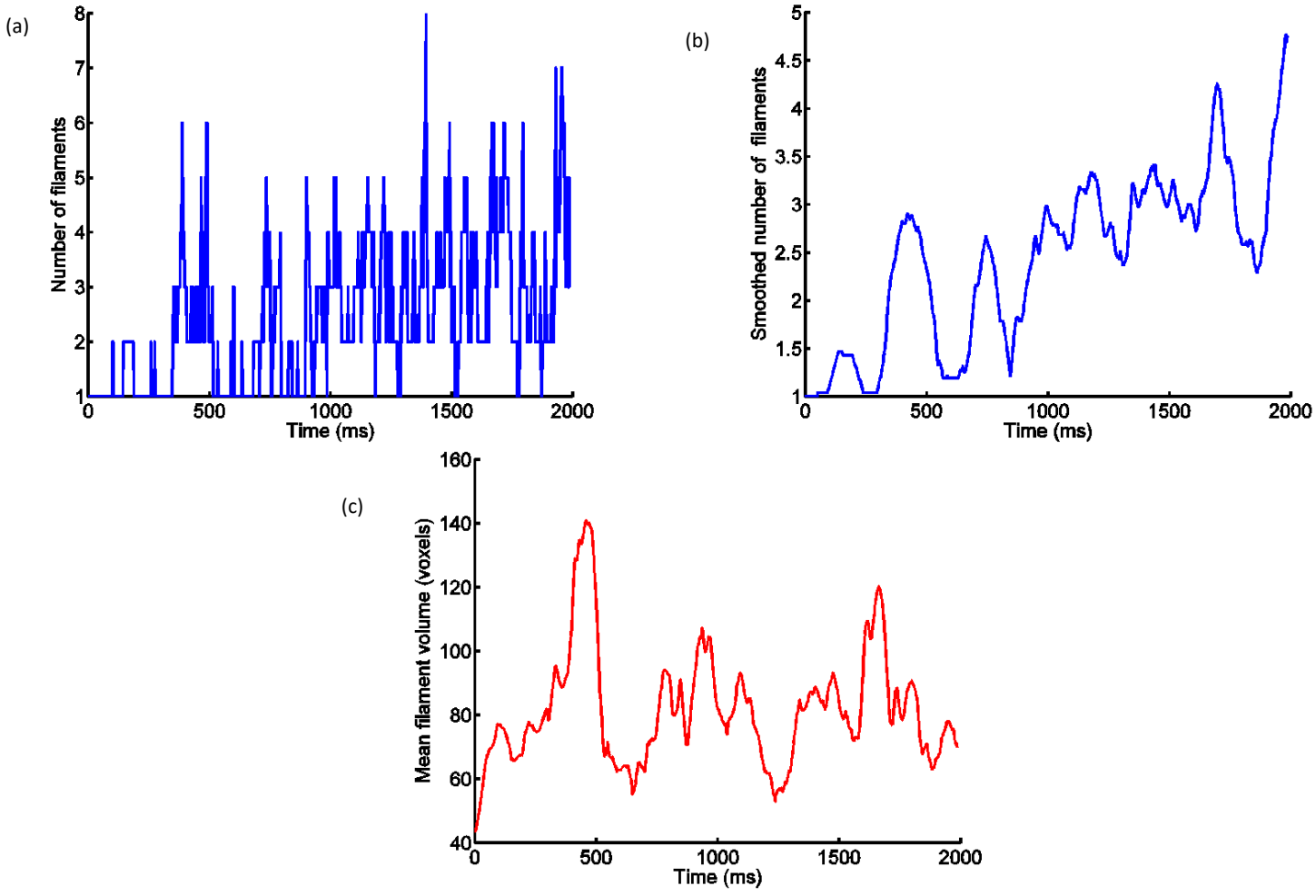

Figure 3.19 (a) Change in number of filaments over time (ms); (b) Smooth view of number of filaments plotted using a moving average was calculated using rectangular window extending ±50ms from each time sample and plotted; (c) Change in mean filament volume over time.

A particular Filament voxel in Face	A particular Filament voxel in Face	Type of filament
Face 5 and face 6	None other	Transmural or 'I' shaped
Face 1 and face 3	None other	'U' shaped filament
Face 2 and face 3	None other	'U' shaped filament
Face 2 and face 4	None other	'U' shaped filament
Face 1 and face 4	None other	'U' shaped filament
Face 1	None other	'U' shaped filament
Face 2	None other	'U' shaped filament
Face 3	None other	'U' shaped filament
Face 4	None other	'U' shaped filament
Face 5	None other	'U' shaped filament
Face 6	None other	'U' shaped filament
None	None	Ring filament or 'o' shaped

Table 3.1 Showing how configuration of filaments were determined in 3D slab.

3.4.5 Configuration of Filaments

Filaments can bend and twist and this changes their shape. Finding the shape of each filament gives the behaviour and interaction with other filaments. The shapes of the filaments are analysed and classified as I, O or U depending upon their shapes. When a filament touches the opposite surface of

the tissue, it is known as an 'I' shaped filament. 'O' shaped filaments are in the form of closed rings and act on the single surface. 'U' shaped filaments have broken ends touching either the same or different surfaces of the tissue.

3.4.5.1 Configuration of Filaments in 3D Slab Geometry

To find the shape of filaments in slab geometry, all six sides of the 3D slab were assigned with face numbers as in Figure 3.20 (a). Figure 3.20 (b) shows filaments detected in the 3D slab. Faces 5 and 6 were considered epicardial and endocardial surfaces respectively. Filaments with lengths less than 5 are ignored. Table 3.1 shows how filament shape was decided. So every time a filament touches face 5, a PS point is counted. If a filament did not satisfy any of the criteria above, it was considered as other (intramural filament) (Figure 3.20 (b)) (Clayton 2008).

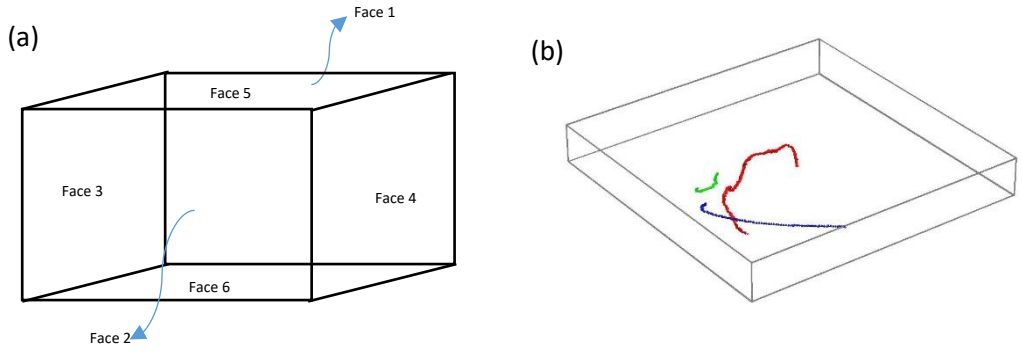

Figure 3.20 (a) schematic representation of six faces of 3D slab geometry; (b) filaments detected in slab.

3.4.5.2 Configuration of Filaments in Idealised Left Ventricle

Grass fire algorithm was used to differentiate epicardial and endocardial surfaces of the idealised geometry as shown in Figure 3.21 (a). The figure shows a slice of ellipsoid geometry at the 250th layer to differentiate epicardial and endocardial surfaces. Endocardial surface has the value of -3 and epicardial surface has the value of -2 as shown in Figure 3.21(a). Figure 3.21 (b) shows filaments detected in an idealized LV.

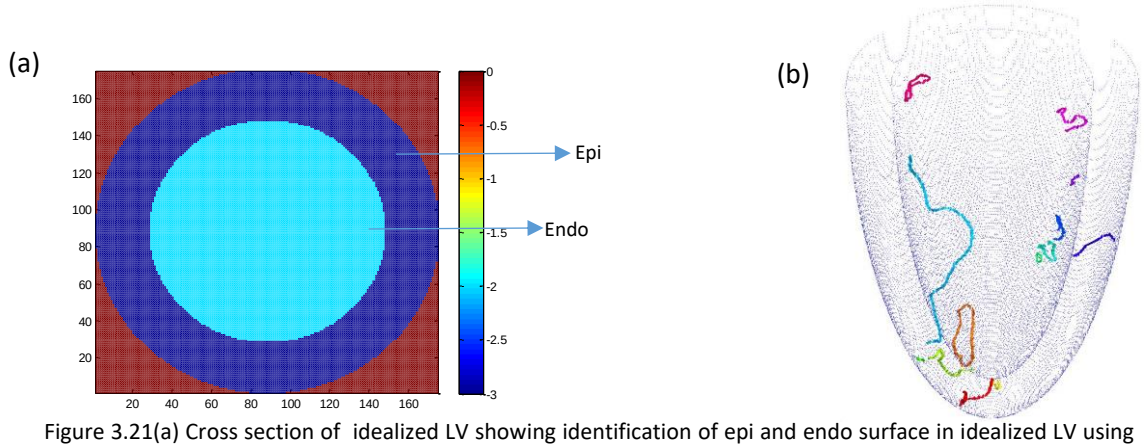

Figure 3.21(a) Cross section of idealized LV showing identification of epi and endo surface in idealized LV using grass fire algorithm; (b) configuration of each filament was determined where the ends of filaments were located.

For each filament detected with a length greater than 5 voxels, the position of each voxel was recorded. For each voxel in the filament, the voxel and its 6 neighbouring voxels were checked to see if they lay in epicardial or endocardial surface. Six neighbours are checked since all these voxels are connected along one of the primary axes. Each voxel with coordinates (x±1, y, z), (x, y±1, z) or (x, y, z±1) is connected to the voxel at (x, y, z). If the filament voxels were present in both epicardial and endocardial surfaces, it was considered a transmural filament. If the filament voxels were present only in epicardium or only in endocardium, it was considered a U shaped filament. Filaments not touching either epicardium or endocardium were considered ring filaments or 'o' shaped filaments (Figure 3.22 (a)) (Clayton 2008). If the filament did not satisfy any criteria, it was considered as 'others' which can be intramural filaments.

Since PS can easily be observed as the intersection of the filament with the surface of the tissue, the filament voxel or its six neighbours being present in the epicardial region was considered as one PS. The coordinates of the voxels in the epicardial surface were recorded and used to calculate the distance between the PS points. If the distance was less than or equal to 1, one of the PS points was not considered to avoid counting PS points that were too close to each other (Figure 3.22(b)).

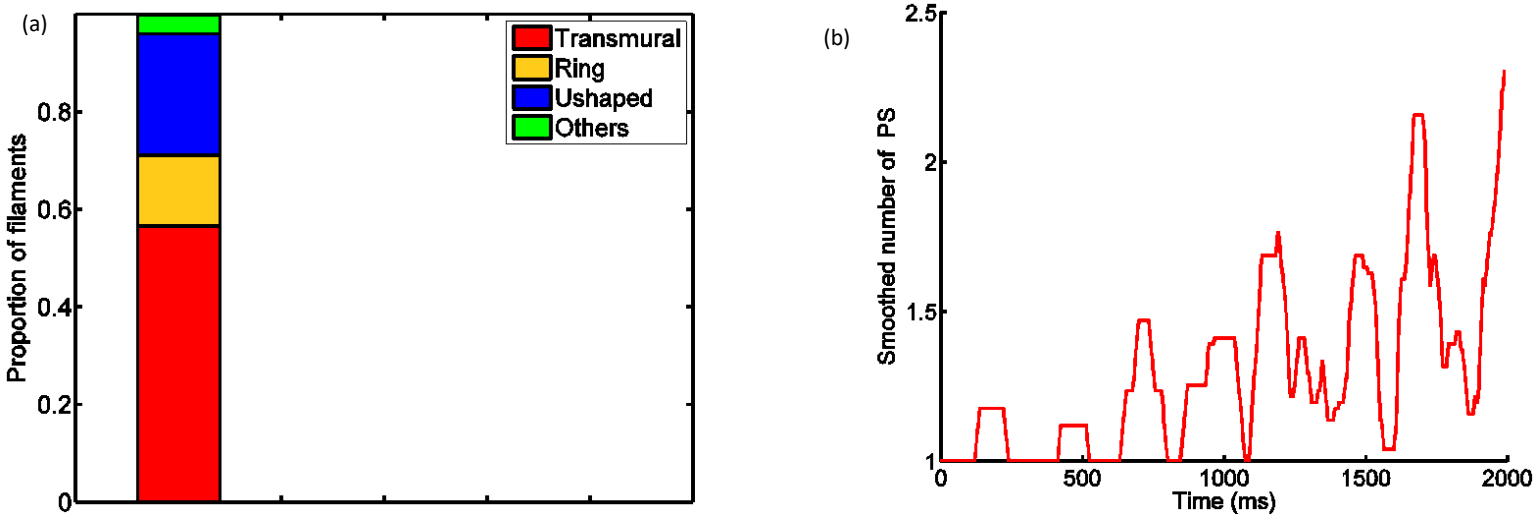

Figure 3.22 (a) showing configuration of filaments over 2000ms simulation; (b) change in number of PS over time (ms).

3.4.6 Filament Interactions and Filament Lifetime

Numbers of filaments change due to filament birth, death, amalgamation and division. Filament interactions were traced throughout each simulation by taking the overlap of filaments from two successive time steps (t and t+1). If the filament in 't+1' was present and not in 't', it was considered filament birth and a new filament id assigned to it. The time of filament birth was recorded. If the filament in time step 't' did not overlap with time step 't+1', the filament was considered dead and the filament id was not reused. The time of death was recorded. Filament life time was calculated as the difference between the time of birth and time of death of a filament plus the lifetime of the parent. Parent life time was set to the start time of the simulation. The filament was considered divided if the filament in 't' seconds overlapped with two or more filaments in 't+1' seconds. New ids were assigned to the newly divided filaments. Each of the divided filaments received the life time of the parent

filament and the time of birth was recorded (Figure 3.23). When two or more filaments in ‘t’ overlapped with one filament in ‘t+1’ seconds, it was considered the amalgamation of filaments in ‘t’ time step to one filament in ‘t+1’ (Figure 3.24). A new filament id was assigned to the amalgamated filament and it was assigned the lifetime of the longest lived parent. The birth of the amalgamated filament was recorded (Clayton and Holden 2002). When the filament in ‘t’ and ‘t+1’ did not completely overlap (perhaps because of meandering of scroll waves) , it was considered a complex event as shown below. The cyan coloured filament in Figure 3.25 (a) at time ‘t’ does not completely overlap with cyan coloured filament in figure 3.25 (b) at time ‘t+1’(Clayton & Holden 2002).

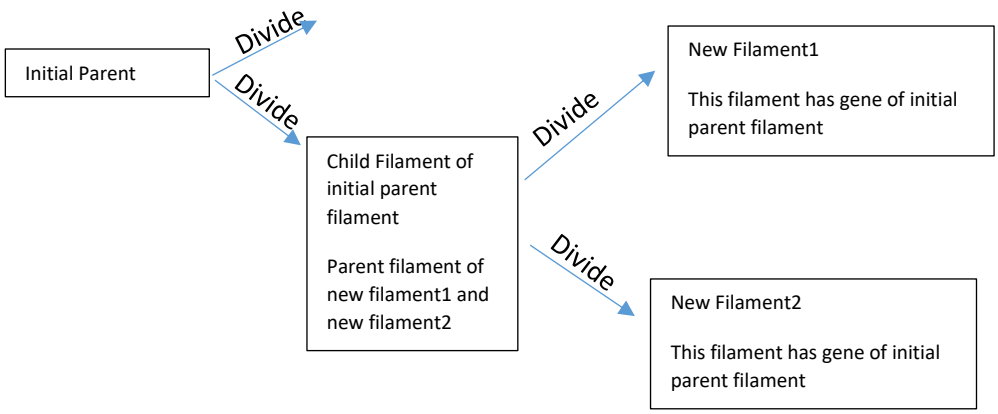

Figure 3.23 Schematic representation of filament division based on (Clayton & Holden 2002).

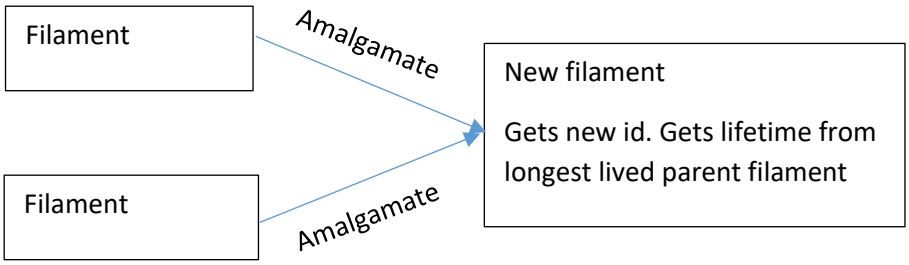

Figure 3.24 Schematic representation filament amalgamation based on (Clayton & Holden 2002).

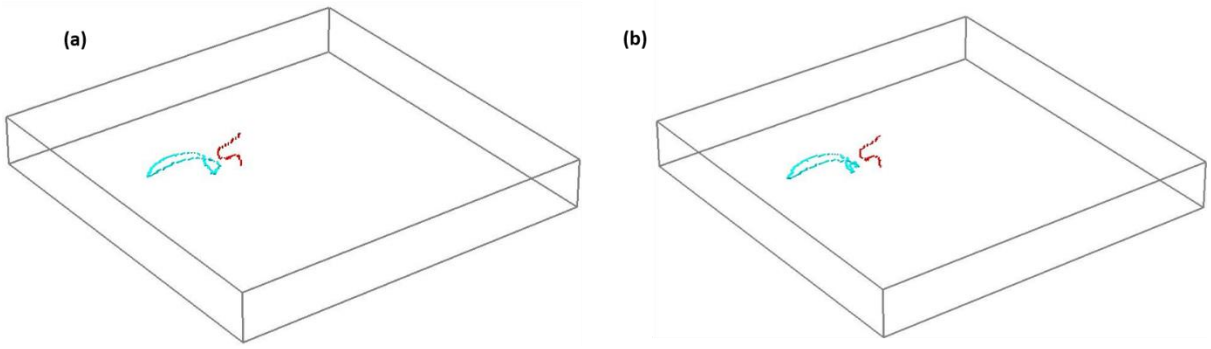

Figure 3.25 Complex event (a) filaments detected in 't' seconds (b) filaments detected in 't+1' seconds. Filaments don't overlap exactly showing complex nature.

The lifetime of each filament can be plotted as shown in Figure 3.26 (a). The X axis shows the time in ms and the Y axis is the filament id. Each horizontal line indicates the lifetime of a single filament; the start of the line indicates the time at which the filament originated from a birth or division and the end of the line, the time at which the filament ended with a death or amalgamation.

Filament lifetime was plotted by drawing lines linking the time at filament birth, and the time at filament death as shown in Figure 3.26 (a). Plotting lifetime provides some information on how long the filament lived but it may not be very clear, so the lifetime of the initial filament in each simulation was observed. When the initial filament amalgamated or divided into new filaments, the initial filament gene is passed into the new filaments. This was traced throughout the simulation to determine when the initial filament completely disappeared. The life time of initial filaments provides information on the amount of time the initial re-entrant wave can sustain in the given tissue configuration (Figure 3.26 (b)). Longest-lived filament time was recorded in simulations. The life time of the longest-lived filament can provide the time of VF sustained in the tissue geometry (Figure 3.26(c)).

Filament birth, death, amalgamation, division and complex events in each single simulation can be plotted as shown in Figure 3.27. This gives an insight into filament interactions.

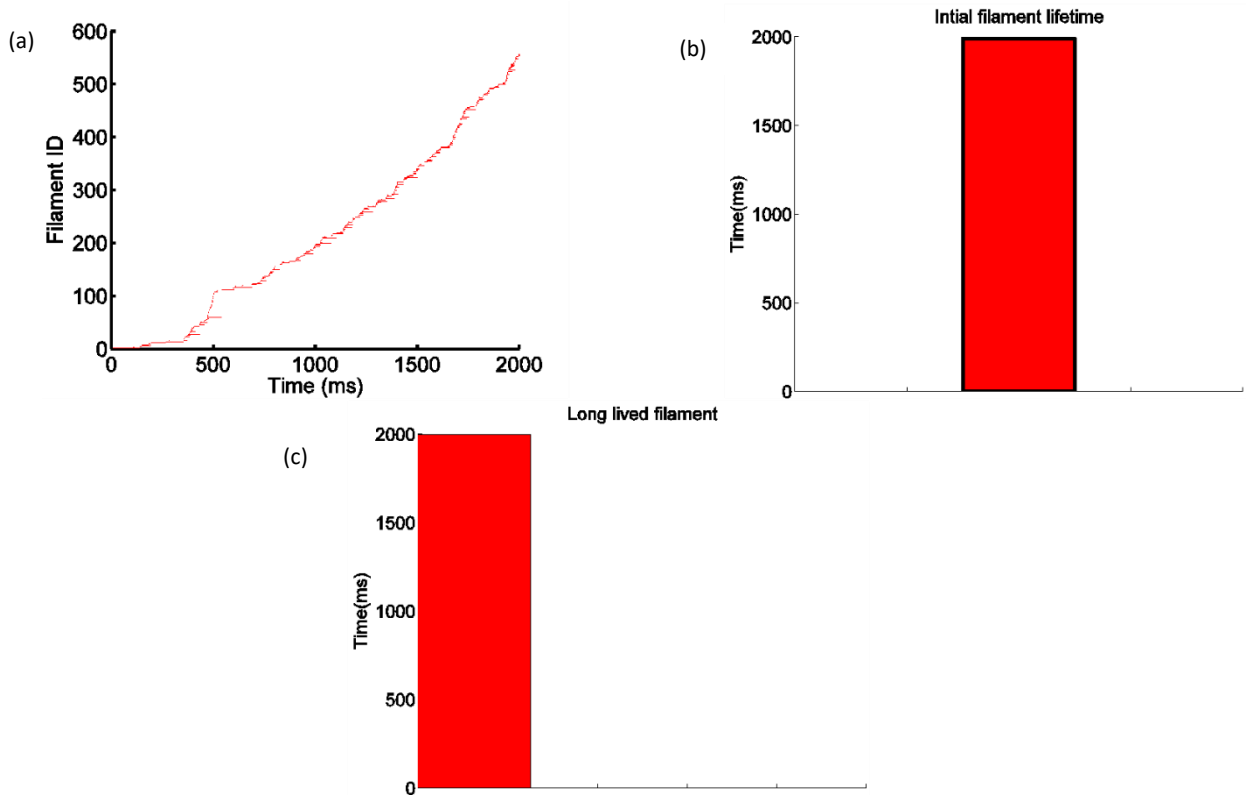

Figure 3.26 (a) Filament Lifetime over shown by drawing lines linking the time at filament birth, and the time at filament death; (b) initial filament life time; (c) long livid filament

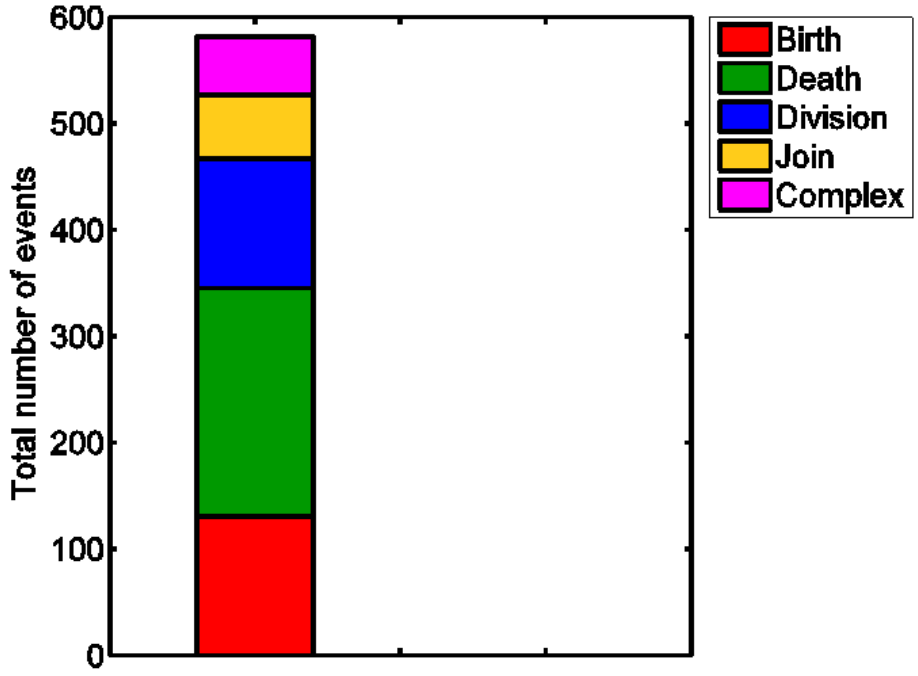

Figure 3.27 showing number of filament events (birth, death, division, amalgamation and complex) over 2000ms of a simulation.

3.4.6.1 Short Lifetime and Cumulative Time

As explained above regarding how filament lifetime was calculated, each filament has a long cumulative life time and short lifetime. Cumulative lifetime gives the total time the parent filament gene is present and the short life time gives the intermediate filament lifetime as shown in Figure 3.28.

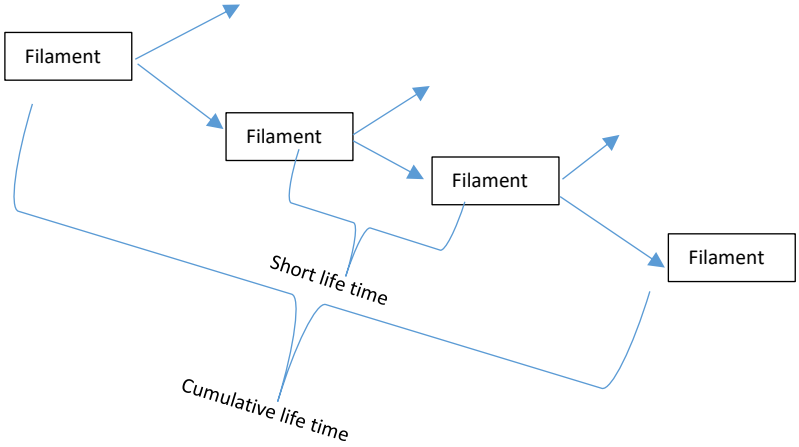

Figure 3.28 Schematic representation of short and the long cumulative life time of a filament.

3.4.7 Period of Re-entry

Nash et al. (2006) showed that the dominant frequency of transmembrane voltage was around 6 Hz at the onset of VF in the human heart. Gray et al. (1998) showed an 8 Hz frequency during VF. Frequency of re-entrant waves gives oscillations of re-entrant waves per second. If the activation period gives the period of re-entry, frequency of re-entrant wave will be reciprocal of period. Since period is measured in ms and frequency is calculated every second, ms is converted to seconds and its reciprocal will give the frequency per second.

To quantify the period of re-entry in a simulation, an average activation interval over 2 seconds was extracted from slab geometry and converted to frequency to see if it exhibited fibrillatory effects (Figure 3.29).

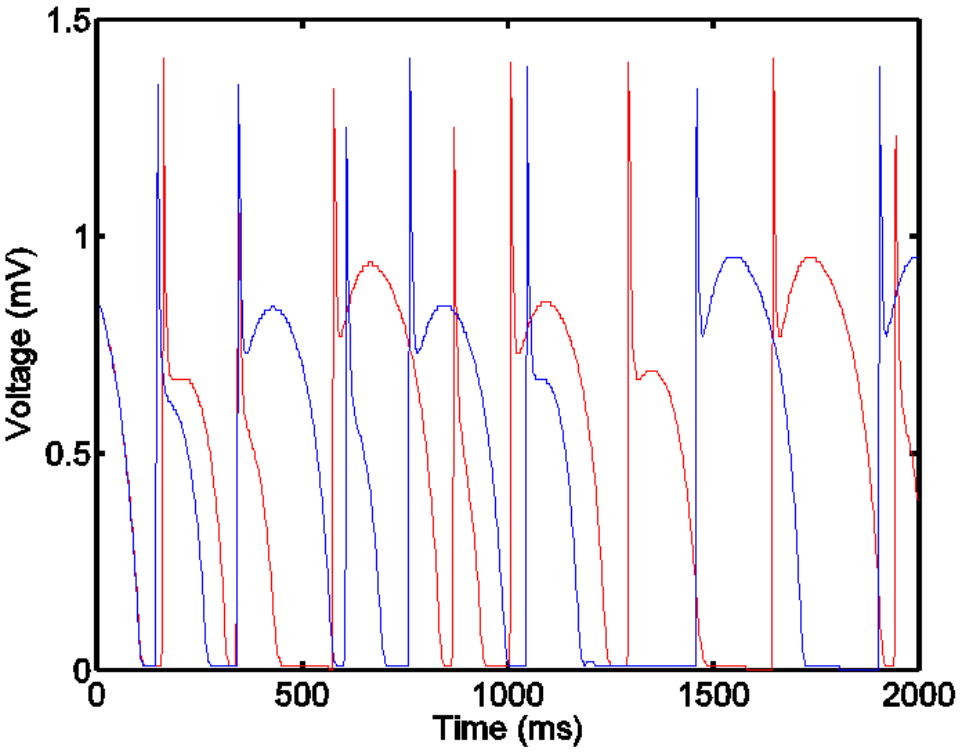

Figure 3.29 Voltage (from a selected grid point) in slab geometry over 2 seconds interval were extracted from two different layers and plotted.

For example, in slab geometry with epiMod2 dynamics, transmembrane voltages from certain points from two different layers were extracted and plotted as shown in Figure 3.29. A code was written that extracts and records activation time in red colour pattern of transmembrane signals and also for blue colour as shown in Table 3.2.

Red colour activation time	Blue colour activation time	Difference in activation time(red and blue)
100	105	
300	300	200
600	595	295
800	900	300
1050	1000	200
1450	1600	250
1950	2010	150
		60
	Total	1455
	mean	207.85714

Table 3.2 showing the calculation of period of re-entry.

The mean calculated as shown in the above table will give period of re-entry, which will be 207.85 ms, and a frequency of 4.8309 Hz. The same was repeated for more locations in the geometry. The mean of period of re-entry from all the locations was calculated and used to calculate frequency of re-entry.

3.4.8 Density of filaments in Slab Geometry

A schematic representation of the computing density of filaments is shown in Figure 3.30(a) and (b). Figure 3.30 (a) shows a schematic view of summing the filament voxels along the Z axis. Figure 3.30 (b) shows a schematic view of a 2D representation of slab geometry. Density of filaments (2D) in the geometry was computed by summing filament voxels along an axis and through time from snapshots taken every 2ms throughout the 2000ms simulation as shown in Figure 3.30 (c). From the 2D density of filaments, 1D representation of density of filaments was computed as shown in Figure 3.31. Figure 3.31 (a) shows a schematic representation of how the 2D view was separated with lines diagonally (h) shown by orange lines with varying angle θ. For each height (h) in 2D view, X and Y coordinates were calculated using trigonometric functions and the density of filaments in X and Y coordinates in 2D (Figure 3.31 (b)) were added together to compute a 1D representation of the clustering of filaments (Figure 3.31 (c)).

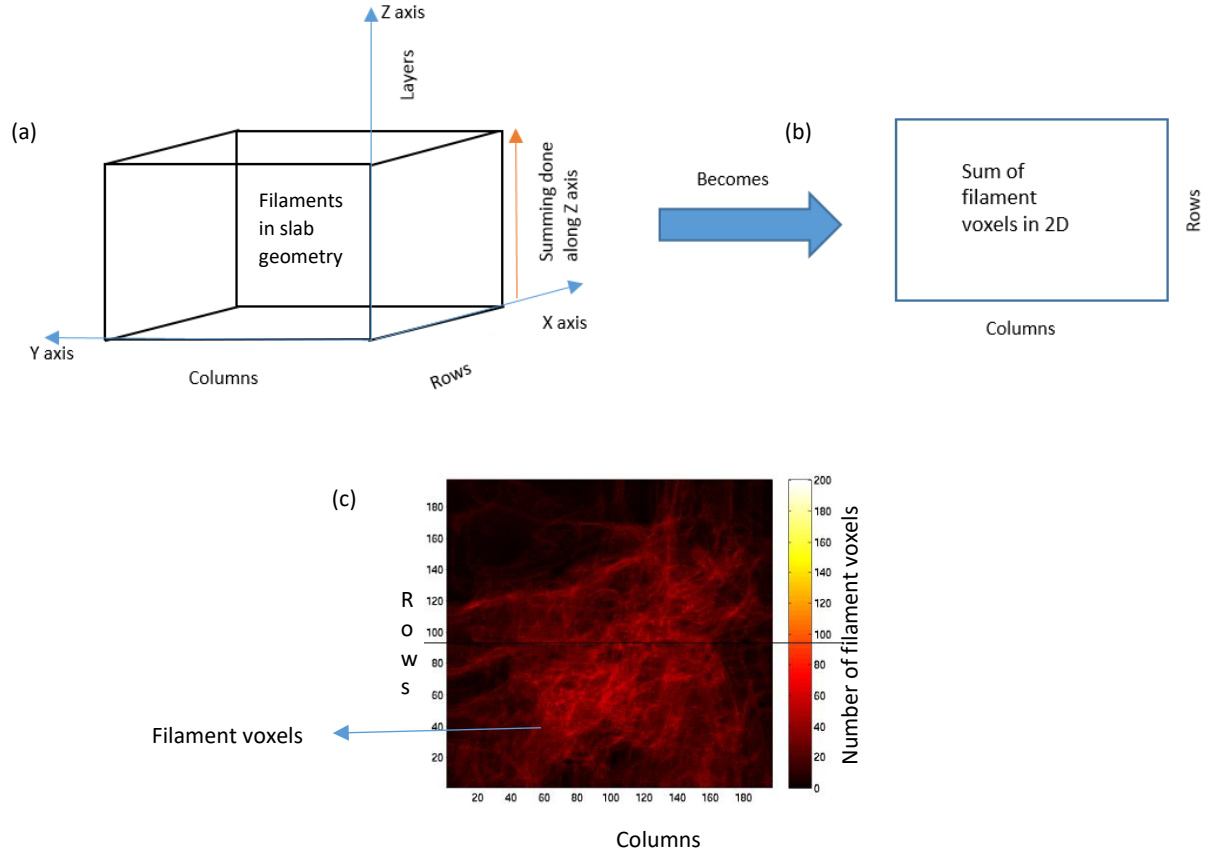

Figure 3.30 (a) schematic representation of slab geometry with filaments detected and summing of filament voxels along Z axis; (b) schematic representation of 2D view of slab geometry with filament voxels summed along Z axis; (c) Actual view of density of filament voxels summed along Z axis.

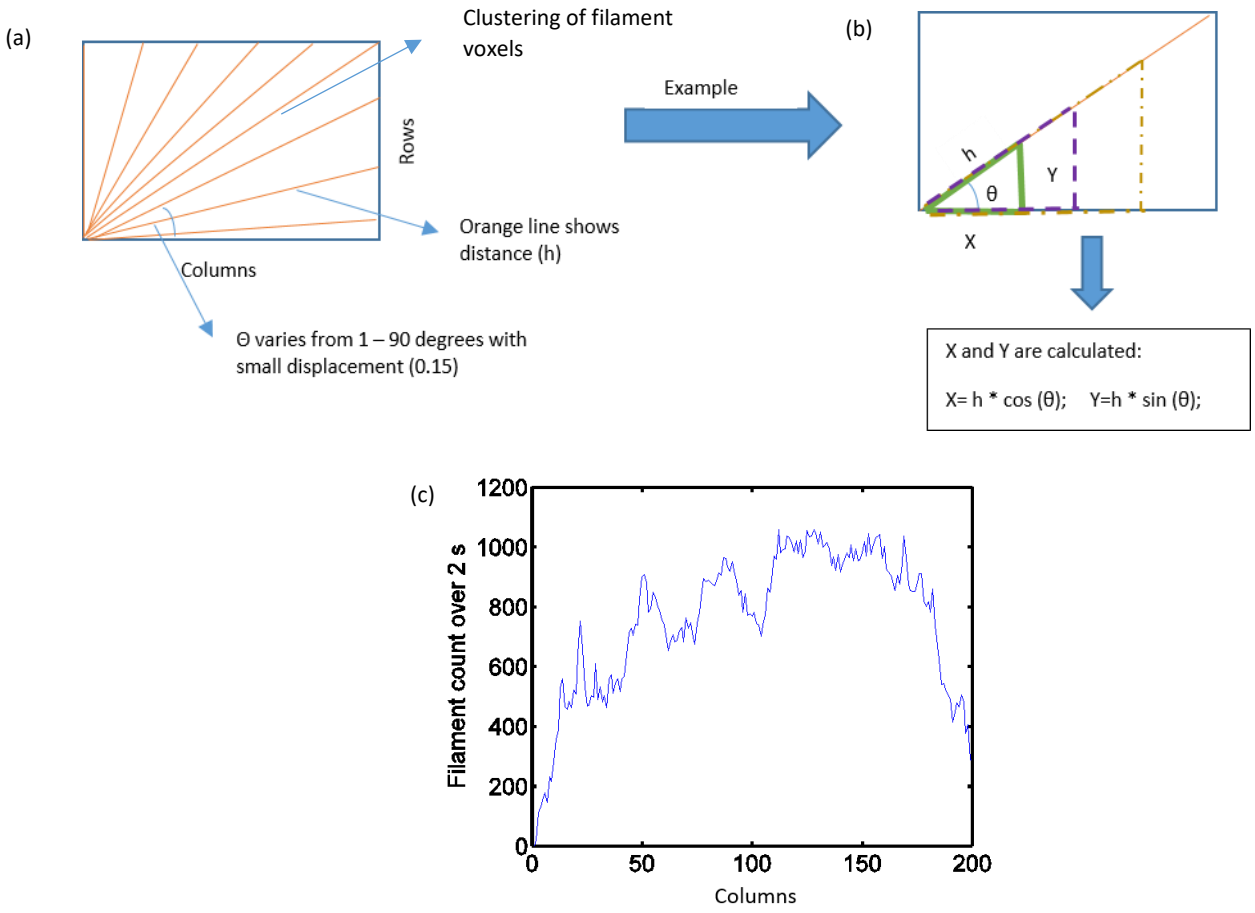

Figure 3.31 (a) schematic view of density of filament voxels in 2D and showing how 2D view was separated by different lines diagonally shown by orange lines and elevation represented by θ (varies from 1^0 to 90^0); (b) schematic representation showing how X and Y coordinates were calculated for each along each line (h) using trigonometric function; (c) Result showing 1D representation of density of filament voxels.

Chapter 4 Influence of Tissue Shape, Structure and Initial Conditions on Filament Dynamics

4.1 Introduction

This chapter focuses on the effects of cell model, initial conditions, transmural heterogeneity, shape of geometry and perturbations of initial conditions on filament dynamics.

Initially simplified and biophysically detailed models were compared in 3D tissue to establish how different the filament dynamics were in each model. If the filament dynamics were similar, then this would justify the use of the simplified model for this thesis.

Computational studies often use a single transmural filament as the initial condition (Clayton and Holden 2002, Qu et al. 2000a). Using this initial condition in 3D will be similar to a PS observed as an initial condition in 2D. However, a more plausible scenario in the human heart is a regional block that forms a ring filament within the ventricular wall. This section, therefore, compares the choice of transmural filament and ring filament as an initial condition on filament dynamics in a 3D slab. According to Qu et al. (2000a), using no-flux boundary conditions, the initial filament can only be perpendicular to fibre direction, i.e. transmural filament. To use ring filament as initial condition, the no-flux boundary condition in one set of opposite sides was replaced with periodic boundary conditions in the slab geometry, making the slab geometry behave as a topological cylinder (Fenton et al. 2002). The similarity of the filament dynamics in both simulations will justify the use of single untwisted transmural filament as an initial condition.

Computational studies (Sridhar 2010, Majumder et al. 2011) on transmural heterogeneity have been done on sharp transition of cells from layer to layer, but Glukhov et al. (2010) showed that the distribution of cell transition may not be sharp. Transmural heterogeneity remains a controversial topic on M cells. Some studies suggest that there are no M cells (Taggart et al. 2001), while Glukhov et al. (2010), (Lin & Scott 2012) suggested M cells are seen and can be in the form of islands in between endo and epi cells. This chapter compares the effect of sharp and smooth distribution of transmural heterogeneity (with M cells, without M cells) on filament dynamics. The effect of transmural heterogeneity with patches of M cells in between epi and endo layers with the transmural heterogeneity of endo-M- epi as distinct layers on filament dynamics is also compared.

Previous studies have shown that the shape of the geometry affects the filament dynamics (Rogers 2002). Hence, comparing filament dynamics in a 3D slab and idealized left ventricle (LV) will give an idea of how the number of filaments, filament configuration, filament volume and filament lifetime are affected by shape of geometry.

Non-linear behaviour of cardiac tissue has been studied (Cherry et al. 2012) in 2D, by perturbing the initial conditions while pacing the tissue using the S1S2 protocol. In this thesis, initial transmural filament is perturbed to check the non-linear nature of slab and idealized LV geometry.

4.2 Methods

4.2.1 Filament Dynamics in Simple and Biophysically Detailed Model

Before comparing filament dynamics in the simplified 4-variable model and biophysically detailed TP06 model, both models needed to be checked for similarity of behaviour. Diffusion coefficient D is ionic flux per unit area and determines conduction of action potential in the tissue. Conduction velocity is the speed of action potential propagation in the tissue. According to studies (Hodgkin 1954, Walton & Fozzard 1983), conduction velocity is proportional to the square root of diffusion coefficient. In both models, when the diffusion coefficient was reduced by half and quarter, there was reduction in conduction velocity (Figures 4.1(a) and 4.1(b)). The original diffusion coefficient (0.001171 cm2/ms) explained in the respective paper for the TP06 (ten Tusscher & Panfilov 2006) and 4-variable model (Bueno-Orovio et al. 2008) was used. Since similar behaviour was observed in both models, it is fair to compare them.

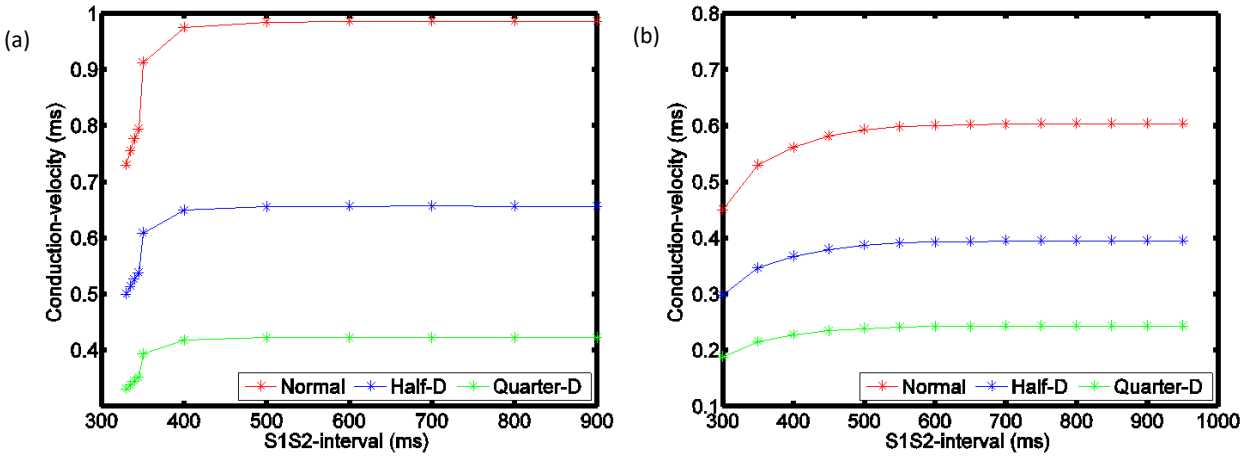

Figure 4.1 (a) Conduction velocity restitution in 4-variable model; (b) Conduction velocity restitution in TP06 model.

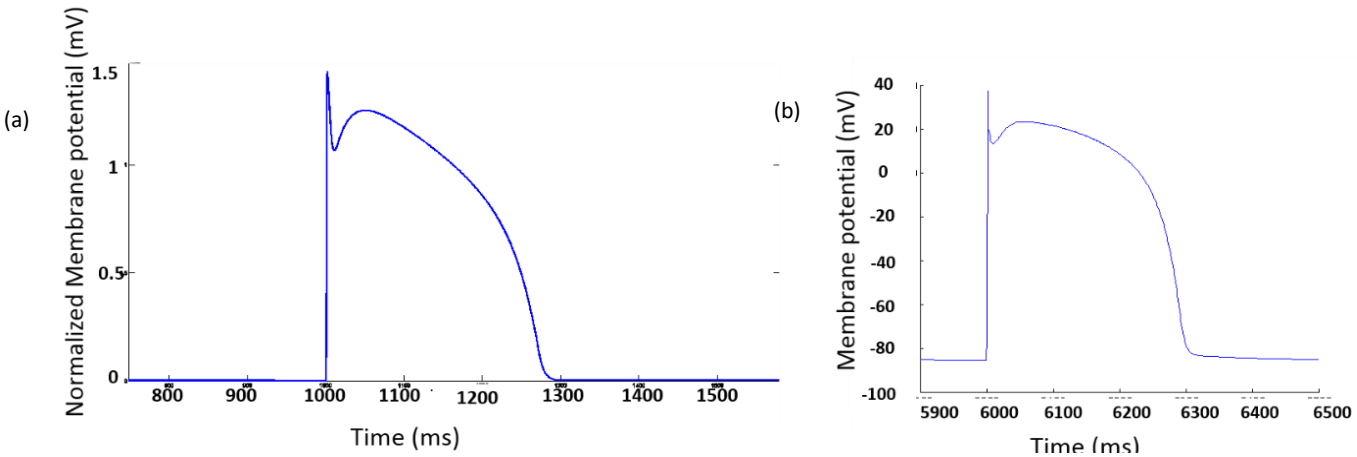

Figure 4.2 Comparing action potentials (AP) between 4-variable model and TP06 model. (a) AP in 4-variable model; (b) AP in TP06 model.

Figure 4.2 shows AP of both the 4-variable and TP06 model. Despite using normalized membrane potential, AP was similar at around 300ms, providing further support for fair comparison of both models.

Three variants of the TP06 model were used with different restitution curves. Parameters G_{Ks}, G_{Kr}, G_{pca}, G_{Pk} and tau_f were altered to get shallow and steeper restitution curves adapting the original paper (ten Tusscher & Panfilov 2006). Increasing the maximum conductances G_{Ks}, G_{Kr}, G_{pca}, G_{Pk} increases the magnitude of currents Iks, Ikr, Ipca and Ipk respectively. These are responsible for the plateau phase (phase 2) of the AP, and so in turn increase APD. Tau_f is time constant for slow voltage dependent inactivation gate responsible for decay of extracellular calcium current. To get steeper and shallow restitution curves tau_f was multiplied by a factor to rescale inactivation as shown in Table 4.1. In Param4 variant of the TP06 model, when the parameter tau_f was multiplied by 2, it produced steeper APDR (see Table 4.2).

Table 4.1 below shows the original and 3 variants of the TP06 model. The variant with shallow restitution curve is called 'Param1'. Variants with steeper restitution are called 'Param3' and 'Param4'.

Model Variants	G_{Ks}	G_{Kr}	G_{Pk}	G_{pca}	Tau_f
Normal	0.392	0.153	0.0146	0.1238	Normal
Param1	0.270	0.134	0.0730	0.0619	× 0.6
Param3	0.441	0.172	0.0073	0.3714	× 1.5
Param4	0.441	0.172	0.0029	0.8666	× 2

Table 4.1 Parameter sets for TP06 model variants (ten Tusscher & Panfilov 2006).

Two variants of the 4-variable model were used in this thesis: epiMod1 with shallow restitution; and epiMod2 with comparatively steeper restitution. Parameter sets used for epiMod1 and epiMod2 are explained in section 3.2.1.5.

To check which variants of both models should be compared, 2D simulations were run on a sheet of 400 by 400 domain. Figure 4.3 shows the APDR of two models and its variants. Table 4.2 shows the slope of restitution curves for both the TP06 model and variants and the 4-variable model and variants.

From Table 4.2, the 4-variable model epiMod1 with TP06 param1 and 4-variable model epiMod2 with TP06 param4 can be compared since the APDR curve slope is comparable.

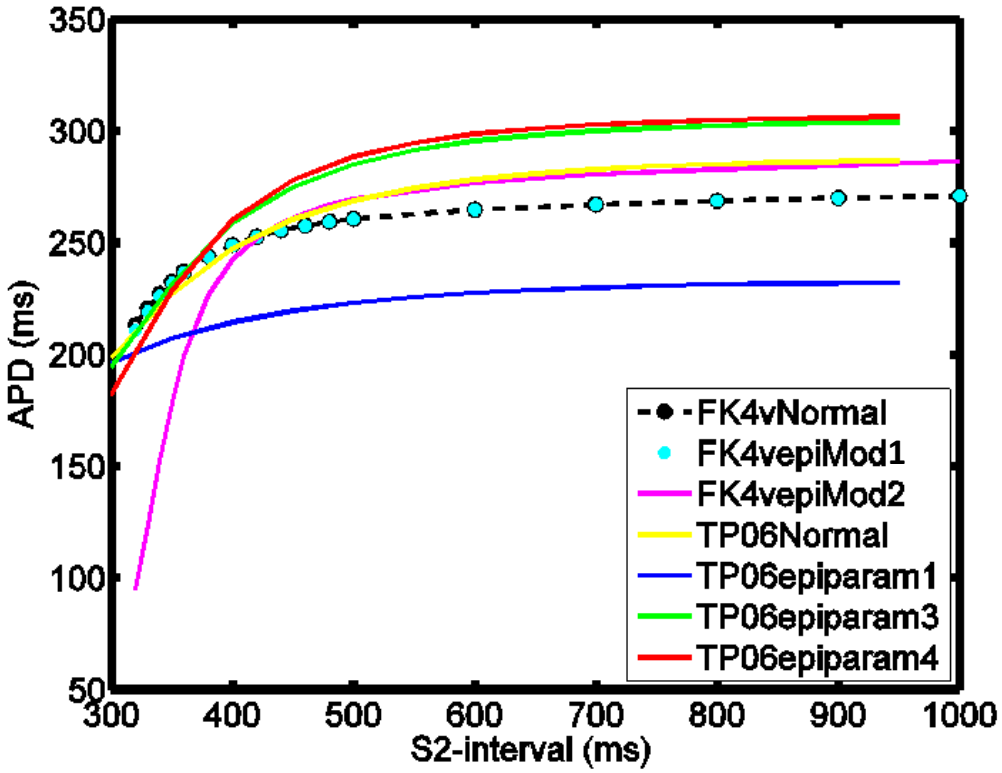

Figure 4.3 Comparing APDR in 4-variable model (FK4v) and TP06 model and their variants.

Model Variants	Slope
TP06- Normal	1.1
TP06-Param1	0.7
TP06-Param3	1.4
TP06-Parm4	1.8
4-variable model Normal	0.76
4-variable model epiMod1	0.8
4-variable model epiMod2	2.9

Table 4.2 slope of TP06 model and variants and 4-variable model and variants.

4.2.2 Modelling Ring Filament and Topological Cylinder

A topological cylinder (Figure 4.4 (b)) was modelled by replacing no-flux boundary conditions with periodic boundary conditions (Figure 4.4 (a)) in two opposite sides of the slab as explained in Fenton et al. (2002). Instead of using a single untwisted transmural filament as an initial condition, a scroll ring was used. This section explains how this was done. Both periodic boundary and scroll ring are changed in the solver (SCAM).

Periodic Boundary

Normally, for each grid point, the code in the solver assigns 26 neighbours. To achieve a periodic boundary condition, the no-flux neighbours of the grid points on the edge of one side of the slab were assigned to the opposite side as shown in Figure 4.4.

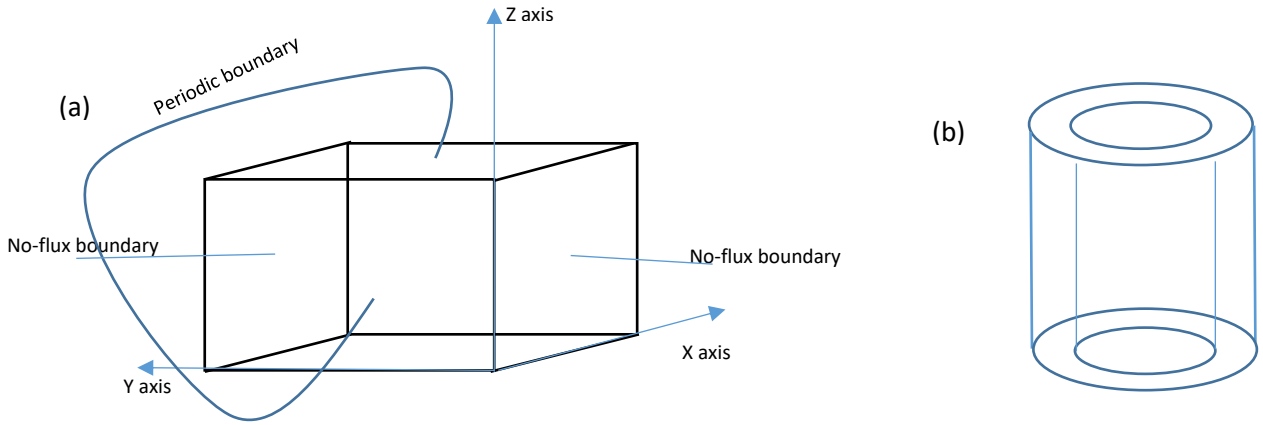

Figure 4.4 Schematic figure showing (a) periodic boundary applied to 3D slab; (b) 3D slab virtually becomes a topological cylinder after applying periodic boundary.

Ring Filament

In the solver (SCAM), the code used to initialise single untwisted transmural filaments using Archimedean spiral was modified to get ring filaments. First, the maximum dimension of a rotating rectangle was calculated by finding the hypotenuse of number of rows and number of columns. From this hypotenuse, the maximum trajectory of spiral was calculated. Polar angle θ was incremented from 0^0 to 360^0 with small increment dθ, and the corresponding Cartesian coordinates (fx, fy, fz) were calculated using the trigonometry function. This Archimedean spiral was repeated in 360 degrees as a circle, so the core of each Archimedean spiral makes a circle forming a ring filament as shown in Figure 4.5.

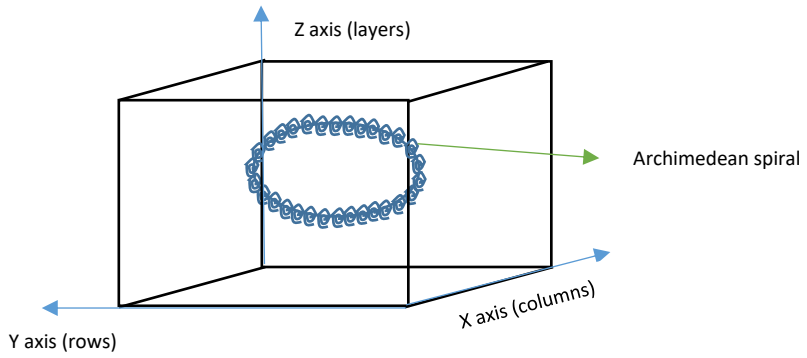

Figure 4.5 Schematic figure showing ring filament modelled using Archimedean spirals along a circle.

Since the input data for the Archimedean spiral were obtained as a result of rapid pacing using the S1S2 protocol, the scroll ring did not propagate in the tissue. Tissue size may be insufficient for scroll wave propagation, so the diffusion coefficient across the tissue was reduced by one fourth to increase tissue size for progation of scroll wave. For the comparison to be fair between transmural and ring filaments as initial condition, a similar reduced diffusion coefficient across the tissue simulation was run on the straight transmural filament in 3D slab geometry.

4.2.3 Modelling Sharp and Smooth Transmural Heterogeneity in the Slab Geometry

In the solver (SCAM), the code that reads the geometry and assigns a cell type to each grid point in each layer was changed to obtain transmural heterogeneity. The rationale for assigning transmural heterogeneity was taken from Glukhov et al. (2010) as shown in Figure 2.12. This experimental study showed the dispersion of APD transmurally in a healthy human heart. In total, the transmural distance was around 12mm. For sharper distribution of endo - epi heterogeneity, layers 1- 20 (4 mm) were assigned endo cells and layers 21-60 (8 mm) were assigned epi cells as shown in Figure 4.7. For sharper distribution of endo - M - epi heterogeneity, layers 1- 20 (4 mm) were assigned endo cells, 21-25 (1 mm) were assigned M cells and 26-60 (7 mm) were assigned epi cells as shown in Figure 4.8. To model a smooth transition of all types from endo to epi, a Hill function (y) was used.

$$y(x) = \frac{b}{1 + \left({}^{x}/_{k}\right)^{n}} \tag{4.1}$$

In Equation 4.1, n is the Hill coefficient that is a steepness parameter, k is the binding constant and b is constant basal rate. The term x is the target layer (transmural distance) in the geometry for which endo or epi needs to be assigned. Figure 4.6 shows x plotted against Hill function y(x) for n= -0.1 and –0.25. It is only possible to model endo-epi distribution when k=1 and b=1 as shown in Figure 4.6, since other values of k and b yielded flat lines. Therefore, the constants k and b are assumed as one; then the Hill function will be as shown in Equation 4.2:

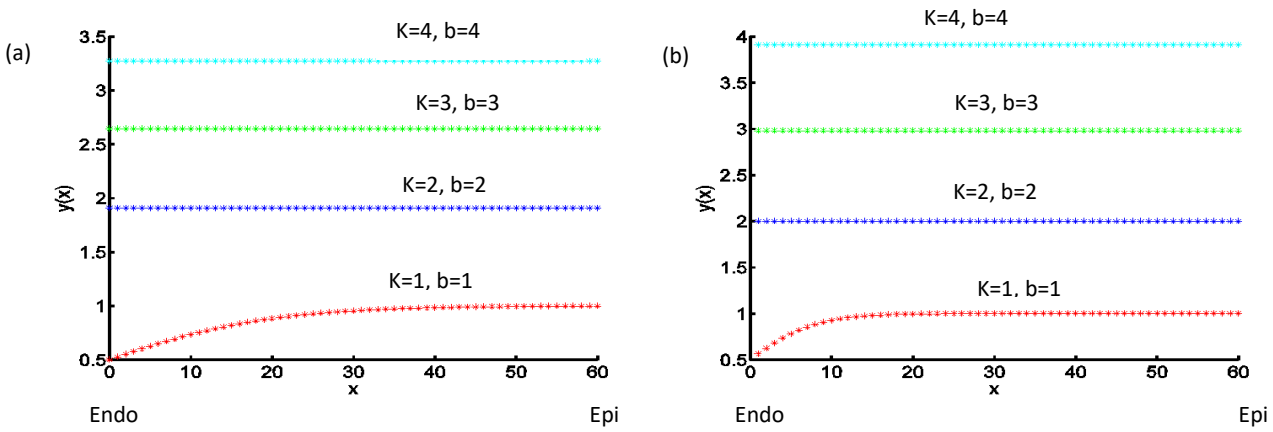

Figure 4.6 showing graphs obtained using Hill function with varied 'k' and 'b', (a) for Hill coefficient n=-0.1; (b) for Hill coefficient n=-0.25. Both figures show that apart from when k=1 and b=1, the curve is flat.

$$y(x) = \frac{1}{1 + x^n} \tag{4.2}$$

Cells were assigned endo or epi probabilistically using the Hill function. Two variants of smooth endo-epi profile were used varying Hill coefficient (n). By substituting n=-0.1, comparatively flatter distribution was obtained as shown in Figure 4.9 (b). Having n=-0.25 resulted in comparatively steeper distribution of endo-epi cells as shown in Figure 4.9 (a). Negative Hill coefficient shows it is used in a repressor function.

The Hill function was used to model smooth distribution of endo - M - epi cells. This time, both activator and repressor functions were used: activator function for modelling epi cells; and repressor to model endo cells. Activator Hill function is shown below by assuming b and k as one.

$$y(x) = \frac{x^n}{1 + x^n} \tag{4.3}$$

The Hill coefficient (n) was set to 0.99. A negative Hill coefficient resulted in a repressor Hill function (Equation 4.2) which was used to model endo cell distribution. A positive Hill coefficient resulted in a repressor Hill function (Equation 4.3) which was used to model epi cell distribution. To model endo cell in the repressor equation, the target layer (transmural distance) x was shifted right to accommodate M cells. Cells were assigned endo or M probabilistically using both activator and repressor Hill functions. Figure 4.9 (c) shows the smooth transition of endo - M - epi in the slab geometry and the dashed line shows the sharp transition of endo-M- epi.

To model islands of M cells in a 3-layer heterogeneous tissue that has 4mm thickness of endocardial layer and 7 mm thickness of epicardial layer, four circular patches of M cells, each having 1mm thickness with a radius of 1cm were placed in the centre of each quadrant of the slab as shown in Figure 4.10 to mimic the effect of M patch shown in Figure 2.12 (Glukhov et al. 2010), (Lin & Scott 2012).

.

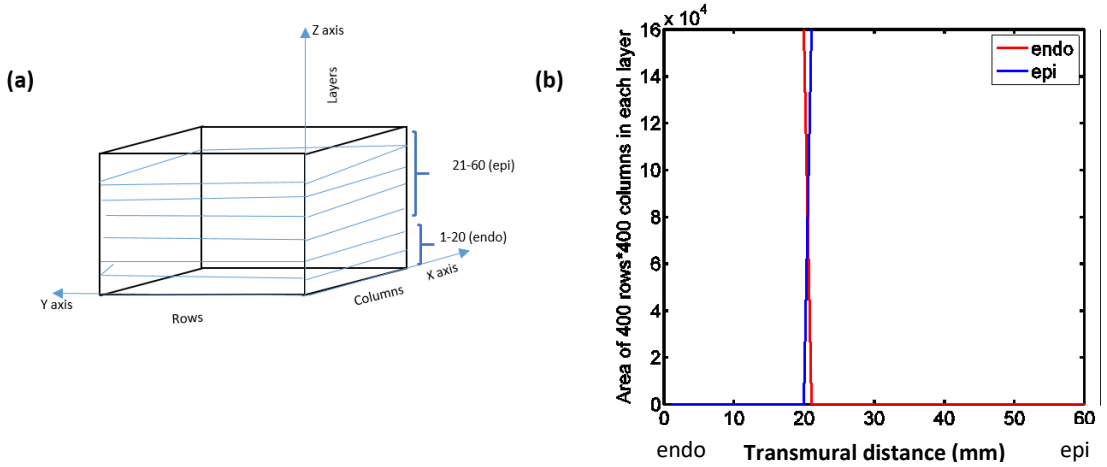

Figure 4.7 (a)Schematic representation of sharp distribution of endo-epi cells along the layers in a 3D slab (layer 1-20 endo cells and layer 21-60 epi cells); (b) View of sharp distribution of endo-epi cells inside a 3D slab

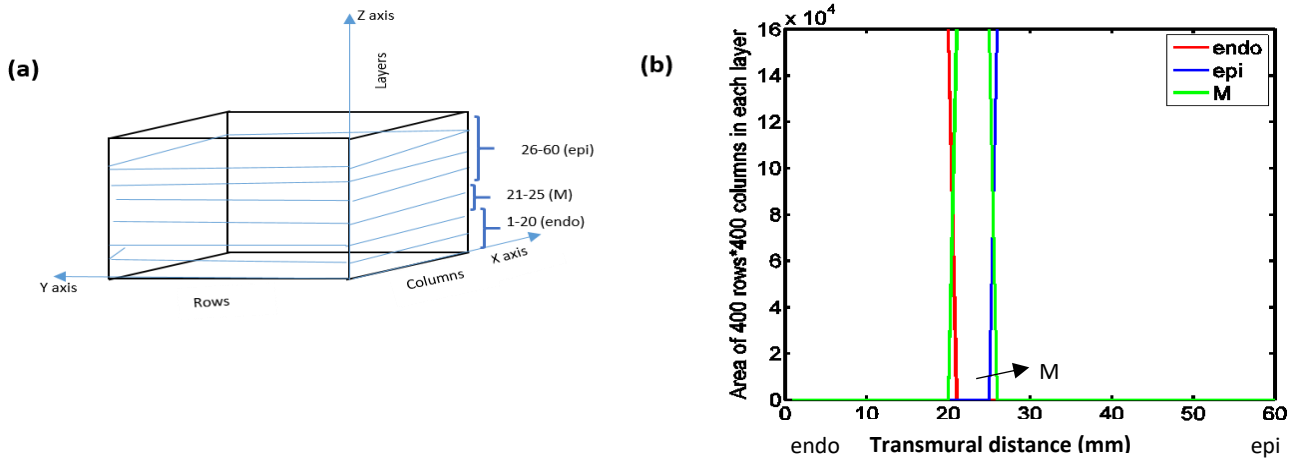

Figure 4.8 (a) Schematic representation of sharp distribution of endo-M-epi cells along the layers in a 3D slab (layer 1-20 endo cells , layer 21-25 M cells and layer 26-60 epi cells); (b) View of sharp distribution of endo-epi cells inside a 3D slab.

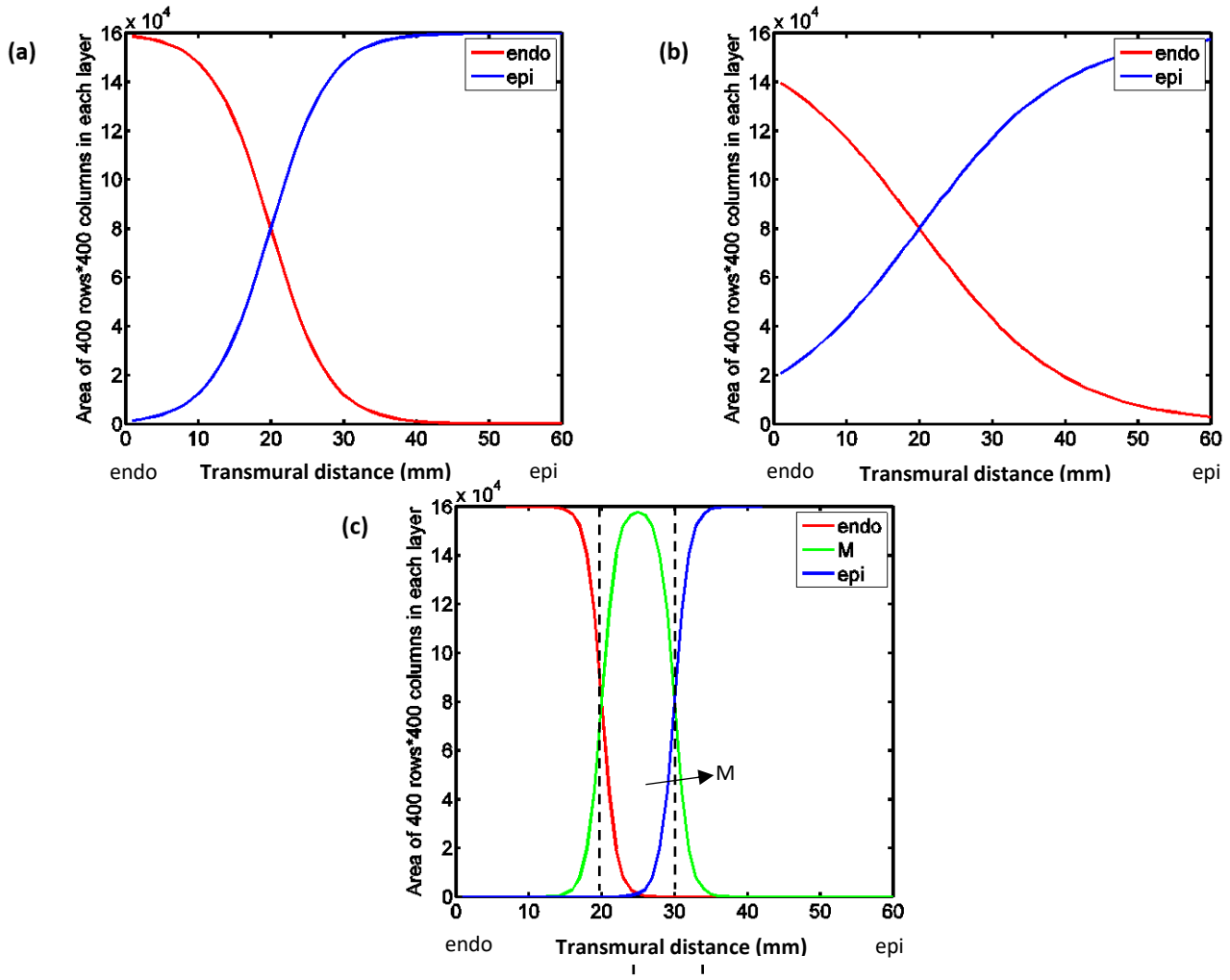

Figure 4.9 (a) and (b) view of smooth distribution of endo-epi cells inside a 3D slab; X axis represents layers, (b) used n=-0.1 and has flatter distribution compared to (a) which used n=-0.25; (c) View of smooth distribution of endo-M-epi cell inside a 3D slab; black dashed lines show sharp distribution.

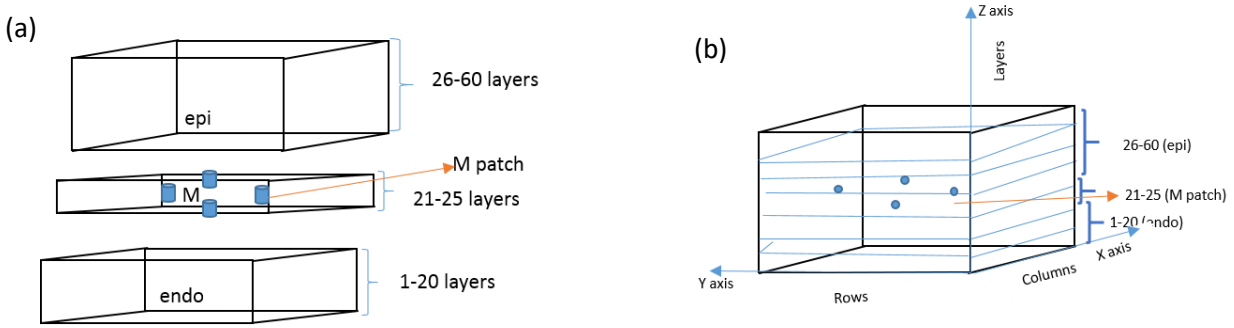

Figure 4.10 Schematic representation of M - patch in a 3D slab.

4.2.4 Modelling the Effect of Perturbations of Activation Pattern during VF in Slab and idealized LV

Cherry et al. (2012) studied the non-linear nature of cardiac tissue in 2D by perturbing the S1S2 protocol and showed the huge effect on the stability of spiral waves. Small differences in S1S2 are equivalent to perturbing the initial filament as shown in Qu et al. (2000a).

Each simulation was run 5 times and in each run. The first simulation was run without perturbing initial membrane voltage. For the next four simulations, the initial membrane voltage at each node was perturbed by adding a small random value between ± 0.05 which is equivalent to about ± 5 mV (Qu et al. 2000b), thus enabling a small change in the input for every simulation. Random value was drawn from uniform distribution (not normal distribution).

In the SCAM code, a function called “srand ()” was used to set the seed value for the random generator function “rand ()”. The seed value of the srand function depends on the time (seconds) the code is compiled. This was to generate different initial voltage values for each perturbation.

4.3 Results

4.3.1 Simplified and Biophysically Detailed Cell Model

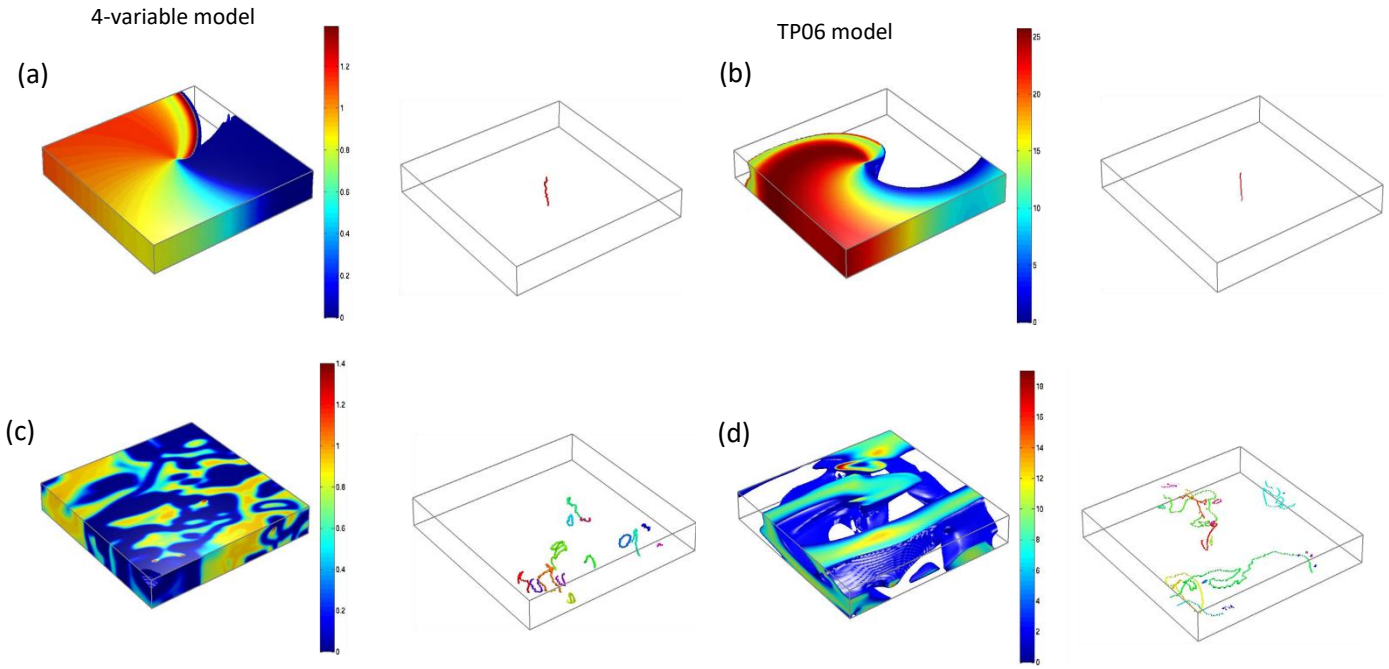

Figure 4.11 Snapshots of re-entry and corresponding filaments in (a) and (c) for 4-variable epiMod2 model at 10ms and 1880ms respectively; (b) and (d) for TP06 param4 model at 10ms and 1880ms respectively.

Figure 4.11 (a), (b) shows snapshots of initial re-entry and the corresponding filament in the TP06 (param4) and 4-variable (epiMod2) models and (c), (d) at 1880ms. TP06 model initial re-entry broke at around 40ms and 80 ms in variants param3 and param1 respectively. In the 4-variable model, initial re-entry broke at around 114 ms and 110 ms in epiMod1 and epiMod2 respectively.

The average number of filaments (± standard deviation) in uniform slab geometry from 1-2 s was 2.4 ± 1.3 for 4-variable model epiMod1, 10.8 ± 6.1 for 4-variable model epiMod2, 1.7 ± 0.8 for TP06 param1 and 6.3 ± 3.2 for TP06 param4. The scroll wave rotation period in 4-variable model epiMod2 was 207 ms and 272 ms for TP06 Param4 model. These numbers should correspond approximately to the activation interval observed during VF. During VF, activation interval is minimum, since minimum APD of 4-variable epiMod2 is smaller compared to TP06 param4 (Figure 4.3), scroll wave rotation

period is reasonable. Table 3.2 shows that 4-variable epiMod2 has steeper APDR compared to TP06 param4. As explained in Garfinkel et al. (2000) and Qu et al. (2000a), steeper APDR produces conduction block and wave break. This may explain the observation of more filaments in the 4-variable epiMod2 compared to the TP06 param4 model.

Number of filaments can be used to quantify the complexity of VF in 3D and number of PS in 2D. Figure 4.12 (a) and (b) shows a small difference in number of filaments at the end of the simulation, but a big difference in the computation time. Similar results were observed with number of PS using both models (Figure 4.12 (c)). Table 4.3 gives some examples of the computation time for simulations with the 4-variable and TP06 models.

Geometry	**Model**	**Computation time**
3D slab geometry (uniform epi)	4-variable model	7 hours and 11 minutes
	TP06 model	22 hours and 52 minutes

Table 4.3 comparing computation time used using the 4-variable and TP06 models using ICEBERG cluster.

Configuration and volume of filaments (Figure 4.12 (d) and (e)) in both simplified (4-variable) and biophysically detailed (TP06) models did not show important differences. Filaments tend to change shape when they interact with tissue heterogeneity (Henze et al. 1990, Vinson et al. 1994); since no tissue heterogeneity is incorporated in the tissue model, this result may be insignificant. The 4-variable and TP06 models gave similar results. The simplified 4-variable model is computationally inexpensive compared to the TP06 model. Since this thesis tests the effect of overall behaviour of activation pattern during VF and does not concentrate on a single ion channel, using the simplified 4-variable model for this thesis is justified.

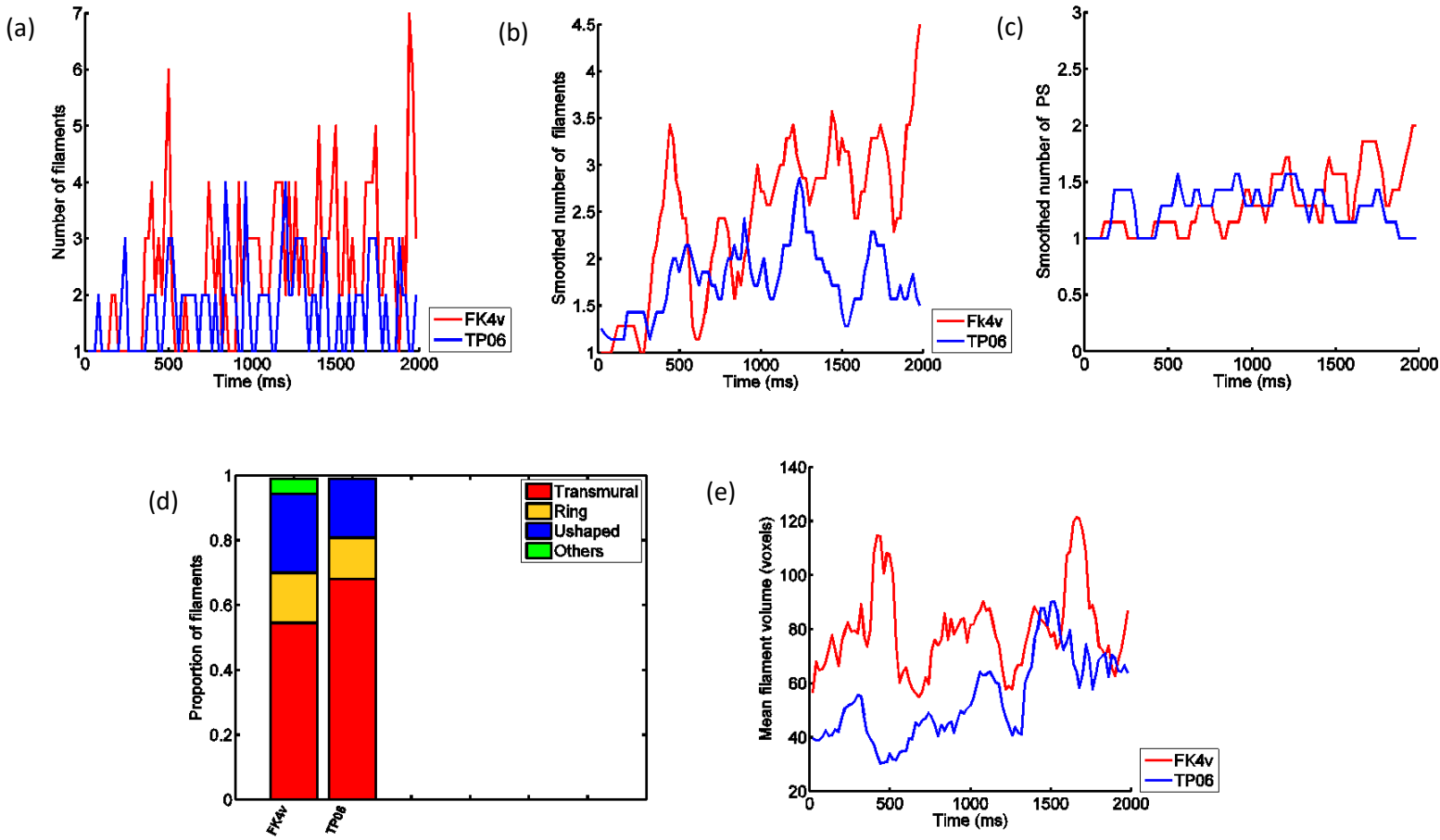

Figure 4.12 (a) Change in number of filaments over time (ms) epiMod1 of 4-variable model and param1 of TP06 dynamics respectively; (b) Smoothed view of change in number of filaments in epiMod1 of 4-variable model and param1 of TP06 dynamics respectively; (c) Change PS over time in epiMod1 of 4-variable model and param1 of TP06 dynamics respectively; (d) Configuration of filaments in epiMod1 of 4-variable model and param1 of TP06 dynamics respectively; (e) Change in mean volume of filaments in epiMod1 of 4-variable model and param1 of TP06 dynamics respectively.

4.3.2 Influence of Shape of Initial Re-entrant Filament on Filament Dynamics

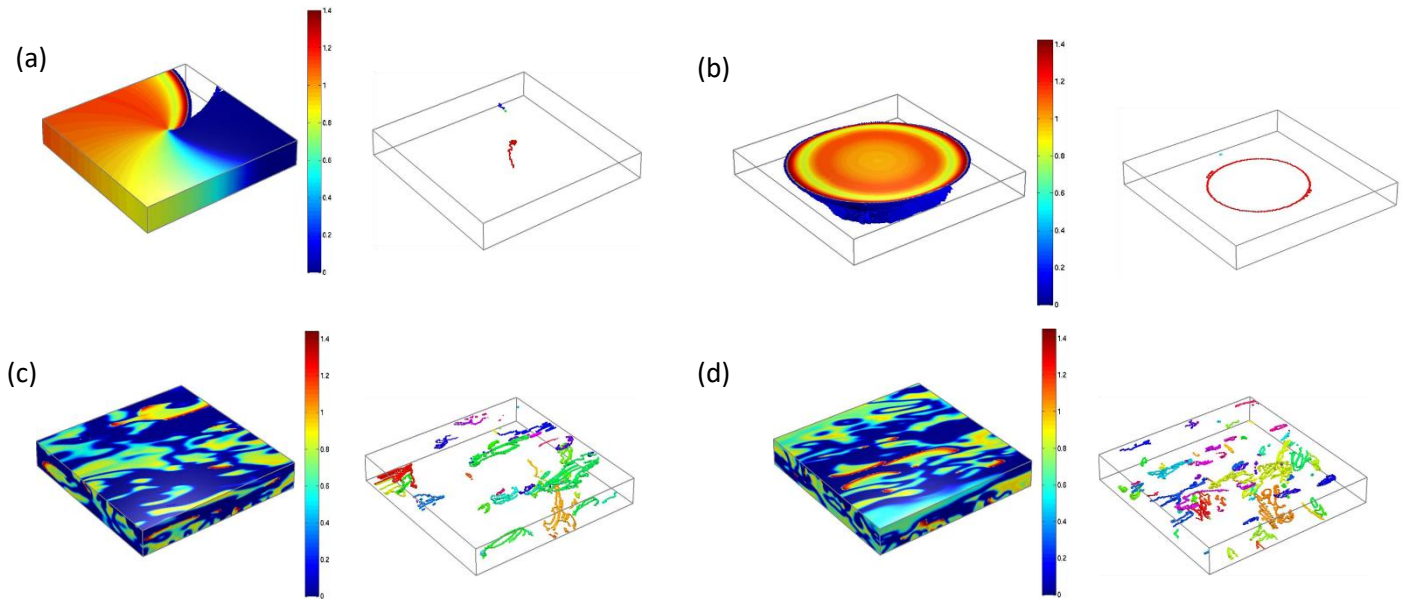

Figure 4.13 Snapshots of re-entry and corresponding filaments in (a) Initial straight filament in 3D slab (b) Ring filament in topological cylinder; (c) and (d) show re-entrant waves and corresponding filaments in 3D slab and topological cylinder at 1990 ms respectively.

When ring filament was used as an initial condition, with epiMod1 dynamics re-entry did not sustain for long. Figure 4.13 shows snapshots of re-entrant waves and corresponding filaments using straight filament and ring filament as an initial condition with epiMod2 dynamics. Initial re-entrant waves broke immediately in both cases. The average number of filaments (± standard deviation) with transmural filament as initial condition from 1-2 s was 46.3 ± 27.1 and for ring filament as initial condition from 1-2 s was 56.4 ± 26.8.

Results (Figure 4.14) show that the number of filaments, volume and the configuration of filaments are similar with both ring filaments and transmural filaments used as initial condition. The lifetime of initial filament and the lifetime of long lived filament are the same in both simulations. Using either ring or transmural filament as initial condition gave similar results. Since modelling straight transmural filament is simple and straightforward this result justifies the use of simple straight transmural filament in this thesis.

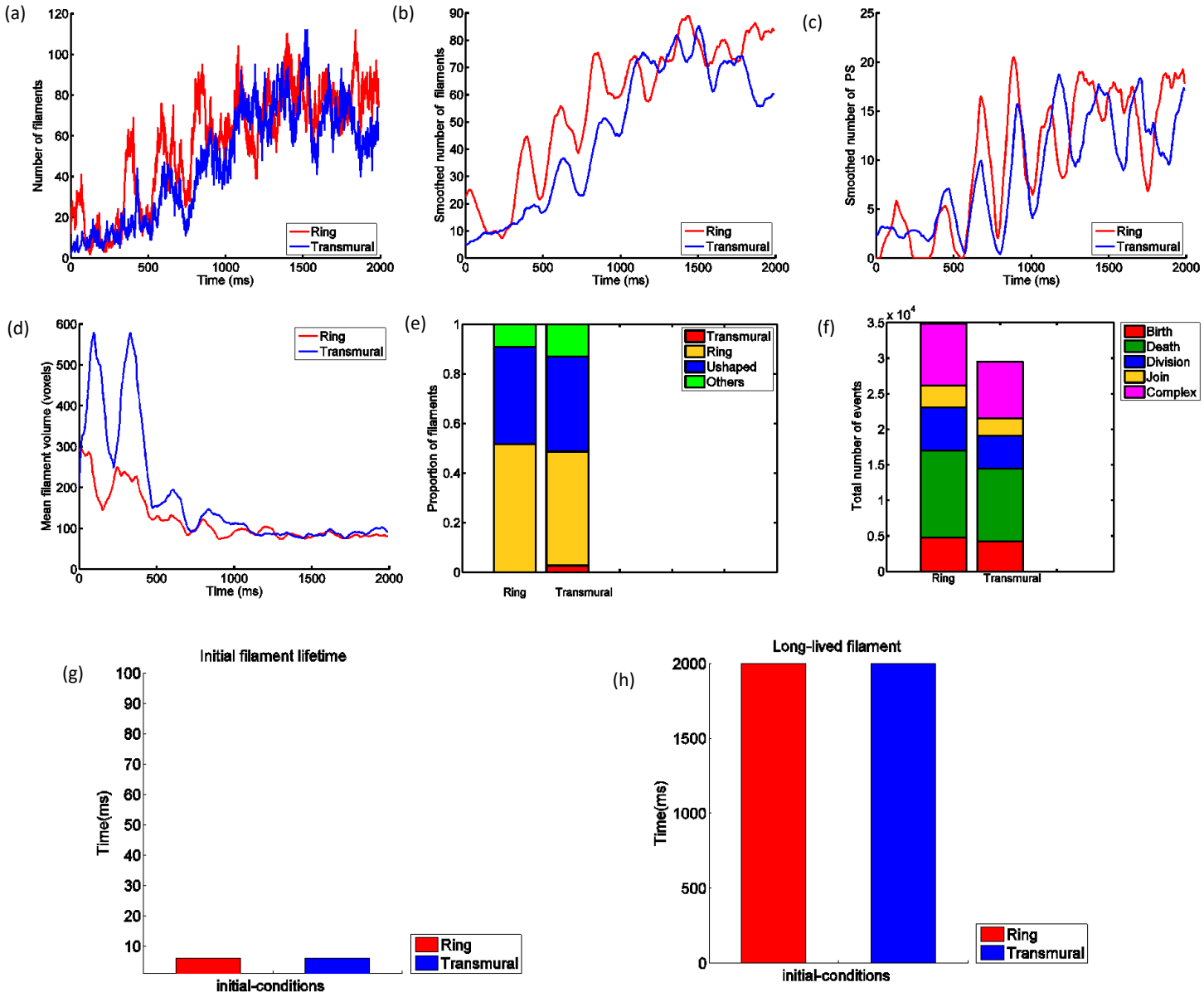

Figure 4.14 (a) Change in number of filaments; (b) smooth number of filaments; (c) Change in number of PS; (d) Change in mean volume of filaments; (e) Configuration of filaments; (f) Number of events; (g) initial filament lifetime; (h) Long lived filaments. Red showing ring filament and Blue showing straight transmural filament as initial condition.

4.3.3 Effect of Sharp and Smooth Transition of Transmural Heterogeneity

4.3.3.1 Uniform Slab

Figure 4.15 shows APD, APDR and conduction velocity restitution in epi, endo and M cells of the 4-variable model embedded in 2D tissue.

The APD of uniform M tissue (450 ms) is larger compared to the other cell types and the APD of uniform endo tissue (280 ms) is shortest.

Since APDR is almost the same in both original epi cells and epiMod1 dynamics as shown in Figure 4.3, epi cells are not included in Figure 4.15. APDR for uniform M tissue is steeper and for endo, it is flatter. Uniform epiMod2 tissue has comparatively sharper APDR than epiMod1 uniform tissue.

Minimum APD in restitution curve with epiMod2 dynamics was minimum compared to other variants of the 4-variable model as shown in Figure 4.15 (b). During VF, activation interval is minimum (minimum DI), so the epi cells in the tissue with transmural heterogeneity with epiMod2 dynamics will still be active while endo and M cells have recovered. Since each variant of cell has different minimum APD, it will be important to see if the transmural heterogeneity affects filament dynamics.

Before finding the influence of sharp and smooth transmural heterogeneity on filament dynamics, filament dynamic behaviour in uniform tissue of epi, endo and M cells in the slab geometry was examined. Results (Figure 4.16) show uniform tissue of epiMod2 dynamics has a higher number of filaments compared to others and a greater number of 'U' shaped filaments. The average number of filaments (± standard deviation) in uniform tissue from 1-2 s was 3.1 ± 1.2 for epiMod1 tissue, 13.8 ± 4.7 for epiMod2 tissue, 1.5 ± 1.4 for endocardial tissue and 1.9 ± 1.0 for M tissue. Scroll wave cycle length for the 4-variable model integrated in the slab model with epi cells was 292 ms; for endo, cycle length was 268.57; for M, it was 312 ms; for epiMod1, it was 292 ms; and for epiMod2 variant, it was 207 ms.

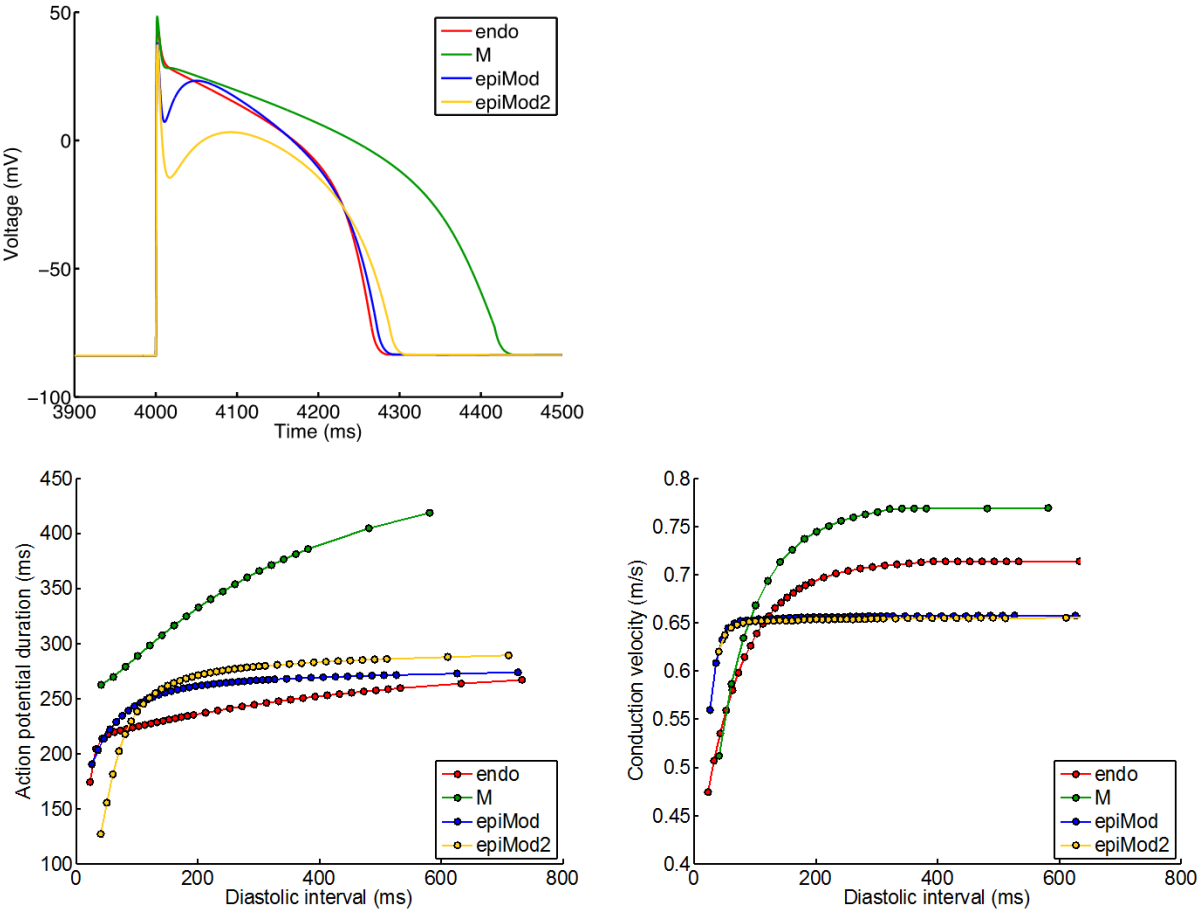

Figure 4.15 shows comparison in uniform tissue of endo, M, epiMod1 and epiMod2 (a) APD; (b APDR; (c) CVR in uniform tissue. In this figure, epiMod shows results for epiMod1.

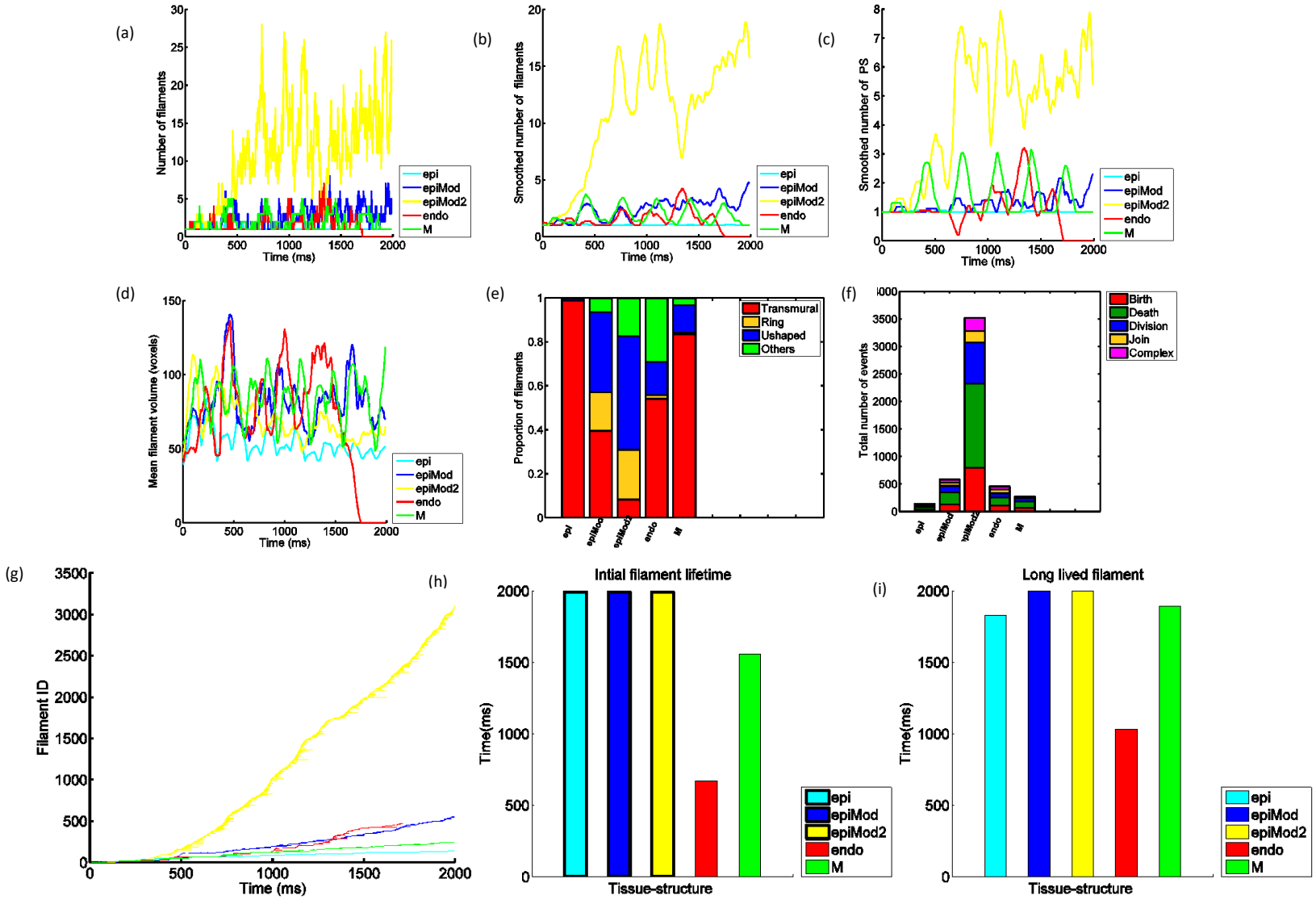

Figure 4.16 Comparing filament dynamics in uniform tissue (a) Change in filaments over time; (b) smooth view of change in number of filaments; (c) change in smooth number of PS over time; (d) change in mean volume of filaments over time; (e) configuration of filaments; (f) number of events; (g) lifetime of filaments; (g) initial filament lifetime BLACK border shows initial filament gene sustained even after 1990ms; (i) long lived filaments In this figure, epiMod shows results for epiMod1. In graphs (e) and (f) the order of results are epi, epiMod1, epiMod2, endo, M.

4.3.3.2.1 Sharp Vs Smooth (endo - epi)

Figure 4.17 (a) shows the distribution of epi cells in sharp and smooth endo - epi distributions. Figure 4.17 (b) shows change in APD with transmural distance for sharp and smooth endo - epi distribution in slab geometry. This Figure shows APD is minimum in endo region and maximum in epi region, which agrees with individual uniform tissue Figure 4.15. The black dotted line around 4mm in Figure 4.17 (b) shows the endo - epi border. This figure shows APD has a similar value in both edges of endo and epi, even though it has different values inside the endo-epi heterogeneous tissue. This might be because of cancelation of gradient in APD transmurally, termed electrotonic effect in Taggart et al. (2003) and Colli Franzone et al. (2006). The smoother the distribution, the minimum and the maximum APD are reduced as shown in Figure 4.15 (b). This figure also shows there is little difference in APD for both smooth and sharp distribution of endo - epi.

In an experimental study, Massé et al. (2007) explained that the fictitious centrifugal force around the rotating system forces it to the border of slow conduction velocity since conduction block occurs at the slow conducting border. Figure 4.15 (c) shows that endo has minimum conduction velocity compared to epiMod1 and epiMod2. So this was tested in sharper and smoother endo - epi profile, and the result shows clustering of filaments in the border of the endo region (Figure 4.17 (c) and (d)). This Figure also showed clustering of filaments to the endo - epi varies in smooth and sharp distribution of endo - epi according to the distribution of endo-epi as shown in Figure 4.17(a). The epiMod2 dynamics have more clustering of filaments compared to epiMod1 dynamics.

The number of filaments, volume of filaments, and configuration of filaments did not show any important difference with both epiMod1 and epiMod2 dynamics in sharp and smooth distributions as shown in Figure 4.19.

4.3.3.2.2 Sharp Vs Smooth (endo - M - epi)

Figure 4.18 (a) shows how epi cells are distributed in sharp and smooth endo - M- epi. As shown in Figure 4.15 (a), M cells have longer APD compared to endo and epi. Figure 4.18 (b) shows APD in smooth and sharp distribution of endo - M- epi profile in epiMod1 dynamics and shows that near the M region, the APD is maximum. The green dotted line around 4mm-5mm in Figure 4.18 (b) shows the endo - M - epi border. This figure shows APD has similar values in both edges of endo and epi, even though it has different values inside the endo -M- epi heterogeneous tissue. This might be because of cancelation of gradient in APD transmurally, called electrotonic effect and explained in Taggart et al. (2003) and Colli et al. (2006). More clustering of filaments is observed in endo - M border and M- epi border (Figure 4.18 (c)) since minimum conduction velocity of endo is less than M and minimum conduction velocity of M is less than epi. This clustering of filaments matches the distribution of epi cells in sharp and smooth endo - M - epi profile. Number and configuration of filaments did not show

any important difference in both smooth and sharp distribution of endo - M - epi cells as shown in Figure 4.20.

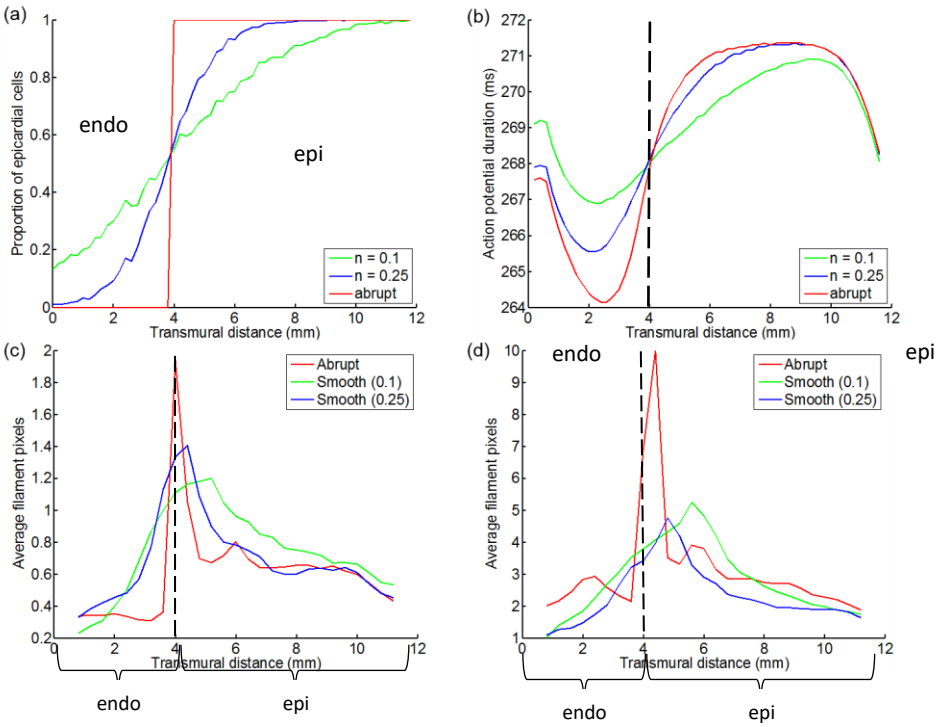

Figure 4.17 Comparing smooth and sharp distribution of endo-epi cells (a) proportion of epicardial cell; (b) APD profile in epiMod1, dashed black lines are added to show endo-epi border (c) and (d) Clustering of filaments to transmural heterogeneity in epiMod1 and epiMod2 dynamics

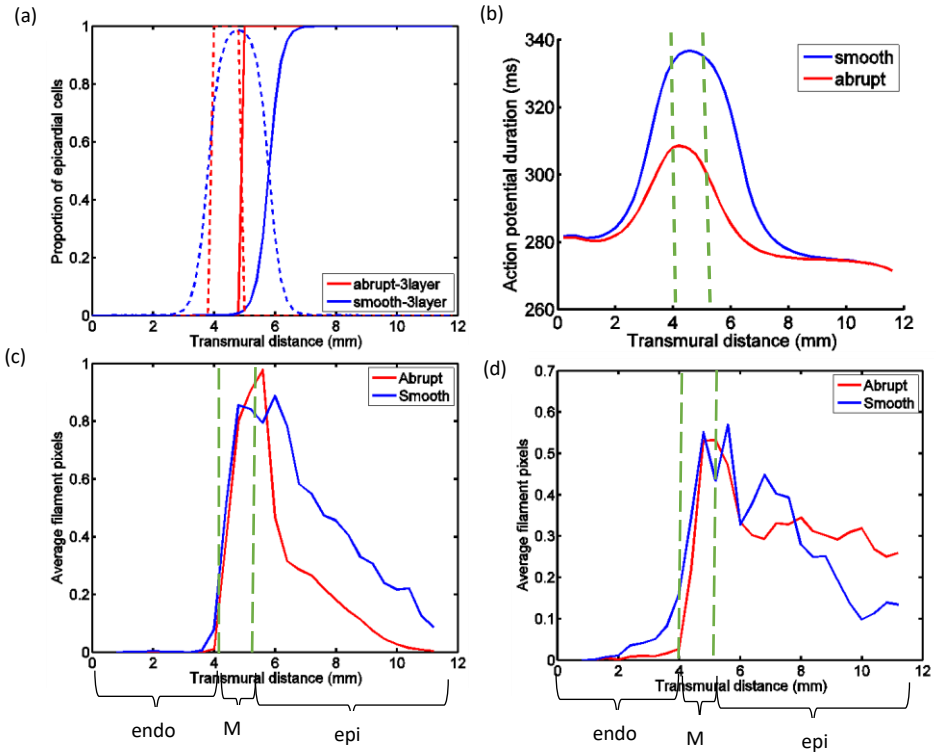

Figure 4.18 Comparing smooth and sharp distribution of endo-M-epi cells: (a) proportion of epicardial cells, dotted lines show distribution of M cells (blue and red dotted lines show smooth and sharp distribution); (b) APD profile in epiMod1; (c) and (d) clustering of filaments to transmural heterogeneity in epiMod1 and epiMod2 dynamics. Dashed green lines are added to show endo-M, M-epi border. Clustering of filament voxels is greater near endo-M and M-epi border.

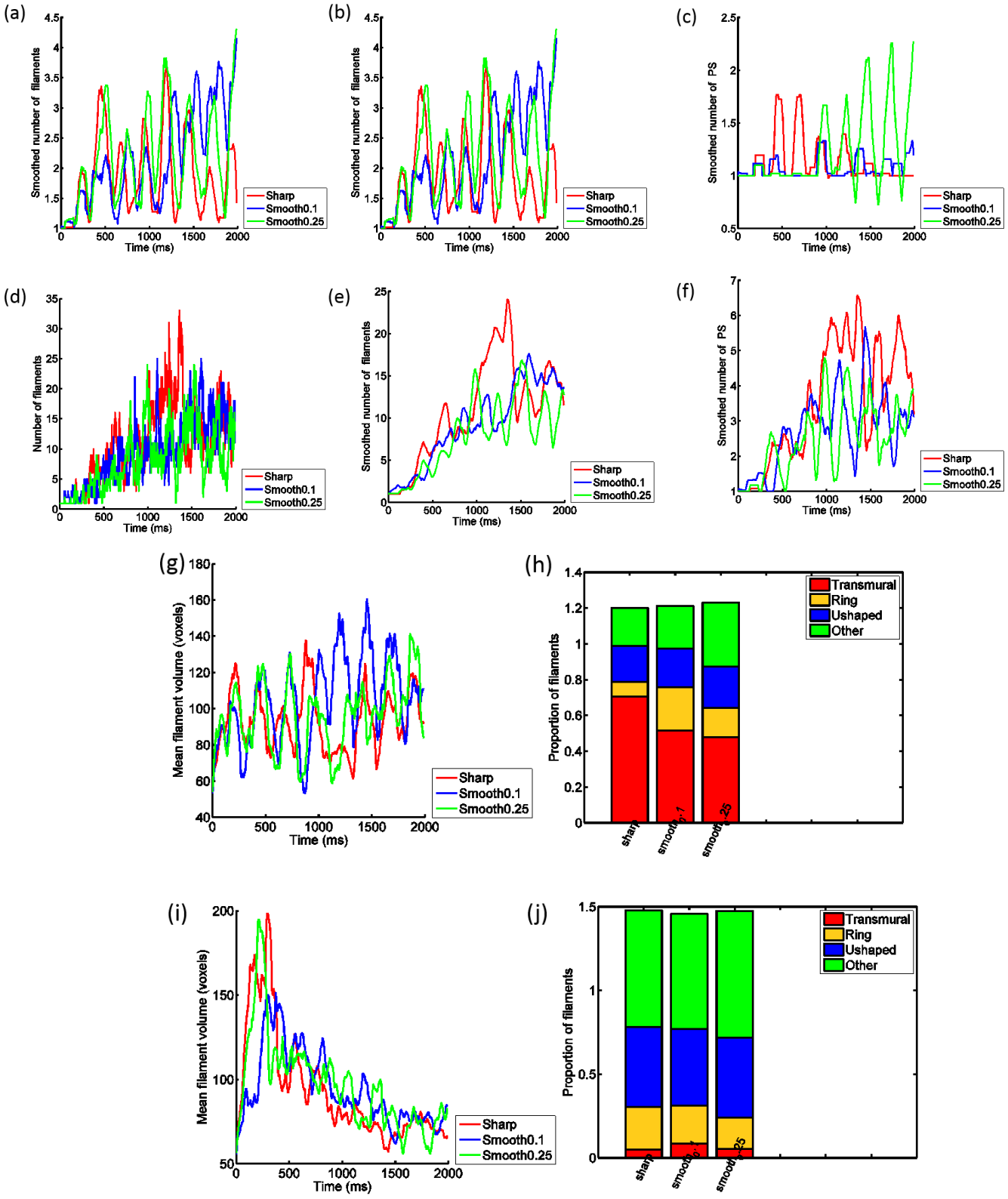

Figure 4.19 Comparing filament dynamics in sharp and smooth distribution of endo-epi tissue in epiMod1 and epiMod2 dynamics: (a) change in filaments over time in epiMod1; (b) smooth view of change in number of filaments in epiMod1; (c) change in smooth number of PS over time in epiMod1; (d) change in filaments over time in epiMod2; (e) smooth view of change in number of filaments in epiMod2; (f) change in smooth number of PS over time in epiMod2; (g) change in mean volume of filaments over time in epiMod1; (h) configuration of filaments in epiMod1; (i) change in mean volume of filaments over time in epiMod2; (j) configuration of filaments in epiMod2. Results in graph (h) and (j) are in the order of sharp, smooth0.1 and smooth0.25.

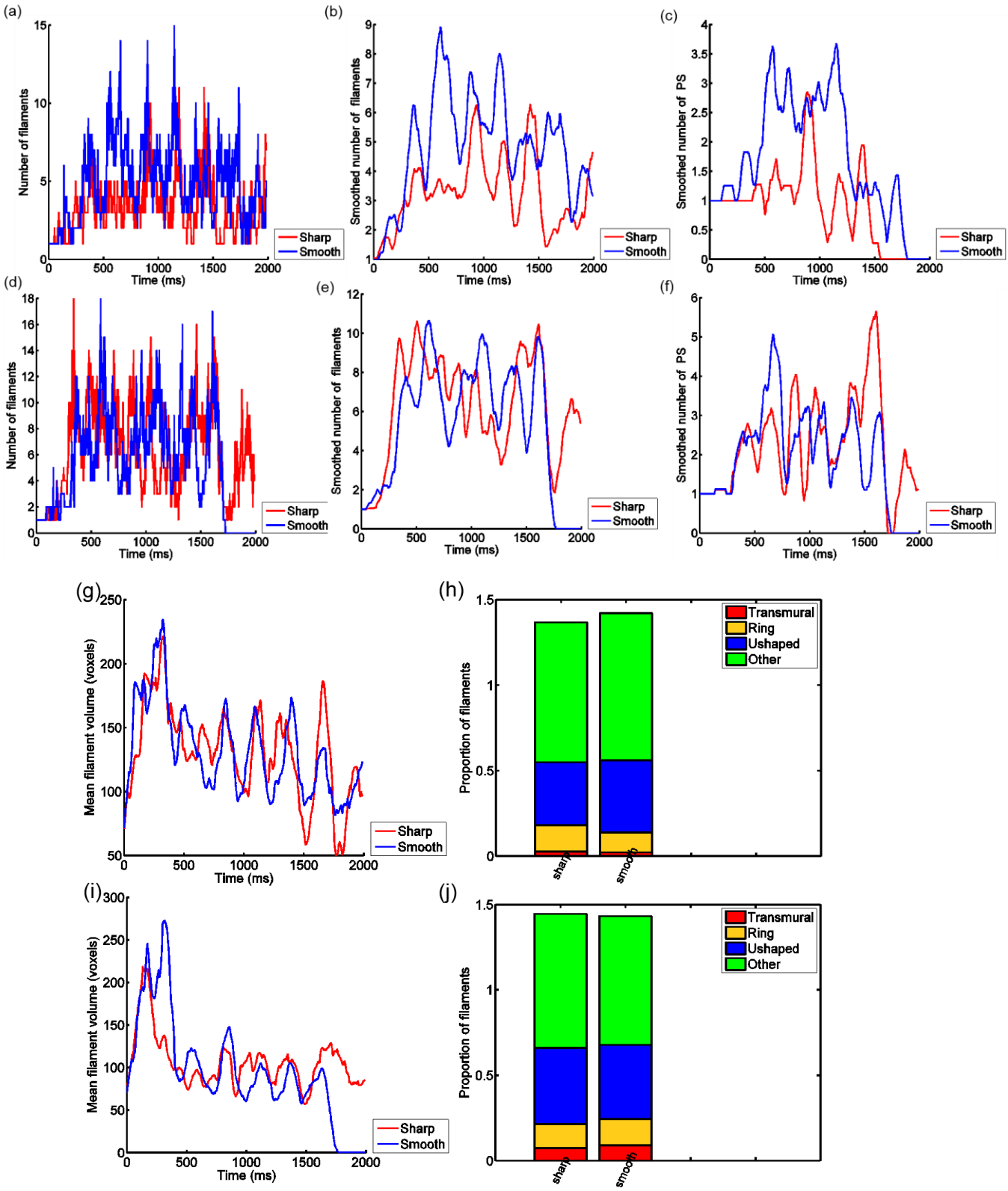

Figure 4.20 Comparing filament dynamics in sharp and smooth distribution of endo-M-epi tissue in epiMod1 and epiMod2: (a) change in filaments over time in epiMod1; (b) smooth view of change in number of filaments in epiMod1; (c) change in smooth number of PS over time in epiMod1; (d) change in filaments over time in epiMod2; (e) smooth view of change in number of filaments in epiMod2; (f) change in smooth number of PS over time in epiMod2; (g) change in mean volume of filaments over time in epiMod1; (h) configuration of filaments in epiMod1; (i) change in mean volume of filaments over time in epiMod2; (j) configuration of filaments in epiMod2. Results in graph (h) and (j) are in the order of sharp and smooth of endo-M-epi distribution.

4.3.4 Effect of Transmural Heterogeneity and Perturbations in Slab Geometry

Since the smooth distribution of cells did not cause any important differences in filament dynamics, a sharp distribution of cells was used for endo - epi (2 layer) and endo - M - epi (3 layer). Clustering of filaments was examined in all uniform, 2- layer, 3 -layer and M - patch tissue as shown in figure 4.21. This shows more clustering in 3 layer with endo – M - epi profile compared to the others, with no clustering as seen in uniform tissue.

In uniform tissue, with epiMod1 dynamics (Figure 4.22 (b)), two perturbations of activation pattern during VF (P1 and P3) resulted in spontaneous termination of re-entry around 1700 ms. The number of filaments in epiMod2 dynamics was much greater than the number of filaments in epiMod1 dynamics, and the effect of perturbation to the activation pattern was seen much sooner at around 500 ms after initiation compared to around 1000 ms for epiMod1 dynamics. Figures 4.23 and 4.24 show the effect of perturbations on filament configuration, filament volume, number of PS and number of events in uniform (epi) tissue.

4.3.4.1 Number of Filaments

Simulations with epiMod2 dynamics had about three times as many filaments as simulations with epiMod1 dynamics, regardless of the type of heterogeneity present (Figure 4.25 (a) and (b)). Ten Tusscher et al. (2007) showed minimum APD of the restitution curve is responsible for larger numbers of filaments. During VF, activation interval is minimum. The epiMod2 variant of the 4-variable model had minimum APD as shown in Figure 4.15 (b). Minimum APD means shorter wavelength and shorter wavelength sustains VF by allowing the re-entrant wave to rotate faster (Fenton & Karma 1998). This perhaps explains minimum APD in epiMod2 and may be the reason for observing more filaments. Steeper restitution curve is the other reason for more filaments observed in epiMod2 dynamics (Fenton et al. 2002), since epiMod2 has steeper restitution compared to epiMod1 (Figure 4.15 (b)).

The effect of perturbations on the activation pattern was also large, especially for epiMod2 dynamics. There was some heterogeneity effect but this was small compared to the other effects, around 2-3 filaments in epiMod1 and 5-6 filaments in epiMod2 dynamics (Figure 4.25 (a) and (b)).

4.3.4.2 Volume of Filaments

Jiménez et al. (2012) showed pinning of filaments to heterogeneity can increase filament length. The 3 -layer tissue had more clustering at the endo - M border as shown (Figure 4.18) and explained above. This is confirmed in Figure 4.25 (e) and (f); the volume in 3 layer is longer compared to other heterogeneity, the next longer filaments are observed in 2-layer. However, epiMod1 dynamics showed comparatively longer filaments than epiMod2 dynamics (Figure 4.25 (e) and (f)).

4.3.4.3 Configuration of Filaments

The bar charts in Figure 4.25 (c) and (d) show corresponding filament configurations. There are two main results. First, for epiMod1 dynamics, the proportion of transmural filaments was much lower for the 3-layer geometry than for the other geometries and this effect was bigger than the effect of perturbations. This is not reflected in simulations with epiMod2 dynamics; more clustering of filament voxels to the endo - M and M - epi border in 3-layer in epiMod1 dynamics (Figure 4.21 (a)) might have caused more intramural filaments. Secondly, there is a higher proportion of transmural filaments for epiMod1 dynamics than for epiMod2 dynamics in 2-layer and patch (Figure 4.25 (c)). Both 2 –layer and patch showed more clustering of filament voxels to endo – epi and endo –Mpatch – epi border in epiMod2 dynamics compared to epiMod1 dynamics and might be the reason for more intramural filaments.

4.3.4.4 Life Time of Filaments

The cumulative and short lifetimes of filaments in all simulations are shown in Figures 4.28 and 4.29. On the X axis, 1-5 show uniform tissue and its perturbations, 6-10 show 2 layer and its perturbations, 11-15 show 3 layer and its perturbations and 16-20 show patch and its perturbations. These results show a longer cumulative lifetime in 2 layer in epiMod1 dynamics and 3 layer in epiMod2 dynamics, whereas short lifetime (Figure 4.29) was longer in uniform epi and patch. Long cumulative lifetime shows longer lived filaments. The lifetime of filaments was affected by transmural heterogeneity rather than perturbations. Filament lifetimes are increased due to pinning of filaments in endo-epi and endo-M in 2 layer and 3 layer profile respectively (Figures 4.17 and 4.18).

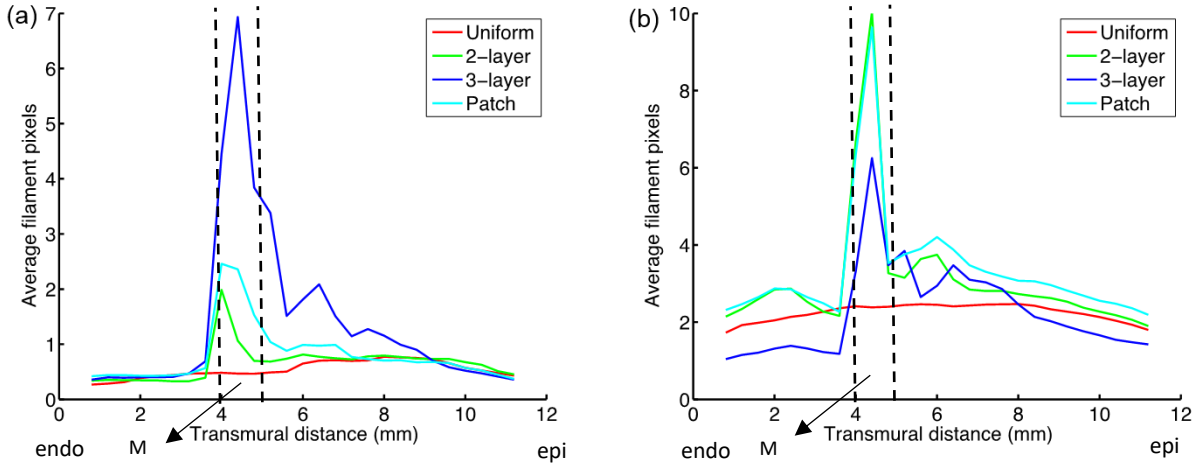

Figure 4.21 Comparing clustering of filaments in uniform, 2 layer, 3-layer and M patch: (a) in epiMod1 dynamics; (b) in epiMod2 dynamics. Black dotted lines show M region. Clustering of filament voxels is greater near endo-M and M-epi border

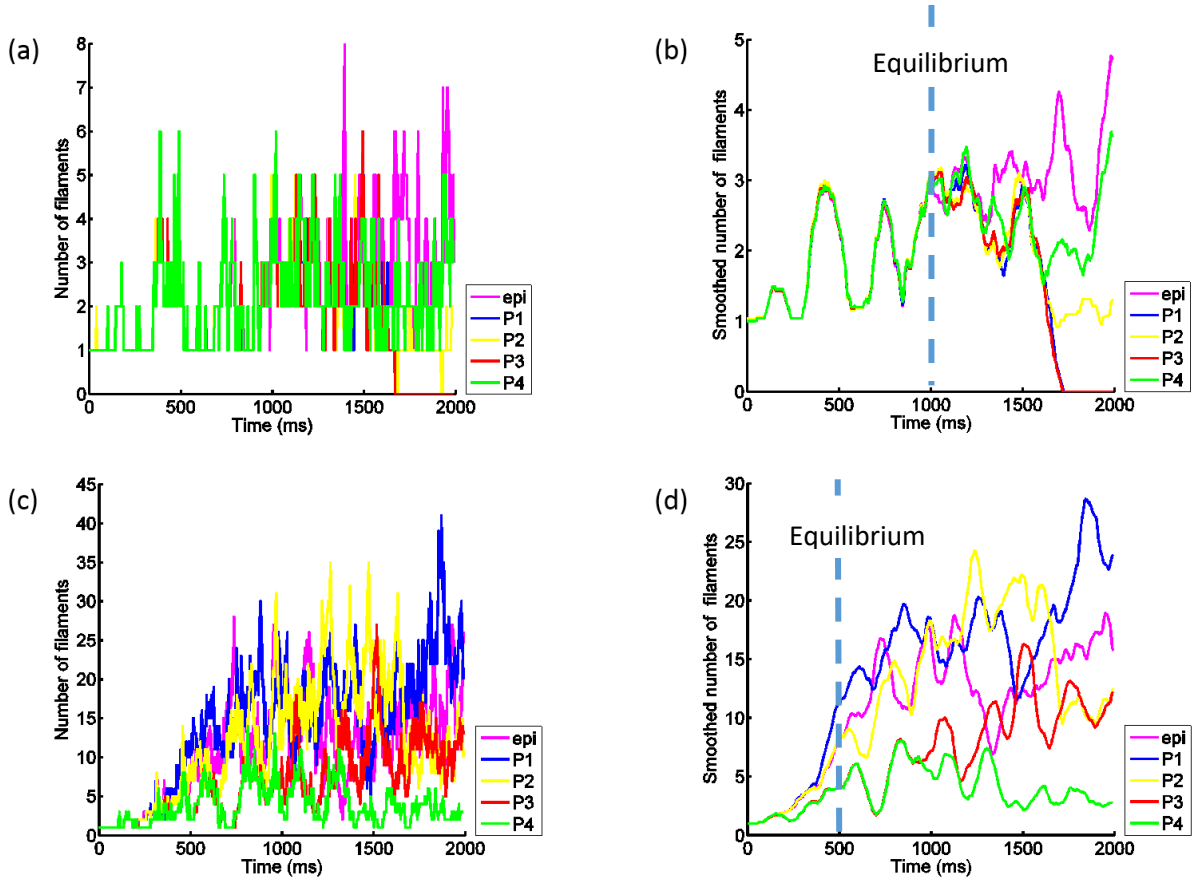

Figure 4.22 Effects of perturbations (uniform, P1, P2, P3, P4) in uniform 3D slab: (a) change in number of filaments over time (ms) in epiMod1 dynamics; (b) smooth view of change in number of filaments in epiMod1 dynamics, equilibrium reached at 1000ms in epiMod1 dynamics; (c) change in number of filaments over time (ms) in epiMod2 dynamics; (d) smooth view of change in number of filaments in epiMod2 dynamics, equilibrium reached at 500ms in epiMod2 dynamics.

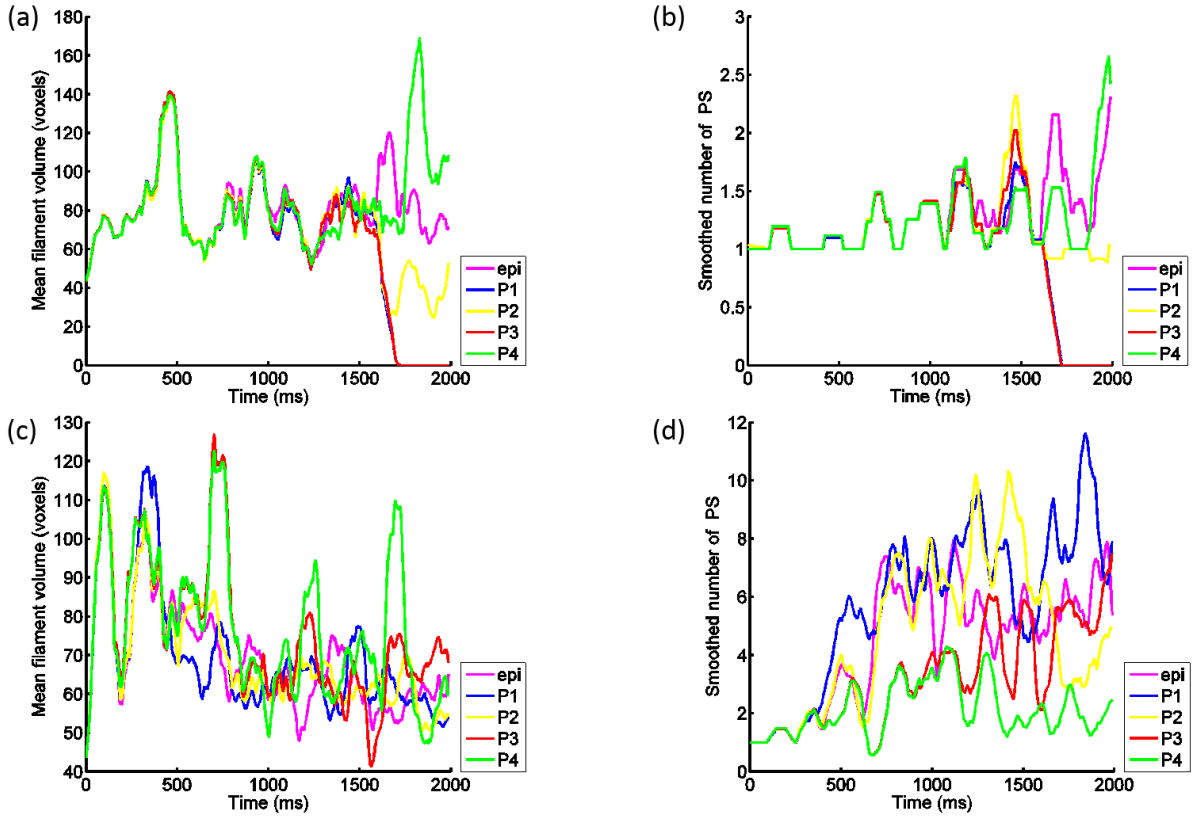

Figure 4.23 Effects of perturbations (uniform, P1, P2, P3, P4) in uniform 3D slab: (a) change in mean volume of filaments over time in epiMod1; (b) change in number of PS over time in epiMod1 dynamics; (c) change in mean volume of filaments over time in epiMod2; (d) change in number of PS over time in epiMod2 dynamics

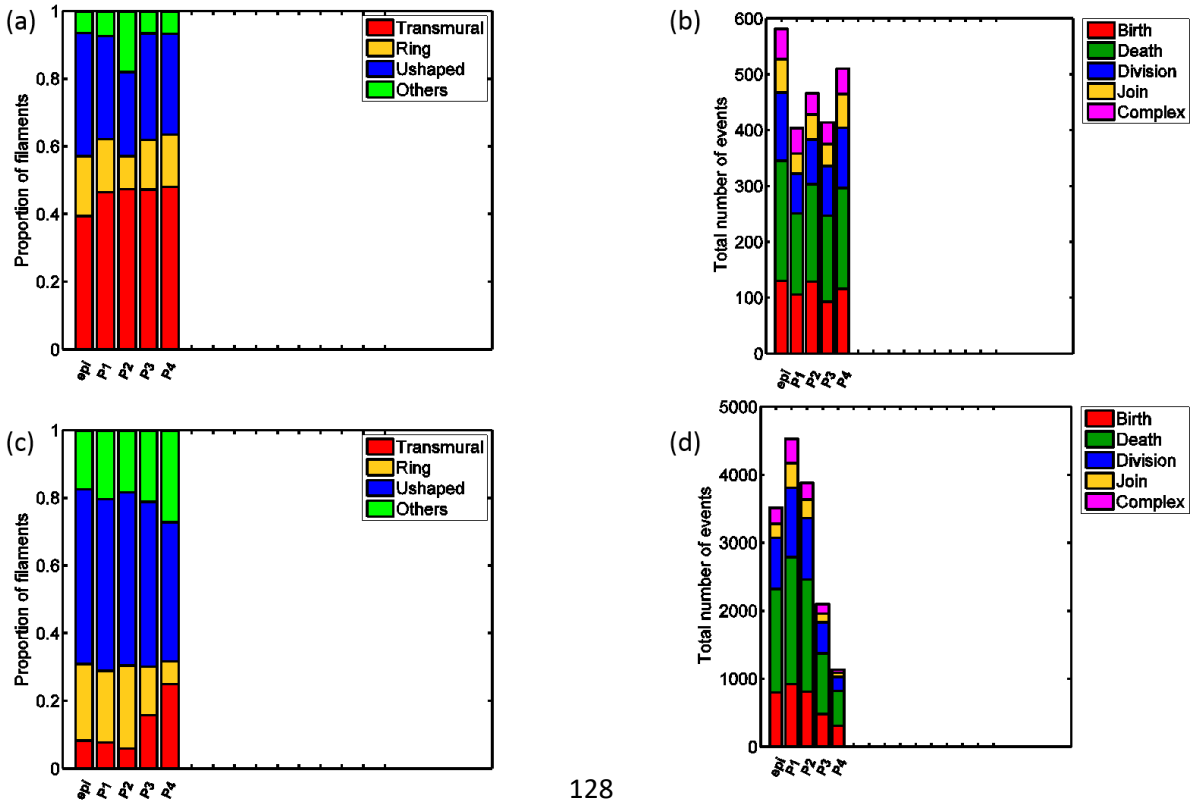

Figure 4.24 Effects of perturbations (uniform, P1, P2, P3, P4) in uniform 3D slab: (a) configuration of filaments in epiMod1 dynamics; (b) number of events in epiMod1 dynamics; (c) configuration of filaments in epiMod2 dynamics; (d) number of events in epiMod2 dynamics.

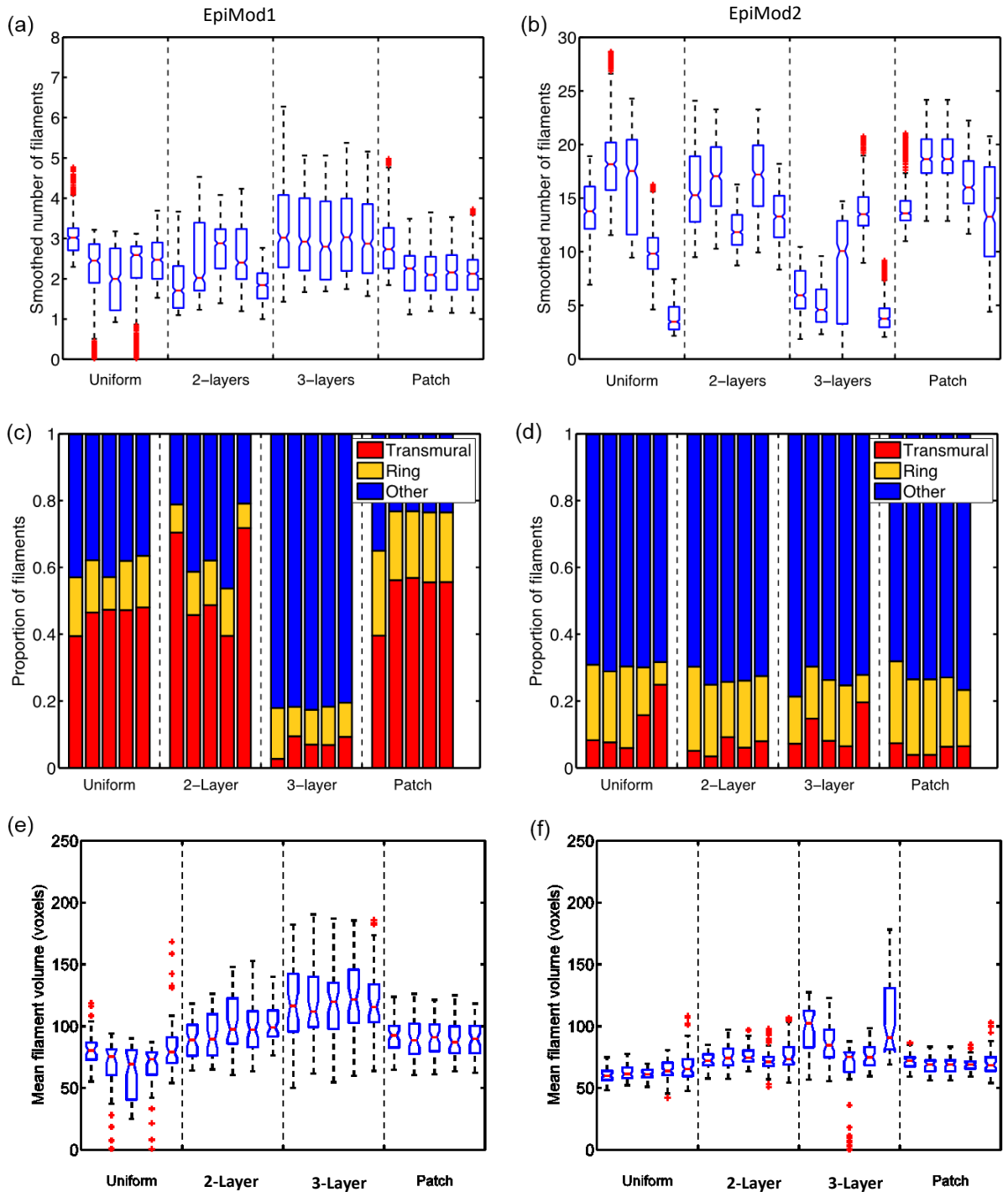

Figure 4.25 Effects of perturbations and transmural heterogeneity (3D slab) in uniform, 2-layers, 3-layer and Mpatch in both epiMod1 and epiMod2 dynamics. In all the figures the first one shows without initial filament perturbed and the second, third, fourth and fifth show the results of initial filament perturbed as P1, P2, P3 and P4; (a) and (b) boxplot of smooth view of comparing number of filaments in epiMod1 and epiMod2; (c) and (d) configuration of filaments in epiMod1 and epiMod2; (e) and (f) boxplot of mean volume of filaments in epiMod1 and epiMod2.

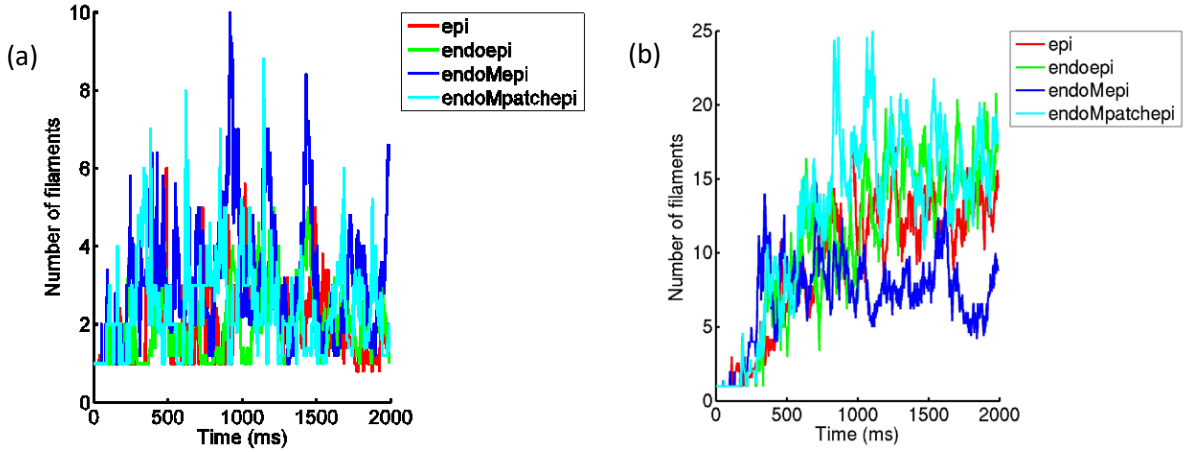

Figure 4.26 Average number of filaments of perturbations in each transmural heterogeneity in 3D slab profile: (a) in epiMod1 and (b) in epiMod2 dynamics.

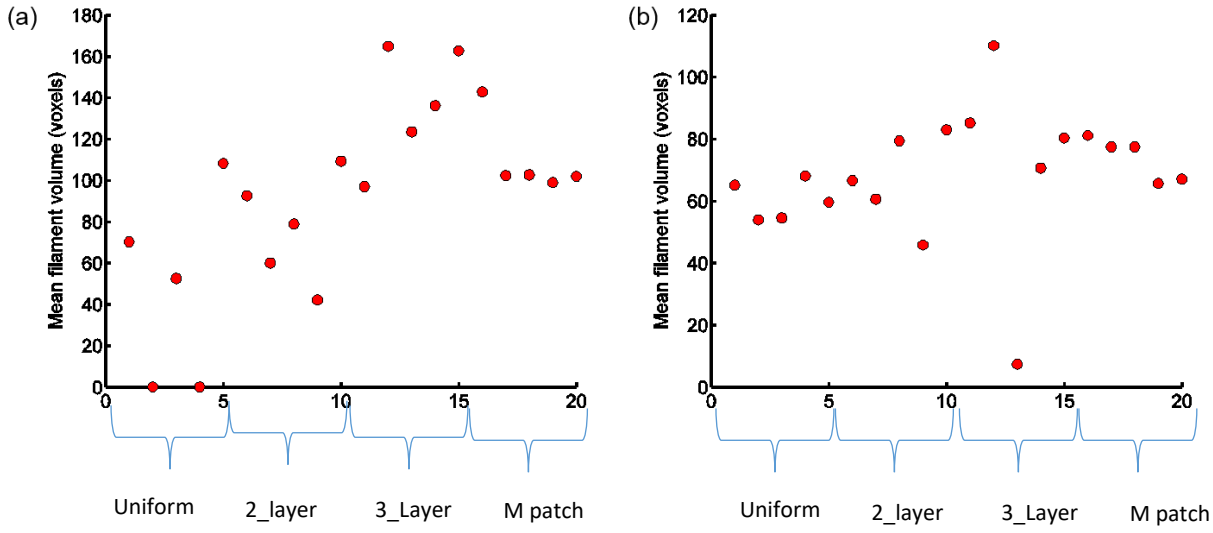

Figure 4.27 Effects of perturbations and transmural heterogeneity (3D slab) to mean filament volume in uniform, 2-layers, 3-layer and Mpatch in both epiMod1 and epiMod2 dynamics. In uniform, 2-layer, 3-layer and M patch, the first one shows result without initial filament perturbed. The second, third, fourth and fifth show the results of initial filament perturbed as P1, P2, P3 and P4 in (a) in epiMod1 and (b) in epiMod2 dynamics.

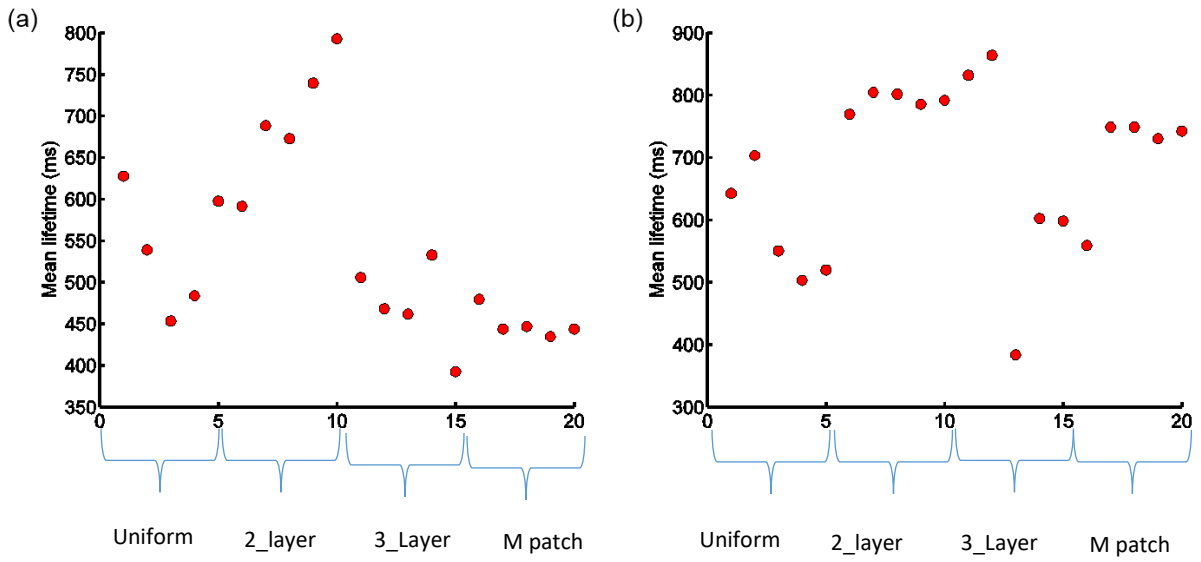

Figure 4.28 Effects of perturbations and transmural heterogeneity (3D slab) on long cumulative lifetime in uniform, 2-layer, 3-layer and Mpatch in both epiMod1 and epiMod2 dynamics. In uniform, 2-layer, 3-layer and M patch, the first one shows result without initial filament perturbed. The second, third, fourth and fifth show the results of initial filament perturbed as P1, P2, P3 and P4 in (a) in epiMod1 and (b) in epiMod2 dynamics.

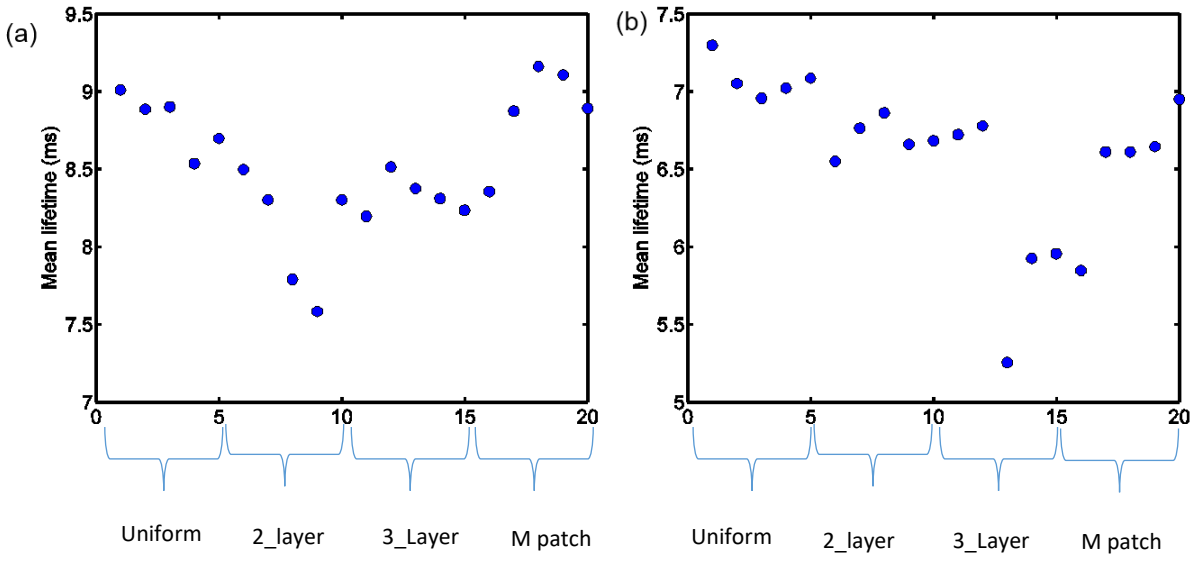

Figure 4.29 Effects of perturbations and transmural heterogeneity (3D slab) on short lifetime in uniform, 2-layer, 3-layer and Mpatch in both epiMod1 and epiMod2 dynamics. In uniform, 2-layer, 3-layer and M patch, the first one shows result without initial filament perturbed. The second, third, fourth and fifth show the results of initial filament perturbed as P1, P2, P3 and P4 in (a) in epiMod1 and (b) in epiMod2 dynamics.

4.3.5 Influence of Sharp and Curved Tissue Geometry on Filament Dynamics

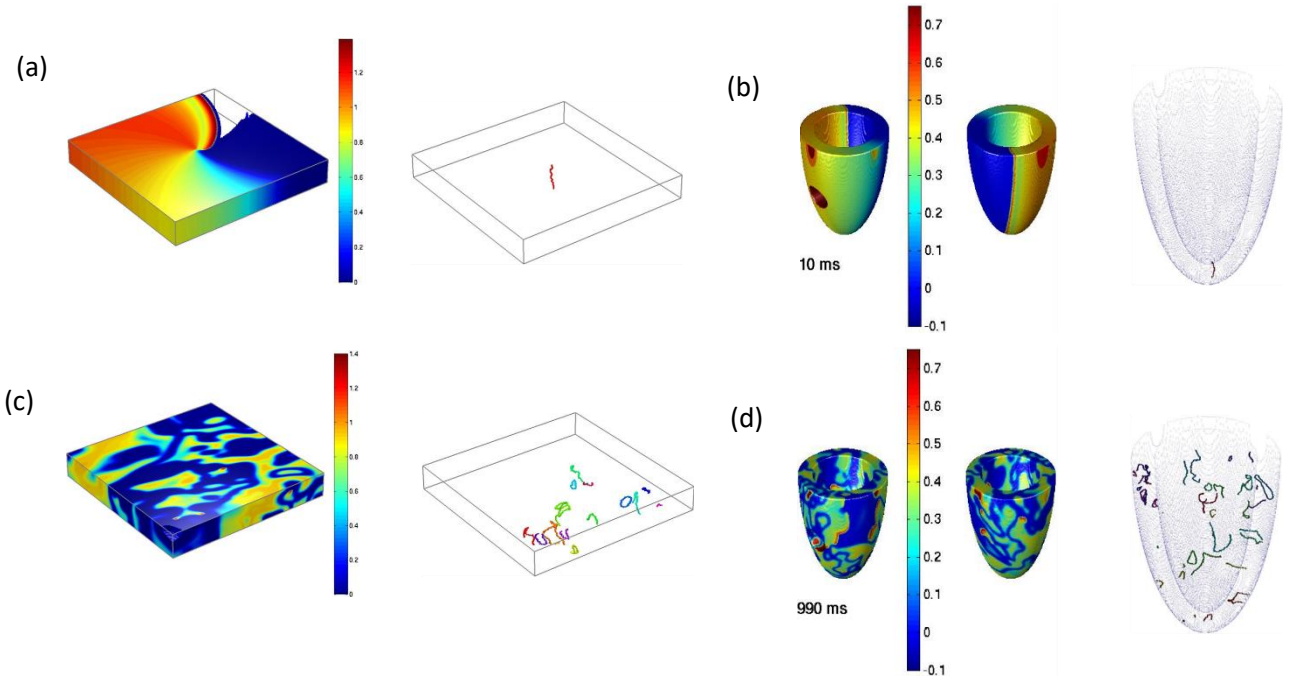

Figure 4.30 Snapshots of re-entry and corresponding filaments in: (a) initial in 3D slab; (b) initial filament in idealized LV both front and back view of re-entry; (c) and (d) show re-entrant waves and corresponding filaments in 3D slab and idealized LV at 1990 ms respectively.

Re-entry in the uniform slab and in an idealized LV with both epiMod1 and epiMod2 dynamics was unstable and the initial transmural filament fragmented almost at the same time. Snapshots in Figure 4.30 show re-entry and corresponding filaments. Slab geometry had more filaments than idealized LV in epiMod1 dynamics (Figure 4.31 (b)). However, idealized LV showed almost double the number of filaments with epiMod2 dynamics than slab geometry (Figure 4.31 (d)). The average number of filaments (± standard deviation) in slab epiMod1 dynamics was 2.4 ± 1.3, in epiMod2 dynamics it was 10.8 ± 6.1. In idealized LV, the average number of filaments (± standard deviation) was 1.7 ± 0.9 in epiMod1 dynamics and 14.9± 14.6 in epiMod2 dynamics. The volume of the idealized LV is twice (150.55 cm^3) the volume of slab geometry (76.8 cm^3) and this can be the reason for observing twice as many filaments in idealised LV in epiMod2 dynamics. In slab geometry, filaments can move away from the boundary and disappear but in idealised LV, filaments can move to the other side; this can be the other reason for observing more filaments in idealised LV.

Slab geometry had larger filaments but the number of PS observed in the idealized LV was comparatively more (Figure 4.32). More transmural filaments and a very small number of ring filaments were observed in the idealized LV; this might be the reason for observing more PS in idealised LV (Figure 4.33 (a) and (c)). The numbers of events in slab and idealized LV were similar with only a few more in epiMod2 dynamics for idealized LV (Figure 4.33 (b) and (d)). Initial filament gene

lived beyond 1990ms in slab geometry, while in idealized LV, it lived for only around 200 ms (Figure 4.34 (a) and (c)). The longest lived filament was seen in slab geometry (Figure 4.34 (b) and (d)).

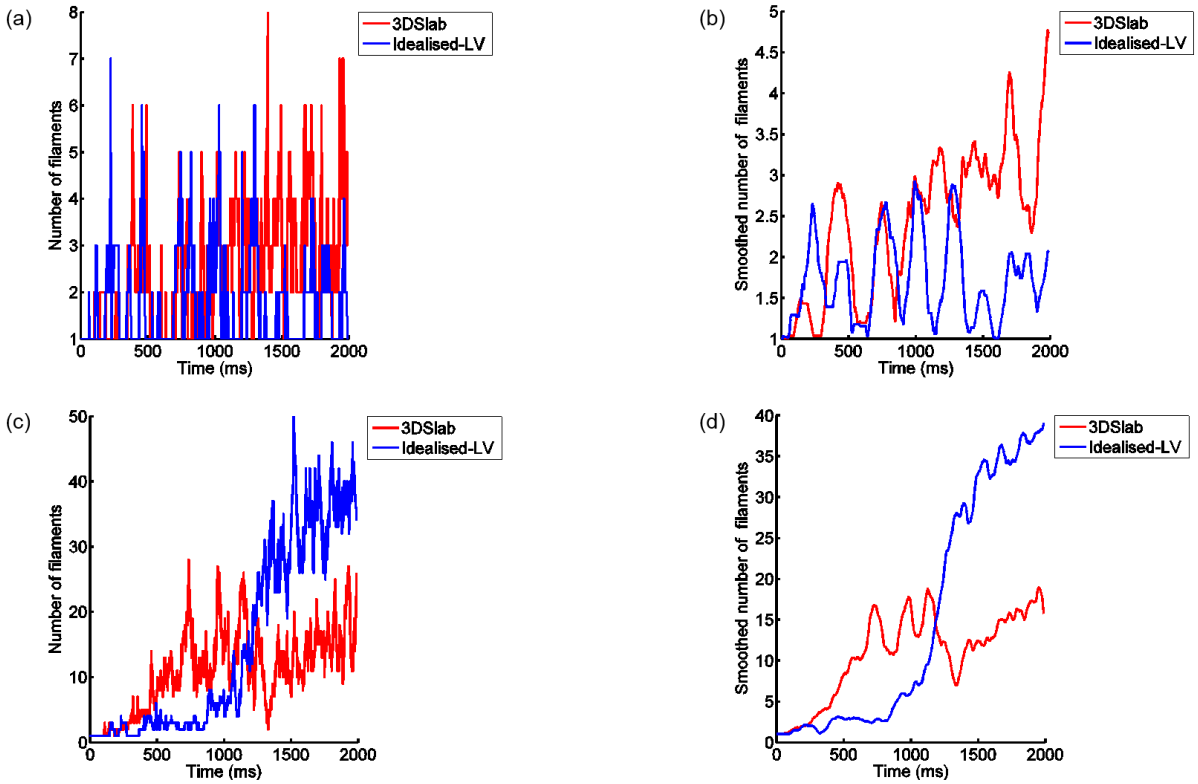

Figure 4.31 (a) Change in number of filaments over time in slab and idealized LV in epiMod1; (b) smooth view of change in filaments over time in epiMod1; (c) change in number of filaments over time in slab and idealized LV in epiMod2; (d) smooth view of change in filaments over time in epiMod2 dynamics.

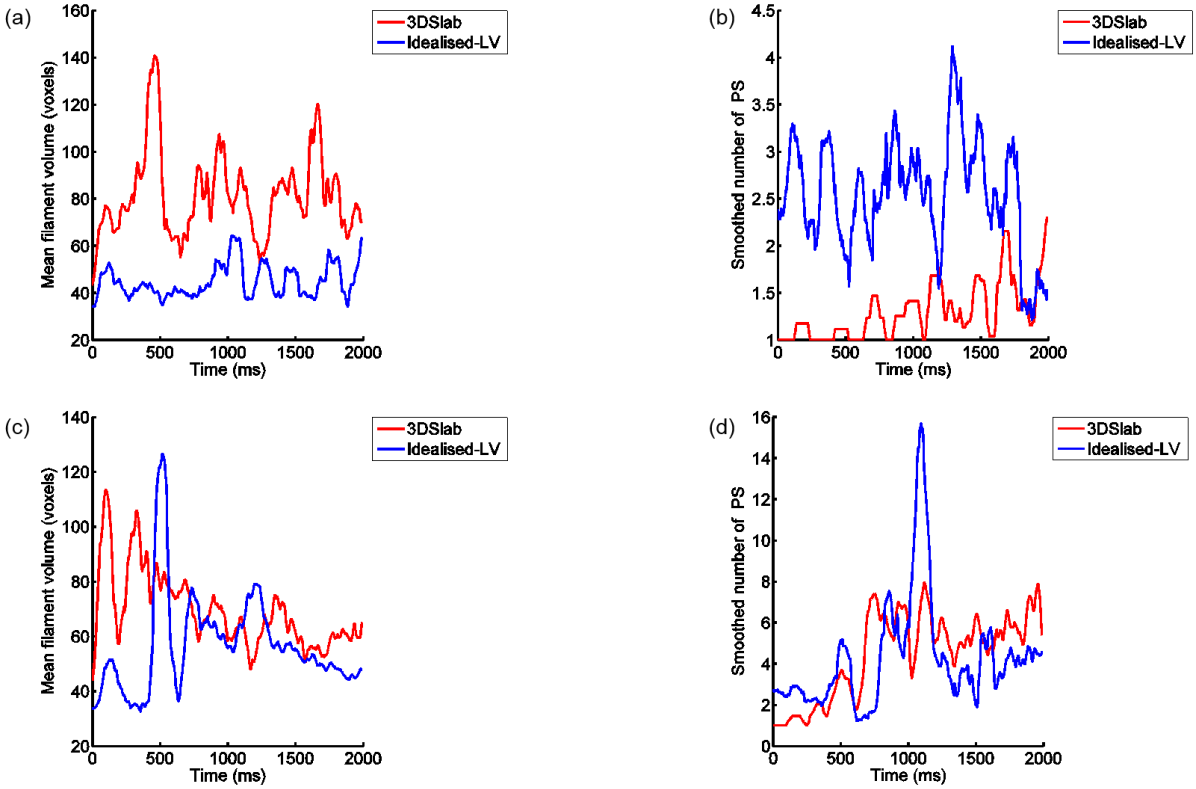

Figure 4.32 (a) Change in mean volume of filaments over time in 3D slab and idealized LV in epiMod1 dynamics; (b) change in number of PS over time in epiMod1 dynamics; (c) change in mean volume of filaments over time in 3D slab and idealized LV in epiMod2 dynamics; (d) change in number of PS over time in epiMod2 dynamics.

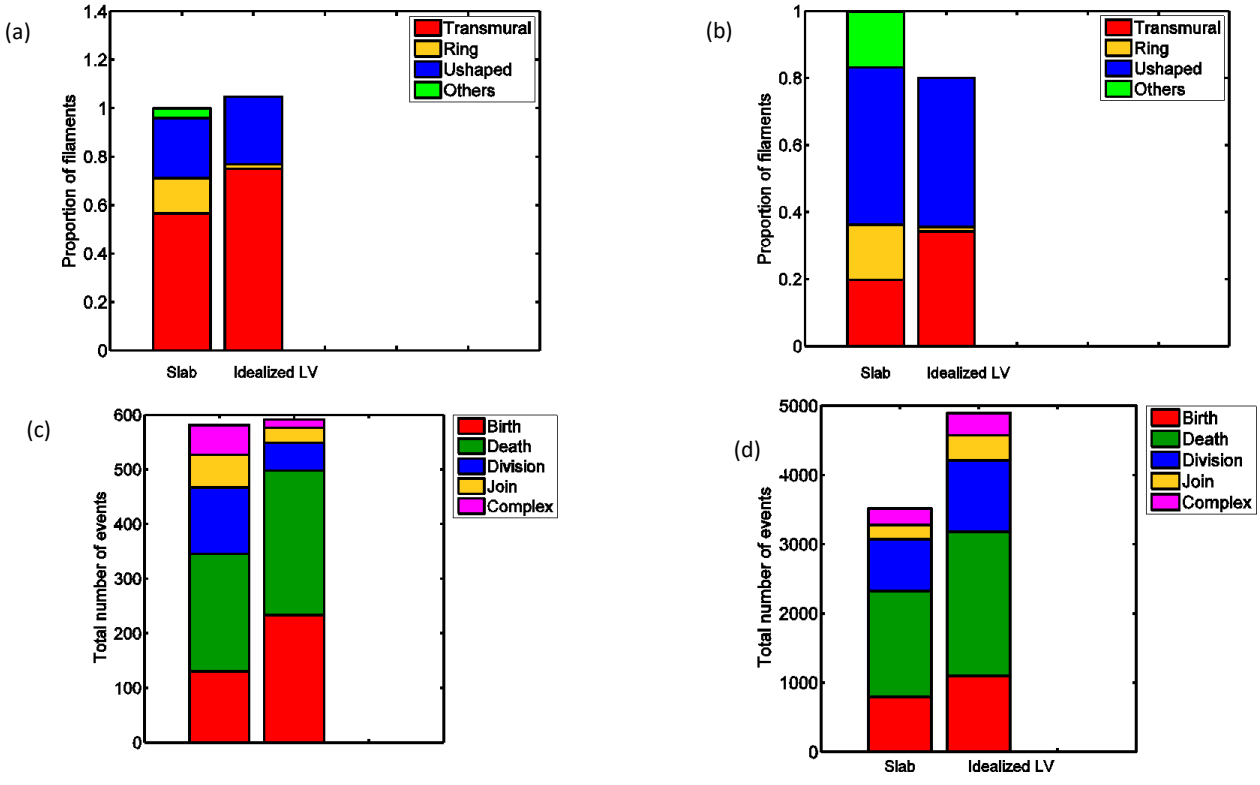

Figure 4.33 (a) and (b) Configuration of filaments in slab and idealized LV in epiMod1 and epiMod2 dynamics; (c) and (d) number of events in epiMod1 and epiMod2 dynamics.

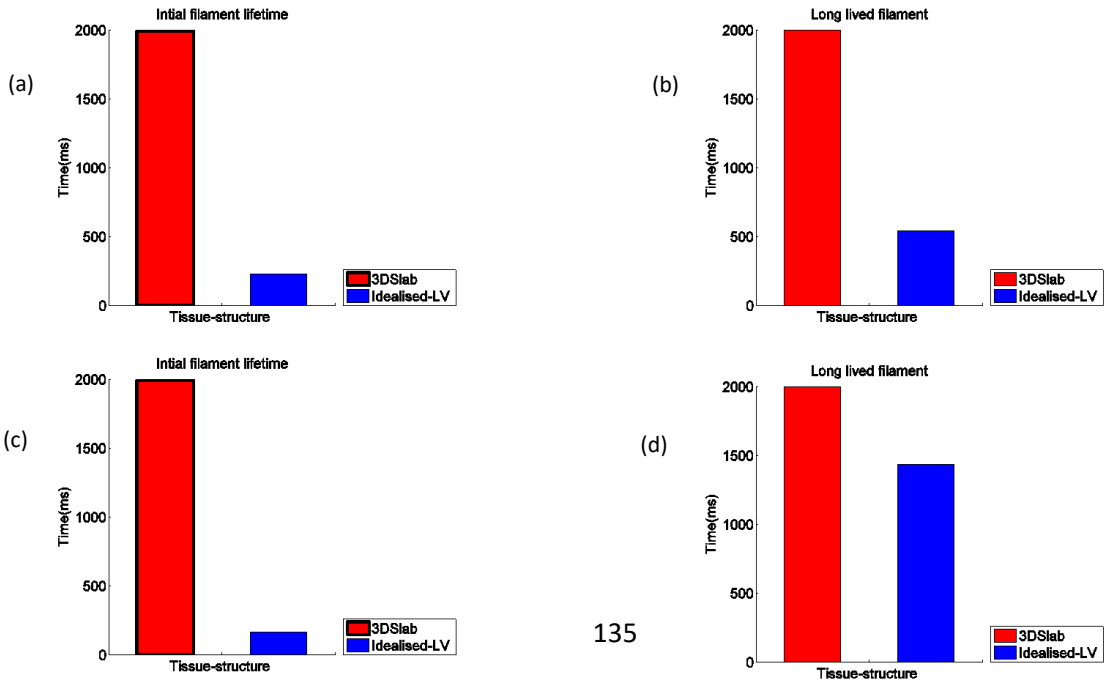

Figure 4.34 (a) Initial filament gene life time in both slab and idealized LV in epiMod1: (b) long lived filament in epiMod1; (c) initial filament gene lifetime in both slab and idealized LV in epiMod2; (d) long lived filament in epiMod2. Red colour represents 3D slab and blue idealized LV. The black border in figure (a) and (c) shows the initial filament gene lived beyond 1990 ms.

4.3.6 Effect of Perturbations of Activation Pattern during VF in Idealized Left Ventricle

In idealized LV, the effect of perturbation was seen much sooner at around 700 ms after initiation compared to around 1000ms with epiMod1 dynamics (Figure 4.35 (b) and (d)). In epiMod1 dynamics even after 1000ms the effect of perturbations was little compared to epiMod2 dynamics. Also, the number of filaments in epiMod2 dynamics was much greater compared to epiMod1 dynamics.

The effect of perturbation did not show any important difference in the filament volume (Figure 4.36 (a) and (c)), number of PS (Figure 4.36 (b) and (d)) and configuration of filaments (Figure 4.37 (a) and (c)). This might be because of no transmural heterogeneity in idealized LV. Number of events in epiMod1 dynamics showed more fluctuations compared to epiMod2 dynamics (Figure 4.37 (b) and (d).

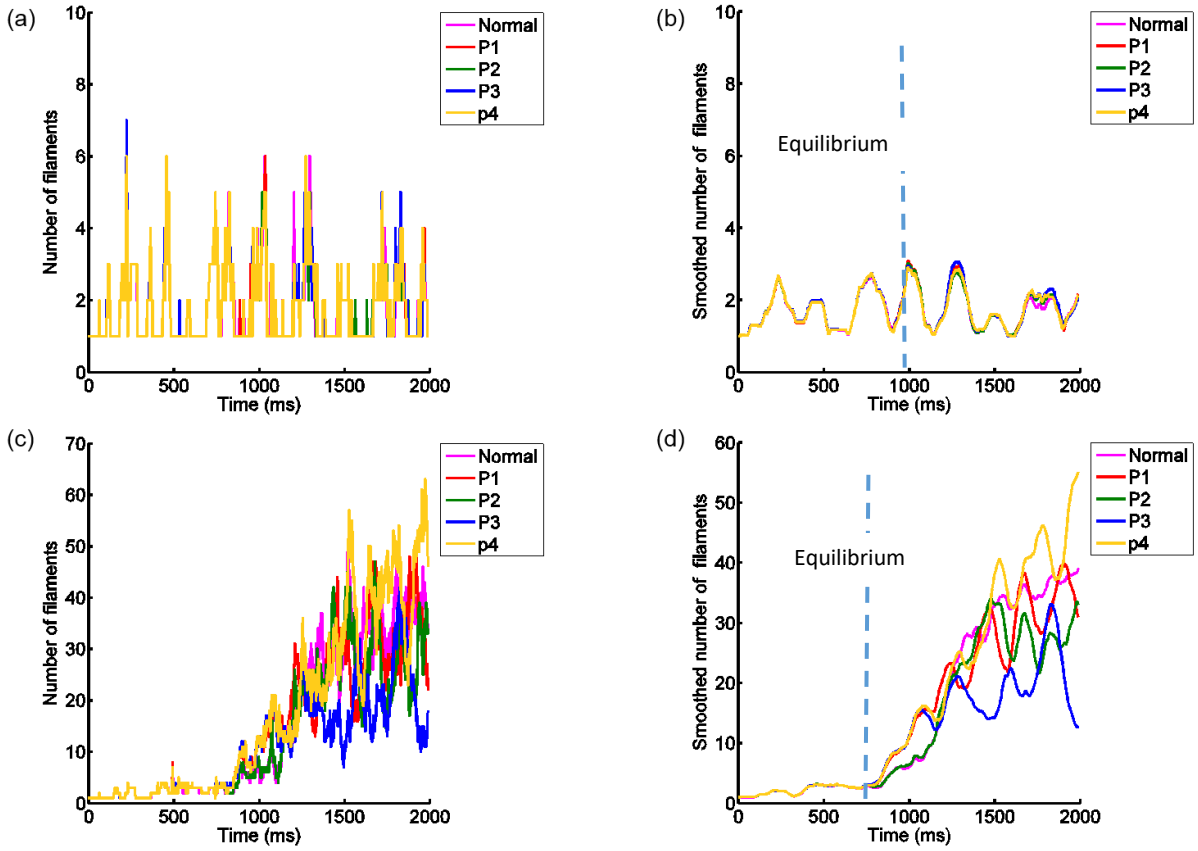

Figure 4.35 Effects of perturbations (uniform, P1, P2, P3, P4) in uniform idealized LV: (a) change in number of filaments over time (ms) in epiMod1; (b) smooth view of change in number of filaments in epiMod1, equilibrium reached at 300ms in epiMod1 dynamics; (c) change in number of filaments over time (ms) in epiMod2; (d) smooth view of change in number of filaments in epiMod2, equilibrium reached at 800ms in epiMod2 dynamics.

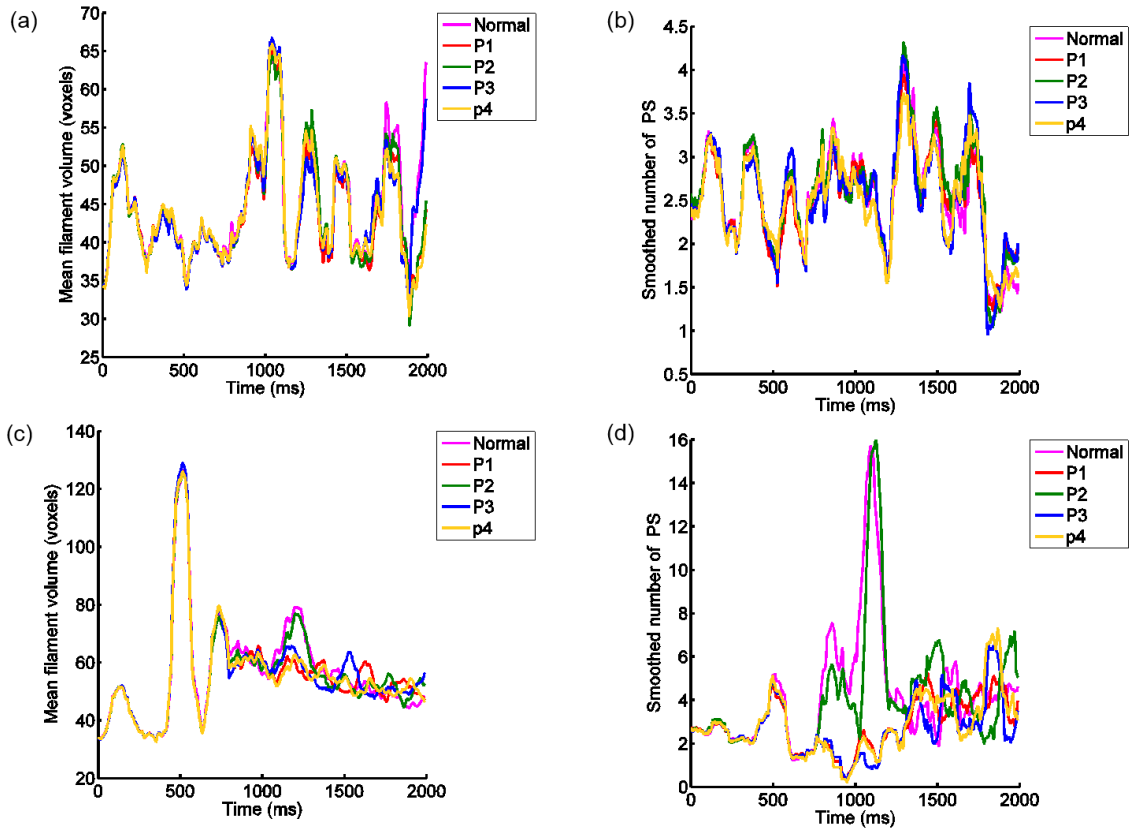

Figure 4.36 Effects of perturbations (uniform, P1, P2, P3, P4) in uniform idealized LV: (a) change in mean volume of filaments over time in epiMod1; (b) change in number of PS over time in epiMod1; (c) change in mean volume of filaments over time in epiMod2; (d) change in mean volume of filaments over time in epiMod2.

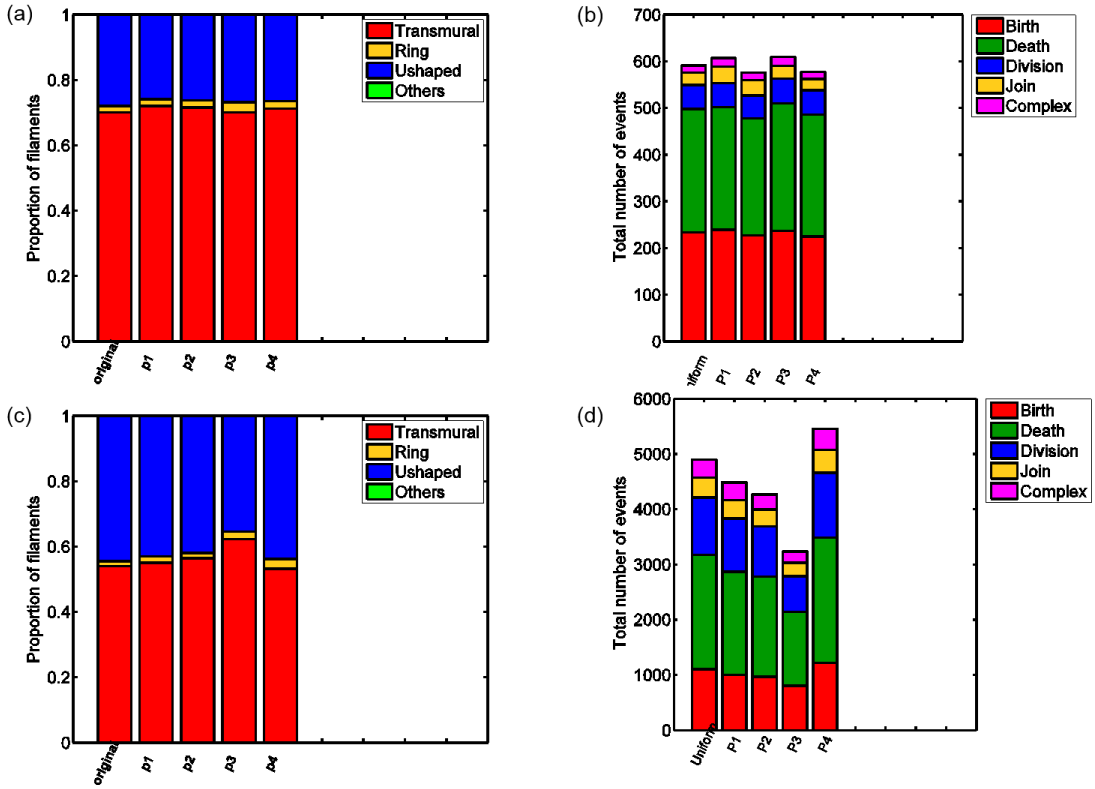

Figure 4.37 Effects of perturbations (Normal, P1, P2, P3, P4) in uniform idealized LV: (a) configuration of filaments in epiMod1; (b) number of events in epiMod1; (c) configuration of filaments in epiMod2; (d) number of events in epiMod2.

4.4 Summary of Results

This chapter investigated the influence of tissue shape, thickness, initial conditions and heterogeneity in tissue structure on filament dynamics as summarized below.

- Simplified model (4-variable model) of cellular electrophysiology integrated in a virtual tissue was sufficient to study filament dynamics (Figure 4.12). Simplified models are not computationally expensive compared to biophysically detailed models. A simple untwisted straight filament was enough as the initial condition (Figure 4.14). Modelling straight filament is simple and straight forward.
- Influence of smooth distribution of cells for modelling transmural heterogeneity did not give important effect compared to sharp distribution in filament dynamics (Figure 4.19 and 4.20). Modelling sharp transmural heterogeneity is simple compared to smooth distribution and hence sharp transmural heterogeneity was used in this thesis.
- On the whole transmural heterogeneity did not give important effect on the number of filaments in the slab geometry (Figure 4.26), so idealized LV was modelled as a uniform tissue. It is simple to model uniform tissue.
- Idealized LV with epiMod2 dynamics had more filaments compared to slab geometry with epiMod2 dynamics showing how the shape of the geometry influences filament dynamics (Figure 4.31 (d)).
- When the initial filament was perturbed, both slab and idealized LV showed differences in the number of filaments displaying non-linear behaviour especially in epiMod2 dynamics (Figure 4.25 and 4.35).
- This finding underscores the non-linear nature of activation patterns during VF where small changes can have a large influence on the overall behaviour (number of filaments) in both 3D slab and idealized LV (Figure 4.25 and 4.35).

4.5 Discussion

A simplified model (4-variable model) of cellular electrophysiology was chosen for this thesis over a biophysically detailed model (TP06) as there was no important difference in filament dynamics between the two. A simple straight transmural filament was used as the initial condition since simulation with ring filament and transmural filament as initial condition gave similar results.

Sharp transmural heterogeneity was used in the simulations as there was no important difference in its filament dynamics compared with smooth distribution. However, sharp transmural heterogeneity did not show an important difference in number of filaments in 2- layer, 3 - layer and patch despite each cell having different APD (Figure 4.15 (a)). These results can be explained by the electrotonic effect described in the studies by Taggart et al. (2003) and Colli Franzone et al. (2006). AP propagation in the tissue causes 'electrotonic effect', i.e., the positive potential along the tissue which gets diminished with distance. These studies (Taggart et al. 2003, Colli Franzone et al. 2006) argued that local electrotonic cancellation of gradients in APD between coupled cells may be the reason for not observing any important difference in filament dynamics.

Tissue with transmural heterogeneity with 2- layer (endo - epi) showed more clustering of filaments in endo-epi border (Figure 4.17 (c) and (d)). Transmural heterogeneity with 3 - layer (endo - M - epi) showed more clustering in endo - M border and M - epi border (Figure 4.18 (c) and (d)). Massé et al. (2007) identified centrifugal force as a fictitious force around the rotating system which may tend to co-localize the rotating system to the border of the slow conducting tissue since conduction block of AP occurs in the border of slow conducting tissue. M cells showed higher conduction velocity compared to endo cells. During VF, diastolic interval (DI) will be minimum. Minimum conduction velocity of endo cells was less than M cells which in turn was less than the epi cells (Figure 4.15 (c)). Clustering of filaments in 2 layer and 3 layer is likely to be the reason for increase in filament length (Jiménez and Steinbock 2012, Dutta and Steinbock 2011) as clustering of filaments could have induced negative tension and therefore increase filament length. Filament lifetime was increased as clustering of filaments influenced the stability of filament to sustain.

Slab geometry showed how a small change in initial condition significantly altered the number of filaments in uniform, 2-layer, 3-layer and patch showing non-linear behaviour. Mean filament volume (Figure 4.27), long cumulative lifetime (Figure 4.28) and short lifetime also showed non-linear behaviour (Figure 4.29). The epiMod2 dynamics showed more non-linear behaviour compared to epiMod1 dynamics. Non-linear behaviour was observed more in 2-layer (endo - epi) compared to other profiles especially in epiMod2 dynamics.

Since transmural heterogeneity in slab geometry did not show much difference in the number of filaments, idealized LV with uniform distribution of epi cells was used in this thesis. The number of filaments was almost double in idealized LV compared with 3D slab in epiMod2 dynamics, showing the shape of the geometry influences filament dynamics. This can be explained in slab geometry by the capacity of filaments to disappear moving away from the boundary, and in idealized LV, filament capacity to move around. The volume of the idealized LV is almost double that of the slab geometry

which can be another reason for observing more filaments in idealized LV. In idealized LV, filament configuration and volume was not affected as filaments are not clustered in uniform tissue (Figure 4.21). Idealized LV showed more non-linear behaviour in epiMod2 dynamics compared to epiMod1 dynamics.

The effect of shape and thickness of tissue and perturbations of initial conditions strongly influenced filament dynamics; the influence was observed to be greater with epiMod2 dynamics compared with epiMod1 dynamics. Transmural heterogeneity did not have an important influence on filament dynamics.

Chapter 5 Influence of Tissue Structure and Disease on Filament Dynamics

5.1 Introduction

This chapter focuses on the effect of different size and types of scar region on filament dynamics.

Several experimental and modelling studies (Shajahan et al. 2007, Jiménez & Steinbock 2012, Majumder et al. 2011) have shown that scroll wave filaments can pin to the edge of a myocardial scar region, but the effect of scarring on filament dynamics has not been studied in detail. Moreover, most modelling studies have used regular cylindrical edges to represent the scar region in slab geometry. Chapter Four showed that geometry had an influence on filament dynamics. In the real heart, scarred regions can be circumferential or transmural. Transmural scar can be full depth or half depth (sub-endocardial) with regular or irregular borders (Cook et al. 1958).

Massé et al. (2007) showed fictitious centrifugal force co-localizes rotating spiral waves to the slow conducting border since conduction block occurs near the slow conducting border in experimental studies. The scar region does not conduct AP, so it is expected to find filaments cluster to the scar boundary. Shajahan et al. (2007) showed theoretically that the fractal like boundary in the scar region separates the 'strange attractor' basins of attractors from 'fixed point' basins of attractors in dynamic systems. An attractor is a set of points in the phase space in which the system tends to evolve. The basin of attraction is the set of neighbouring points to the attractor which also behave similarly to attractors. This basin of attractors pins filaments to the edge of the scar boundary. These attractors are fixed points; however, in chaotic dynamics, these are not fixed but distributed in space making them 'strange attractors'. Since strange attractors are distributed in space, they can pin more filaments. The previous chapter showed that both slab and ellipsoid geometry showed non-linear behaviour in epiMod2 dynamics compared to epiMod1 dynamics. Slab geometry with endo - epi profile showed more non-linear behaviour (Figure 4.25 (b)). So this chapter investigates the effect of scar regions on filaments.

Modelling studies (Shajahan et al. 2007, Xie et al. 1998) have shown that the size of scar can have an important influence on pinning of filaments to the scar boundary. So in this chapter the filament dynamics and clustering of filaments close to the edge of the scar region are studied, with different sizes of scar.

Slab geometry with sharp distribution of endo - epi was used for this since it showed more non-linear behaviour compared to uniform, 3 layer and patch profile. A uniform idealized LV was used in

this section to keep it simple and to concentrate solely on the influence of scar regions on filament dynamics without other complications.

5.2 Methods

Since scar tissue does not conduct AP propagation, the scar region was represented by a region of inexcitable but diffusively coupled tissue in both slab and idealized LV. In tissue geometry, it is easier to model scar region as inexcitable but diffusively coupled tissue by just assigning a number '2' different from '1' which is excitable tissue and '0' representing outside tissue which is non- excitable and non-diffusive. This section shows how the scar region was modelled in slab geometry, how circumferential scar was modelled in idealized LV and how transmural scar was modelled in idealized LV.

Circumferential scar, mainly situated in the mid wall of the ventricle, which extends less than 10 mm from endocardium was modelled in a idealized LV (Cook et al. 1958). Transmural scar was modelled as full depth showing fully extended transmural scar. Half depth scar represents sub endocardial transmural scar. Both full extended transmural scar and sub endocardial transmural scar were modelled in the mid wall of an idealized LV. Full depth and half depth scar had either regular or irregular borders.

5.2.1 Incorporating Region of Scar in Slab Geometry

In the existing slab geometry with endo - epi profile, the scar region was incorporated as a quarter cylinder extending from the endocardium with a thin layer of surviving epicardial tissue as explained in Hackel and Wagner (1995). The scar region was modelled as a quarter cylinder of 30mm radius representing the slab of tissue removed from the left ventricle with transmural scar as shown in Figure 5.1. Sharp transmural heterogeneity of endo - epi was incorporated in the slab geometry.

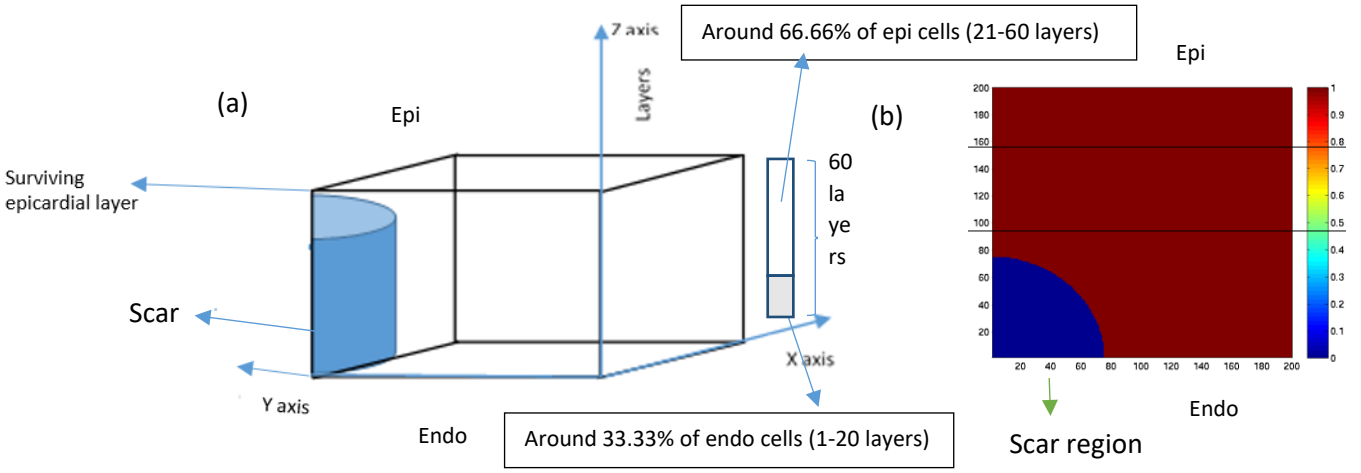

Figure 5.1 (a) Schematic representation of region of scar incorporated in slab geometry as quarter cylinder extending from endocardium; (b) Cross section view of slab geometry with scar.

5.2.2 Incorporating Circumferential Scar in Idealised LV

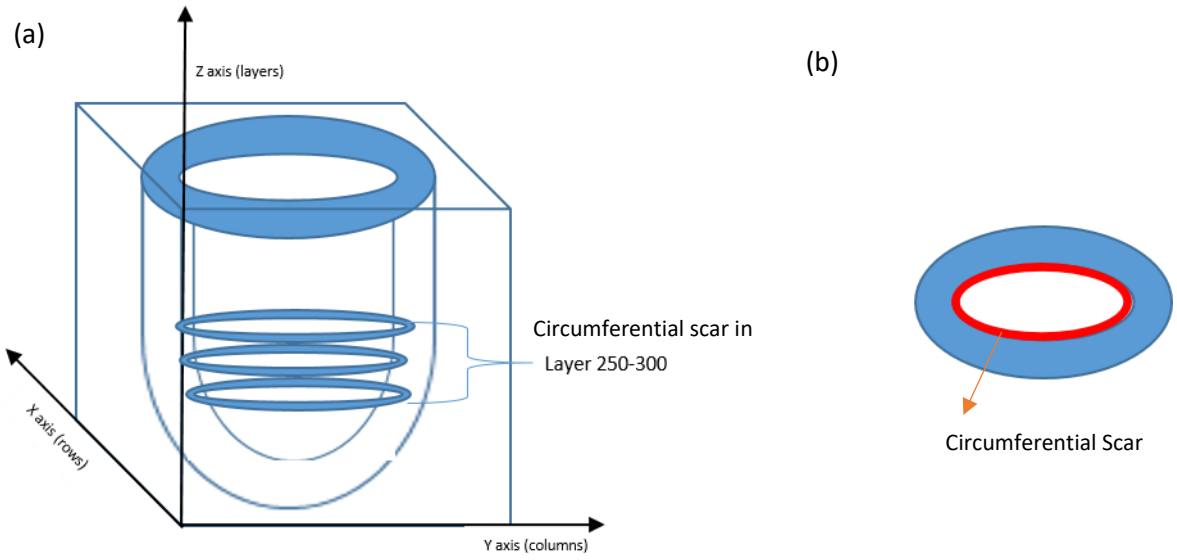

Figure 5.2 Schematic representation of (a) circumferential scar incorporated in an idealized LV; (b) cross section view of the middle layer of an idealised LV with circumferential scar.

Circumferential scar was modelled in the middle layers of the idealized LV as shown in Figure 5.2 (a) as this type of scar is found near the endocardial region of tissue and is less than 10mm in wall thickness. The scar was modelled as a ring shape of about 0.6 % of wall thickness of an idealized LV. Figure 5.2 (b) shows the cross section view of the circumferential scar.

5.2.3 Incorporating Transmural Scar in Idealised LV

As in the slab geometry, the scar was represented by a cylindrical region of inexcitable but irregularly coupled tissue with a radius of 10mm, 15mm, 20mm, 25mm, 30mm and 35 mm and extending either through the full width (full transmural scar) of the tissue or half way (sub endocardial scar) through. The scar region was either with a regular or irregular border located in the middle of the wall as shown in Figure 5.3. To model the irregular cylindrical scar region, random numbers were used to get a mixture of 50 percent excitable and 50 percent inexcitable tissue. Figure 5.4 shows cross sections of an idealized LV with scar region.

The scar region was modelled along columns. For example, 50 columns is 10 mm scar radius (50 * 0.2 =10mm) where 0.2 is the space step used in the geometry. The number of grid points in the vertical section of the idealized LV is 175x175x255. So the maximum number of columns the scar can have is 175 (i.e. 35 mm). Scar region was modelled with different radii of 50, 75, 100, 125, 150, 175 columns which equates to 10mm, 15mm, 20mm, 25mm, 30mm and 35 mm respectively. Scars with 10mm, 15mm and 20mm radii can be classified as small, 25mm and 30mm radii as moderate and 35mm radius as large.

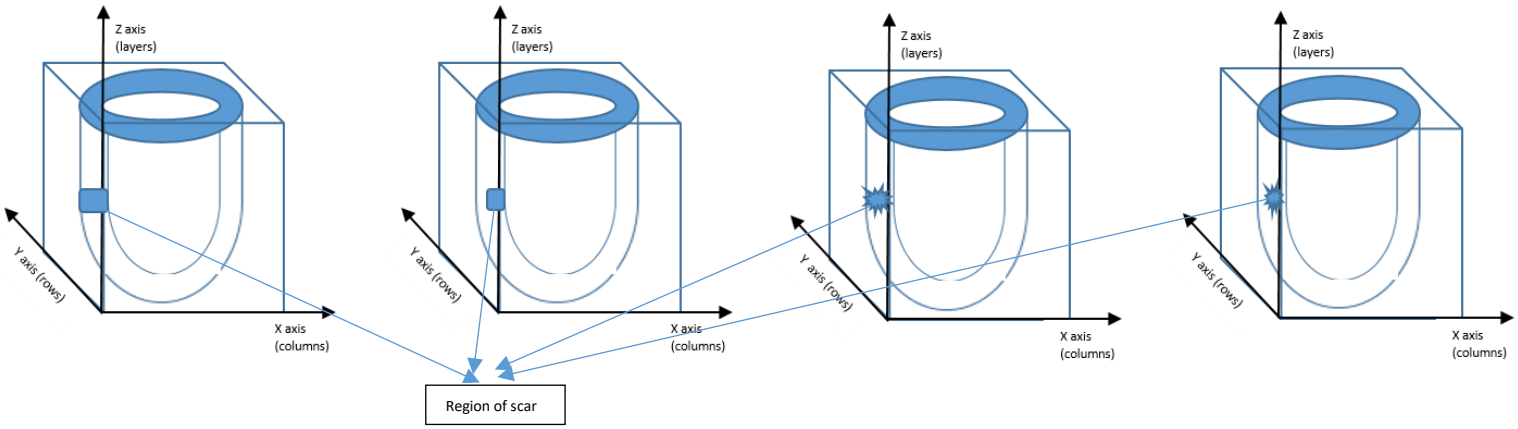

Figure 5.3 Schematic representation of transmural scars in an idealized LV (a) full depth regular scar;(b) half depth (sub endocardium) regular scar; (c) full depth irregular scar; (d) half depth (sub endocardium) irregular scar.

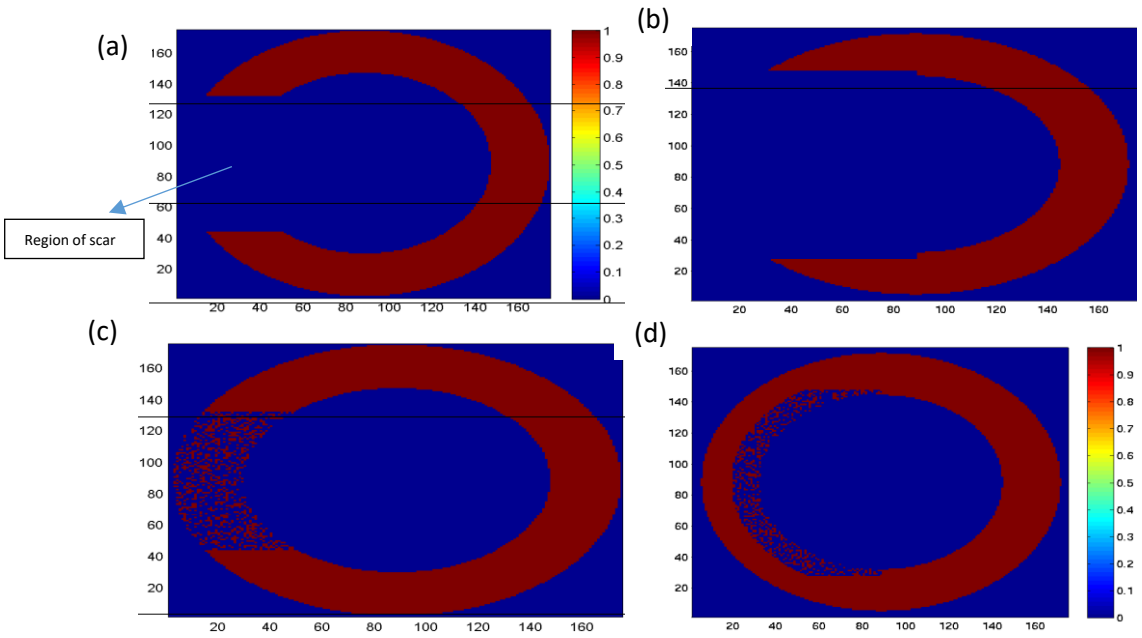

Figure 5.4 Cross section view of (a) Full depth regular scar; (b) Half depth regular scar; (c) Full depth irregular scar; (d) Half depth irregular scar modelled in Idealized LV.

5.2.4 Clustering of Filaments

In the slab geometry, to compute the clustering of filaments to the scar boundary, filament voxels were summed along the z axis since the scar is aligned along the same axis (i.e. along layers). To get a clear view of clustering, the density of filament voxels in 1D was computed as explained in section 3.4.7.

In the idealized left ventricle geometry, summing was done along the x axis since the scar was modelled along that axis (columns) and masked on the surface of the idealized LV.

5.3 Results

5.3.1 Effect of Scar Region in Slab Geometry on Clustering of Filaments and Filament Dynamics

5.3.1.1 Clustering of Filament voxels

In the slab geometry, filament voxels were distributed regularly in normal tissue. However, close to the scar boundary in the slab geometry, the number of filament voxels spiked to around 5 times the mean value in normal tissue (Figure 5.5). In the surviving epicardial layer, the number of filament voxels was around one fifth of the mean. Slab geometry with epiMod2 dynamics showed double the amount of clustering close to the scar boundary compared to epiMod1 (Figure 5.5 (d)).

Clustering seen near the scar boundary are filament voxels, not to be confused with individual filaments, since voxels of filament were counted.

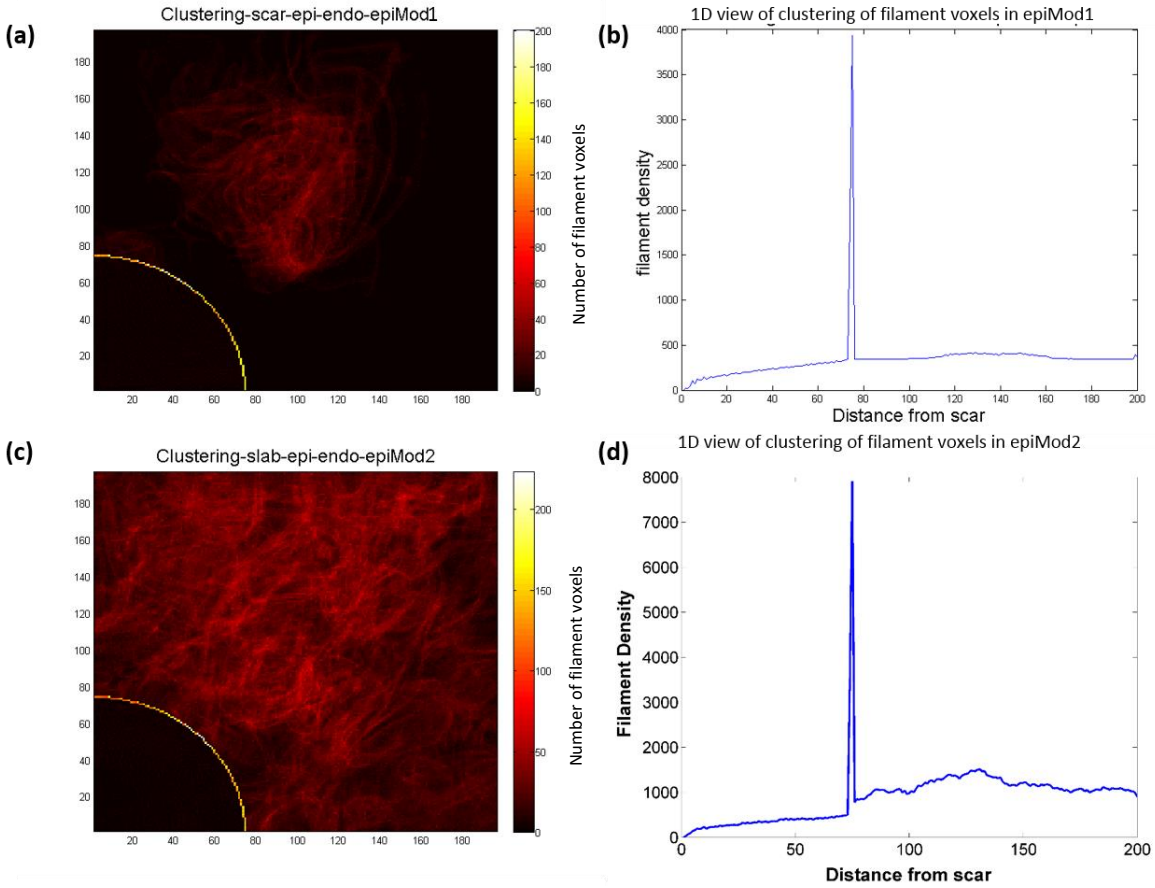

Figure 5.5 (a) and (b) clustering of filament voxels to scar boundary in epiMod1 dynamics in 2D and 1D views respectively; (c) and (d) clustering of filament voxels to scar boundary in epiMod2 dynamics in 2D and 1D views respectively.

5.3.1.2 Filament Dynamics

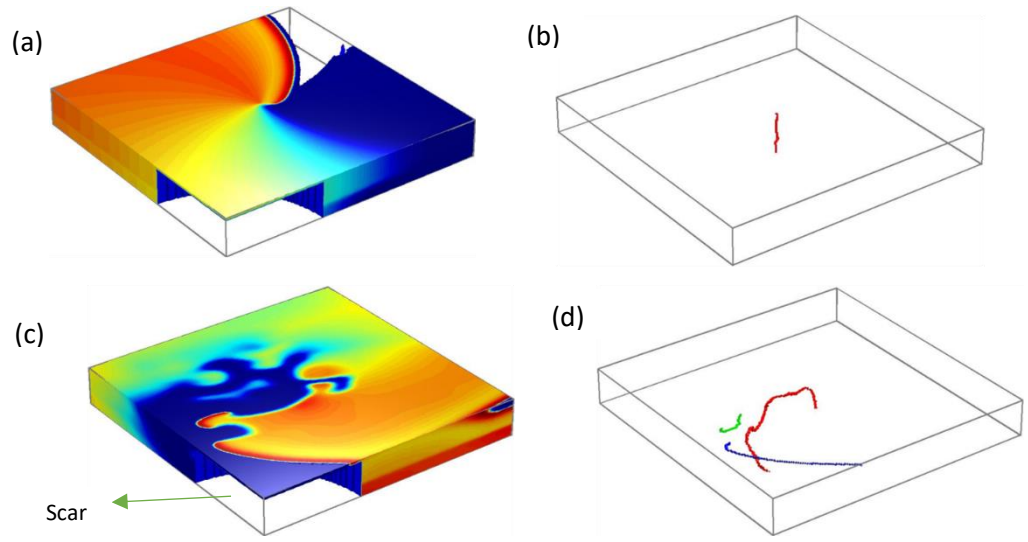

Figure 5.6 Snapshots of re-entry and corresponding filaments in slab geometry with scar region in epiMod1 dynamics (a) and (b) at 10ms; (c) and (d) at 1890 ms.

In most of the simulations, the initial filament broke up around 100ms - 200ms. Figure 5.6 shows snap shots of re-entry and corresponding filaments in the slab geometry with a scar region. The average number of filaments (± standard deviation) from 1-2 s was 2.3± 1.4 for epiMod1 dynamics and 13.3 ± 8.0 for epiMod2 dynamics in the slab with scar region. Whereas the average number of filaments (± standard deviation) from 1-2 s was 1.8 ± 1.1 for epiMod1 dynamics and 10.8 ± 6.7 for epiMod2 dynamics in the slab without scar region.

Overall, the number, volume and configuration of filaments and the number of PS showed little difference in endo-epi slab geometry with or without scar as shown in Figure 5.7, showing transmural scar in slab geometry has no significant effect on filament dynamics. The number of events with a scar region was higher compared to no scar with both dynamics (Figure 5.7 (i) and (l)). The scar region with epiMod1 dynamics had almost double the number of events compared to epiMod2 dynamics. Clustering of filaments in epiMod2 dynamics was twice that in epiMod1 dynamics (see Figure 5.5); pinned filaments cannot branch (Winfree et al. 1984). This might be the reason for observing twice as many events with scarring in epiMod1 compared to epiMod2 dynamics.

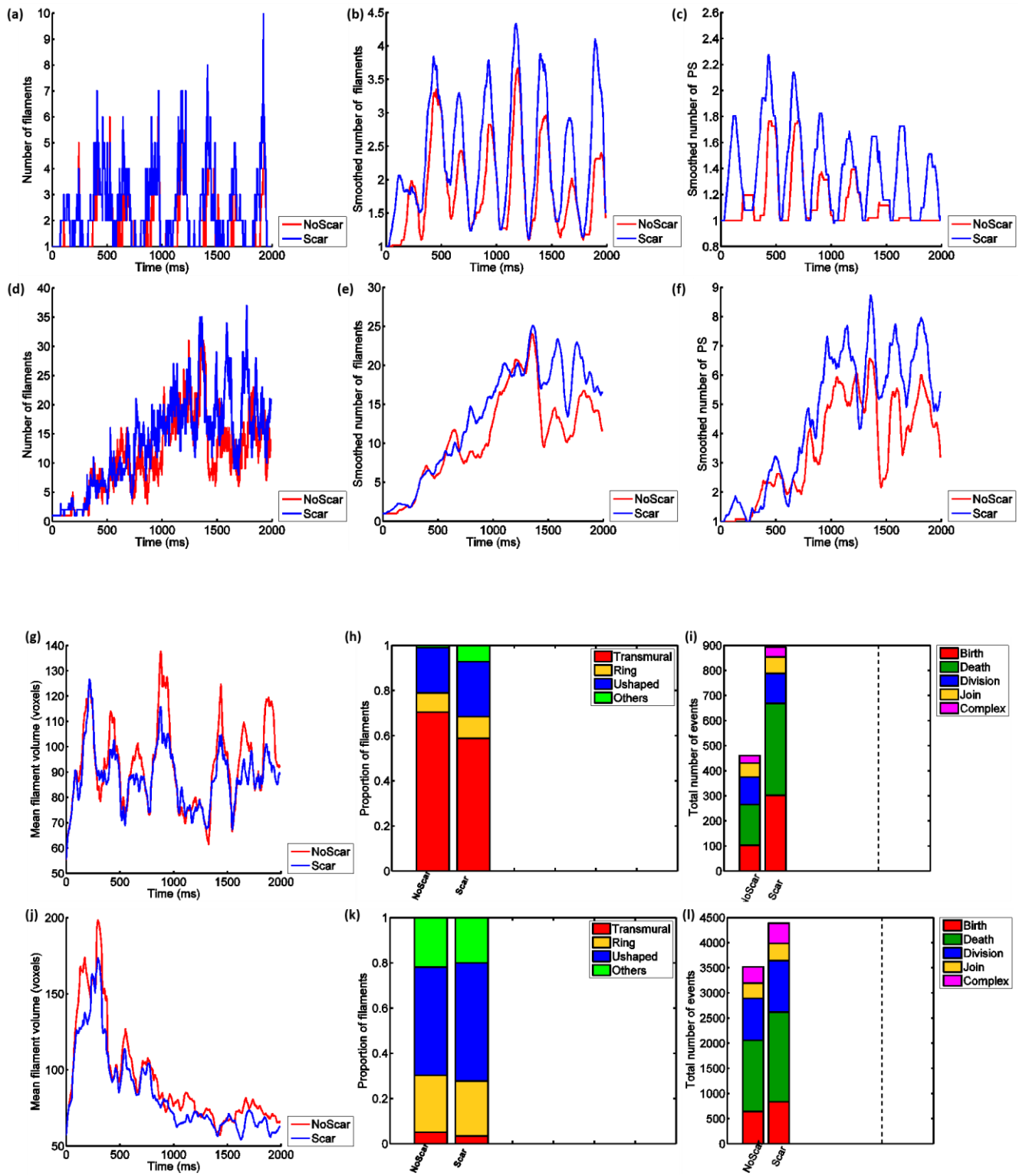

Figure 5.7 Comparing filament dynamics in scar and no scar region in slab geometry. (a) - (c) and (g) - (i) epiMod1 dynamics, (d) - (f) and (j) - (l) epiMod2 dynamics. (a) Change in number of filaments over time (ms) in epiMod1; (b) Smooth view in change in number of filaments in epiMod1; (c) smooth view of change in PS over time in epiMod1; (d) Change in number of filaments over time (ms) in epiMod2; (e) Smooth view in change in number of filaments in epiMod2; (f) smooth view of change in PS over time in epiMod2; (g) Mean volume of filaments over time in epiMod1; (h) configuration of filaments in epiMod1; (i) Total number of events in epiMod1; (j) Mean volume of filaments over time in epiMod2; (k) configuration of filaments in epiMod2; (l) Total number of events in epiMod2. In graph (h), (i), (k) and (l) first bar shows results for no scar and second bar shows results with scar.

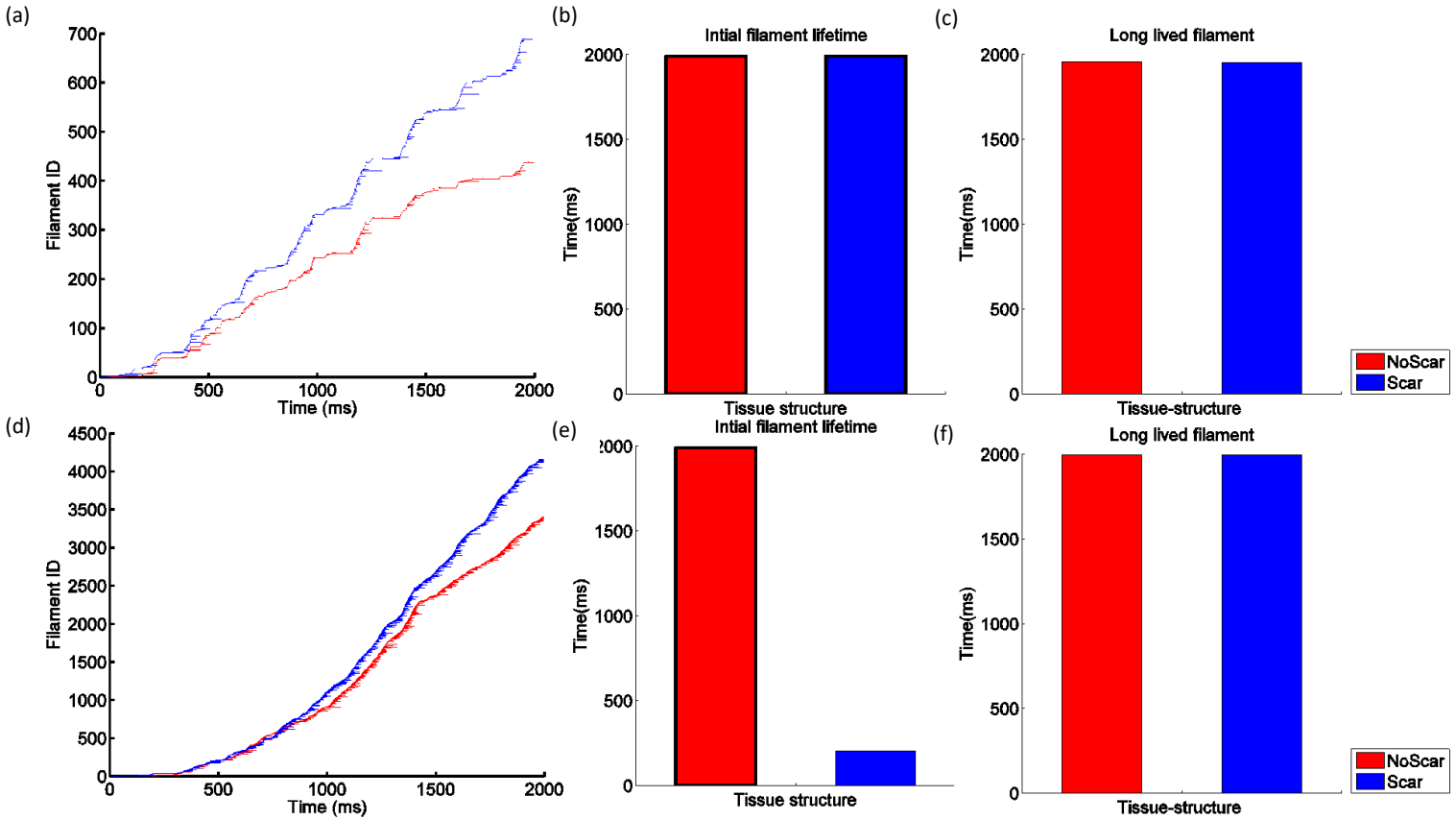

Figure 5.8 (a) Life time of filaments in epiMod1; (b)) initial filament lifetime in epiMod1,BLACK border shows initial filament gene sustained even after 1990ms; (c) long lived filament in epiMod1; (d) life time of filaments in epiMod2; (e) initial filament lifetime in epiMod2 BLACK border shows initial filament gene sustained even after 1990ms; (f) long lived filament in epiMod2 . Red colour -no scar, blue colour – scar

5.3.2 Effect of Circumferential Scar Region in Idealized LV Geometry on Clustering of Filaments and Filament Dynamics

5.3.2.1 Clustering of Filament Voxels

The idealized LV with circumferential scar did not show any clustering close to the scar region as shown in Figure 5.9. In epiMod1 dynamics, small clustering of filaments is seen near the apex; whereas, epimod2 dynamics showed more clustering near the base as shown in Figure 5.9.

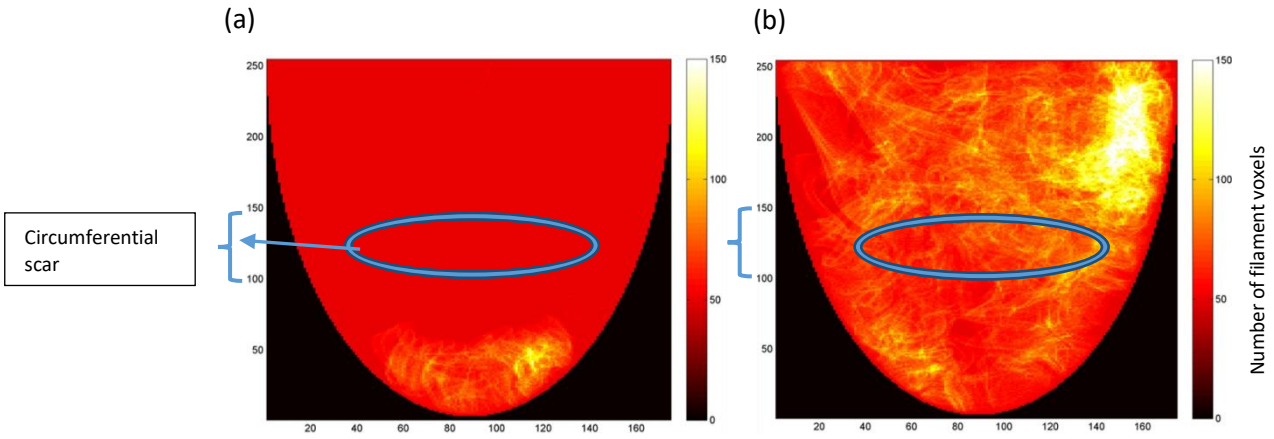

Figure 5.9 No clustering of filaments near the circumferential scar border: (a) in epiMod1 dynamics; (b) in epiMod2 dynamics.

5.3.2.2 Filament Dynamics

In these simulations, circumferential scar did not show any difference in number, configuration and volume of filaments or number of events as shown in Figure 5.10. The size of the scar at only 0.6% of wall thickness of the idealized LV may explain why difference in filament dynamics was not observed.

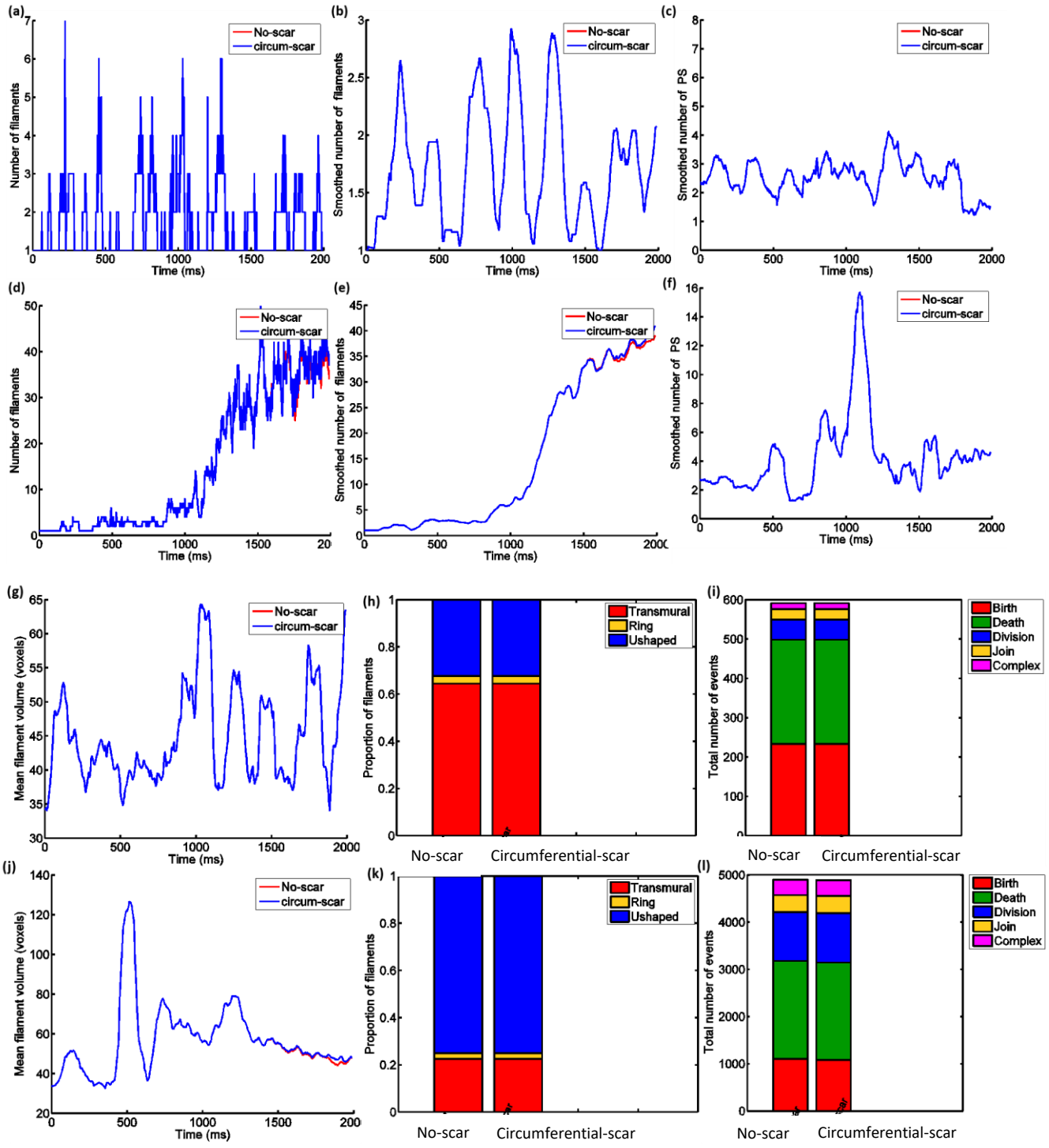

Figure 5.10 Comparing filament dynamics in circumferential scar and no scar region in an idealized LV (a)-(c) and (g)-(i) epiMod1 dynamics, (d-f) and (j)-(l) epiMod2 dynamics: (a) Change in number of filaments over time (ms) in epiMod1; (b) smooth view in change in number of filaments in epiMod1; (c) smooth view of change in PS over time in epiMod1; (d) change in number of filaments over time (ms) in epiMod2; (e) smooth view in change in number of filaments in epiMod2; (f) smooth view of change in PS over time in epiMod2; (g) mean volume of filaments over time in epiMod1; (h) configuration of filaments in epiMod1; (i) total number of events in epiMod1; (j) mean volume of filaments over time in epiMod2; (k) configuration of filaments in epiMod2; (l) total number of events in epiMod2.

5.3.3 Effect of Transmural Scar on Clustering of Filaments and Filament Dynamics

5.3.3.1 Clustering of Filament Voxels

APD restitution dynamics had a strong effect on clustering (Figure 5.11). The idealized LV with epiMod2 had more clustering of filaments to the edge of the scar region compared to epiMod1 dynamics. Half depth scar showed more clustering compared to full depth scar. Full depth irregular scar had more clustering compared to full depth regular scar. In half depth irregular scar, clustering was somewhat inconsistent with epiMod1 and epiMod2 dynamics. More clustering was evident with increased radius of scar region Figures 5.11 and 5.12.

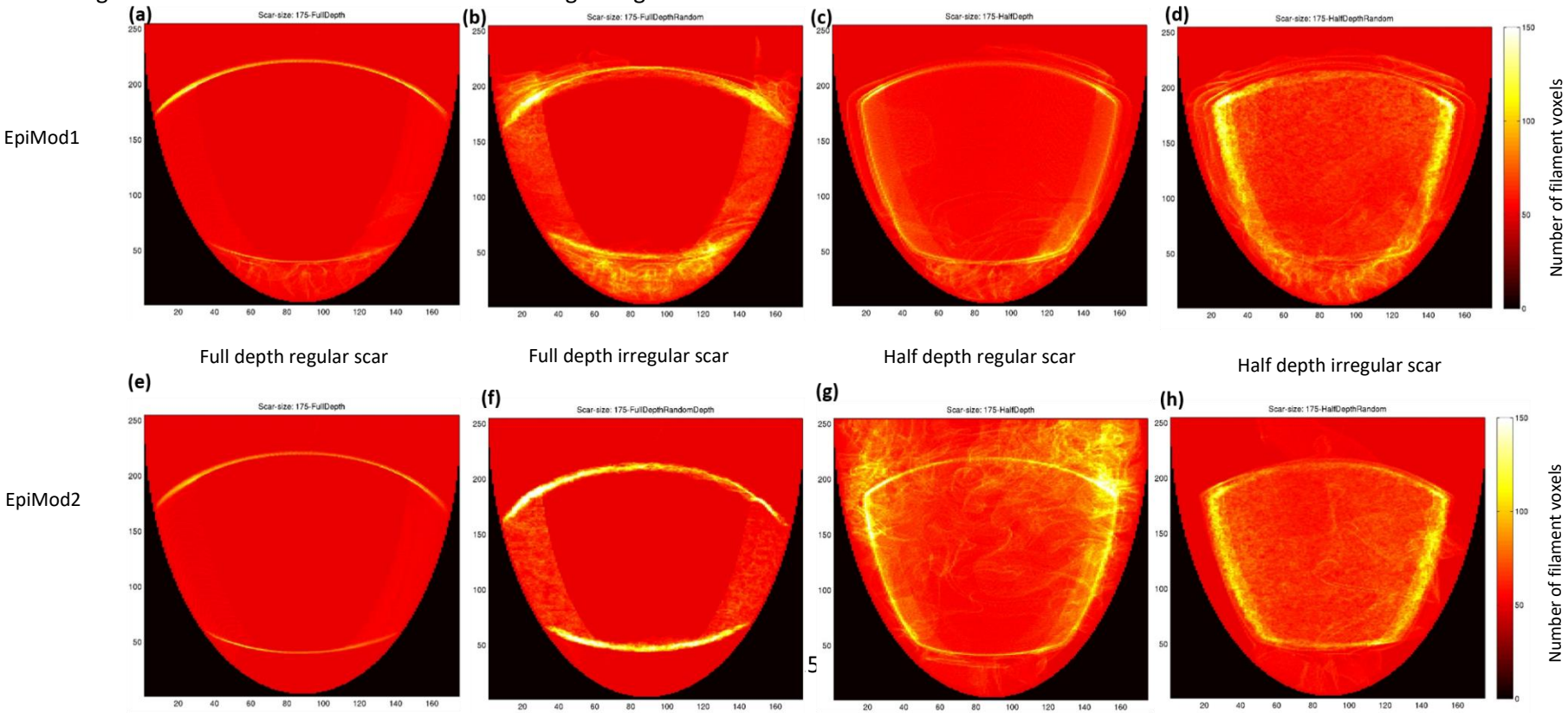

Figure 5.11 Clustering of filaments to scar boundary of 35 mm radius scar: (a)- (d) in epiMod1 dynamics, (e)-(h) in epiMod2 dynamics; (a) and (e) full depth regular scar; (b) and(f) full depth irregular scar; (c) and (g) half depth regular scar; (d) and (h) half depth irregular scar.

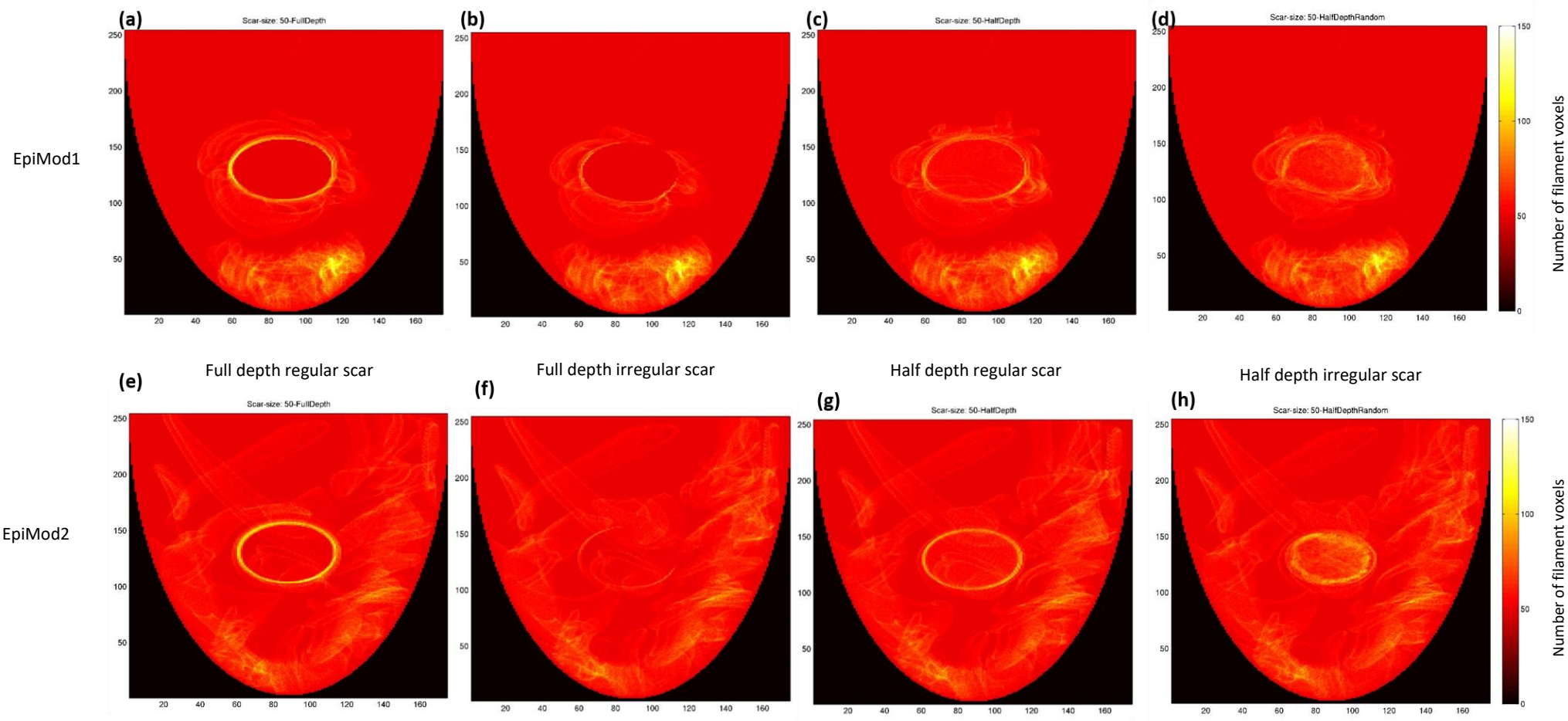

Figure 5.12 Clustering of filaments to scar boundary of 10 mm radius scar: (a)- (d) in epiMod1 dynamics, (e)-(h) in epiMod2 dynamics; (a) and (e) full depth regular scar; (b) and(f) full depth irregular scar; (c) and (g) half depth regular scar; (d) and (h) half depth irregular scar.

5.3.3.2 Filament Dynamics

In most of the simulations, the initial filament broke up around 100ms - 200ms. Results are shown from 1000ms - 2000ms after equilibrium was reached. Filament dynamics in the idealized LV with full depth regular transmural scar with a varying radius are shown in Figure 5.13.

5.3.3.2.1 Number of Filaments

The number of filaments present at a particular time is shown in figure 5.14. With epiMod1 dynamics, the idealized LV with scar region had more filaments compared with the no scar region and vice-versa for epiMod2 dynamics. Clustering of filament voxels was greater in epiMod2 dynamics compared to epiMod1 dynamics. This may be why less filaments were observed with the scar region in idealised LV compared to idealised LV without the scar region since pinned filaments cannot branch and form new filaments (Winfree & Strogatz 1984). The idealised LV with half depth scar had an increased number of filaments in epiMod2 dynamics compared with other types of scar region; this increase in number of filaments was higher with the increase in the radius of the scar region. However, in epiMod1 dynamics, increase in number of filaments was only evident in bigger scars. Full depth and half depth irregular scars with increased radius had more filaments compared to their respective regular scar regions. However, increase in number of filaments in half depth irregular scar was not consistent compared to full depth scar in epiMod1 and epiMod2 dynamics. Overall, the size of the scar region had a lesser effect on the number of filaments (Figure 5.19).

5.3.3.2.2 Volume of Filaments

Volume of filament gives an insight into the increase in filament length and can be used to assess filament tension. Negative filament tension affects the stability of the filament causing it to break and form more filaments.

Overall, mean volume of filaments (Figure 5.15) increased when there was a scar region in the idealised LV compared to no scar region. Comparatively, a half depth scar region yielded longer filaments than full depth scar in both dynamics. The longest filaments were seen in epiMod1 dynamics with the increased scar radius with half depth irregular scars of 30 and 35 mm. Even in epiMod2 dynamics, the longest filaments were seen with half depth irregular scar. Negative tension may be one reason for observing more filaments in both dynamics.

5.3.3.2.3 Phase Singularities

Phase singularities (PSs) are points observed when the filament touches epicardial surface. Increasing the size of the radius produced more PSs in both dynamics (Figure 5.16). The number of PSs observed with half depth and full depth scar regions with varying size was very similar. Full depth irregular scar produced more PSs in epiMod2 dynamics, whilst epiMod1 dynamics did not show any significant difference. The bigger the scar, the more PSs were observed in full depth irregular scar in epiMod2 dynamics.

5.3.3.2.4 Configuration of Filaments

The initial condition of re-entry was a single, simple and straight transmural filament. Over the course of time, the filaments formed can bend and twist because of underlying tissue properties and boundary conditions. This twist and bend can form U shaped filaments and ring filaments. Overall, the idealised LV shows very few ring filaments and this did not change when the scar region was incorporated (Figure 5.17). The majority of the filaments observed were transmural filaments, which may not be as straight as initial filaments. The half depth scar produced slightly more U shaped filaments compared to the full depth scar region. Irregular scars did not produce consistent configuration with epiMod1 and epiMod2 dynamics.

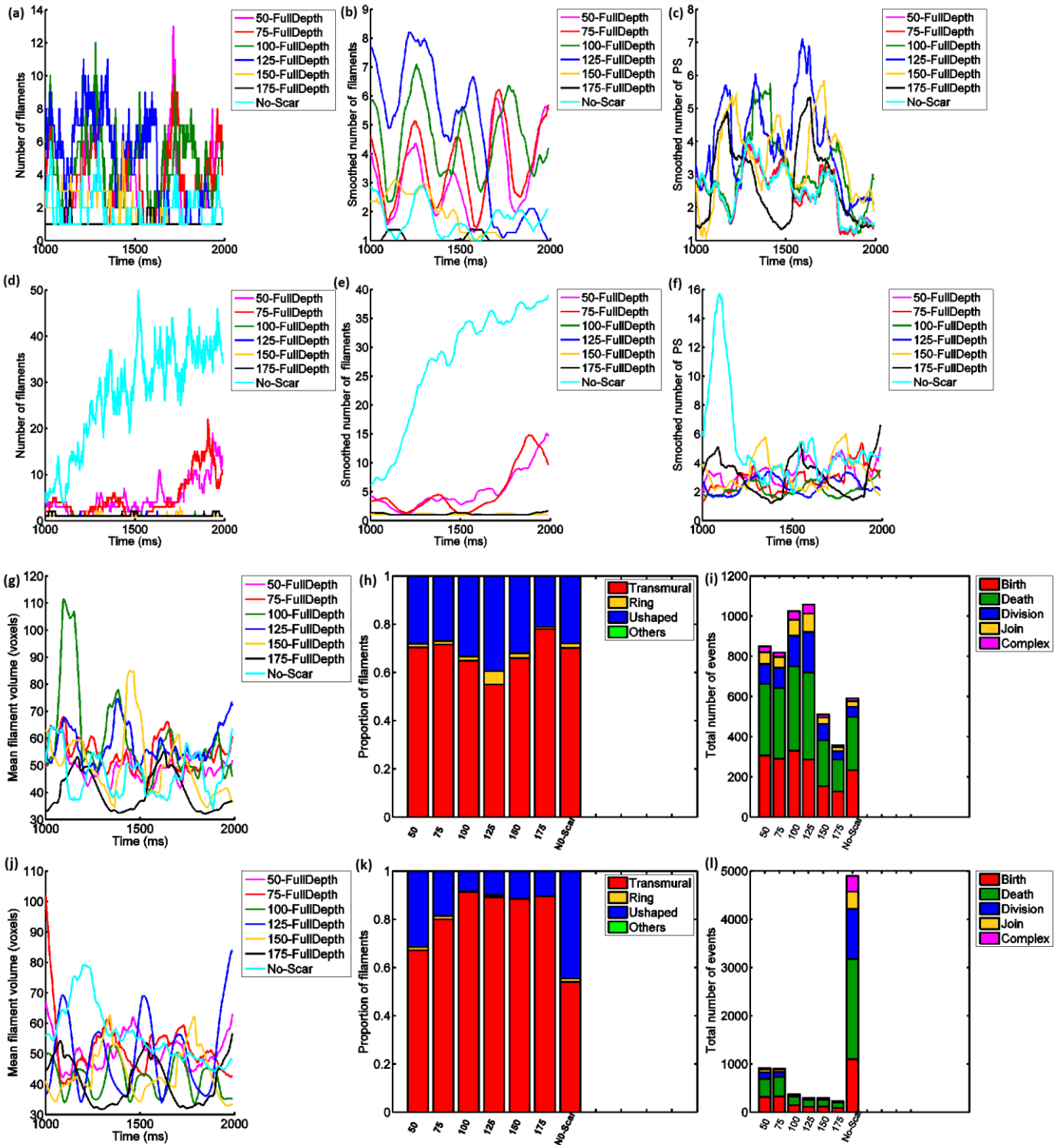

Figure 5.13 Comparing filament dynamics in fulldepth scar and no scar region in idealized LV (a)-(c) and (g)-(i) epiMod1 dynamics, (d-f) and (j)-(l) epiMod2 dynamics. (a) Change in number of filaments over time (ms) in epiMod1; (b) Smooth view in change in number of filaments in epiMod1; (c) smooth view of change in PS over time in epiMod1; (d) Change in number of filaments over time (ms) in epiMod2; (e) Smooth view in change in number of filaments in epiMod2; (f) smooth view of change in PS over time in epiMod2; (g) Mean volume of filaments over time in epiMod1; (h) configuration of filaments in epiMod1; (i) Total number of events in epiMod1; (j) Mean volume of filaments over time in epiMod2; (k) configuration of filaments in epiMod2; (l) Total number of events in epiMod2. In (h), (i), (k), (l) each bar are in the order as 50 (10mm), 75(15mm), 100 (20mm), 125 (25mm), 150(30 mm), 175 (35mm).

5.3.3.5 Life Time of Filaments

The lifetime of the initial filament gives an insight into filament behaviour. Figure 5.23 shows initial filament lifetime. The greater the radius of the scar region, the higher the initial filament lifetime as was the case in half depth scar. With a half depth scar of radius 30mm, initial filament gene sustained even after 1990ms.

Half depth irregular and full depth irregular scars had similar initial filament lifetimes. Filament lifetime was not consistent with half depth irregular scar with epiMod1 and epiMod2 dynamics.

Full depth irregular scars had longer lived filaments compared to full depth regular scars and the lifetime increased with radius size since clustering of filaments near irregular full depth scar border was greater compared to full depth regular scar.

5.3.3.6 Number of Events

The number of events gives an insight into how the number of filaments changes over the course of time. With epiMod1 dynamics, the number of events was higher when the scar region was incorporated in the idealized LV. However, when the radius of the full depth scar was either 30mm or 35 mm, the number of events was not high.

Figure 5.24 shows the proportion of events. Simulations with epiMod2 dynamics had c. 40-50 percent more events compared to simulations with epiMod1 dynamics. With epiMod2 dynamics, the number of events was higher compared to epiMod1 dynamics in the idealized LV without scar.

The proportion of filaments that divide and amalgamate was much smaller compared to the number of births and deaths overall, with or without transmural scarring. With epiMod2 dynamics, division and amalgamation was slightly reduced with scarring. According to Winfree and Strogatz (1984), pinning of filament inside cardiac tissue can only be possible for pairs of filaments that rotate in opposite directions, because of continuous phase around the filament. These pinned filaments cannot branch. As clustering of filaments to scar boundary in epiMod2 dynamics was greater compared to epiMod1, the filaments in epiMod2 dynamics did not divide and amalgamate much.

Half depth scars had more events compared to full depth scars. Irregular half depth and regular full depth scars had more events compared to half depth and full depth irregular scars. The number of events increased with size of scar but not consistently in epiMod2 dynamics. As the size of scar increased, full depth irregular scars produced more events compared to half depth irregular scars.

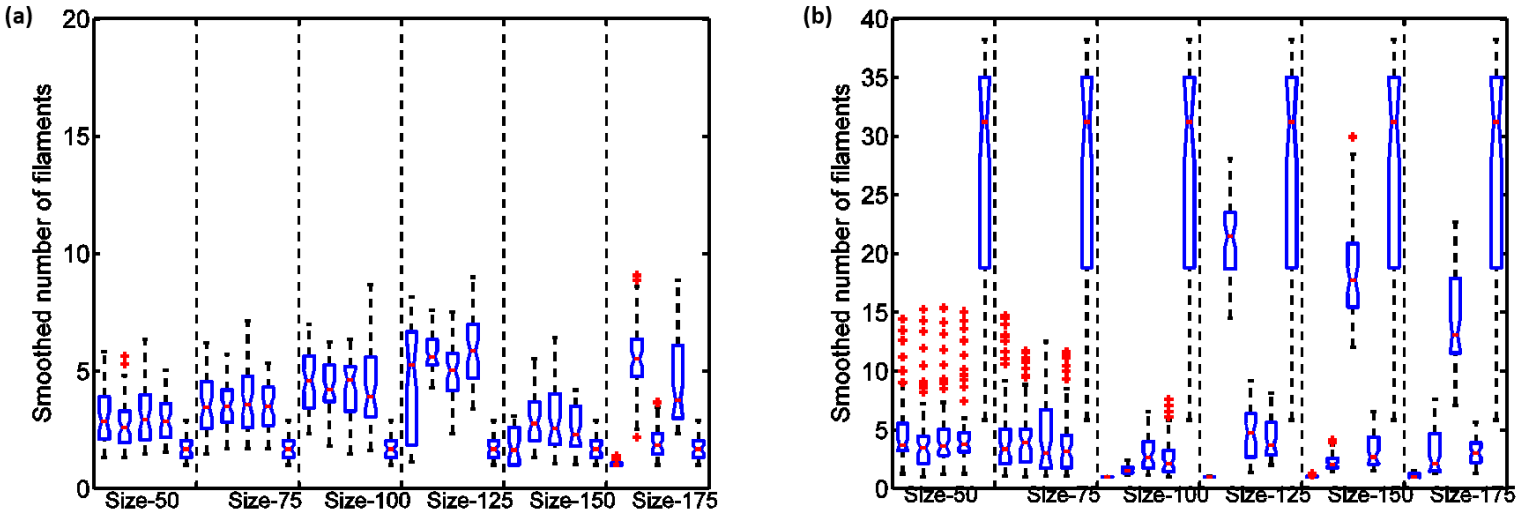

Figure 5.14 Box plot showing smooth number of filaments in (a) epiMod1 dynamics; (b) epiMod2 dynamics. In box plot for each radius the results show: full depth regular scar, full depth irregular scar, half depth scar, half depth irregular scar, no scar region. Size 50 is 10 mm scar, Size75 is 15mm scar, Size 100 is 20mm is scar, Size 125 is 25mm is scar, Size 150 is 30mm scar and Size 175 is 35mm scar.

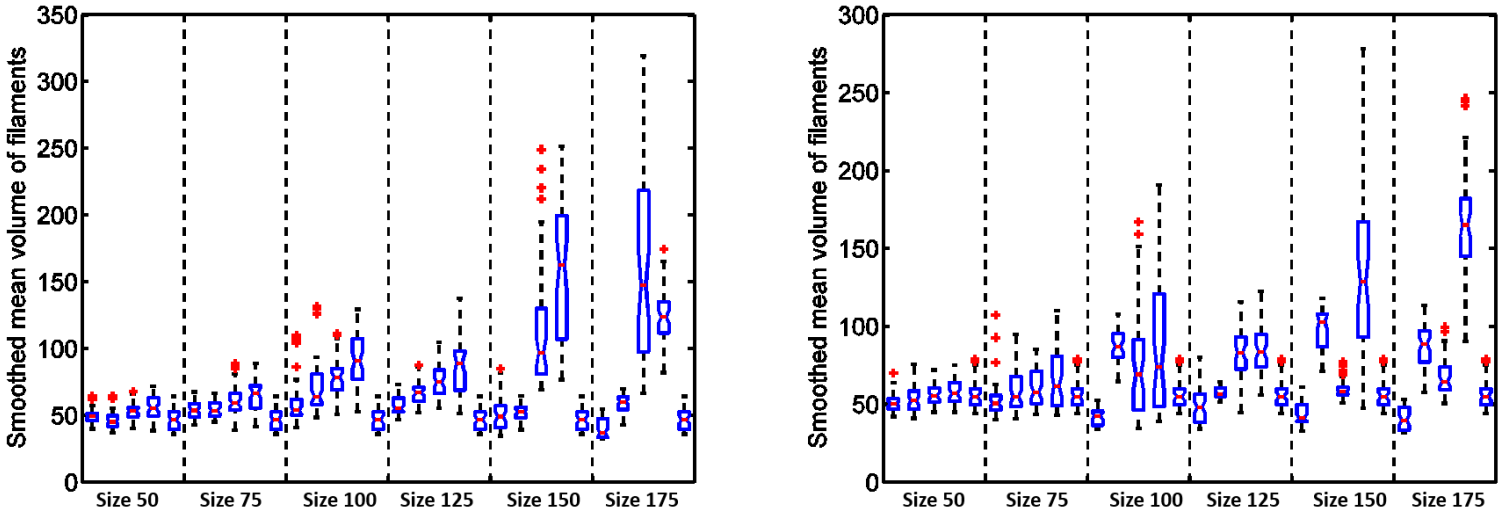

Figure 5.15 Box plot showing mean volume of filaments in (a) epiMod1 dynamics; (b) epiMod2 dynamics. In box plot for each radius the results show: full depth regular scar, full depth irregular scar, half depth scar, half depth irregular scar, no scar region. Size 50 is 10 mm scar; size75 is 15mm scar; size 100 is 20mm is scar; size 125 is 25mm is scar; size 150 is 30mm scar; and size 175 is 35mm scar.

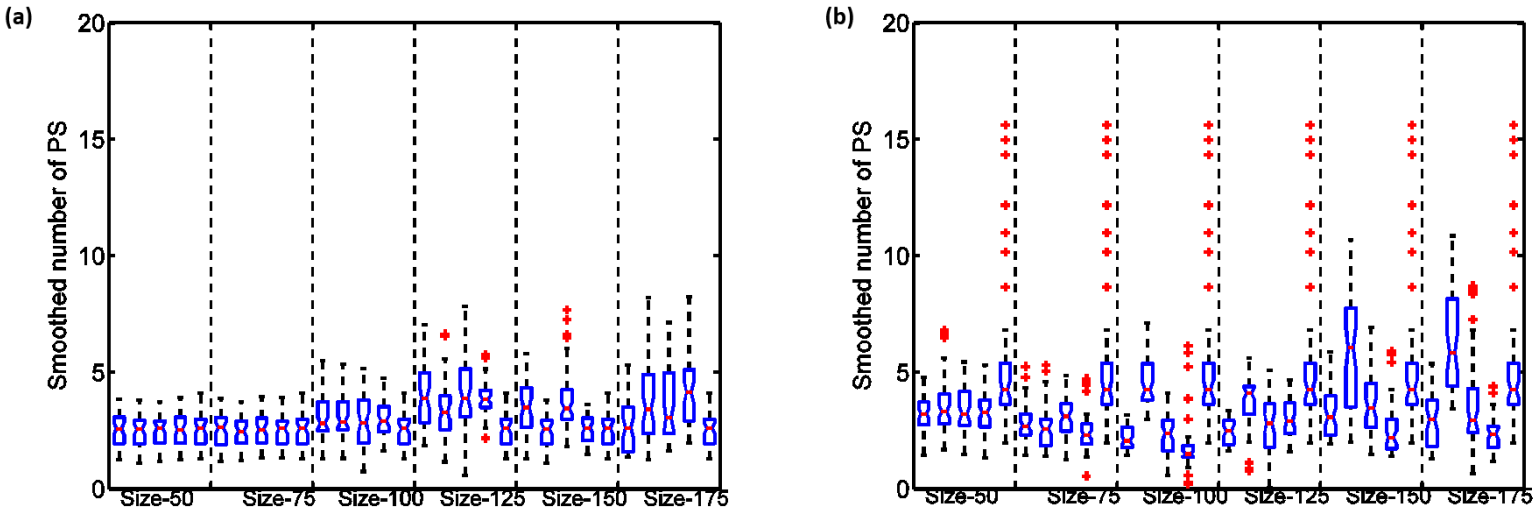

Figure 5.16 Box plot showing smooth number of PD in (a) epiMod1 dynamics; (b) epiMod2 dynamics. Box plot for each radius the results show: full depth regular scar, full depth irregular scar, half depth scar, half depth irregular scar, no scar region. Size 50 is 10 mm scar; size75 is 15mm scar; size 100 is 20mm is scar; size 125 is 25mm is scar; size 150 is 30mm scar; and size 175 is 35mm scar.

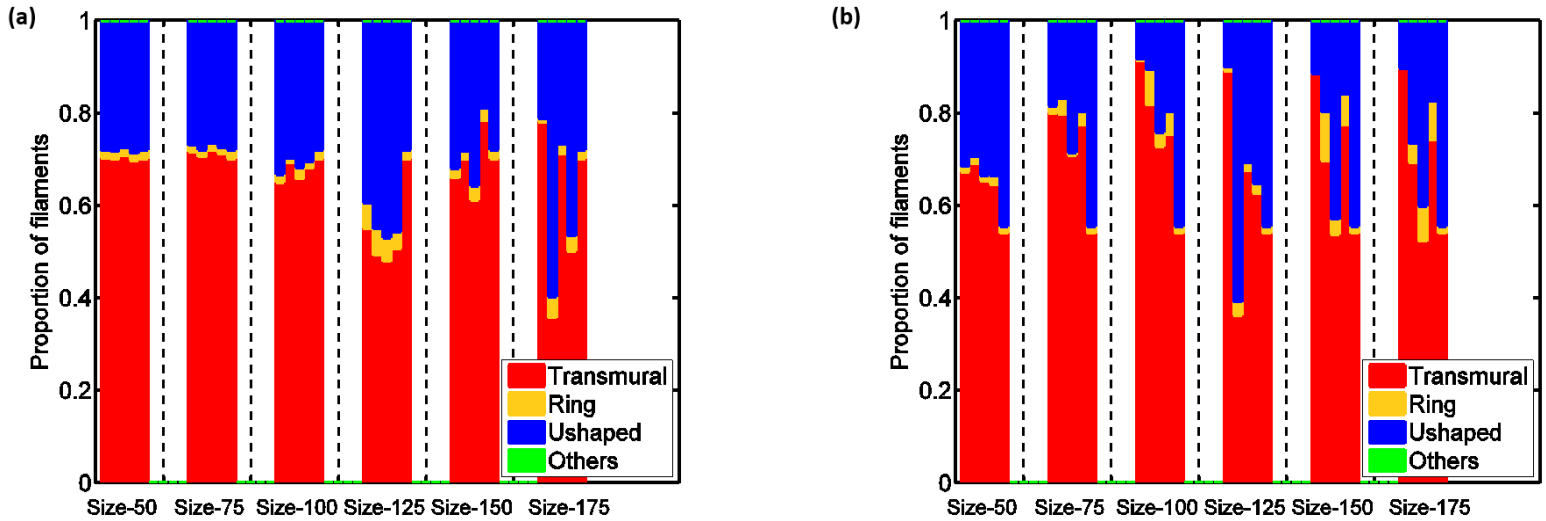

Figure 5.17 Stack bar showing proportion of configuration of filaments in (a) epiMod1 dynamics; (b) epiMod2 dynamics. Stack plot for each radius the results show: full depth regular scar, full depth irregular scar, half depth scar, half depth irregular scar, no scar region. Size 50 is 10 mm scar; size75 is 15mm scar; size 100 is 20mm is scar; size 125 is 25mm is scar; size 150 is 30mm scar; and size 175 is 35mm scar.

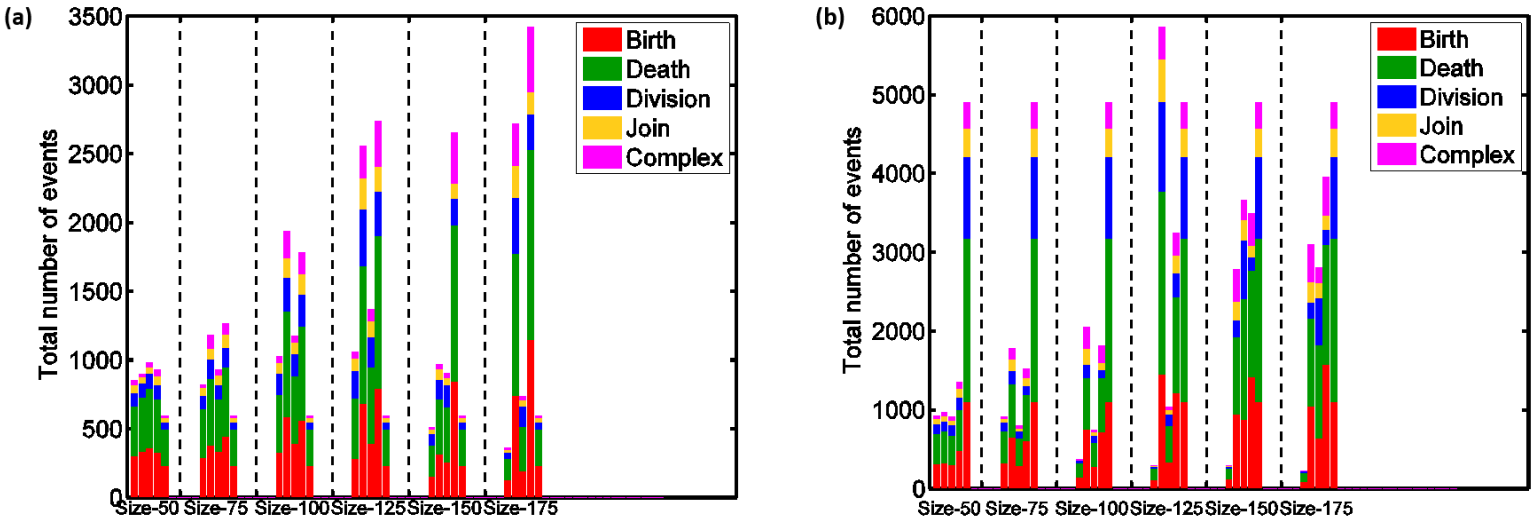

Figure 5.18 Stack bar showing proportion of events (a) epiMod1 dynamics; (b) epiMod2 dynamics. Stack plot for each radius the results show: full depth regular scar, full depth irregular scar, half depth scar, half depth irregular scar, no scar region. Size 50 is 10 mm scar; size75 is 15mm scar; size 100 is 20mm is scar; size 125 is 25mm is scar; size 150 is 30mm scar; and size 175 is 35mm scar.

5.4 Summary of Results

This chapter investigated the influence of circumferential, transmural sub endocardial scars with regular and irregular boundaries on filament dynamics as summarized below:

- Transmural scars in the slab geometry did not greatly influence the number or configuration of filaments (Figure 5.7 (a), (b), (d) and (e)).
- Number of events increased with transmural scars compared to no scar region, especially with epiMod1 dynamics in the slab geometry (Figure 5.7 (i) and (l)).
- Circumferential scars in the idealized LV showed no significant influence on filament dynamics (Figure 5.10).
- Varying the size of transmural and sub endocardial transmural scars with regular and irregular boundaries in the idealized LV :
    1) Did not show important differences in the number of filaments and filament configuration in both dynamics (Figures 5.14 (a) and (b) and 5.17 (a) and (b)).
    2) Filament length, lifetime and number of events were increased (Figure 5.15 (a) and (b), Figure 5.21 (a) and (b), Figure 5.18 (a) and (b)).
    3) A smaller number of events and increased filament lifetime were observed with epiMod2 dynamics compared to epiMod1 dynamics (Figures 5.18 (a) and (b)5.21 (a) and (b)).
- Clustering of filaments was observed at the border of the transmural scar in both the slab and idealized LV. With epiMod2 dynamics, more clustering of filaments was observed compared to epiMod1 dynamics (Figure 5.11 (a) and (b)).
- Sub endocardial transmural scars (half depth) had more clustering of filaments compared to transmural (full depth) scars. With epiMod2 dynamics more clustering of filaments was observed compared to epiMod1 dynamics (Figure 5.11 (a) and (b)).
- Irregular scar boundaries had more clustering of filaments compared to regular scar boundaries (Figure 5.11 (a) and (b)).
- Sub endocardial irregular scar boundaries showed inconsistency with epiMod1 and epiMod2 dynamics (Figure 5.26 (d), (e), (f), (j), (k) and (l)).

5.5 Discussion

As epiMod2 dynamics showed more non-linear behaviour in both the slab and idealized LV, when there was small change in the initial filament, there was a large difference in number of filaments (Figures 4.22 (d) and 4.35 (d)); pinning of filaments to the scar boundary was seen more with epiMod2 dynamics compared to epiMod1. Non-linear dynamic systems support multiple attractors. Increase in the size of scar region showed more clustering of filaments at the scar boundary as increased radius tends to have more multiple attractors in non-linear dynamic systems and, therefore, anchors more filaments. As explained by Massé et al. (2007), fictitious centrifugal force around the rotating system may tend to co-localize the rotating system to the border of the slow conducting tissue since conduction block of AP occurs in the border of slow conducting tissue. This may be why clustering of filament voxels near the scar boundary was observed.

Overall, the different sizes of transmural scar did not show significant differences in the average number of filaments as shown in Figure 5.19. With epiMod2 dynamics, a transmural scar of radius 10 mm produced approximately 10 more filaments on average compared to the largest scar (35 mm). This may be because as the radius increases, so does clustering of filaments at the border of the scar region. Pinning reduces the branching of filaments (Winfree and Strogatz 1984), which could explain why less filaments were seen. Pinning increased filament volume as seen in Figure 5.20; therefore, increase in scar region radius increased filament volume.

Cumulative life of filaments increases proportionately with the radius of scar, whereas it is the opposite with short lifetime (Figures 5.21 and 5.22). This shows sustainment of filaments without breaking because of pinning to the scar boundary. The lesser number of events in epiMod2 dynamics in Figure 5.17 also supports the view that sustainment of filaments results from pinning of filaments to scar boundary. Correlation in Figure 5.26 is not smooth because of inconsistent clustering of filaments to the half depth non regular scar boundary.

The lifetime of the initial re-entrant filament increased with scar region radius but the effect was seen more in epiMod2 than epiMod1 dynamics. Initial filament lifetime was increased up to 400 ms in simulations with bigger scars. For epiMod2 dynamics, with a half depth regular scar region of 30 mm, the initial filament lived beyond 1990 ms. This can be explained as more clustering of filaments was seen with a 30 mm half depth regular scar compared with other scars as shown in Figure 5.25.

Half depth regular scars (sub-endocardial) showed more clustering compared to full depth regular scars (transmural scars). Clustering of filaments to irregular scar boundaries was greater compared to regular scar boundaries. As explained in Shajahan et al. (2007), in dynamic systems, a fractal like boundary separates the strange attractor basins of attractors from fixed point basins of attractors. So non-linear behaviour is associated with strange attractors and this might be the reason for observing more filament clustering near half depth regular scar and irregular scar boundaries (Figure 5.11). Half

depth irregular scars showed inconsistency in filament clustering and dynamics with epiMod1 and epiMod2 dynamics (Figure 5.26). More clustering of filaments was observed with epiMod1 dynamics compared to epiMod2 dynamics. This explains why the fractal like boundary (Shajahan et al. 2007) has more influence than steep and shallow restitution dynamics. In the real heart, irregular scarring is likely and, therefore, more clustering of filament voxels to the irregular boundary indicating more sustained filaments and hence sustained VF. Consequently, it may be necessary to measure the radius and depth of the pre-existing scar in VF patients to determine the strength of defibrillation needed to stop VF.

This simulation shows that transmural and sub-endocardial transmural scars had more sustained filaments compared to circumferential scars. Circumferential scar did not affect filament dynamics and showed no clustering of filaments at the scar boundary as the proportion of circumferential scarring was very small compared to the proportion of LV wall and, perhaps, because of the position (Figures 5.9 and 5.10).

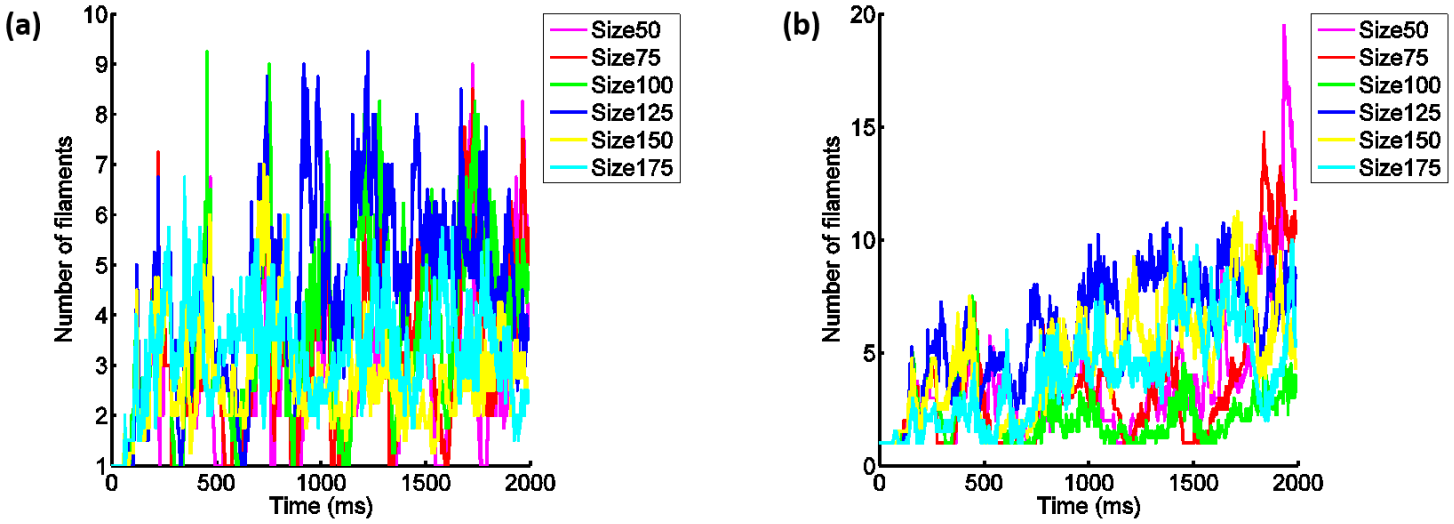

Figure 5.19 Average of (full, half depth in both regular and irregular scar) number of filaments in each radius (a) epiMod1 dynamics; (b) epiMod2 dynamics. Size 50 is 10 mm scar; size75 is 15mm scar; size 100 is 20mm scar; size 125 is 25mm scar; size 150 is 30mm scar; and size 175 is 35mm scar.

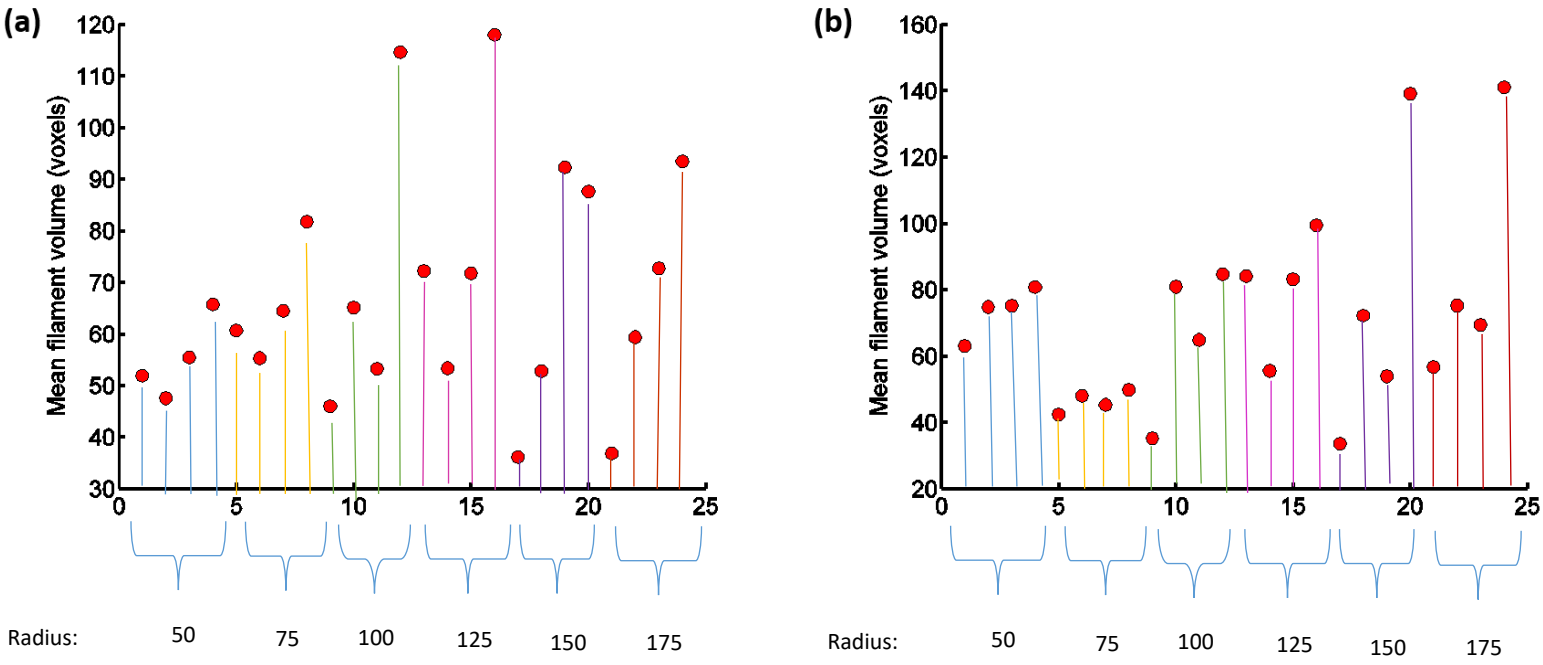

Figure 5.20 Scatter graph showing how mean filament volume changes with different radius and with regular and irregular full depth and half depth scar region in (a) epiMod1 dynamics; (b) epiMod2 dynamics. Coloured lines shows are added for clear view. For each radius scatter plot shows in the order: full depth regular scar, full depth irregular scar, half depth scar, half depth irregular scar. Size 50 is 10 mm scar, Size75 is 15mm scar, Size 100 is 20mm is scar, Size 125 is 25mm is scar, Size 150 is 30mm scar and Size 175 is 35mm scar.

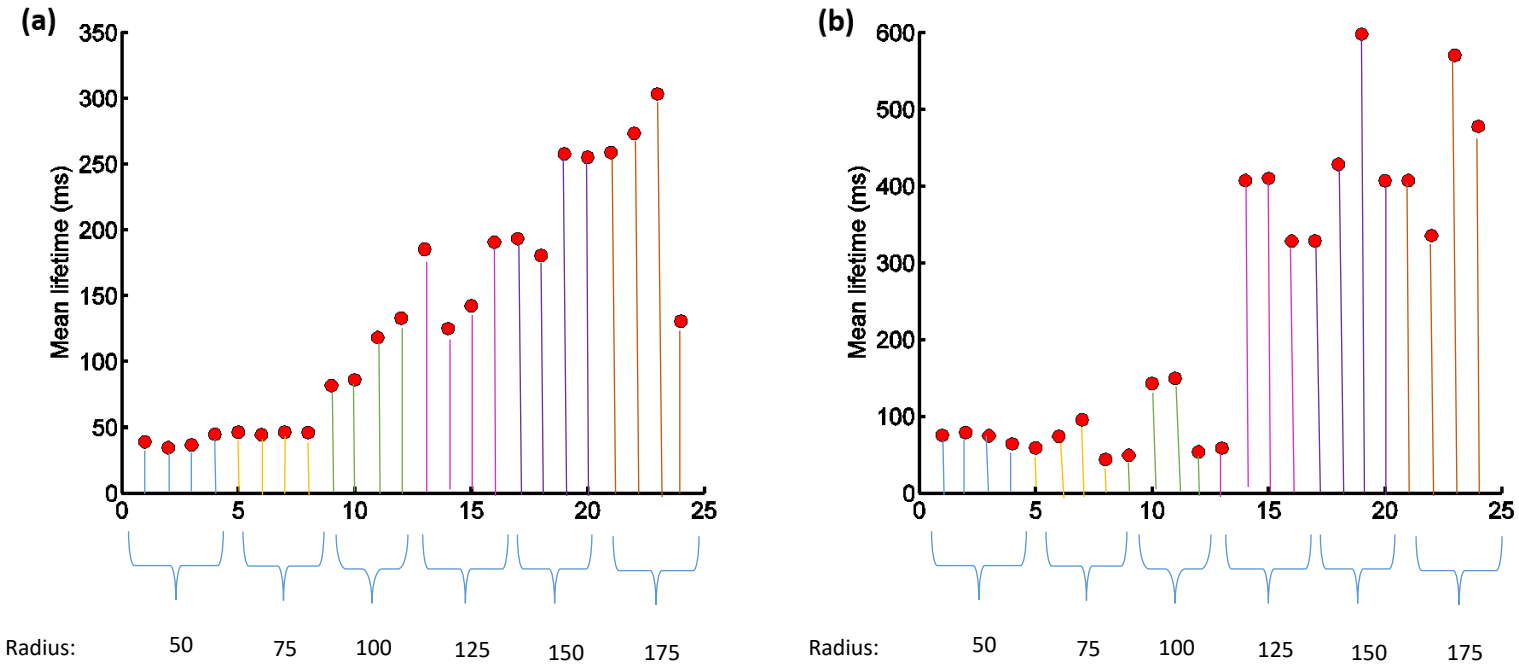

Figure 5.21 Scatter graph showing how cumulative life time changes with different radius and regular and irregular full depth and half depth scar region in (a) epiMod1 dynamics; (b) epiMod2 dynamics. Coloured lines shows are added for clear view. For each radius scatter plot shows in the order: full depth regular scar, full depth irregular scar, half depth scar, half depth irregular scar. Size 50 is 10 mm scar; size75 is 15mm scar; size 100 is 20mm scar; size 125 is 25mm is scar; size 150 is 30mm scar; and size 175 is 35mm scar.

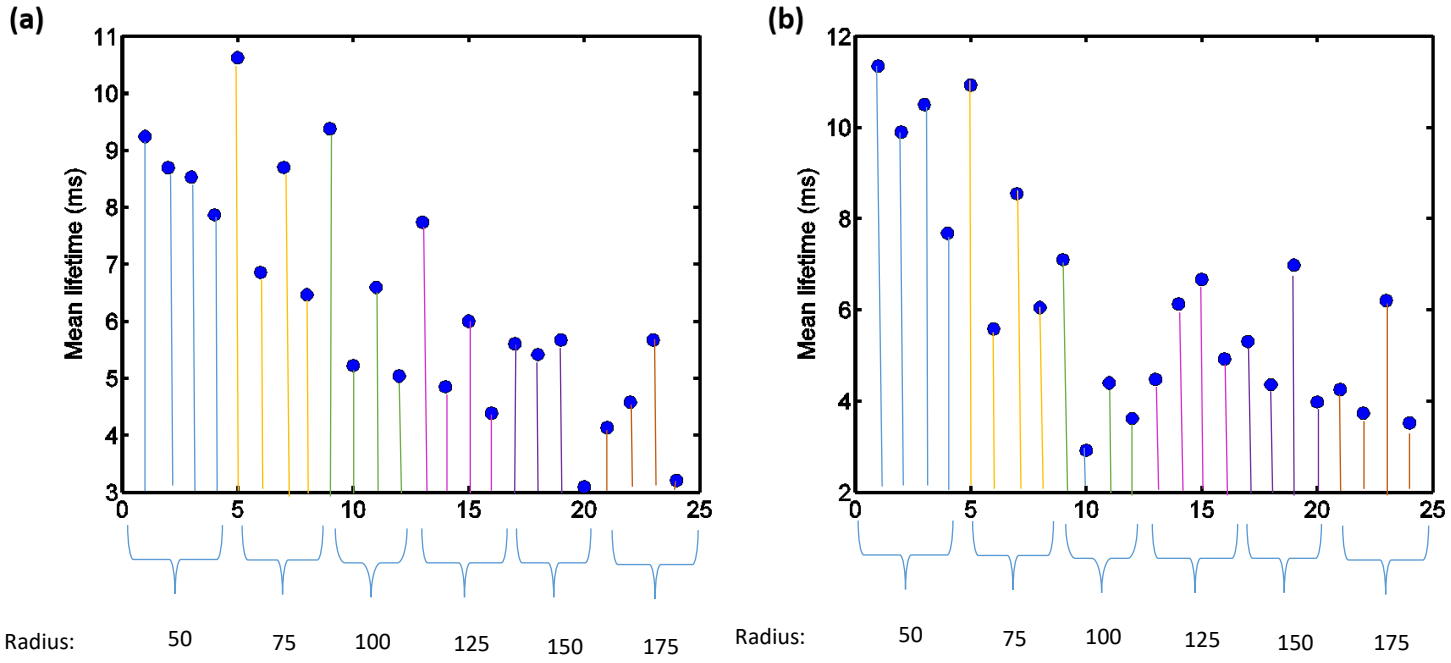

Figure 5.22 Scatter graph showing how short life time changes with different radius and regular and irregular full depth and half depth scar region in (a) epiMod1 dynamics; (b) epiMod2 dynamics. Coloured lines shows are added for clear view. For each radius scatter plot shows in the order: full depth regular scar, full depth irregular scar, half depth scar, half depth irregular scar. Size 50 is 10 mm scar; size75 is 15mm scar; size 100 is 20mm scar; size 125 is 25mm scar; size 150 is 30mm scar; and size 175 is 35mm scar.

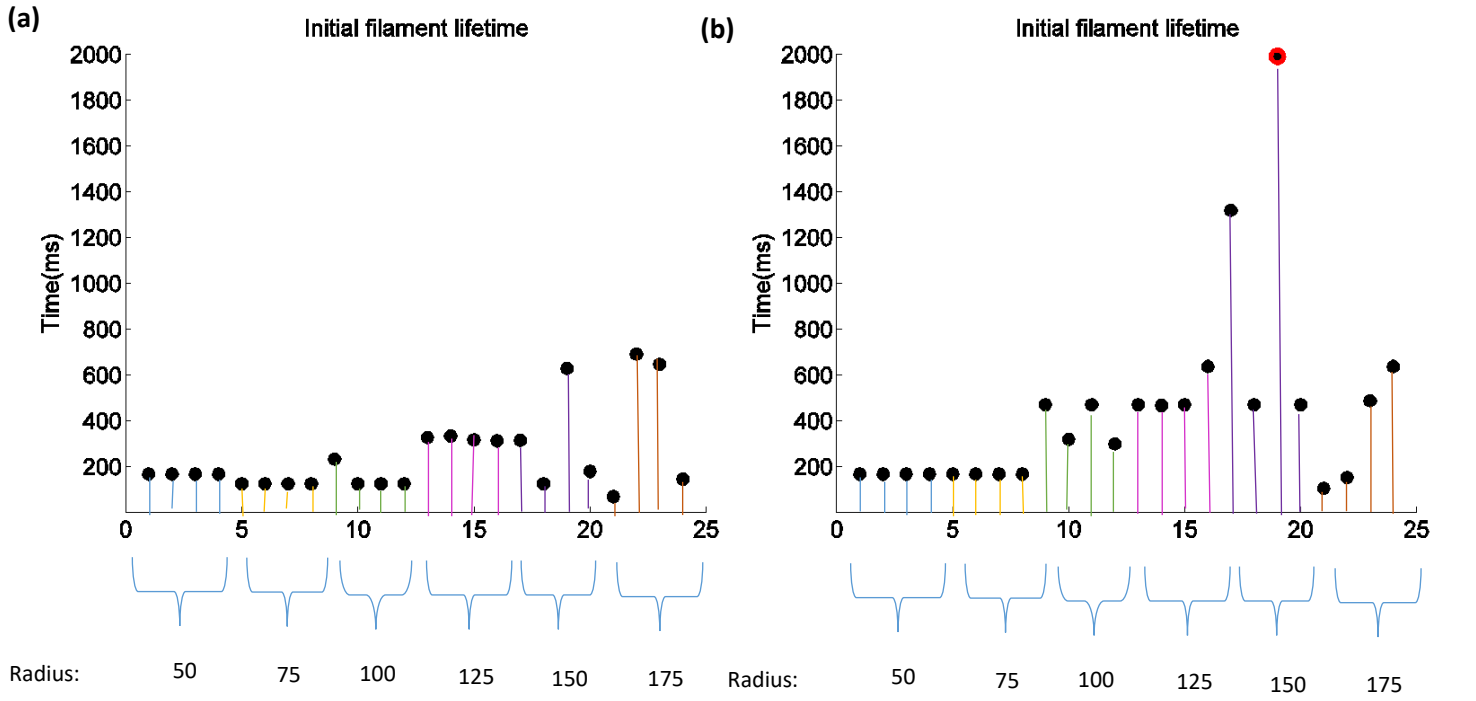

Figure 5.23 Scatter graph showing how initial filament life time changes with different radius and regular and irregular full depth and half depth scar region in (a) epiMod1 dynamics, (b) epiMod2 dynamics. Red bordered scatter plot shows initial filament lived even after 1990ms. Coloured lines shows are added for clear view. For each radius scatter plot shows in the order: full depth regular scar, full depth irregular scar, half depth scar, half depth irregular scar. Size 50 is 10 mm scar; size75 is 15mm scar; size 100 is 20mm is scar; size 125 (25 mm) scar; size 150 (30 mm) scar; and size 175 (35 mm).

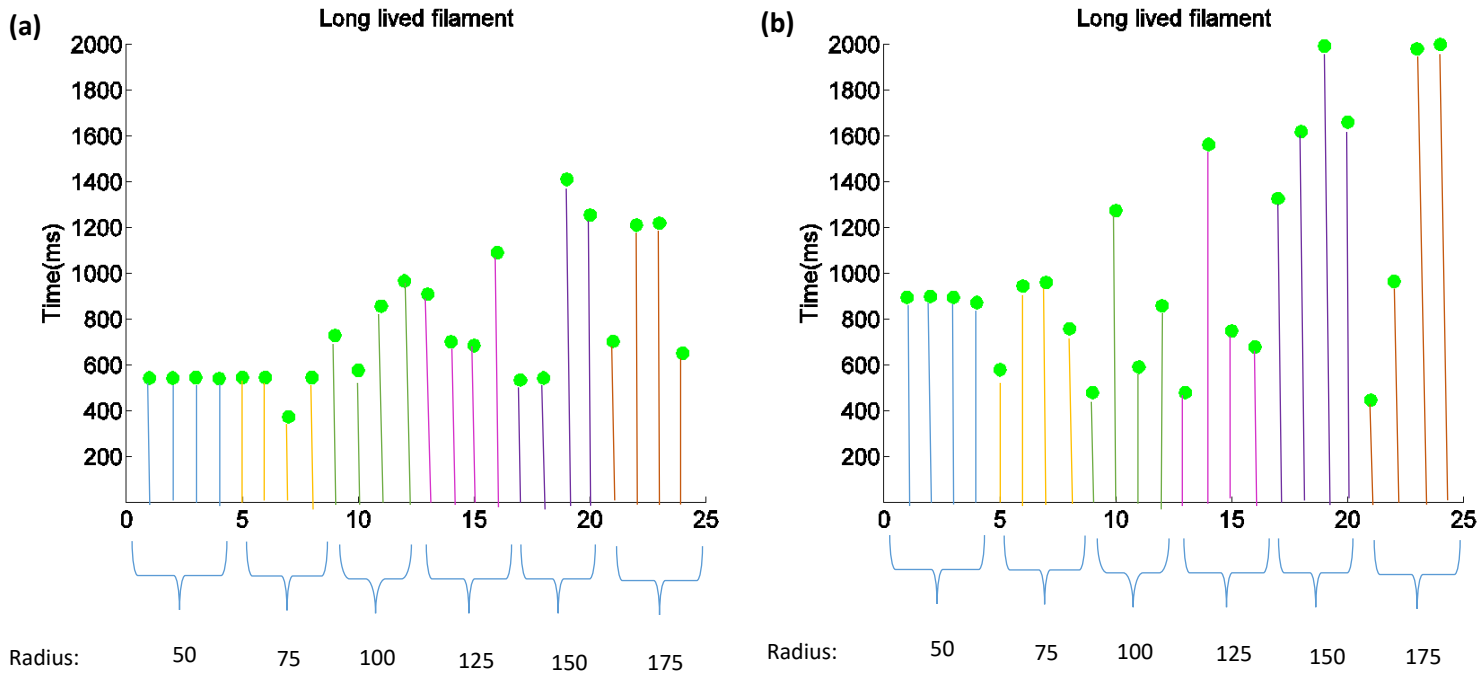

Figure 5.24 Scatter graph showing how 'long lived' filament changes with different radius and regular and irregular full depth and half depth scar region in (a) epiMod1 dynamics; (b) epiMod2 dynamics. Coloured lines shows are added for clear view. For each radius scatter plot shows in the order: full depth regular scar, full depth irregular scar, half depth scar, half depth irregular scar. Size 50 is 10 mm scar; size75 is 15mm scar; size 100 (20 mm) scar; size 125 (25 mm) scar; size 150 (30mm) scar; and size 175 (35mm) scar.

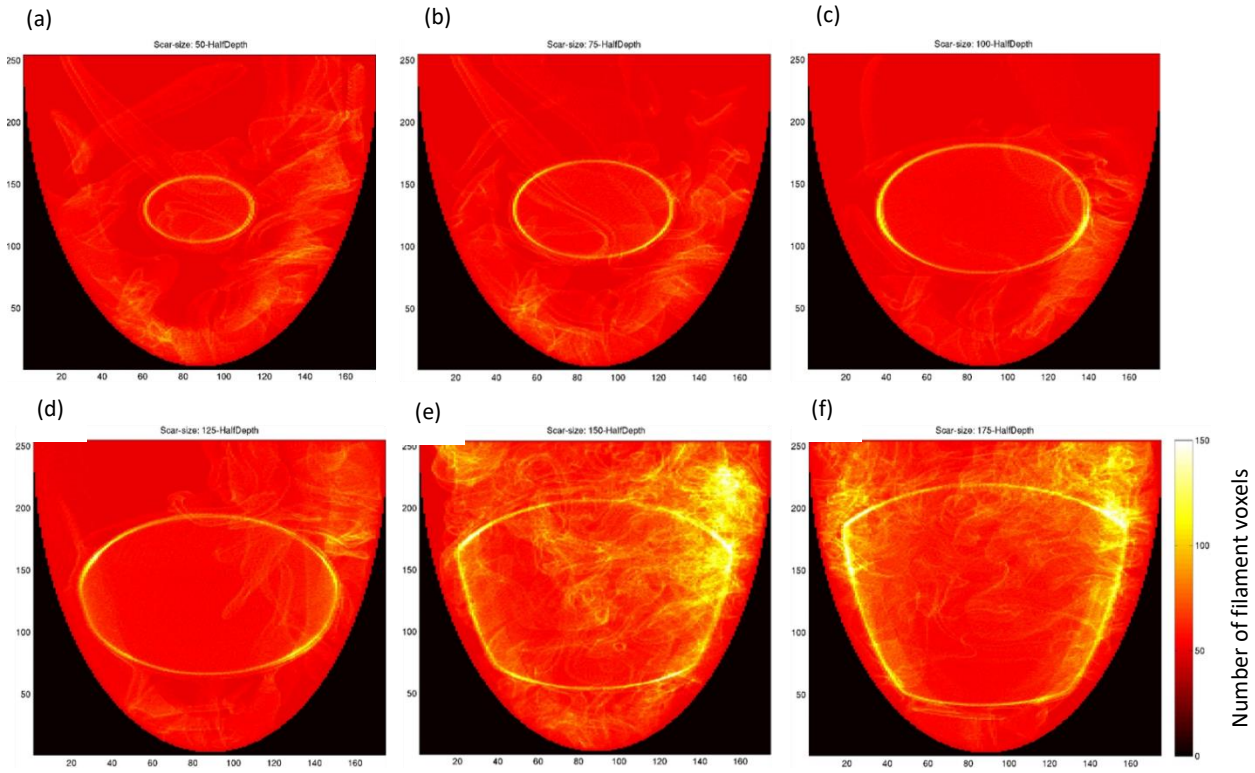

Figure 5.25 clustering of filaments in epiMod2 dynamics with varying size half depth radius (regular scar) (a) 50 (10mm); (b) 75 (15mm), (c) 100 (20mm); (d) 125(25mm); (e) 150(30 mm) and (f) 175 (35 mm).

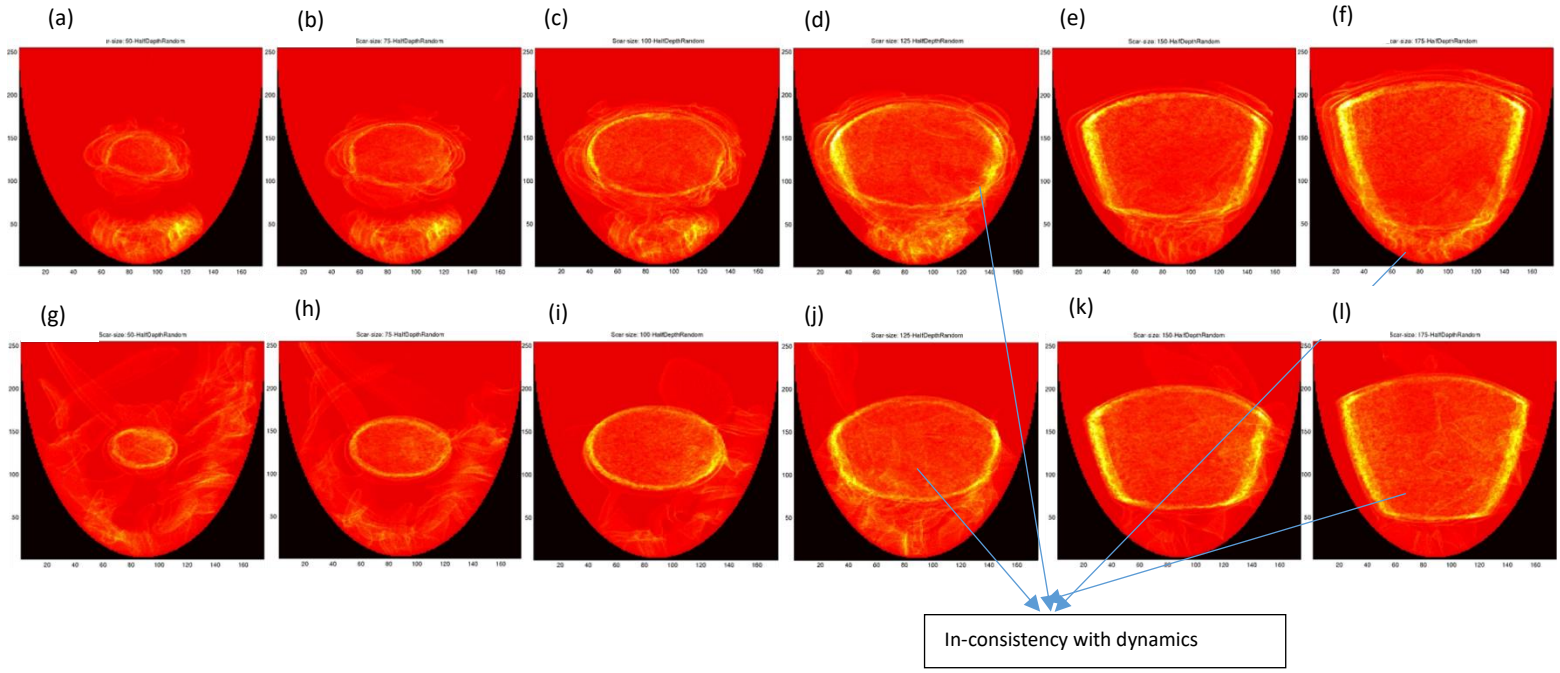

Figure 5.26 Clustering of filaments near half depth irregular scar boundary (a)-(f) in epiMod1 dynamics; (g)-(l) in epiMod2 dynamics. In varying radius (a) and (g) shows 50(10mm); (b) and (h) shows 75(15 mm); (c) and (i) shows 100 (20 mm); (d) and (j) shows 125 (25 mm; (e) and (k) shows 150 (30mm); (f) and (l) shows 175 (35 mm).

5.5.1 Oscillations in Number of Filaments

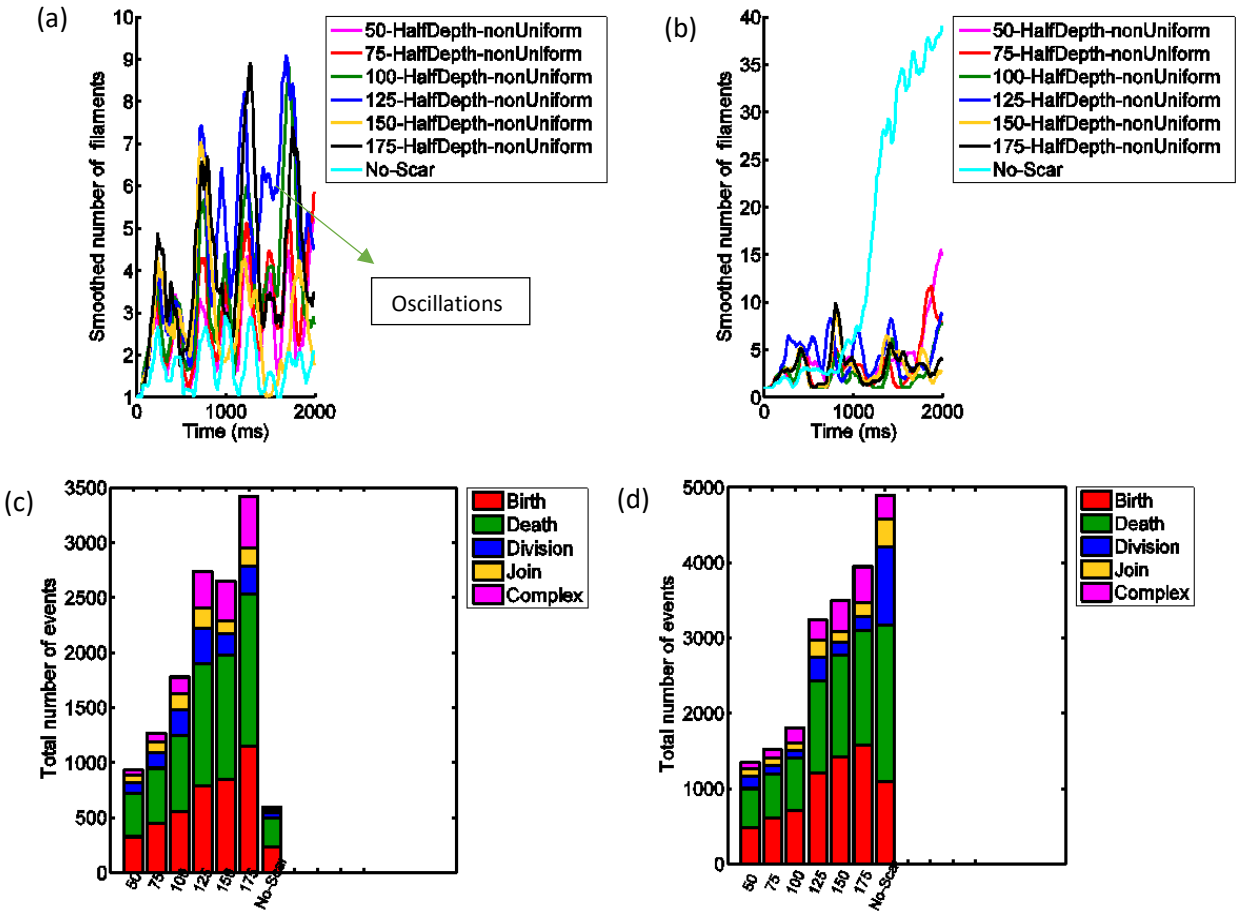

Figure 5.27 Smooth number of filaments in half depth irregular scar in different radius in idealized LV (a) showing oscillations in smooth number of filaments in epiMod1 dynamics; (b) Smooth number of filaments in epiMod2 dynamics; (c) Total number of events in epiMod1 dynamics (in the order: 50, 75, 100, 125, 150, 175 and No scar); (d) Total number of events in epiMod2 dynamics (in the order: 50, 75, 100, 125, 150, 175 and No scar). (In the above figure nonUniform means irregular scar).

The smooth view of number of filaments in epiMod1 dynamics showed more oscillations compared to epiMod2 dynamics. Fluctuations in the number of filaments can be caused by a very quick change in number of filaments in a short period of time as shown in Figure 5.27. With epiMod1 dynamics, the total number of events was higher in the idealized LV with scar region compared with no scar region, showing more events can be associated with fluctuations in the number of filaments.

An additional reason for the lower number of events in the idealized LV with scar region with epiMod2 dynamics could be more pinning of filaments to the scar boundary; this may not have allowed filaments to branch (Winfree and Strogatz 1984).

The reason for oscillations in number of filaments in epiMod1 dynamics was investigated by examining the period of re-entry. The re-entry period in epiMod1 dynamics for scar region of radius

25 mm with half depth non-regular scar was around 231 ms, and for epiMod2, it was around 282.5ms. This seems to be reasonable since epiMod2 dynamics have bigger APD than epiMod1 dynamics (see Figure 4.15 (a)). So the frequency of re-entry with epiMod1 dynamics was around 4.3196 Hz, and for epiMod2 dynamics, it was around 3.5398 Hz. So with epiMod1 dynamics, re-entry has higher frequency compared to epiMod2 dynamics. High frequency of re-entrant wave affects its stability and frequently breaks forming more filaments; this might explain oscillations in number of filaments.

Chapter 6 Discussion and Conclusions

The aim of this thesis was to investigate the effect of the shape, initial conditions, tissue structure and disease on the human ventricular tissue and filament dynamics. This chapter summarises the main hypothesis examined in this thesis, discusses possible mechanisms, answers key questions and outlines limitations and future directions of study.

6.1 Summary of Results

Transmural heterogeneity of distribution of different cell types did not show significant differences in numbers of filaments, presumably because of electrotonic effects; however, clustering of filaments was observed in the border of endo - epi with 2 layer profile and in the border of endo - M and M - epi with 3 layer profile. During VF, the activation interval has a small DI as shown in the conduction velocity restitution curve (Figure 4.15 (c)) and minimum DI shows minimum conduction velocity. In the conduction velocity restitution curve, minimum conduction velocity of endo cell was less than M cell, and minimum conduction velocity of M cell was less than epi cells. Clustering of filaments in endo - epi and endo - M , M - epi in transmural heterogeneity might be caused by fictitious centrifugal force pushing filaments to the border of slow conduction velocity as explained by Massé et al. (2007). Clustering of filaments near slow conducting border did have an impact on filament lifetime and volume.

Since transmural heterogeneity showed no important difference in the number of filaments in the slab geometry, transmural heterogeneity was not incorporated in the idealized LV as the key interest was to see if the shape of the geometry had an impact on filament number. Chapter Four showed that in epiMod2 dynamics, the number of filaments was twice as high in idealized LV compared to slab geometry as the volume of the idealized LV was twice that of the slab.

Both uniform (idealized LV and 3D slab) and transmural heterogeneity in the slab geometry indicated non-linear behaviour by showing huge change in the number of filaments when there was small change in initial condition, as explained by Cherry et al. (2012). Transmural heterogeneity of endo - epi profile in the slab geometry showed more non-linear behaviour compared to uniform, endo - M - epi and endo - M patch epi. In both the geometries, epiMod2 dynamics showed more non-linear behaviour compared to epiMod1.

Non-linear dynamic systems support multiple attractors. These multiple attractors can pin more filaments. Both slab (endo-epi) with scar region and idealized LV with scar region showed more clustering of filaments near the scar boundary in epiMod2 compared to epiMod1 dynamics. Since epiMod2 dynamics showed more non-linear behaviour compared to epiMod1 dynamics, this might be the reason for observing more clustering near scar boundary in epiMod2 dynamics as multiple attractors are supported.

Circumferential scar did not show any impact on filament dynamics or on the clustering of filaments near the scar boundary; this may be because of the very small scarring compared to the proportions of the idealized LV wall and the position of the scar. On the other hand, transmural scar had an impact on the clustering of filaments near the scar boundary and thus increased the filament volume and lifetime and decreased the number of events. This impact increased with the increase in the size of the transmural scar. Transmural scar did have a small effect on filament shape because of the heterogeneity in the tissue structure as normally uniform tissue did not affect filament configuration (Figure 4.16 (e)). Half depth regular scar (sub-endocardial) showed more clustering compared to full depth regular scar (transmural scar). Clustering of filaments to irregular scar boundary was more compared to regular scar boundary. As explained in Shajahan et al. (2007), in dynamic systems, fractal like boundaries separate the 'strange attractor' basins of attractors from fixed point basins of attractors, and the non-linear behaviour is associated with strange attractors. This might be the reason for observing more clustering of filaments near half depth regular scar and irregular scar boundaries. Half depth irregular scar showed inconsistency in clustering of filaments and in filament dynamics with epiMod1 and epiMod2 dynamics; Figure 5.26 shows the fractal-like boundary associated with multiple attractors has more influence on pinning filaments to the scar boundary (Shajahan et al. 2007) than steep or shallow restitution dynamics.

6.2 Answers to Key Questions

In Chapter Two, a list of key questions was formulated. In this section, brief answers to those questions are given and discussed in the light of the experiments conducted in this thesis. Key questions were formulated on filament dynamics and clustering of filaments to scar boundary. Filament dynamics refers to the number of filaments, shape or configuration of filaments, volume of filaments, lifetime of filaments and number of events. Clustering of filaments refers to clustering of filament voxels to scar boundary.

- **Comparison of the filament dynamics in simulated VF with simplified and biophysically detailed cell models**

  Both the detailed (TP06) and simplified (4-variable model) models showed similar behaviour in conduction velocity restitution in 2D. Model variants were compared depending on APDR curves.

  Even though the biophysically detailed TP06 model (ten Tusscher & Panfilov 2006) captures details of ion channels and calcium handling, there was no significant impact on the number, configuration and volume of filaments compared to the simplified model, the 4-variable model (Bueno-Orovio et al. 2008). Biophysically detailed models are computationally expensive, and so the simplified model was used in this thesis. Since both models showed similar filament dynamics, simulation results in this thesis will give similar results using the TP06 model. The focus of this thesis was the overall behaviour of re-entrant scroll wave filaments and not any specific ion channel effects. This justifies the use of the simplified 4-variable model for this thesis.

Moreover, research has shown (Qu et al. 2000a) that steep APD restitution is an important mechanism underlying re-entry compared to biological detail of ion channels. Two variants of the simplified 4-variable model were used: one with comparatively shallow restitution (epiMod1); and one with steep restitution (epiMod2) (Bueno-Orovio et al. 2008).

- **Does initial shape of the filament have an effect on filament dynamics?**

The effect of the initial filament configuration was tested by comparing filament dynamics in simulations where the initial condition was a single straight filament with simulations where the initial condition was a ring filament. The results showed similar numbers, configurations and lifetimes of filaments for the two cases. Modelling simple straight filaments is easier compared to ring filaments in 3D tissue. A simple untwisted filament was used as initial condition in this thesis. However, ring filaments are a more likely initial condition in real hearts.

- **Does transmural heterogeneity have effect on filament dynamics?**

Experimental and clinical studies have shown the existence of transmural heterogeneity of endo, epi and mid-myocardium regions in cardiac tissue, each region exhibiting differences in APD in animals (Sicouri & Antzelevitch 1991a, Antzelevitch et al. 1991). M cells have a longer APD compared to endo and epi cells. However, the existence of M cells remains a controversial topic. A study (Glukhov et al. 2010) on in vitro human left ventricular wall using optical mapping, showed the presence of M cells possibly in the form of islands. This study also showed that the regions of endo, epi and M cells are not sharply distributed as specified in other computational studies like Majumder et al. (2011). Consequently, this thesis studied the effect of sharp and smooth distribution of transmural heterogeneity including/excluding M cells and found that there was no important difference in the number of filaments.

Simulations with a sharp distribution of transmural heterogeneity and endo - epi (2 layer), endo- M - epi (3 layer) and M cells modelled as islands in between endo and epi regions (M-patch) did not show a huge impact on number of filaments. Uniform endo, epi and M tissue showed differences in APD as shown in Figure 4.15 (a). Tissue incorporated with transmural heterogeneity showed no difference in APD in both endo and epi edge of the tissue (Figures 4.17 (b) and 4.18 (b) even though the middle of the tissue had different APD measurement. As explained in Taggart et al. (2003) and Collie et al. (2006), local electrotonic cancellation of gradients in APD between diffusively coupled different cell types may be the reason for not observing any important difference in number of filaments.

Massé et al. (2007) recorded electrical activity from epicardium and endocardium of in vivo human heart and found that re-entrant waves pin to the border of region with the slowest conduction velocity because fictitious centrifugal force drives re-entrant waves to the slow conducting border in the tissue. This fictitious force is responsible for conduction block near slow

conducting domains. Minimum conduction velocity of endo cells was less than M cells and minimum conduction velocity of M cells was less than epi cells (Figure 4.15 (c)). Results showed clustering of filaments in endo-epi region in 2 layer and endo-M and M-epi in 3 layer (Figures 4.17 and 4.18) supporting the point made by Massé et al. (2007). Clustering of filaments increased filament lifetime.

- **Does the shape of the tissue geometry (sharp against curved) have an effect on filament dynamics?**

The shape of the tissue geometry had an effect on number of filaments. With epiMod2 dynamics, the idealized LV had nearly double the number of filaments compared to slab geometry. The surface area of the idealized LV (18000 mm^2) was more than the 3D slab (6400 mm^2); the number of filaments was greater in idealized LV compared to 3D slab. Even the volume of the idealized LV was twice that of the slab geometry. In slab geometry, filaments could move away from a boundary and disappear, whereas in idealized LV geometry, filaments could move around to the other side of the geometry and the volume of the idealized LV was approximately twice that of the slab.

Comparing filament configurations in 3D slab and idealized geometry was not straightforward as the endo and epi surfaces in both geometries were different. In spite of that, the configuration of filaments showed similar results. Only slab geometry showed filaments that were categorized as 'others' because of the sharp edges of the slab and 6 different faces. Idealized LV, however, has curved edges with 2 faces, so categorisation of filaments as 'others' was not applicable. The category 'others' can be considered as intramural filaments; due to the shape of the idealized LV, it had only transmural, ring and U shaped filaments.

- **Testing the non-linear behaviour of VF**

A small change in the input resulting in a huge difference in output is considered non-linear behaviour. Non-linear behaviour of cardiac tissue was studied in 2D by making small changes to the S1S2 protocol (Cherry et al. 2012). In this thesis, non-linear behaviour of the activation pattern during VF in 3D slab and idealized LV was studied by perturbing the initial filament.

Non-linear behaviour of activation pattern during VF was tested on uniform epi and sharp distribution of transmural heterogeneity on 2-layer, 3-layer and patch in 3D slab. Since transmural

heterogeneity in 3D slab did not show a huge effect on the filament numbers, in the idealized LV, transmural heterogeneity was not included. Non-linear nature in uniform idealized LV was tested.

Both slab and idealized LV showed more non-linear behaviour in activation pattern during VF in epiMod2 dynamics compared to epiMod1 dynamics. A small change to the input by perturbing initial filament gave a huge change in output, i.e. number of filaments. This shows that in both slab and idealized LV, epiMod2 dynamics is a more dynamic system compared to epiMod1 dynamics. Transmural heterogeneity of 2-layer in 3D slab showed more non-linear behaviour compared to uniform, 3- layer and M - patch.

- **Do size, depth, regular and irregular boundaries influence pinning of filaments to the scar boundary?**

    - **Size of scar region**

      Size of scar had a huge effect on clustering of filaments to the scar boundary. The greater the radius of the scar showed more clustering in both dynamics, but comparatively more in epiMod2 dynamics. Non-linear behaviour was observed with epiMod2 dynamics compared to epiMod1 dynamics. Non-linear systems support multiple attractors, so the bigger the radius, the more attractors (strange attractors). More strange attractors in the scar boundary pin more filaments to it as explained in Shajahan et al. (2007).

    - **Depth of scar region**

      Half depth scar (sub-endocardial) had more clustering compared to full depth scar proving the fractal-like boundary (Shajahan et al. 2007) in half depth scar is more chaotic compared to full depth scar.

- **Regular and irregular scar boundary**

  Irregular scar had more clustering compared to regular scar, proving again that the fractal-like boundary in non-uniform scar is more chaotic compared to uniform scar boundary (Shajahan et al. 2007).

- **Does the region of scar affect the filament dynamics?**

  - **Comparing the effect of scar region on filament dynamics in slab geometry**

    The number and configuration of filaments did not show significant effects. The number of events was almost doubled in the slab with scar in epiMod1 dynamics compared to no scar; however, this was not the case with epiMod2 dynamics. This may be because more clustering of filaments was observed in epiMod2 dynamics compared to epiMod1. Filaments pinned to the scar boundary cannot branch (Winfree and Strogatz 1984); this may be the reason for observing lesser events with epiMod2 dynamics.

  - **Comparing the effect of circumferential scar on filament dynamics in idealized LV**

    The number, volume and configuration of filaments did not show any differences in both epiMod1 and epiMod2 dynamics. Even number of events did not show difference, since there was no clustering of filaments near the scar boundary. This may be because of the very low proportion of scar region compared to the proportions of the wall of the idealized LV and the position of the scar. In dynamic systems, a fractal-like boundary separates the 'strange attractor' basins of attractors from the fixed point basins of attractors, and the reason for not observing non-linear behaviour may be associated with fixed point attractors (Shajahan et al. 2007).

  - **Does the size of the scar have an effect on filament dynamics in idealized LV?**

    There was an increase in the number of filaments in epiMod1 dynamics with scar compared to without scar, but the difference was not huge. The difference ranged from 4 - 6 filaments. Volume of filaments without scar in idealized LV was around 50, but with scar region the volume of filaments increased from 60 to 210 with increase in size of scar. Shape of filaments was not affected. In epiMod1 dynamics, the number of events increased with size of scar region.

    In epiMod2 dynamics, the number of filaments in the idealized LV without scar was greater compared with the idealized LV with scar region; the difference was around 5 - 25 filaments

for small to big scar radius. Volume of filaments increased from 60 - 250 with size of the scar. The number of events increased with the size of the scar, but the number of events in idealized LV without scar was comparatively greater than idealized LV with scar.

Overall, the size of the scar did not influence the number or configuration of filaments but did increase filament volume and lifetime.

- **Does the depth of the scar-size in the scar have an effect on filament dynamics in idealized LV?**

Bigger scars showed difference in the number of filaments when the depth of the scar was halved in both dynamics; however, this was not great in epiMod1 dynamics. In epiMod2 dynamics, the number of filaments showed a difference of 20 filaments in bigger scars (30 mm and 35 mm radius) compared to smaller scars. Even the volume of filaments increased in bigger scars when the depth of the scar was halved. The number of events and filament lifetime increased in half depth scar compared to full depth scar in both dynamics.

- **Do the regular and irregular scar boundaries affect filament dynamics in idealized LV?**

The number, volume and configuration of filaments did not show important differences between regular and irregular scars. The number of events was always higher in irregular scars compared to regular scars in both epiMod1 and epiMod2 dynamics. However, irregular half depth scars did not show consistent results.

Overall, fractal-like scar region boundary and scar radius played more important roles in filament dynamics and in clustering of filaments to the scar boundary.

6.3 Validation

Results obtained from simulation studies need to be carefully validated against experimental/clinical results. The results in this thesis were validated on point singularities (PS). The human heart is a 3D object and the electrical activity recorded mostly from epicardial surface; it is easier to compare epicardial PS observed in experimental/clinical studies with PS observed in simulation studies. This section shows how the results from this thesis were validated. Since APD restitution of normal epicardial cells and epimod1 variant showed similar results (Figure 4.3), validation was made with PS observed in uniform epicardial tissue with epiMod1 dynamics.

During VF in the human heart, experimental studies have reported that the median number of epicardial PS is 8 (Nash et al. 2006, Bradley et al. 2011). If the human heart is considered to be a half ellipse with a basal diameter of 80 mm and a base apex distance of 100 mm, the epicardial surface area is about 21,000 mm^2.

According to Nash et al. (2006), the dominant frequency of transmembrane voltage was around 6Hz at the onset of VF in the human heart.

6.3.1 Slab and Idealized LV

Slab

The surface area of the human heart is about 3.3 times the epicardial surface area of the slab geometry used in this study (6400 mm^2). Assuming linear scaling, a median value of 2.4 epicardial PS in uniform epiMod1 would be expected for comparison with human data.

In the 3D slab, which was about one third of the volume of typical human ventricles, VF frequency of about 4.8309 Hz is reasonable in epiMod2 dynamics. This can be used as a validation point for checking fibrillatory nature of re-entry in slab geometry.

Idealized LV

The surface area of the idealized LV geometry used in this study was approximately 18000 mm^2. The surface area of the human heart is around 1.2 times the surface area of the idealized LV used in this study. Therefore, linear scaling of observed PS in the human heart gives around 6.7 epicardial PS. However, in the epiMod1 dynamics with no scar, the PS observed was around 4.9. This can be justified by use of a simplified idealized left ventricle. In the idealized LV, VF frequency measured around 4.205 Hz in epiMod2 dynamics.

6.4 Limitations

There are several limitations underlying the approach taken in this thesis, and these are discussed in turn below.

6.4.1 Simplified Geometry

Simplified tissue geometry was used in this thesis. The complexity of real geometry with uncertain fibre orientations, complex boundary conditions, etc. was not used. Bishop & Plank (2012) showed that the fine scale anatomical features in detailed geometry did not show much difference in filament dynamics compared to simplified geometry. Simplified geometries give an insight into the electrical propagation and mechanisms underlying VF without the complications of tissue structure; also, it is simple to model and test hypotheses. Moreover, incorporation of scar regions with various radii and types is unproblematic in simplified geometry; hence, simplified slab and idealized LV models were used in this thesis.

6.4.2 Single Transmural Filament as Initial Condition

In this thesis, a single transmural filament was used as the initial condition for inducing re-entry. The initial conditions of re-entry in the real heart that are likely to occur spontaneously are either a single ring filament or a pair of filaments. However, ring filaments as an initial condition did not show much difference in filament dynamics compared to a single transmural filament. Clearly, it would be interesting to test pairs of filaments as initial condition.

For transmural heterogeneity - sharp vs smooth - input to the initial condition of re-entry has not been changed according to the smooth distribution. Initial condition was based on sharp heterogeneity. Since the electrotonic effect nullifies transmural electrical gradient (Taggart et al. 2003, Colli Franzone et al. 2006), this initial condition should not affect filament dynamics significantly.

6.4.3 Including Orthotropic Diffusion

Benson et al. (2011) compared orthotropic diffusion mapped from rat heart histology with anisotropic diffusion and showed there was a difference in filament behaviour. The code in the SCAM that includes anisotropic diffusion can be changed to include the orthotropic diffusion equation in Equation 6.1.

$$d_{ij} = D_1 f f^T + D_2 s s^T + D_3 n n^T \quad (6.1)$$

where D_1 D_2 and D_3 are diffusion coefficients longitudinal to fibres, normal to fibres in the sheet plane, and normal to both fibres and sheets (Colli Franzone et al. 2005); fibre sheet orientation can be adopted from the study done in canine ventricle (Costa et al. 1997). Sheet orientation changes linearly from $+30^o$ at the endocardium to -10^o at the sub epicardium. Diffusion coefficients D1, D2 and D3 can be set in the ratio of 4:1.8:1 as in Caldwell et al. (2009) to get plausible conduction velocity.

Experimental studies have shown fibre and fibre sheet structure in animal hearts (LeGrice et al. 1995, Lunkenheimer et al. 2006). At the time of writing, fibre sheet data were not available for the human heart. Ten Tusscher et al. (2007) showed the difference in organisation of VF in animal heart is more complex compared to the human heart, since minimum APD in the restitution for the human heart is longer compared to the animal heart. Since in this thesis VF was induced by steep (epiMod2) and relatively shallow restitution (epiMod1) variants of the cell model, fibre sheet information obtained from animals was not included.

6.4.4. Mechanics

Cardiac mechanics were not included in this thesis. However, studying the effect of tissue structure and disease on mechanical contractions during simulated VF is an important area of research. An electromechanical modelling study (Keldermann et al. 2010) reported that the deformation of ventricular tissue during contractions was enough for scroll wave breakup. Consequently, factors such as negative filament tension, fibre orientation and restitution are not required for scroll wave breakup.

Fibre and fibre sheet orientation in cardiac tissue plays a crucial role during mechanical contractions (Geerts et al. 2002). However, at the time of writing, fibre sheet data from human ventricles were not available.

6.4.5 Simulated Scar

In this thesis, a simulated scar region was modelled where the region scar had inexcitable cells but diffusively coupled to the virtual tissue. However, in the real human heart, the border zone of scar regions interlocks with regions of normal tissue. This thesis studied only one type of simulated scar at a time, but in the real human heart, it might be possible to have multiple scars of different type formed due to myocardial infarction (MI). This was not tested in this thesis.

6.4.6 Change in Fibre Structure in the Region of Scar

Fibre orientation in and around the scar region was not varied in the simulations, whereas in real cardiac tissue, the fibre orientation might restructure during the formation of myocardial scar regions (Wickline et al. 1992).

Despite the above six limitations, this thesis has managed to compare the effect of transmural heterogeneity, the non-linear nature of the heart and the influence of simulated scar regions with regular and irregular edges, with full depth and half depth on re-entrant filaments during VF; something which is difficult to observe experimentally.

6.5 Future Direction

6.5.1 Idealised Ventricle Incorporating Both Left and Right Ventricle with Fibre Direction

Idealized geometry incorporating LV and Right ventricle (RV) can be used to test how filament dynamics change. A right ventricle was created exactly like the left ventricle as a half ellipsoid (base-apex 7.5 cm, wall thickness 0.4 cm) with LV radius 1.9cm since RV has thin wall compared to LV and different apex base dimensions. The RV was cut in half and attached to the LV. Figure 6.1 shows a cross section of idealized geometry incorporating both LV and RV. Even though fibre rotation is linear in LV and RV wall, there is discontinuity of fibre orientation between RV and LV at the septum (Nielsen et al. 1991) as shown in Figure 6.1 (b). As shown in Keldermann et al. (2009), it would be very interesting to study further mother rotor fibrillation and filament dynamics. Since the bi-ventricle is not symmetric, it could be used to study the effect of anterior and posterior scars on filament dynamics and clustering of filaments to the scar boundary.

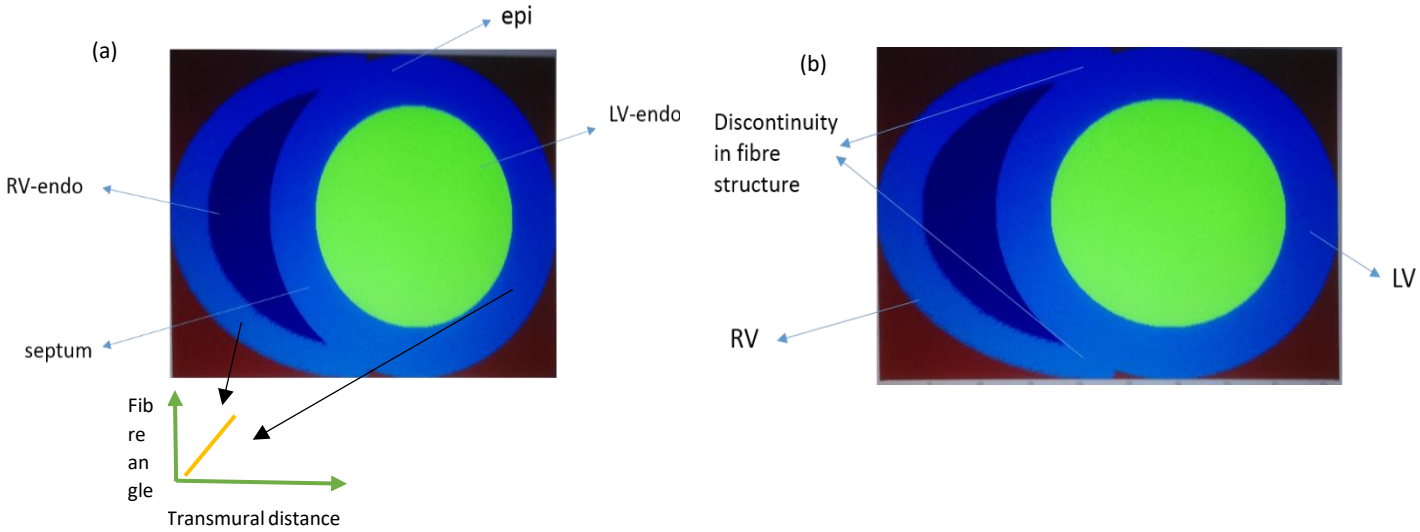

Figure 6.1 Cross section of RV+LV (a) showing linear change in fibre direction in RV and LV wall; (b) showing position of discontinuity in fibre orientation between RV and LV.

6.5.2 Anatomically Detailed Geometry

The next logical step would be to study filament dynamics in anatomically detailed ventricular geometry obtained from MRI, to test the influence of individuals' ventricle shapes on filament dynamics. Healthy and unhealthy (scar) anatomically detailed MRIs of ventricles can be obtained from Johns Hopkins (hopkinsmedicine.org). Raw MRI images normally include noise and need to be filtered. MRI images should be changed to Cartesian coordinates to be compatible with SCAM. If fibre orientation information is not available in MRI, either anisotropic or orthotropic fibre orientation can be modelled.

6.6 Conclusions

- Transmural heterogeneity of cell distribution did not affect the number of filaments but did show clustering near endo-epi border in 2 layer and endo-M in 3 layer and hence increased filament lifetime.
- The shape of the tissue influenced the number of filaments.
- This thesis highlights non-linear behaviour of activation patterns during VF where small changes can have a large influence on the number of filaments in both 3D slab and idealized LV especially in epiMod2 dynamics.
- Circumferential scars did not affect filament dynamics or the clustering of filaments along the scar boundary as they were small in comparison to the wall thickness in idealized LV; position of the scar can be another reason for this.
- In the presence of full depth transmural scar, epiMod2 dynamics had more clustering compared to epiMod1 dynamics.
- Transmural sub-endocardial scars showed more clustering compared to fully developed transmural scars.
- Scar regions with irregular boundaries showed more clustering compared to scar regions with regular boundaries.
- Half depth (sub-endo) irregular scars showed inconsistency in clustering of filaments and in filament dynamics with epiMod1 and epiMod2 dynamics. More clustering of filaments was observed with epiMod1 dynamics compared to epiMod2 dynamics. This explains how the fractal-like boundary association with strange attractors (Shajahan et al. 2007) had more influence on pinning filaments than steep or shallow restitution dynamics.
- Generally, transmural scar region (full and sub-endocardial) did not increase the number of filaments much but did increase the length (volume) and lifetime of filaments due to scar boundary clustering, which can be hard to remove using defibrillation techniques (Luther et al. 2011).

In the real heart, ischemic scars tend to have irregular boundaries since the border zone of the scar region interlocks with normal tissue regions. Consequently, the fractal-like boundary zone can play an important role in pinning of filaments. Clustering of filaments to the scar boundary increases the lifetime and, hence, sustainment of filaments, i.e. VF.

Accurate measurement of the radius and depth of pre-existing scar tissue in patients may be needed as bigger (sub endocardial) scars are likely to have more clustering of filaments to their boundaries and increase the stability of filaments. In this way, it may be easier to predict the strength of defibrillation necessary to stop VF.

Bibliography

Antzelevitch, C. et al., 1991. Heterogeneity Within the Ventricular Wall. *Circulation research*, 69(6), pp.1427–1449.

Antzelevitch, C., 2010. M Cells in the Human Heart. , 18(9), pp.1199–1216.

Baher, A. et al., 2007. Short-term cardiac memory and mother rotor fibrillation. *American journal of physiology. Heart and circulatory physiology*, 292(1), pp.H180–9.

Beeler, B.Y.G.W. & Reuter, H., 1977. Reconstruction of the action potential of ventricular myocardial fibres. *Journal of Physiology*, pp.177–210.

Benoist, D. et al., 2012. Cardiac arrhythmia mechanisms in rats with heart failure induced by pulmonary hypertension. *American journal of physiology. Heart and circulatory physiology*, 302(11), pp.H2381–95.

Benson, A.P. et al., 2011. Construction and validation of anisotropic and orthotropic ventricular geometries for quantitative predictive cardiac electrophysiology. , (September 2010), pp.101–116.

Biktashev, V.N., 1998. Reentrant Waves and their Elimination in a Model Mammalian Ventricular Tissue. *Chaos*, 8(June), p.48.

Biktashev, V.N., Holden, A.V. & Zhang, H., 1994. Tension of Organizing Filaments of Scroll Waves. *Philosophical Transactions of the Royal Society A: Mathematical, Physical and Engineering Sciences*, 347(1685), pp.611–630.

Bishop, M. & Plank, G., 2010. Development of an anatomically detailed MRI-derived rabbit ventricular model and assessment of its impact on simulations of electrophysiological function. *American journal of physiology. Heart and circulatory physiology*.

Bishop, M.J. & Plank, G., The role of fine-scale anatomical structure in the dynamics of reentry in computational models of the rabbit ventricles Running title : Anatomical heterogeneity in arrhythmia. , 8500.

Bishop, M.J. & Plank, G., 2012. The role of fine-scale anatomical structure in the dynamics of reentry in computational models of the rabbit ventricles. *The Journal of physiology*, 590(Pt 18), pp.4515–35.

Bleeker, G.B. et al., 2006. Effect of posterolateral scar tissue on clinical and echocardiographic improvement after cardiac resynchronization therapy. *Circulation*, 113(7), pp.969–76.

Bradley, C.P. et al., 2011. Human ventricular fibrillation during global ischemia and reperfusion: paradoxical changes in activation rate and wavefront complexity. *Circulation. Arrhythmia and electrophysiology*, 4(5), pp.684–91.

Bray, M. a et al., 2001. Experimental and theoretical analysis of phase singularity dynamics in cardiac tissue. *Journal of cardiovascular electrophysiology*, 12(6), pp.716–22.

Bray, M.-A. & Wikswo, J.P., 2003. Interaction dynamics of a pair of vortex filament rings. *Physical review letters*, 90(June), p.238303.

Bray, M.-A. & Wikswo, J.P., 2002. Use of topological charge to determine filament location and dynamics in a numerical model of scroll wave activity. *IEEE transactions on bio-medical engineering*, 49(10), pp.1086–93.

Bueno-Orovio, A., Cherry, E.M. & Fenton, F.H., 2008. Minimal model for human ventricular action potentials in tissue. *Journal of theoretical biology*, 253(3), pp.544–60.

Caldwell, B.J. et al., 2009. Three distinct directions of intramural activation reveal nonuniform side-to-side electrical coupling of ventricular myocytes. *Circulation. Arrhythmia and electrophysiology*, 2(4), pp.433–40.

van Capelle, F.J. & Durrer, D., 1980. Computer simulation of arrhythmias in a network of coupled excitable elements. *Circulation Research*, 47(3), pp.454–466.

Cherry, E.M., Fenton, F.H. & Gilmour, R.F., 2012. Mechanisms of ventricular arrhythmias: a dynamical systems-based perspective. *American journal of physiology. Heart and circulatory physiology*, 302(12), pp.H2451–63.

Cherry, E.M., Greenside, H.S. & Henriquez, C.S., 2003. Efficient simulation of three-dimensional anisotropic cardiac tissue using an adaptive mesh refinement method. *Chaos*, 13(3), pp.853–865.

Choi, B.R., Liu, T. & Salama, G., 2001. The distribution of refractory periods influences the dynamics of ventricular fibrillation. *Circulation research*, 88(5), pp.E49–E58.

Choudhury, L. et al., 2002. Myocardial scarring in asymptomatic or mildly symptomatic patients with hypertrophic cardiomyopathy. *Journal of the American College of Cardiology*, 40(12), pp.2156–2164.

Clayton, R.H., 2008. Vortex filament dynamics in computational models of ventricular fibrillation in the heart. *Chaos (Woodbury, N.Y.)*, 18(4), p.043127.

Clayton, R.H. & Holden, A. V, 2002. A method to quantify the dynamics and complexity of re-entry in computational models of ventricular fibrillation. *Physics in medicine and biology*, 47(2), pp.225–38.

Clayton, R.H. & Panfilov, a V, 2008. A guide to modelling cardiac electrical activity in anatomically detailed ventricles. *Progress in biophysics and molecular biology*, 96(1-3), pp.19–43.

Colli Franzone, P., Pavarino, L.F. & Taccardi, B., 2006. Effects of transmural electrical heterogeneities and electrotonic interactions on the dispersion of cardiac repolarization and action potential duration: A simulation study. *Mathematical Biosciences*, 204, pp.132–165.

Colli Franzone, P., Pavarino, L.F. & Taccardi, B., 2005. Simulating patterns of excitation, repolarization and action potential duration with cardiac Bidomain and Monodomain models. *Mathematical biosciences*, 197(1), pp.35–66.

Cook, R.W., Edwards, J.E. & Pritt, R.-M.D., 1958. Electrocardiographic Changes in Acute Subendocardial Infarction. I. Large suben-docardial and large transmural infarcts. *Circulation*, 18, pp.603– 612.

Costa, K.D. et al., 1997. Three-dimensional residual strain in midanterior canine left ventricle. *The American journal of physiology*, 273(4 Pt 2), pp.H1968–H1976.

Durrer, D. et al., 1970. Total Excitation of the Isolated Human Heart. *Circulation*, 41(6), pp.899–912.

Dutta, S. & Steinbock, O., 2011. Topologically Mismatched Pinning of Scroll Waves. *The Journal of Physical Chemistry Letters*, 2(9), pp.945–949.

Ernest Frank, 1953. A comparative analysis of the eccentric double-layer representation of the human heart. *American journal of physiology. Heart and circulatory physiology*, 46, pp.364–378.

Fenton, F. & Karma, A., 1998. Vortex dynamics in three-dimensional continuous myocardium with fiber rotation: Filament instability and fibrillation. *Chaos (Woodbury, N.Y.)*, 8(1), pp.20–47.

Fenton, F.H. et al., 2002. Multiple mechanisms of spiral wave breakup in a model of cardiac electrical activity. *Chaos (Woodbury, N.Y.)*, 12(3), pp.852–892.

Fink, M. et al., 2011. Cardiac cell modelling: observations from the heart of the cardiac physiome project. *Progress in biophysics and molecular biology*, 104(1-3), pp.2–21.

Fink, M. et al., 2008. Contributions of HERG K+ current to repolarization of the human ventricular action potential. *Progress in biophysics and molecular biology*, 96(1-3), pp.357–76.

Fraser, A.M. & Swinney, H.L., 1986. Independent coordinates for strange attractors from mutual information. *Physical Review A*, 33(2), pp.1134–1140.

Frazier, D.W. et al., 1989. Stimulus-induced critical point. Mechanism for electrical initiation of reentry in normal canine myocardium. *The Journal of clinical investigation*, 83(3), pp.1039–52.

Garfinkel, a., 1999. An advanced algorithm for solving partial differential equation in cardiac conduction. *IEEE Transactions on Biomedical Engineering*, 46(9), pp.1166–1168.

Garfinkel, A. et al., 2000. Preventing ventricular fibrillation by flattening cardiac restitution. *Proceedings of the National Academy of Sciences of the United States of America*, 97(11), pp.6061–6.

Geerts, L. et al., 2002. Characterization of the normal cardiac myofiber field in goat measured with MR-diffusion tensor imaging. *American journal of physiology. Heart and circulatory physiology*, 283(1), pp.H139–H145.

Gilbert, S.H. et al., 2007. Regional localisation of left ventricular sheet structure: integration with current models of cardiac fibre, sheet and band structure. *European journal of cardio-thoracic surgery : official journal of the European Association for Cardio-thoracic Surgery*, 32(2), pp.231–49.

Glukhov, A. V et al., 2010. Transmural dispersion of repolarization in failing and nonfailing human ventricle. *Circulation research*, 106(5), pp.981–91.

Gordan, M., 1963. A computer model of atrail fibrillation. *American Heart Association and the National Heart Institute*.

Grandi, E., Pasqualini, F.S. & Bers, D.M., 2010. A novel computational model of the human ventricular action potential and Ca transient. *Journal of molecular and cellular cardiology*, 48(1), pp.112–21.

Gray, R. a. & Jalife, J., 1998. Ventricular fibrillation and atrial fibrillation are two different beasts. *Chaos (Woodbury, N.Y.)*, 8(1), pp.65–78.

Gray, R.A., 1995. Mechanisms of Cardiac Fibrillationin. *Science*, 270, pp.1222–1223.

Gray, R.A., Pertsov, A.M. & Jalife, J., 1998. Spatialandtemporal organizationduring cardiacfibrillation. *Nature*, 393, pp.1–5.

Greenbaum, R., Ho, S. & Gibson, D., 1981. Left ventricular fibre architecture in man. *British heart*, (July 1980), pp.248–263.

Hackel, D. & Wagner, G.S., 1995. Acute Circumferential Subendocardial Infarction. *Clinical Pathologic Correlations*, 174, pp.167–174.

Henriquez, C.S., 1993. Simulating the electrical behavior of cardiac tissue using the bidomain model. *Crit Rev Biomed Eng.*, 21(1), pp.1–77.

Henze, C., Lugosi, E. & Winfree, a. T., 1990. Helical organizing centers in excitable media. *Canadian Journal of Physics*, 68, pp.683–710.

Hodgkin, A. & Huxley, A.F., 1952. A quantitative description of membrane current and its application to conduction and excitation in nerve. *Journal of Physiology*, 117, pp.500–544.

Hodgkin, B.Y.A.L., 1954. A Note On Conduction Velocity. *Physiological laboratory*, (I 954), pp.221–224.

Holden, A. V & Zhang, H., 1993. Modelling propagation and re-entry in anisotropic and smoothly heterogeneous cardiac tissue. *Journal of the Chemical Society, Faraday Transactions*, 89(15), p.2833.

Hyatt, C., Mironov, S. & Wellner, M., 2003. Synthesis of voltage-sensitive fluorescence signals from three-dimensional myocardial activation patterns. *Biophysical journal*, 85(October), pp.2673–2683.

Janse, M.J. et al., 1980. Flow of “injury” current and patterns of excitation during early ventricular arrhythmias in acute regional myocardial ischemia in isolated porcine and canine hearts. Evidence for two different arrhythmogenic mechanisms. *Circulation Research*, 47(2), pp.151–165.

Jiménez, Z.A. & Steinbock, O., 2012. Scroll wave filaments self-wrap around unexcitable heterogeneities. *Physical Review E*, 86(3), p.036205.

Keener, P.J. & Tyson, J., 1992. The Dynamics of Scroll Waves in Excitable Media. *Society for Industrial and Applied Mathematics*, 34(1), pp.1–39.

Keldermann, R.H. et al., 2009. A computational study of mother rotor VF in the human ventricles. *American journal of physiology. Heart and circulatory physiology*, 296(2), pp.H370–9.

Keldermann, R.H. et al., 2010. Electromechanical wavebreak in a model of the human left ventricle. , (64), pp.134–143.

Kim, Y.H. et al., 1997. Spatiotemporal complexity of ventricular fibrillation revealed by tissue mass reduction in isolated swine right ventricle. Further evidence for the quasiperiodic route to chaos hypothesis. *The Journal of clinical investigation*, 100(10), pp.2486–500.

Krinsky VI, 1966. Spread of excitation in an inhomogeneous medium (state similar to cardiac fibrillation). *Biofizika (USSR)*, 11, pp.776–784.

Lane, R.E., Cowie, M.R. & Chow, A.W.C., 2005. Prediction and prevention of sudden cardiac death in heart failure. *Heart (British Cardiac Society)*, 91(5), pp.674–680.

Lee, J. & Smith, N.P., 2012. The multi-scale modelling of coronary blood flow. *Annals of Biomedical Engineering*, 40(11), pp.2399–2413.

Lee, J.J. et al., 1996. Reentrant Wave Fronts in Wiggers' Stage II Ventricular Fibrillation Characteristics and Mechanisms of Termination and Spontaneous Regeneration. *Circ.Res*, 78, pp.660–675.

Lee, M.H. et al., 2001. Patterns of wave break during ventricular fibrillation in isolated swine right ventricle. *American journal of physiology. Heart and circulatory physiology*, 281(1), pp.H253–H265.

LeGrice, I.J. et al., 1995. Laminar structure of the heart: ventricular myocyte arrangement and connective tissue architecture in the dog. *The American journal of physiology*, 269(2 Pt 2), pp.H571–82.

Lewis, T., 1925. *The Mechanism and graphic Registration of the Heart Beat*, Shaw and Sons Ltd.

Li, L. et al., 2010. Activation becomes highly organized during long-duration ventricular fibrillation in canine hearts. *American journal of physiology. Heart and circulatory physiology*, 298(6), pp.H2046–53.

Lin, C.-J. et al., 2012. Partitioning the heart: mechanisms of cardiac septation and valve development. *Development (Cambridge, England)*, 139(18), pp.3277–99.

Lin, G.G. & Scott, J.G., 2012. Transmural Heterogeneity and Remodeling of Ventricular Excitation-Contraction Coupling in Human Heart Failure Qing. *NIH Public Access*, 100(2), pp.130–134.

Lunkenheimer, P.P. et al., 2006. Three-dimensional architecture of the left ventricular myocardium. *The anatomical record. Part A, Discoveries in molecular, cellular, and evolutionary biology*, 288(6), pp.565–78.

Luther, S. et al., 2011. Low-energy control of electrical turbulence in the heart. *Nature*, 475(7355), pp.235–239.

Majumder, R., Nayak, A.R. & Pandit, R., 2011. Scroll-wave dynamics in human cardiac tissue: lessons from a mathematical model with inhomogeneities and fiber architecture. *PloS one*, 6(4), p.e18052.

Malyala, S. & Clayton, R., 2013. Clustering of re-entry close to scar boundaries in ventricular tissue during simulated ventricular fibrillation. *Computing in Cardiology*, 40, pp.1131–1134.

Malyala, S., Clayton, R.H. & Kingdom, U., 2014. The Effect of Scar Tissue on Complexity of Activation Patterns in Simulated Human Ventricular Fibrillation. *Computing in Cardiology*, 41, pp.1133–1136.

Massé, S. et al., 2007. Ventricular fibrillation in myopathic human hearts: mechanistic insights from in vivo global endocardial and epicardial mapping. *American journal of physiology. Heart and circulatory physiology*, 292, pp.H2589–H2597.

Mines, G.R., 1913. On dynamic equilibrium in the heart. *The Journal of physiology*.

Muzikant, A.L. et al., 2002. Region specific modeling of cardiac muscle: Comparison of simulated and experimental potentials. *Annals of Biomedical Engineering*, 30(7), pp.867–883.

Nash, M.P. et al., 2006. Evidence for multiple mechanisms in human ventricular fibrillation. *Circulation*, 114(6), pp.536–42.

Nerbonne, J.M. & Kass, R.S., 2005. Molecular physiology of cardiac repolarization. *Physiological reviews*, 85(4), pp.1205–53.

Neu, J. & W, K., 1993. Homogenization of syncytial tissues. *Crit Rev Biomed Eng*, 21(2), pp.137–199.

Niederer, S. a et al., 2009. A meta-analysis of cardiac electrophysiology computational models. *Experimental physiology*, 94(5), pp.486–95.

Nielsen, P. et al., 1991. Mathematical model of geometry and fibrous structure of the heart. *Am. J. Physiol*.

Noble, D., 1960. Cardiac action and pacemaker potentials based on the hodgkin-huxley equations. *NATURE*, 188, pp.495–497.

O'Hara, T. et al., 2011. Simulation of the undiseased human cardiac ventricular action potential: model formulation and experimental validation. *PLoS computational biology*, 7(5), p.e1002061.

Panfilov, a. V. & Rudenko, a. N., 1987. Two regimes of the scroll ring drift in the three-dimensional active media. *Physica D: Nonlinear Phenomena*, 28, pp.215–218.

Panfilov, A. & Keener, J., 1995. Re-entry in an anatomical model of the heart. *Chaos, Solitons & Fractals*, 5(93), pp.681–689.

Panfilov, A. & Keener, J., 1995a. Re-entry in three-dimensional Fitzhugh-Nagumo medium with rotational anisotropy. *Physica D: Nonlinear Phenomena*, 84, pp.545–552.

Panfilov, A. & Keener, J., 1995b. Re-entry in three-dimensional Fitzhugh-Nagumo medium with rotational anisotropy. *Physica D: Nonlinear Phenomena*, 84, pp.545–552.

Panfilov, A. V & Keener, J.P., 1993. Effects of High Frequency Stimulation on Cardiac Tissue with an Inexcitable Obstacle. *J.theor.Biol*.

Panfilov, A.., 2000. Three dimensional wave propagation in mathematical models of ventricular fibrillation. In *Cardiac Electrophysiology: from Cell to Bedside*. pp. 271–277.

Panfilov, A.. & Keener, J., 1993. Generation of Reentry in Anisotropic Myocardium. *Journal of cardiovascular electrophysiology*, 4, pp.412–421.

Panfilov, A.. & Pertsov, A.., 1984. Vortex ring in a 3-dimensional active medium described by reaction-diffusion equations. *Dokl.Akad.Nauk USSR*, 274, pp.1500–1503.

Panfilov, A.., Rudenko, A.. & Krinskii, V.., 1986. Vortex rings in 3-dimensional active media with diffusion in two components. *Biophysical journal*, 31, pp.926–931.

Panfilov, A.., Rudenko, A.. & Krinsky, V.., 1986. Scroll rings in three-dimensional active medium with two component diffusion. *Biofizika*, 31, pp.850–854.

Panfilov, A.., Rudenko, A.. & Pertsov, A.., 1984. Twisted Scroll Waves in Three-Dimensional Active Media. In *Self-Organization Autowaves and Structures Far from Equilibrium*. pp. 103–105.

Panfilov, A.V. & Winfree, A.T., 1985. Dynamical simulations of twisted scroll rings in three-dimensional excitable media. *Physica D: Nonlinear Phenomena*, 17(3), pp.323–330.

Pertsov, A. et al., 2000. Topological Constraint on Scroll Wave Pinning. *Physical Review Letters*, 84(12), pp.2738–2741.

Pertsov, A.., 2000. Scroll wave Dynamics in a three-dimensional Cardiac tissue Model. In *Cardiac Electrophysiology: from Cell to Bedside*. pp. 336–344.

Pertsov, A.M. et al., 1993. Spiral waves of excitation underlie reentrant activity in isolated cardiac muscle. *Circulation Research*, 72(3), pp.631–650.

Plank, G. et al., 2009. Generation of histo-anatomically representative models of the individual heart: tools and application. *Philosophical transactions. Series A, Mathematical, physical, and engineering sciences*, 367(1896), pp.2257–92.

Potse, M. et al., 2006. A comparison of monodomain and bidomain reaction-diffusion models for action potential propagation in the human heart. *IEEE transactions on bio-medical engineering*, 53(12 Pt 1), pp.2425–35.

Qu, Z. et al., 2000a. Scroll wave dynamics in a three-dimensional cardiac tissue model: roles of restitution, thickness, and fiber rotation. *Biophysical journal*, 78(6), pp.2761–75.

Qu, Z. et al., 2000b. Scroll wave dynamics in a three-dimensional cardiac tissue model: roles of restitution, thickness, and fiber rotation. *Biophysical journal*, 78(6), pp.2761–75.

Quinn, T.A. & Kohl, P., 2011. Systems biology of the heart: hype or hope? *Annals of the New York Academy of Sciences*, 1245, pp.40–3.

Rankin, J.S. et al., 1976. The three-dimensional dynamic geometry of the left ventricle in the conscious dog. *Circulation research*, 39, pp.304–313.

Rappel, W.-J., 2001. Filament instability and rotational tissue anisotropy: A numerical study using detailed cardiac models. *Chaos (Woodbury, N.Y.)*, 11(1), pp.71–80.

Roberts, D.E., Hersh, L.T. & Scher, a M., 1979. Influence of cardiac fiber orientation on wavefront voltage, conduction velocity, and tissue resistivity in the dog. *Circulation research*, 44(1976), pp.701–712.

Rogers, J.M. et al., 1999. Incidence, evolution, and spatial distribution of functional reentry during ventricular fibrillation in pigs. *Circulation research*, 84, pp.945–954.

Rogers, J.M., 2002. Wave front fragmentation due to ventricular geometry in a model of the rabbit heart. *Chaos*, 12(2002), pp.779–787.

Rubin, E. & Reisner, H.M., 2014. *Essentials of Rubin's Pathology* Edition 6., Lippincott Williams & wilkins.

Rudy, Y., 1995. Reentry: Insights From Theoretical Simulations in a Fixed Pathway. *Journal of cardiovascular electrophysiology*, 6(4), pp.294–312.

Rush, S. & Larsen, H., 1978. A Practical Algorithm for Solving Dynamic Membrane Equations. *IEEE Transactions on Biomedical Engineering*, 25, pp.389–392.

S.Sridhar, 2010. *Nonlinear Dynamics of Wave Propagation in Heterogeneous Excitable Media*.

Sambelashvili, A. & Efimov, I., 2004. Dynamics of virtual electrode-induced scroll-wave reentry in a 3D bidomain model. *American Journal of Physiology- …*, 63005, pp.1570–1581.

Samie, F.H. et al., 2001. Rectification of the Background Potassium Current: A Determinant of Rotor Dynamics in Ventricular Fibrillation. *Circulation Research*, 89(12), pp.1216–1223.

Samie, F.H. & Jalife, J., 2001. Mechanisms underlying ventricular tachycardia and its transition to ventricular fibrillation in the structurally normal heart. *Cardiovascular Research*, 50(2), pp.242–250.

Samie, F.H. & Jalife, J., 2001. Mechanisms underlying ventricular tachycardia and its transition to ventricular fibrillation in the structurally normal heart. *Cardiovascular research*, 50(2), pp.242–50.

Shajahan, T., Sinha, S. & Pandit, R., 2007. Spiral-wave dynamics depend sensitively on inhomogeneities in mathematical models of ventricular tissue. *Physical Review E*, 75(1), p.011929.

Shannon, T.R. et al., 2004. A mathematical treatment of integrated Ca dynamics within the ventricular myocyte. *Biophys. J*, 87(November), pp.3351–3371.

Sicouri, S. & Antzelevitch, C., 1991a. A subpopulation of cells with unique electrophysiological properties in the deep subepicardium of the canine ventricle. The M cell. *Circulation research*, 68(6), pp.1729–1741.

Sicouri, S. & Antzelevitch, C., 1991b. A subpopulation of cells with unique electrophysiological properties in the deep subepicardium of the canine ventricle. The M cell. *Circulation research*, pp.1729–1741.

Streeter, D.D. et al., 1969. Fiber Orientation in the Canine Left Ventricle during Diastole and Systole. *Circulation Research*, 24(3), pp.339–347.

Taccardi, B. et al., 1994. Effect of myocardial fiber direction on epicardial potentials. *Circulation*, 90(6), pp.3076–90.

Taggart, P. et al., 2003. Electrotonic cancellation of transmural electrical gradients in the left ventricle in man. *Progress in Biophysics and Molecular Biology*, 82, pp.243–254.

Taggart, P. et al., 2001. Transmural repolarisation in the left ventricle in humans during normoxia and ischaemia. *Cardiovascular Research*, 50, pp.454–462.

Thygesen, K., Alpert, J.S. & White, H.D., 2007. Universal definition of myocardial infarction. *European heart journal*, 28(20), pp.2525–38.

ten Tusscher, K.H.W.J. et al., 2004. A model for human ventricular tissue. *American journal of physiology. Heart and circulatory physiology*, 286(4), pp.H1573–89.

ten Tusscher, K.H.W.J. et al., 2009. Organization of ventricular fibrillation in the human heart: experiments and models. *Experimental physiology*, 94(5), pp.553–62.

Ten Tusscher, K.H.W.J., Hren, R. & Panfilov, A. V, 2007. Organization of ventricular fibrillation in the human heart. *Circulation research*, 100(12), pp.e87–101.

ten Tusscher, K.H.W.J. & Panfilov, a V, 2006. Alternans and spiral breakup in a human ventricular tissue model. *American journal of physiology. Heart and circulatory physiology*, 291(3), pp.H1088–100.

Vadakkumpadan, F. et al., 2010. Image-based models of cardiac structure in health and disease. *Wiley Interdisciplinary Reviews: Systems Biology and Medicine*, 2(4), pp.489–506.

Victorri, B. et al., 1985. Numerical integration in the reconstruction of cardiac action potentials using Hodgkin-Huxley-type models. *Computers and biomedical research, an international journal*, 18, pp.10–23.

Vigmond, E.J. & Leon, L.J., 1999. Computationally efficient model for simulating electrical activity in cardiac tissue with fiber rotation. *Annals of biomedical engineering*, 27, pp.160–70.

Vinson, M., Pertsov, A. & Jalife, J., 1994. Anchoring of vortex filaments in 3D excitable media. *Physica D: Nonlinear Phenomena*, 72, pp.119–134.

Waller, I. & Kapral, R., 1984. Spatial and temporal structure in systems of coupled nonlinear oscillators. *Phys. Rev. A*, 30(4), p.2047.

Walton, M.K. & Fozzard, H.A., 1983. The conducted action potential. Models and comparison to experiments. *Biophysical Journal*, 44(1), pp.9–26.

Wickline, S. a. et al., 1992. Structural remodeling of human myocardial tissue after infarction. Quantification with ultrasonic backscatter. *Circulation*, 85(1), pp.259–268.

Wiener, N. & Rosenbllueth, A., 1946. The mathematical formulation of the problem of conduction of impulses in a network of connected excitable elements, specifically in cardiac muscle. *Arch Inst Cardiol Mex.*, 16(3), pp.205–65.

Wiggers, C.J., 1940. The mechanism and nature of ventricular fibrillation. *American Heart Journal*, 20(4), pp.399–412.

Winfree, A.. & Strogatz, S.., 1984. Organizing centres for three-dimensional chemical waves. *Nature*, 311, pp.611–615.

Winfree, A.T., 1989. Electrical instability in cardiac muscle: phase singularities and rotors. *Journal of theoretical biology*, 138, pp.353–405.

Winfree, A.T.T., 1973. Scroll-shaped waves of chemical activity in three dimensions. *Science*, 181(4103), pp.937–939.

Winslow, R.. . et al., 1993. Generation and propagation of ectopic beats induced by spatially localized Na-K pump inhibition in atrial network models. *Proceedings. Biological sciences / The Royal Society*, 254, pp.55–61.

Witkowski, F.X. et al., 1998. Spatiotemporal evolution of ventricular fibrillation. *Nature*, 392(6671), pp.78–82.

Wolf, C.M. & Berul, C.I., 2008. Molecular mechanisms of inherited arrhythmias. *Current genomics*, 9(3), pp.160–8.

Wu, T.J. et al., 2002. Two types of ventricular fibrillation in isolated rabbit hearts: Importance of excitability and action potential duration restitution. *Circulation*, 106, pp.1859–1866.

Xie, F. et al., 2004. A simulation study of the effects of cardiac anatomy in ventricular fibrillation. , 113(5).

Xie, F., Qu, Z. & Garfinkel, A., 1998. Dynamics of reentry around a circular obstacle in cardiac tissue. *Physical Review E*, 58(5), pp.6355–6358.

Zipes, D.P. & Jalife, J., 2004. *Cardiac Electrophysiology from Cell to Bedside* 4th ed., Philadelphia:Elsevier inc.

Zipes, D.P. & Wellens, H.J.J., 1998. Sudden Cardiac Death. *Circulation*, 98(21), pp.2334–2351.